Ocean Impact on Southern African Climate Variability and Water Resources

Report to the
Water Research Commission

by

Mathieu Rouault[1,2], Bellinda Monyela[1], Rodrigue Anicet Imbol Kounge[1,2], Arielle Stella Nkwinkwa Njouodo[1,2], Bastien Dieppois[1,3], Serena Illig[4], Noel Keenlyside[5]

[1]Dept of Oceanography, University of Cape Town
[2]Nansen Tutu Center for Marine Environmental Research, University of Cape Town
[3]Centre for Agro-ecology, Water and Resilience, Coventry University, Coventry, UK
[4]ICEMASA, LEGOS, IRD, France
[5]University of Bergen, Norway

WRC Report No. 2425/1/18
ISBN 978-0-6392-0079-8

February 2019

Obtainable from
Water Research Commission
Private Bag X03
Gezina, 0031

orders@wrc.org.za or download from www.wrc.org.za

Executive summary

The oceans have a profound influence on the weather and climate of South Africa. Not only, most rainfall comes from condensation of water vapor originating from the flux of moisture from ocean to atmosphere but the temperature of the remote and surrounding oceans have an impact of the interannual variability of rainfall. A good example of this remote effect is the impact of the ocean during El Nino when the temperature of the Pacific and Indian Ocean is higher than normal. This creates more rainfall above the higher sea surface temperature thus modifying the global Walker and Hadley circulation. Air usually rises in the equatorial regions, especially above the ocean creating rainfall which increases further the ascending motion of air. The air is eventually pushed poleward and then cools and sinks in the subtropical region where Southern Africa sits, creating high pressure and subsidence which is not favorable to rainfall. This is one of the teleconnection mechanisms linking remote oceanic region to South Africa. The aim of the project was to better understand the role of the ocean on weather, climate and rivers of Southern Africa. Little work has been done to connect streamflow to the El Nino Southern Oscillation previous to that project. We also looked at the tropical Atlantic Ocean, which is closer to us although but smaller where a similar phenomenon to El Nino occurs, the Benguela Nino. Closer to South Africa, the Agulhas Current was known to impact the atmosphere above it due to high turbulent flux of moisture from sea to atmosphere. In the past, due to low resolution reanalyzed climate data that did not integrate the Agulhas Current, it was not possible to study the impact of the Agulhas Current on local climate with reanalyzed climate dataset such as ERA or NCEP. This project made some important advance to that matter using new high resolution reanalyzed climate data and a model and offer some sounds evidence on the impact of the Agulhas Current on coastal rainfall. A list of publication originating directly from the project and a list of student and thesis supported by the project is found at the end of the executive summary.

In more details, chapter 1 highlight the impact of the El Nino Southern Oscillation with its warm phase, El Nino and its cold phase La Nina on streamflow. We highlight important difference from mean condition in streamflow from El Nino years to La Nina years at the Water Management scale with most low flow years occurring during El Nino and high flow years during La Nina. Time series of rain rate and observed streamflow volumes are averaged and analysed according to the 19 former Water Managements Area of South Africa but the conclusion will be valid for the new one. Rain rate and streamflow volumes are analysed from hydrological year 1969/1970 to 2015/2016 and basic useful statistics are presented such as annual cycle, mean, maximum and minimum peak seasonal average and correspond percentage from total. Mean values during El Nino years, La Nina years and normal years are also presented. Correlation with El Nino Southern Oscillation is statistically significant for all summer rainfall areas. El Nino triggers drought and low streamflows and La Nina lead to high rainfall and high streamflows for all summer rainfall areas. Streamflows volumes are 4 to 2 time higher during La Nina than during El Nino. Moreover considering observed streamflows from 1969/1970 to 215/2016, 3 to 5 out of 5 lowest volumes for peak flow season for summer rainfall region correspond to El Nino years and the reverse occurs during La Nina. This offer predictability at the Water Managements Area scale in summer time. At last the severe 2015/2016 drought did not lead to the lowest rainfall or streamflow on record since 1969/1979 or does not rank in the top five for most WMAs. The 2015/2016 drought was in the top 5 lowest volume only for 7 out of 14 summer rainfall WMAs. In chapter 2, we focus on a severe drought that occurred over South Africa during the summer seasons of 2014/2015 and 2015/2016. At the same time the Pacific Ocean was warmer than normal starting in 2014 and leading to the very strong 2015/2016 El Nino. While 2015/2016 was one of the strongest El Nino on record 2014/215 was a weak El Nino. However, both conditions led to extreme drought in Southern Africa and South Africa.

The first objective of chapter 2 is to document the oceanic and climate conditions that occurred during the summer seasons 2014/2015 and 2015/2016 in southern Africa. NCEP Reanalysis data is used to compute the monthly and seasonal scale composite mean and anomalies of large-scale circulations during the summer season 2014/2015 and 2015/2016. Results shows that some months of 2014/2015 and 2015/2016 were typical of the effect of El Niño over Southern Africa, but not all of them. Not all months were dry. We also use the Standard Precipitation Index at different time scales (3 months duration, 5 months duration and 17 months duration) to assess the severity of 2014/2015 and 2015/2016 summer drought compared to the other droughts of the 20 and 21st century (1921 to 2016). The South African Weather Services rainfall data shows that KwaZulu-Natal was the only region within South Africa to have 2015/2016 as the strongest summer drought since 1921. For South Africa summer rainfall region, the 2015/2016 season had the fifth worst drought after the El Nino related drought of 1982/1983 and 1991/1992 and the Non El Nino related drought of 1967/1968 and 1944/1945. At the 17 month scale, an index that encompass two summer season, 2014/2015 and 2015/2016 and the months in-between, this was the third worst drought since summer of 1921/1922.

In chapter 3, we look at the decadal variability of Southern African rainfall and we find that the well know 18 year old cycle reported by others is actually linked to the Pacific Ocean. We examine the changing characteristics of summer and winter southern African rainfall, and their teleconnections with large-scale climate through the dominant timescales of variability since 1901. As determined by wavelet analysis, the summer and winter rainfall indices exhibit three significant timescales of variability over the century: interdecadal (15-28 year), quasi-decadal (8-13 year) and interannual (2-8 years). Teleconnections with global sea-surface temperature and atmospheric circulation anomalies are established here, but are different for each timescale. El Niño Southern Oscillation is the main driver of summer rainfall variability, even at the decadal timescale through its forcing on the Pacific Decadal Oscillation and its colinearity with the Interdecadal Pacific Oscillation. This El Niño Southern Oscillation influence leads to shifts in the Walker circulation, which, at the regional scale, impacts the position of the Southern Indian Convergence Zone modulating the development of deep-convection and the synoptic-scale rain bearing systems over the north-eastern regions of southern Africa. Summer rainfall variability is also related to latitudinal shifts in the subtropical atmospheric circulation, which are, for instance, generating an anomalous low-level easterly moisture flux over the Mascarene High region. Winter rainfall variability, however, is more influenced by the mid-latitude atmospheric variability, in particular the Southern Annular Mode, but interactions with El Niño Southern Oscillation remain, especially in the subtropics.

In chapter 4, we look at the impact of the Agulhas Current on South African Climate. We first study the drivers of the flux of moisture, also called turbulent flux of latent heat; from ocean to atmosphere above the Agulhas current and we seek to find out if the new climate reanalysis datasets do represent well the high exchange of moisture at the surface of the Agulhas Current. In-situ observations (NOCS), climate reanalysis (CFSR, MERRA-2, ERA-Interim, NCEP-R2 and ERA-40) and satellite remote sensing (HOAPS3, SEAFLUX) are used to study the annual cycle of turbulent latent heat flux (LHF) in the Agulhas Current system. We use monthly fields of LHF, sea surface temperature, surface wind speed, saturated specific humidity at the sea surface (Qsst) and specific humidity at 10 m (Q10). We conducted a comparison of products in the Agulhas Current system. CFSR and MERRA-2 are similar to SEAFLUX. ERA-Interim underestimates the LHF. The differences in LHF when compared with SEAFLUX are due to the difference in Q10 and surface wind speed. NCEP-R2 and ERA-40 reanalysis have lower SST in the core of the Agulhas Current due to their low spatial resolution. The highest LHF of about 250 W/m² is found in the Retroflection in winter. The lowest LHF is 100 W/m² off Port Elizabeth in summer. In Durban, Qsst-Q10 is the main driver of the amplitude of the annual cycle of

LHF while it is the wind speed in the Retroflection. Both Qsst-Q10 and wind speed drive the annual cycle of LHF off Port Elizabeth. Having established that CFRS does represent well the intense flux of moisture above the Agulhas Current, we use satellite remote sensing and CFRS climate reanalysis and a regional atmospheric model to show that the Agulhas Current is the main cause of the observed band of rainfall off the south-eastern African coast. The Agulhas current's warm core causes sharp gradients in sea surface temperature and sea level pressure that drive a convergence of low-level winds, resulting in a co-located band of precipitation. Correlations among wind convergence, SLP and SST indicate that the pressure adjustment mechanism is responsible for the low-level convergence and increased rainfall above the Current and adjacent coastal area. Model experiments confirm these results, and indicate that the Agulhas Current generates convective rainfall along the coast.

The next two chapters look at Benguela Niños, an ocean phenomenon that impact rainfall in Southern Africa. Chapter 6 is a detailed study of Benguela Niño that developed in November 2010 and lasted for 5 months along the Angolan and Namibian coastlines. Maximum amplitude was reached in January 2011 with an interannual monthly Sea Surface Temperature anomaly larger than 4°C at the Angola Benguela Front. It was the warmest event since 1995. Consistent with previous Benguela Niños, this event was generated by a relaxation of the trade winds in the western equatorial Atlantic, which triggered a strong equatorial Kelvin wave propagating eastward along the equator and then southward along the southwest African coast. In the equatorial band, the associated ocean sub-surface temperature anomaly clearly shows up in data from the PIRATA mooring array. In contrast to previous Benguela Niños, the initial propagation of sub-surface temperature anomalies along the equator started in October and the associated warming in the Angolan Benguela Front Zone followed on in November 2010. The warming was then advected further south in the Northern Benguela upwelling system as far as 25°S by an anomalously strong poleward sub-surface current. This is similar to mechanisms of El Nino propagation in the Pacific Ocean. Chapter 7 outlines the link between equatorial Atlantic Ocean variability and the coastal region of Angola and Namibia from 1998 to 2012 and opens the door to predictability of Benguela Niños. An index of equatorial Kelvin wave activity is defined based on Prediction and Research Moored Array in the Tropical Atlantic (PIRATA). Along the equator, results show a significant correlation between PIRATA monthly dynamic height anomalies, altimetric monthly Sea Surface Height anomalies (SSHA) and SSHA calculated with an Ocean Linear Model. This allows us to interpret PIRATA records into equatorial Kelvin wave. Estimated phase speed of eastward propagations from PIRATA equatorial mooring remains in agreement with the linear theory, emphasizing the dominance of the second baroclinic mode. Systematic analysis of all strong interannual equatorial SSH anomalies shows that they precede by 1-2 months extreme interannual SST Anomalies (SSTA) along the African coast, which confirm the hypothesis that that major warm and cold events in the Angola-Benguela current system are remotely forced by ocean atmosphere interactions in the equatorial Atlantic. Equatorial wave dynamics is at the origin of their developments. Wind anomalies in the Western Equatorial Atlantic force equatorial downwelling and upwelling Kelvin waves that propagate eastward along the equator and then polewards along the African coast triggering extreme warm and cold events respectively. A proxy index based on linear ocean dynamics appears to be significantly more correlated with coastal variability than an index based on wind variability. Results show a seasonal phasing, with significantly higher correlations between our equatorial index and coastal SSTA in October-April.

Publications originating from the project

Dieppois, B., Pohl, B., Rouault, M., New, M., Lawler, D. and Keenlyside, N., 2016. Interannual to Interdecadal variability of winter and summer southern African rainfall, and their teleconnections. *Journal of Geophysical Research: Atmospheres*. 2016, vol. 121, no 11, p. 6215-6239.

Imbol Koungue R.A., Illig S. and M Rouault 2017 Role of interannual Kelvin wave propagations in the equatorial Atlantic on the Angola Benguela Current system. Geophys. Res. Oceans, 122, 4685-4703, doi:10.1002/2016JC012463.

Nkwinkwa Njouodo, A.S., Koseki, S., Keenlyside, N. and Rouault, M., 2018. Atmospheric signature of the Agulhas Current. Geophysical Research Letters. 45, 5185-5193,

Rouault, M., Illig, S., Lübbecke, J. and Koungue, R.A.I., 2018. Origin, development and demise of the 2010-2011 Benguela Niño. *Journal of Marine Systems*. https://doi.org/10.1016/j.jmarsys.2017.07.007

Theses originating from and students supported by the project

Arielle Stella Nkwinkwa Njouado, PhD in Oceanography, Impact of the Agulhas Current on South African weather and Climate, University of Cape Town, thesis submitted in 2018.

Rodrigue Anicet Imbol Koungue, PhD in Oceanography, Benguela Niños. University of Cape Town, Graduated in 2018.

Georges-Noel Tiersmondo Longandjo, PhD in Oceanography, Central Africa climate variability, University of Cape Town. Graduated in 2018.

Bellinda Monyela, Master of Science in Oceanography, Role of the Ocean in the 2014/2015 and 2015/2016 drought in South Africa summer rainfall region. University of Cape Town. Graduated in 2017.

Tumelo Maja, Benguela Nino, BSc. Hons Oceanography: a view from space, University of Cape Town. Graduated in 2017.

Contents

This page was intentionally left blank

1 Impact of ENSO on groundwater, vegetation and streamflows

1.1 Introduction

While the impact of El Nino Southern Oscillation on Southern Africa rainfall has been well documented (Rouault and Richard, 2003, 2005) with El Nino leading to droughts and La Nina leading to higher summer rainfall 50% of the time El Nino and La Nina occur, less work was done on relating ENSO to streamflow, groundwater, dam level or vegetation. Landman et al. (2001) considered streamflow at the inflow of twelve dams in the Vaal and upper Tugela catchments and a clear link with ENSO was found with correlation of up to 0.7 between streamflows and ENSO index NINO3.4. Sunday et al. (2014) confirm the association between ENSO and streamflows for the Inkomati River Basin in South Africa with a few months lags which offer predictability. The aim of this chapter is do a systematic analysis of 145 streamflow time series from the hydrological year 1969/1970 to 2015/2016 for each of the 19 former Water Management Areas of South Africa with the associated rainfall and look at the association between streamflows and ENSO as well as presenting mean basic parameters such as what percentage of the total annual rainfall fall in the peak rainfall season, what is the peak months for rainfall and streamflow. What are the maximum and minimum averaged streamflow or rainfall ever recorded, what are the 5 driest and wettest years, what are the 5 high or low stream flows years and what is the mean behaviour at the water management scale for El Niños years, La Nina years and normal years. Another objective was to find out what was the behaviour of streamflow during the severe 2014-2016 drought and was it the most severe drought on record while that period corresponded to the strongest El Nino event on record.

Figure 1.1: The 19 former Water Management Areas of South Africa: 1 Limpopo, 2 Luvuvhu and Letaba, 3 Crocodile West and Marico, 4 Olifants, 5 Inkomati, 6 Usutu to Mhlatuze and Swaziland, 7 Thukela, 8 Upper Vaal, 9 Middle Vaal, 10 Lower Vaal, 11 Mvoti and Umzimkulu, 12 Mzimvubu and Umzimkulu, 13 Upper Orange, 14 Lower Orange, 15 Fish to Tsitsikamma, 16 Gouritz, 17 Olifants Doring, 18 Breede, 19 Berg.

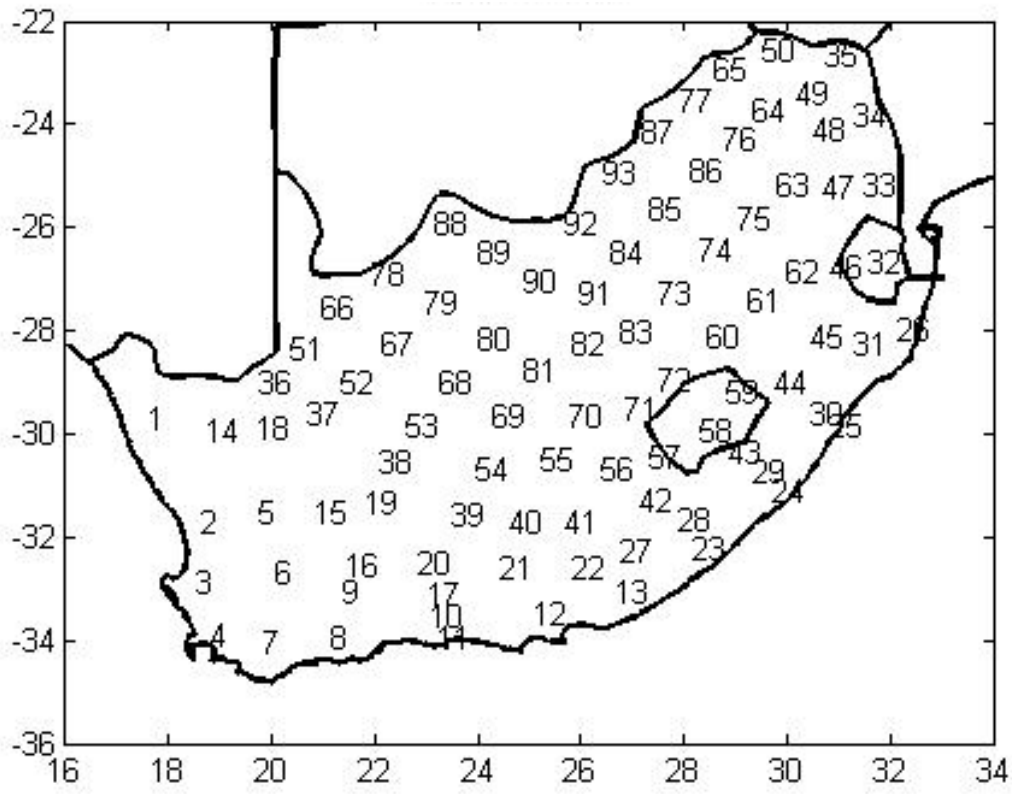

Figure 1.2: The 93 SAWS rainfall districts.

1.2 Data

1.2.1 Rainfall

The SAWS divides the country into 93 rainfall districts based on a cluster analysis of South African rainfall. Each district combines an average of typically 5 to 15 rain-gauge stations. Districts corresponding to the 19 WMAs were averaged together. Figure 1.2 shows the location of the 93 districts and their number. Rainfall dataset start in 1920 and end up in 2016 and is updated continuously while a few stations start in 1928. In that report, we present an analysis of the 95 districts corresponding to the 19 WMAs, namely annual cycle of rainfall, annual total, monthly median, mean peak seasonal total, % contribution of peak seasonal total to annual total, peak seasonal total during El Niño, Normal year and La Nina and ratio between La Nina year peak seasonal total and El Nino years peak seasonal total (Table 1.1). Various statistics are also inferred such as trends, correlations with ENSO and 5 driest and wettest peak season rainfall totals per WMA as well as ratio between La Nina Year and El Nino year. Normalised anomalies and also presented for each WMA together with WMA mean streamflow during peak streamflow season.

1.2.2 Streamflows

We are using streamflows data from WR2005 up to 2003/2004 updated with data available on the DAWF web site up to hydrological year 2015/2016. Here we are using 150 stations for 19 WMAs with record longer than 45 years starting in 1969/1970 and finishing in 2015/2016. We are using hydrological year starting in October and finishing in September. In WR2005 or the web site, data are coded according to the quaternary catchment and tertiary or WMA they represent. In WR2005, A list of all

streamflows gauging stations was obtained and new stations were identified. However, patching (by linear regression) was only done where a good correlation was achieved with nearby gauges. Patched observed volume in million cubic meter flow data files were grouped according to WMA and averaged. We are presenting here time series of data averaged per WMA from 1969/1970 to 2015/2016

1.3 Results

1.3.1 Annual cycle

Mean rainfall was calculated by averaging all rain gauges of each WMA and results are presented in Figure 1.2 and Table 1.1. Most stations start in 1920 and end up in 2004 while a few station starts in 1928 but we only present the mean from 1969/1970 to 2015/2016. The annual cycle of rainfall for WMA 1 Limpopo to WMA 8 Upper Vaal is quite similar with distinct maximum in January ranging for 80 to 150 and most rainfall falling from November to March (Figure 1.2 and Table 1.2). The annual cycle for WMA 9 Middle Vaal to WMA 13 Upper Orange maximum is less distinct than previous WMA with less difference from November to March than the rest of the year as for previous WMA and very similar maximum at about 100 mm in January. WMA 14 Lower Orange and WMA 15 Fish to Tsitsikamma have a peak in March. WMA 16 Gouritz experiences equal rainfall all year long while WMA 17 to 19 Olifants, Doring and Berg have a clear winter peak in rainfall with maximum in June ranging from 40 to 110 mm. The annual and peak season total (5 months) totals are given in Table 1.1. Observed streamflows volume time series data from the common period 1969/1970 to 2015/201604 were summed per WMA when the most data was available across all WMAs. The mean monthly streamflows volumes are presented in Figure 1.3 while Table 1.2 is showing the number of stations used to sum up each WMA, the mean annual mean monthly streamflow volume in millions of cubic meter, the median, the peak season average monthly mean streamflow volume (December to April for WMA 15, October to September for WMA 16. May to September WMA 17 to 19), the percentage peak season volume mean versus annual total volume which corresponds to the peak season contributions to annual total, the maximum peak season mean monthly streamflow volume that occurred from 1969 to 2004, the minimum peak season mean streamflow volume that occurred from 1969 to 2004, the average monthly peak season mean streamflow volume during El Niño years, normal years and La Nina La Nina years and the ration of peak season mean streamflows during La Nina divided by El Niño. The number of stations used was from 1 to 15 stations per WMA (Table 1.2). The most striking result is that for WMA corresponding to summer rainfall areas, volumes are between 1.7 to 4.2 times higher during La Nina years than during El Niño years while ration for rainfall ration El Nina versus El Nino varies from 1.2 to 1.9. This give ample time for early warning at the water management areas scale because El Niño and La Nina start well before austral summer and are fully mature in summertime. Otherwise, the annual cycle of streamflows volume is following the annual cycle of rainfall with one month lag or no lag. Maximum volume month in the annual cycle is February for WMA 1 to 11 and 13 while it is in March for WMA 14 and 15. For the winter areas WMA 17 and 19, maximum occurs in July, a month after the maximum rainfall month while there is a two month lag for WMA 8. Not surprisingly WMA 16 has a bimodal flow all year long with a peak in November and a peak in August. WMA 17 to 19 experiences about 15% higher flow during El Niño than during La Nina. Maximum peak season is 3 to 5 time the mean annual total while the minimum peak season volume range from 25% to 1% of mean peak season volume. Next we are looking at the annual cycle of rainfall and mean streamflow for the 19 WMAs.

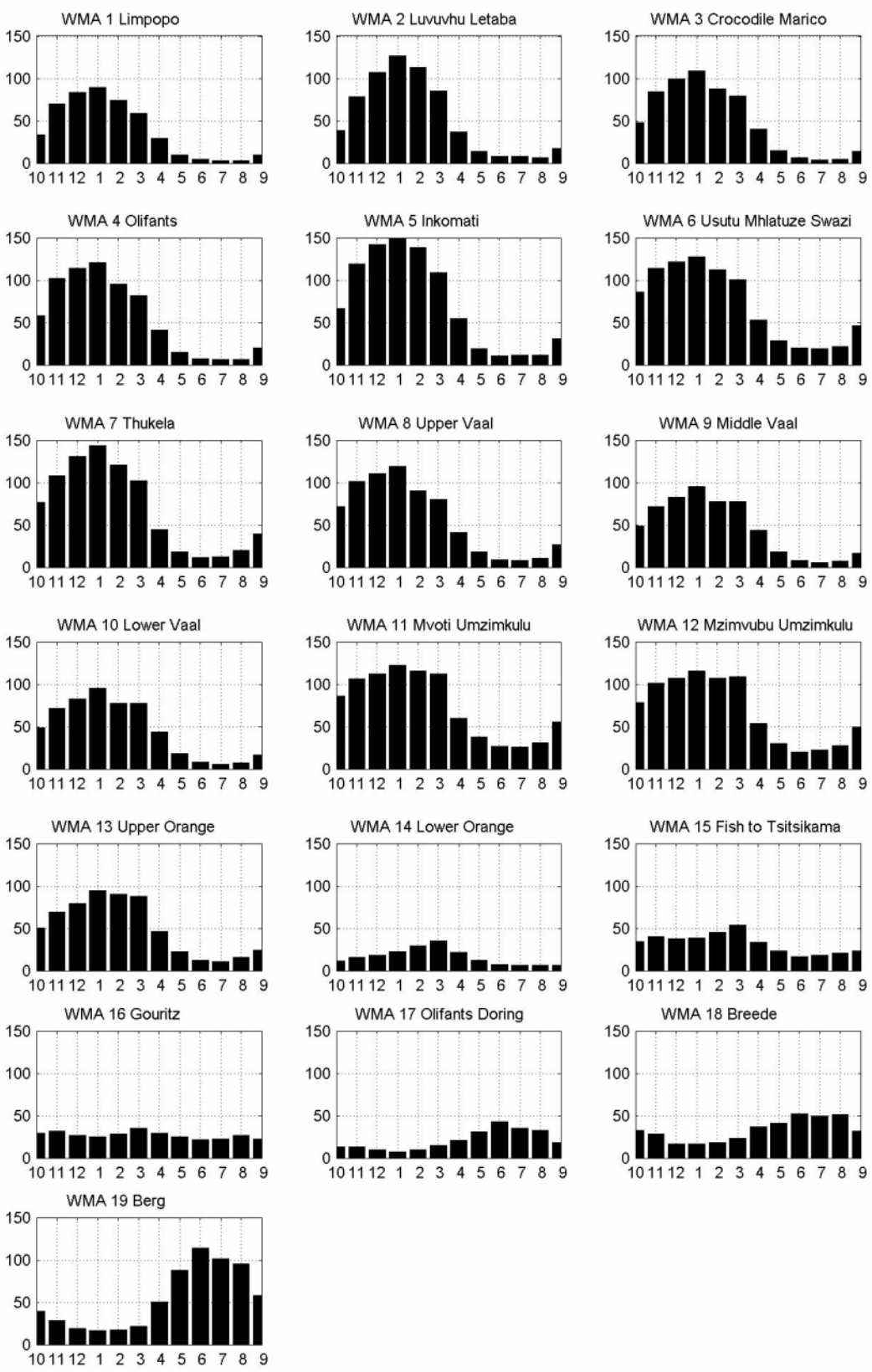

Figure 1.3: Annual cycle of rainfall in mm from October to September for the 19 WMAs

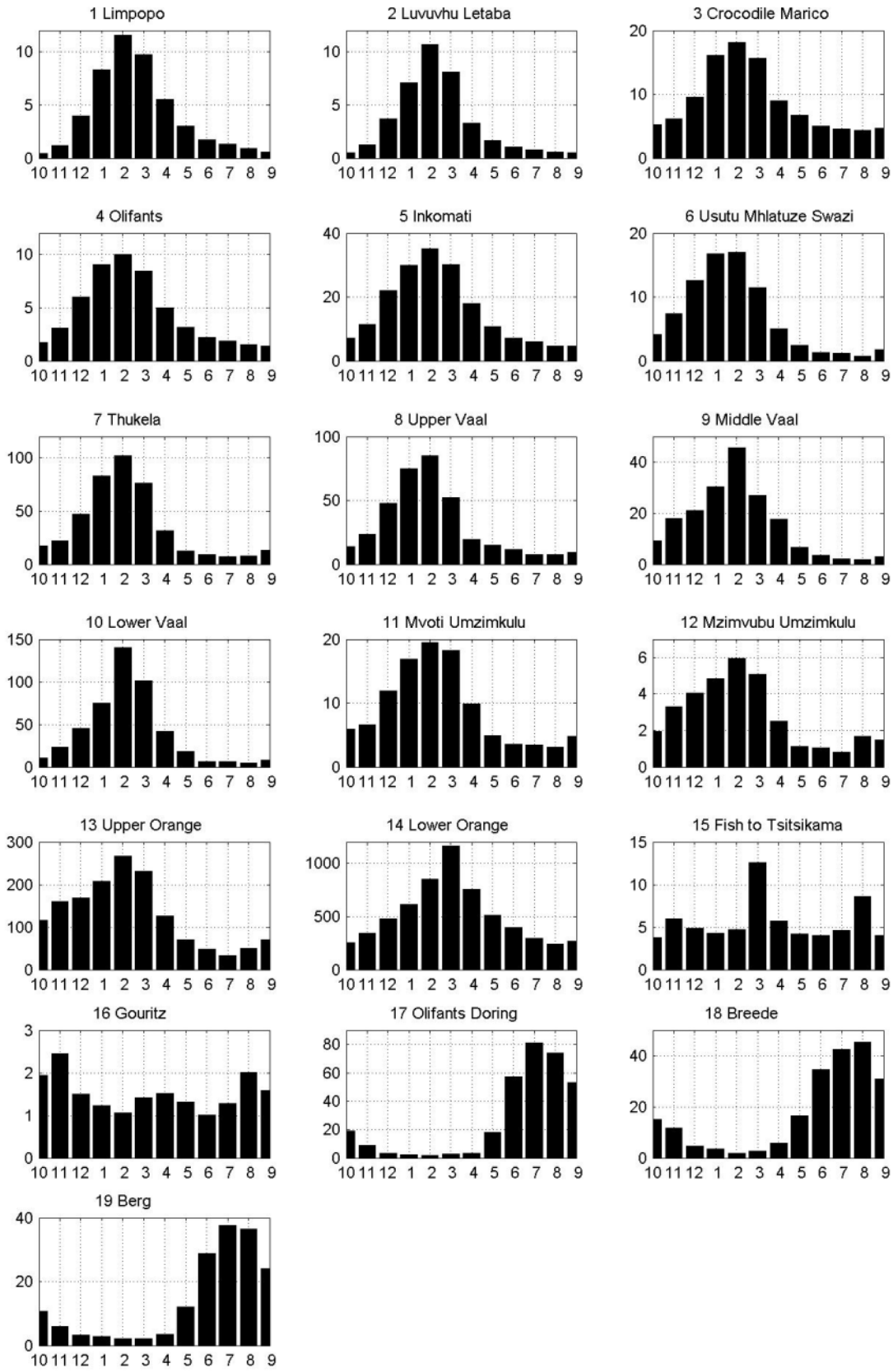

Figure 1.4: Mean annual cycle of total observed volume in millions cubic meter per WMA from October to September

Table 1.1: WMA number, mean annual rainfall total (mm), mean total peak season, Percentage contribution from peak season to total rainfall in % (November to March for WMA 1 to 15, October to September for WMA 16. May to August for WMA 17 to 19), mean peak season total, 1920-2005 maximum peak season total, minimum peak season total, average peak season total during El Niño, average peak season total during normal years, average peak season total during La Nina (mm). Ratio between La Nina and El Niño years.

WMA	Annual rain total (mm)	Total peak season (mm)	% peak season versus total (%)	Mean monthly peak season (mm)	Max peak season monthly (mm)	Min peak season total (mm)	Mean peak season El Niño (mm)	Total peak season Normal (mm)	Total peak season La Nina (mm)	% La Nina vs El Niño
1	461	370	80	74	717	205	311	383	426	1.370
2	639	507	79	101.4	1150	208	403	522	618	1.533
3	586	462	79	92	716	232	403	468	529	1.313
4	661	513	78	102.6	886	317	438	524	592	1.352
5	861	661	77	132.2	1205	301	523	678	817	1.564
6	836	567	68	113.4	1074	262	486	586	641	1.319
7	825	604	73	120.8	996	331	540	617	665	1.231
8	677	497	73	99.4	828	284	458	499	547	1.194
9	560	409	73	81.8	651	172	365	410	467	1.279
10	560	409	73	81.8	651	172	365	410	467	1.279
11	883	557	63	111.4	943	291	498	554	645	1.296
12	840	548	65	109.6	955	264	496	527	661	1.333
13	634	446	70	89.2	806	216	379	441	545	1.439
14	204	131	64	26.2	379	44	99	121	195	1.965
15	408	232	57	46.4	479	81	192	222	306	1.600
16	345	345	100	69	611	189	305	372	366	1.199
17	267	173	65	34.6	289	81	176	174	158	0.897
18	418	246	59	49.2	396	149	260	245	224	0.862
19	645	446	69	89.2	741	266	452	441	425	0.940

Table 1.2: Observed patched streamflows. Number of stations used to sum up each WMA (N) r, mean annual total (mean), median annual total (median), peak season total (November to March for WMA to 15, October to September for WMA. Mai to August for WMA17 to 19), percentage peak season total versus annual total (%), maximum peak season total (max), minimum peak season total (min), average peak season total during El Niño years (Niño), average peak season total during normal years (Norm), average peak season total during Normal years (Nina)

WMA	N	mean	median	peak	%	max	min	Niño	Norm	Nina	%
1	9	4	3	8	80	29	0	4	8	13	3.028
2	2	3	3	7	84	54	0	3	6	13	4.223
3	8	9	6	14	64	48	2	11	12	20	1.910
4	8	4	4	8	72	27	2	5	8	12	2.374
5	16	16	15	27	72	97	3	16	27	43	2.736
6	8	7	6	13	76	43	1	10	13	15	1.601
7	10	37	31	69	78	203	9	45	63	103	2.270
8	6	31	17	56	75	330	3	40	47	96	2.429
9	2	15	9	28	77	164	1	17	22	56	3.366
10	3	40	9	81	83	503	4	56	57	161	2.885
11	10	9	8	15	70	50	4	12	14	22	1.750
12	9	3	3	4	66	14	0	3	4	7	2.433
13	6	129	109	200	64	683	28	141	193	298	2.118
14	1	513	296	772	63	3867	55	680	591	1297	1.908
15	7	6	4	6	48	51	0	4	4	15	3.705
16	17	2	1	2	100	5	0	1	2	2	1.045
17	2	27	22	57	89	195	12	65	53	57	0.874
18	15	18	17	34	80	99	9	39	33	32	0.830
19	6	14	13	28	83	68	8	31	27	27	0.866

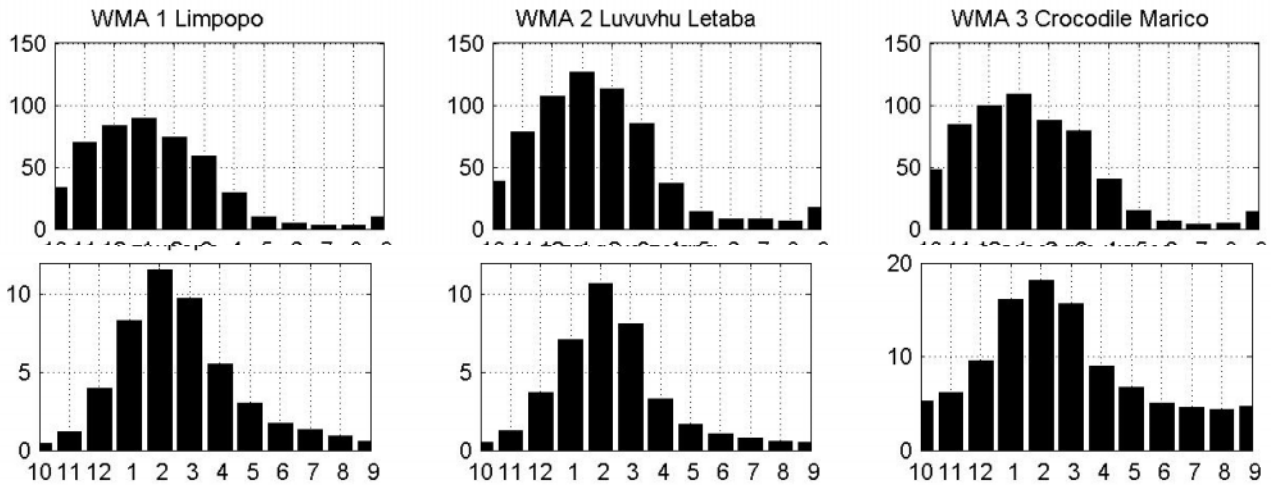

Figure 1.5: Annual cycle of rainfall (top) and average streamflow (bottom) volume for WMA 1 to 3

Mean rainfall is maximum in January for WMA 1 while mean streamflow volume is maximum in February. Peak season rainfall (November to March) contribution to annual total is 80%. Monthly mean rainfall during peak season is 74 mm/month while peak season volume for WMA 1 is 40 million cubic metres which correspond to 80% of annual total. Mean rainfall is maximum in January for WMA 2 while mean streamflow volume is maximum in February. Peak season rainfall (November to March) contribution to annual total is 79%. Monthly mean rainfall during peak season is 101 mm/month while peak season volume for WMA 2 is 35 million cubic metres which correspond to 84% of annual total. Mean rainfall is maximum in January for WMA 3 while mean streamflow volume is maximum in February. Peak season rainfall (November to March) contribution to annual total is 79%. Monthly mean rainfall during peak season is 92 mm/month while peak season volume for WMA is 70 million cubic metres which correspond to 64% of annual total

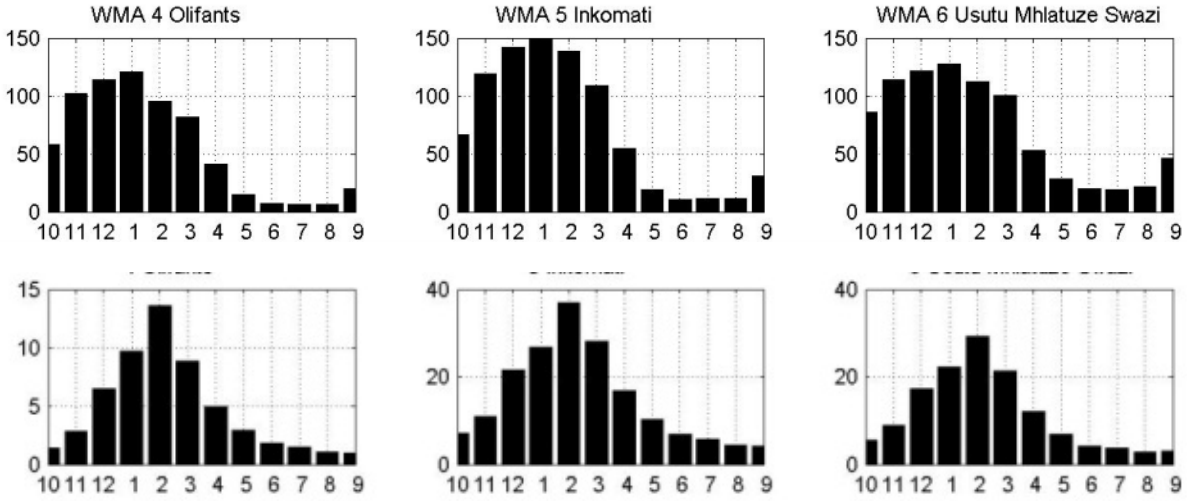

Figure 1.6: Annual cycle of rainfall (top) and streamflow (bottom) for WMA 4 to 6

Mean rainfall is maximum in January for WMA 4 while mean streamflow volume is maximum in February. Peak season rainfall (November to March) contribution to annual total is 78%. Monthly mean rainfall during peak season is 102 mm/month while peak season volume for WMA is 40 million cubic metres which correspond to 72% of annual total. Mean rainfall is maximum in January for WMA 5

while mean streamflow volume is maximum in February. Peak season rainfall (November to March) contribution to annual total is 77%. Monthly mean rainfall during peak season is 132 mm/month while peak season volume for WMA 5 is 135 million cubic metres which correspond to 72% of annual total. Mean rainfall is maximum in for WMA 6 while mean streamflow volume is maximum in February. Peak season rainfall (November to March) contribution to annual total is 68%. Monthly mean rainfall during peak season is 113 mm/month while peak season volume for WMA is 65 million cubic metres which correspond to 76% of annual total. Mean rainfall is maximum in January for WMA 7 while mean streamflow volume is maximum in February. Peak season rainfall (November to March) contribution to annual total is 73%. Monthly mean rainfall during peak season is 120 mm/month while peak season volume for WMA 7 is 345 million cubic metres which correspond to 78% of annual total. Mean rainfall is maximum in January for WMA 8 while mean streamflow volume is maximum in February. Peak season rainfall (November to March) contribution to annual total is 73%. Monthly mean rainfall during peak season is 99 mm/month while peak season volume for WMA 8 is 280 million cubic metres which correspond to 75% of annual total. Mean rainfall is maximum in January for WMA 9 while mean streamflow volume is maximum in February. Peak season rainfall (November to March) contribution to annual total is 73%. Monthly mean rainfall during peak season is 81 mm/month while peak season volume for WMA 9 is 140 million cubic metres which correspond to 77% of annual total

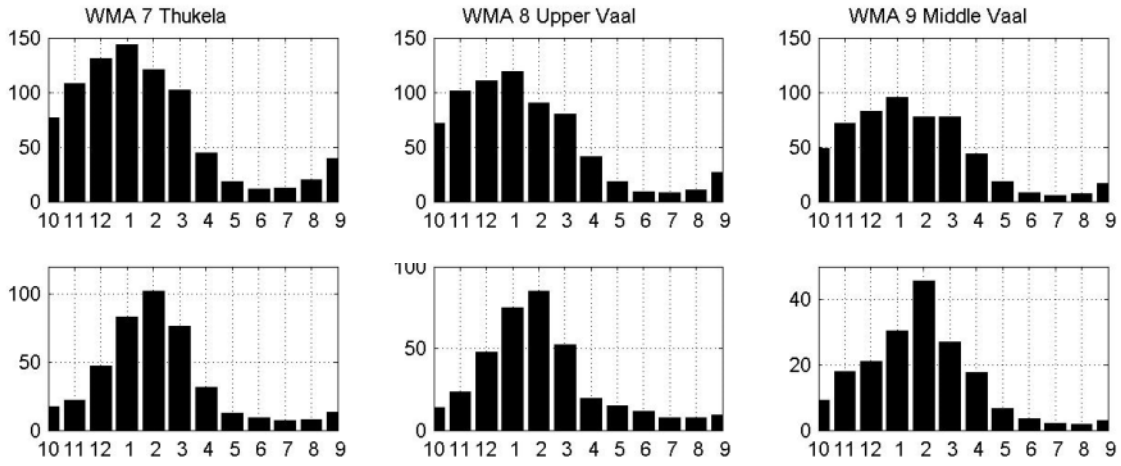

Figure 1.7: Annual cycle of rainfall (top) and streamflow (bottom) for WMA 7 to 9

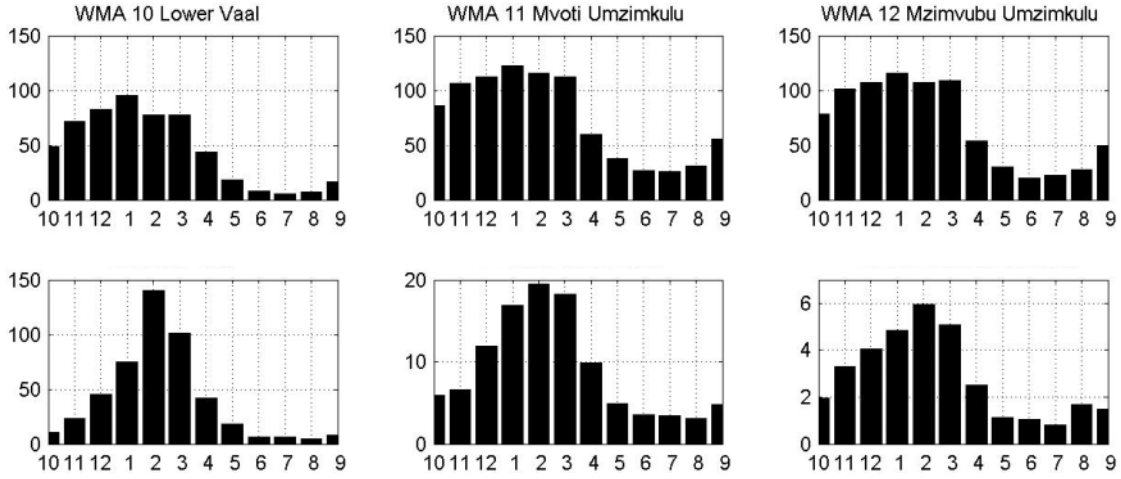

Figure 1.8: Annual cycle of rainfall (top) and streamflow (bottom) for WMA 10 to 12

Mean rainfall is maximum in January for WMA 10 while mean streamflow volume is maximum in February. Peak season rainfall (November to March) contribution to annual total is 73%. Monthly mean rainfall during peak season is 82 mm/month while peak season volume for WMA 10 is 405 million cubic metres which correspond to 83% of annual total. Mean rainfall is maximum in January for WMA 11 while mean streamflow volume is maximum in February. Peak season rainfall (November to March) contribution to annual total is 63%. Monthly mean rainfall during peak season is 111 mm/month while peak season volume for WMA 11 is 75 million cubic metres which correspond to 70% of annual total. Mean rainfall is maximum in January for WMA 12 while mean streamflow volume is maximum in February. Peak season rainfall (November to March) contribution to annual total is 65%. Monthly mean rainfall during peak season is 109 mm/month while peak season volume for WMA 12 is 20 million cubic metres which correspond to 66% of annual total. Mean rainfall is maximum in January for WMA 13 while mean streamflow volume is maximum in February. Peak season rainfall (November to March) contribution to annual total is 70%. Monthly mean rainfall during peak season is 89 mm/month while peak season volume for WMA 13 is 1000 million cubic metres which correspond to 64% of annual total.

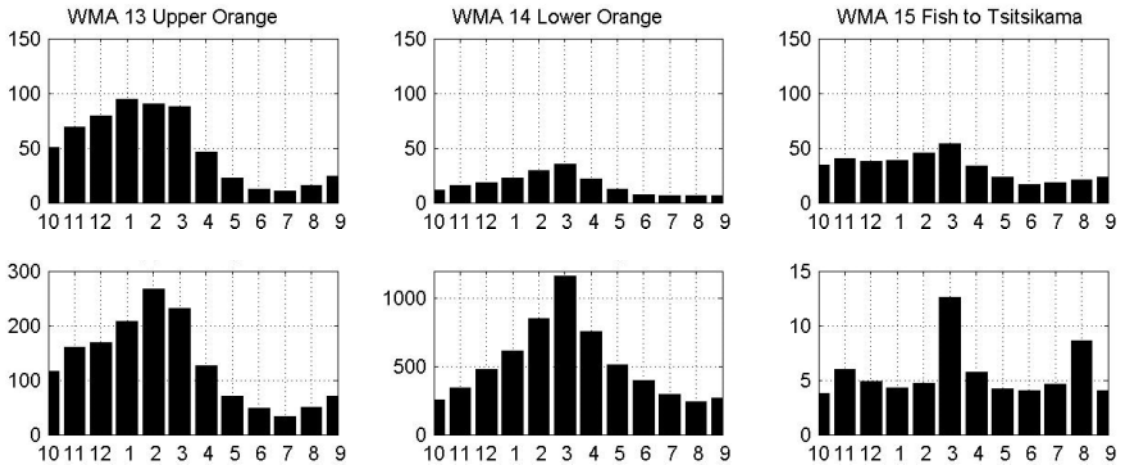

Figure 1.9: Annual cycle of rainfall (top) and streamflow (bottom) for WMA 13 to15

Mean rainfall is maximum in March for WMA 13 while mean streamflow volume is maximum in March. Peak season rainfall (November to March) contribution to annual total is 64%. Monthly mean rainfall during peak season is 24 mm/month while peak season volume for WMA 14 is 3860 million cubic metres which correspond to 63% of annual total. Mean rainfall is maximum in March for WMA 15 while mean streamflow volume is maximum in March. Peak season rainfall (November to March) contribution to annual total is 57%. Monthly mean rainfall during peak season is 6 mm/month while peak season volume for WMA 15 is 30 million cubic metres which correspond to 48% of annual total.

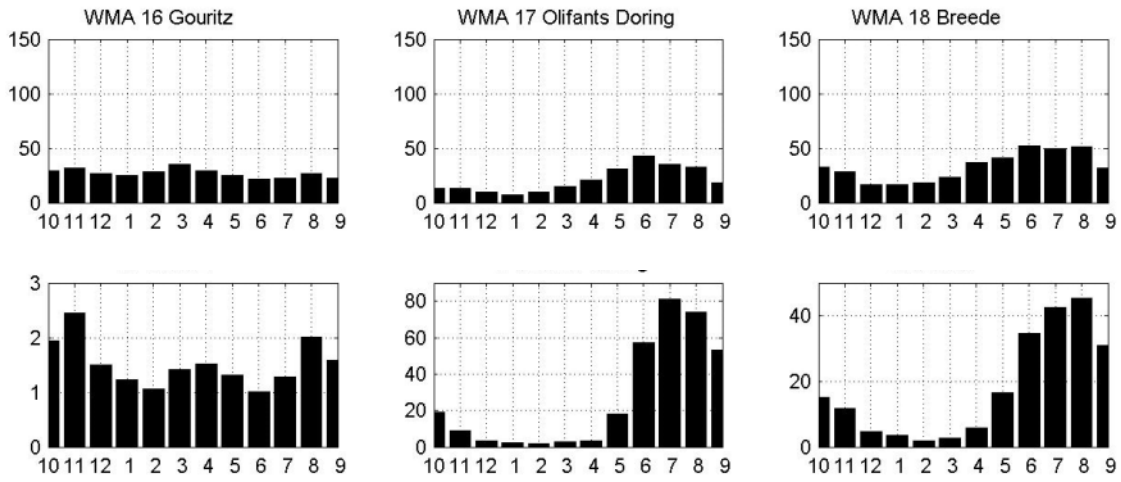

Figure 1.10: Annual cycle of rainfall (top) and streamflow (bottom) for WMA 16 to18

Mean rainfall is maximum in March for WMA 16 while mean streamflow volume is maximum in November. Monthly mean rainfall during peak season is 31 mm/month while peak season volume for WMA 16 is 2 million cubic metres. There is a problem in the calculation of rainfall and stream flow here as mean rainfall is higher than it should be according to Figure 1.10. Mean rainfall is maximum in June for WMA 17 while mean streamflow volume is maximum in July. Peak season rainfall (May to September) contribution to annual total is 65%. Monthly mean rainfall during peak season is 34 mm/month while peak season volume for WMA is 185 million cubic metres which correspond to 89% of annual total. Mean rainfall is maximum in June for WMA 18 while mean streamflow volume is maximum in August. Peak season rainfall (May to September) contribution to annual total is 59%. Monthly mean rainfall during peak season is 49 mm/month while peak season volume for WMA 18 is 70 million cubic metres which correspond to 80% of annual total

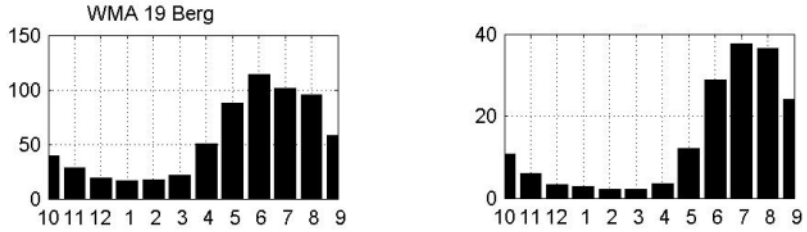

Figure 1.11: Annual cycle of rainfall (left) and streamflow (right) for WMA 19

Mean rainfall is maximum in June for WMA 19 while mean streamflow volume is maximum in July. Peak season rainfall (May to September) contribution to annual total is 69%. Monthly mean rainfall during peak season is 89 mm/month while peak season volume for WMA 19 is 145 million cubic metres which correspond to 83% of annual total.

1.3.2 Interannual variability

In this section, we analyse the interannual variability of rainfall, observed for the 19 WMAs. We are investigating the correlation between ENSO and the 19 WMAs peak rainfall season and we are identifying the 10 driest and wettest years for the 19 WMAs as well as the 5 lowest and highest flow peak flow year. Other climate index such as the Antarctic Annular Oscillation, the Indian Ocean Dipole,

the subtropical Indian Ocean Dipole were found to be not well correlated with South African rainfall in a previous WRC report (Rouault et al., 2001) and in Pohl et al. (2010). They were therefore not considered for that study. Before looking at those results, we are presenting the El Niño (red), normal (black) and La Nina (blue) years from 1920 to 2005 in Figure 1.6 for summer (top), winter (middle) and all year long (bottom). Correlation between ENSO and WMA are respectively: WMA 1 -0.4794; WMA 2 -0.5015; WMA 3 -0.4501; WMA 4 -0.4830; WMA 5 -0.6334; WMA 6 -0.4683; WMA 7 -0.4715; WMA 8 -0.4011; WMA 9 -0.4937; WMA 10 -0.4937; WMA 11 -0.4586; WMA 12 -0.5691; WMA 13 -0.5955; WMA 14 -0.5648; WMA 15 -0.6130; WMA 16 -0.3166; WMA 17 0.1638; WMA 18 0.2682; WMA 19 0.1110.

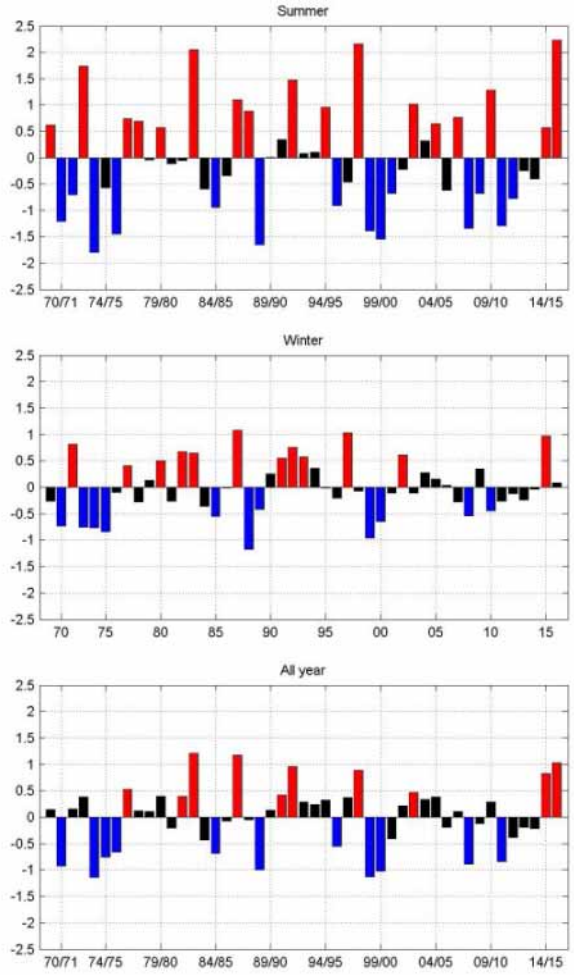

Figure 1.12: Top: El Niño years (red), normal years (black) and La Nina years (Blue) used in that study from 1969/1970 to 2015/2016 for summer (November to March). Middle: May to August. Bottom: all year long (October to September) based on the NIÑO3.4 index.

For the summer rainfall regions corresponding to WMA 1 to 15, we are using 11 Nina years and 11 Niño years and 23 normal years out of 45 years by averaging the NIÑO3.4 Index, an index representing the El Niño Southern Oscillation quite well and usually well correlated with Southern African rainfall. Years are picked up based on two criteria. First, we want the same number of Niño years and Nina years and the index must be greater or smaller than one standard deviation. However, since the NIÑO3.4 INDEX seems to be skewed towards positive values, the limit for La Nina is set at -0.7 to have the same number of La Nina and El Niño events. It is by no mean a definitive ENSO classification but it is giving some indication of anomalous events in the Pacific. El Niño years (red) and La Nina year (Blue) used

in that study from 1969/1970 to 2015/2016 are obtained by averaging the NIÑO3.4 Index from November to March for summer and WMA 1 to 15, October to September for all year long WMA 16 and May to August for the winter region WMA 17 to 19 and are presented in Figure 1.12. For WMA 1 to 15, La Nina years by order of intensity (highest to lowest) are 1973/1974, 1988/1989, 1999/2000, 1975/1976, 1998/1999, 1970/1971, 1984/1985, 1983/1984, 1995/1996, 2010/2011, 2011/2012 and 1974/1975. For WMA 1 to 15, El Niño years are 1997/1998, 2015/2016, 1982/1983, 1991/1992, 1972/1973, 2009/2010, 1986/1987, 2002/2003, 1994/1995, 1987/1988, 1976/77, 2014/2015. For WMA 16 corresponding to the all year rainfall region, we average the NIÑO3.4 all year round from October to September and pick up 11 La Nina years and 11 Niño years. There are less Niño and Nina years than for summer only because some ENSO events lasted less than a year. For WMA 16, La Nina years that we considered are 1988/1989, 1973/1974, 1955/1956, 1998/1999, 1999/2000, 1970/1971, 1984/1985, 1974/1975, 1975/1976 and El Niño years are 1982/1983, 1986/1987, 1991/1992, 2015/2016, 1997/1998, 2014/2016; 2002/2003; 1990/1991, 1976/1977, 1980/1981. For the winter rainfall region corresponding to WMA 17 to 19, we average the NIÑO3.4 index from May to August. We pick up 11 Niño and 11 Nina years. Because ENSO start developing usually in austral autumn we have therefore fewer events to consider than for summer only. Corresponding La Nina years are 1998, 1974, 1970, 1973, 1988, 1999, 1987, 1984, 2008, 2010 and corresponding El Niño years are 2015, 1987, 1997, 1992, 1983, 1993, 1982, 1991, 1977,1980, 2002. Figure 1.13 presents the corresponding seasonal anomalies from the mean divided by the standard deviation. One can objectively define an abnormal event when the normalised seasonal anomaly is above 1 or below -1. Figure 1.13 indicate the high interannual variability of rainfall in South Africa and the important role of La Nina for wetter than normal season and of El Nino for drier than normal for summer rainfall region while it is the opposite for the winter rainfall regions WMA 17 to 19. Total peak season rainfall during El Niño, normal years and La Nina are shown in Table 1.1. On average it rains 20 to 25% more during La Nina than during El Niño for the summer rainfall areas. Another interesting result is that during some El Niño one can have high peak season total. Some El Niño years sometimes fails to create any droughts. Likewise, some La Nina years do not lead to higher than normal rainfall. Also the intensity of ENSO is not proportional to the climate disturbance for instance 1991/1992 was not a strong El Niño but led to widespread droughts similar to droughts created by the 1982/1983 strong El Niño event. Observed streamflows time series data were summed per WMA for the period 1969 to 2004. Yearly total for peak season streamflows for each WMA is presented in Figure 1.10 with corresponding El Nino years (red), La Nina years (blue) and normal years (black) while Table 1.2 gives the average peak season total during El Nino years, normal years, La Nina years and the percentage of average peak season streamflows during La Nina versus El Nino for WMA 1 to 15 and the inverse for WMA 17 to 19. The most striking result is that for WMA 1 to 15, summer rainfall areas, flows are between 1. 6 to 2.8 time higher during La Nina years than during El Nino years. Because El Nino and La Nina start before austral summer, this gives enough time to establish an early warning at the water management area scale. The 5 highest flow and lowest flow years for all WMAs with corresponding El Nino years (red), La Nina years (blue) and normal years (black) are presented in appendix 2. 4 or 5 out of the 5 lowest flow years in summer occur during El Nino, while 4 or 5 out of the 5 highest flow years occur during La Nina. Similar relationship for the recent period are observed for the naturalised river flows (Figure 1.11) with an overwhelming role of ENSO in high and low years and a lesser percentage El Nino years versus Nina years. For WMA 1, the 5 driest are 2002/2003 1985/1986 1991/1992 1972/1973 1982/1983 and the 5 wettest years are 1999/2000 2003/2004 2008/2009 1987/1988 1973/1974 4 out of the 5 driest years are El Nino and 3 years out of the 5 wettest year are La Nina years. The 5 lowest volume year are 1991/1992 1992/1993 1985/1986 1994/1995 1982/1983. 3 of the lowest volume year out of 5 happen during El Nino.

For WMA 2, the 5 driest are 1991/1992 1982/1983 1969/1970 1972/1973 1985/1986 and the 5 wettest years are 1999/2000 2013/2014 1990/1991 1984/1985 2012/2013. 4 out of the 5 driest years are El Nino and 3 years out of the 5 wettest years are La Nina years. The 5 lowest volume year are 1991/1992 1972/1973 2004/2005 2002/2003 1982/1983. 5 of the lowest volume year out of 5 happen during El Nino.

For WMA 3, the 5 driest are 2006/2007 1991/1992 1978/1979 1985/1986 1982/1983 and the 5 wettest years are 1999/2000 1980/1981 2008/2009 1987/1988 1970/1971. 3 out of the 5 driest years are El Nino and 3 years out of the 5 wettest years are La Nina years. The 5 lowest volume year are 1972/1973 1985/1986 1969/1970 1982/1983 1984/1985 and the 5 highest volume years are 1999/2000 2014/2015 2012/2013 1976/1977 2015/2016. 3 of the lowest volume year out of 5 happen during El Nino.

For WMA 4, the 5 driest are 4 2002/2003 1991/1992 1982/1983 1978/1979 1985/1986 and the 5 wettest years are 1999/2000 2008/2009 2007/2008 1989/1990 1987/1988. 3 out of the 5 driest years are El Nino and 3 years out of the 5 wettest years are La Nina years. The 5 lowest volume year are 1982/1983 1991/1992 2015/2016 2002/2003 1994/1995. 5 of the lowest volume year out of 5 happen during El Nino.

For WMA 5, the 5 driest are 2002/2003 2015/2016 1982/1983 1991/1992 1969/1970 and the 5 wettest years are 1999/2000 1983/1984 1984/1985 1990/1991 1987/1988. 5 out of the 5 driest years are El Nino and 3 years out of the 5 wettest years are La Nina years. The 5 lowest volume year are 1982/1983 1994/1995 1993/1994 2015/2016 1991/1992. 4 of the lowest volume year out of 5 happen during El Nino

For WMA 6, the 5 driest are 2015/2016 1982/1983 1994/1995 2014/2015 1991/1992 and the 5 wettest years are 1983/1984 1987/1988 2000/2001 1988/1989 2010/2011. 5 out of the 5 driest years are El Nino and 4 years out of the 5 wettest years are La Nina years. The 5 lowest volume year are 1982/1983 2015/2016 1994/1995 1984/1985 1991/192. 4 of the lowest volume year out of 5 happen during El

For WMA 7, the 5 driest are 2015/2016 1982/1983 2002/2003 2011/2012 1994/1995 and the 5 wettest years are 1995/1996 2008/2009 1980/1981 1993/1994 1989/1990. 4 out of the 5 driest years are El Nino and 3 years out of the 5 wettest years are La Nina years. La Nina year 2011/2012 was a top 5 dry year. The 5 lowest volume year are 1982/1983 1994/1995 2015/2016 1992/1993 2002/2003. 4 of the lowest volume year out of 5 happen during El Nino

For WMA 8, the 5 driest are 1982/1983 1978/1979 1991/1992 2006/2007 1981/1982 and the 5 wettest years are 1995/1996 1983/1984 1973/1974 1990/1991 1993/1994. 3 out of the 5 driest years are El Nino and 3 years out of the 5 wettest years are La Nina years. The 5 lowest volume year are 1982/1983 1978/1979 1991/1992 1981/1982 1972/1973. 3 of the lowest volume year out of 5 happen during El Nino

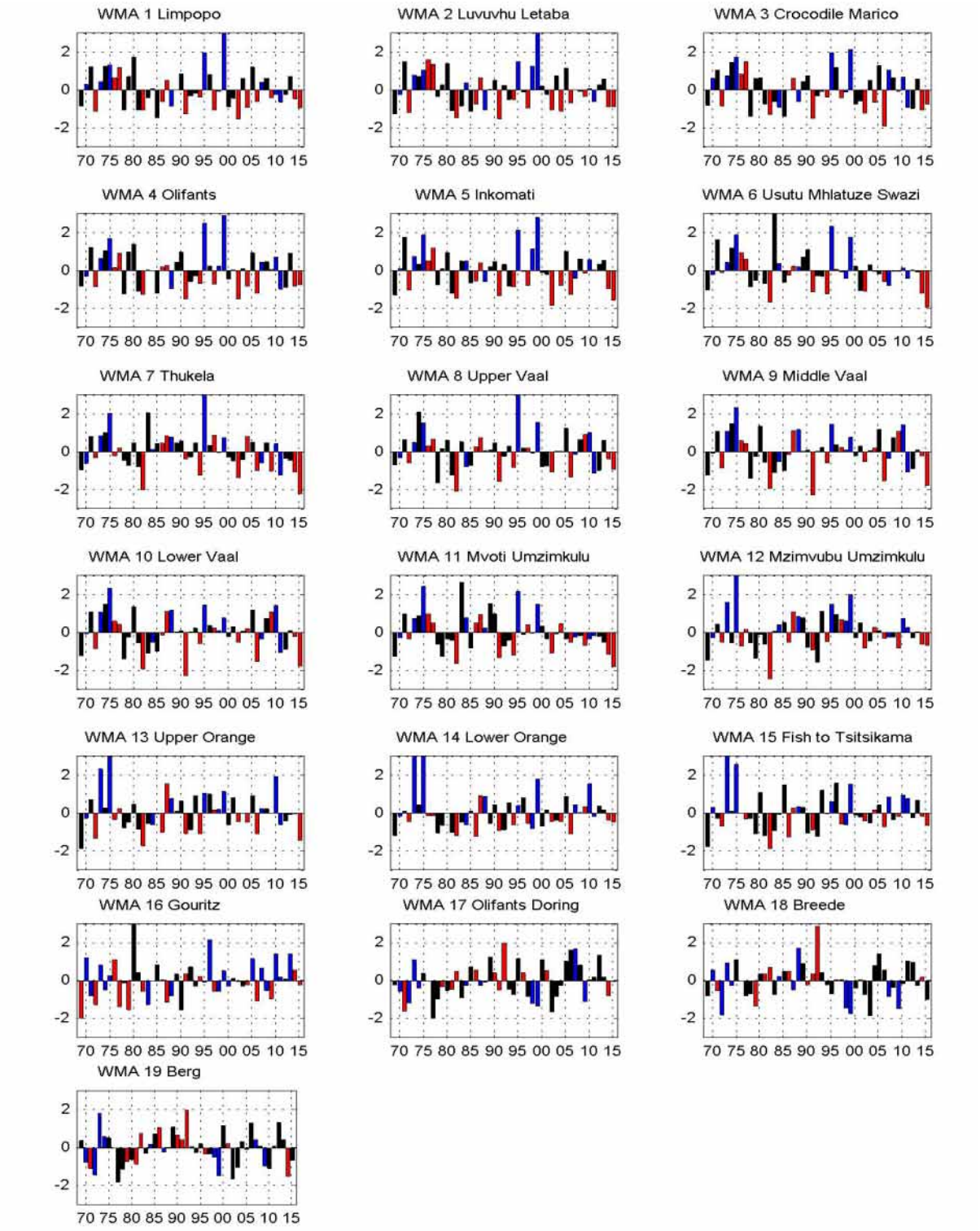

Figure 1.13: mean seasonal rainfall normalized anomalies in number of standard deviation for peak rainfall season for all WMAs. El Niño years are in red and La Nina years are in blue. For WMA 1 to 15 rainfall is averaged from November to March. For WMA 16 from October to September and for WMA 17 to 19 from May to August. Year plotted above correspond to start of hydrological year.

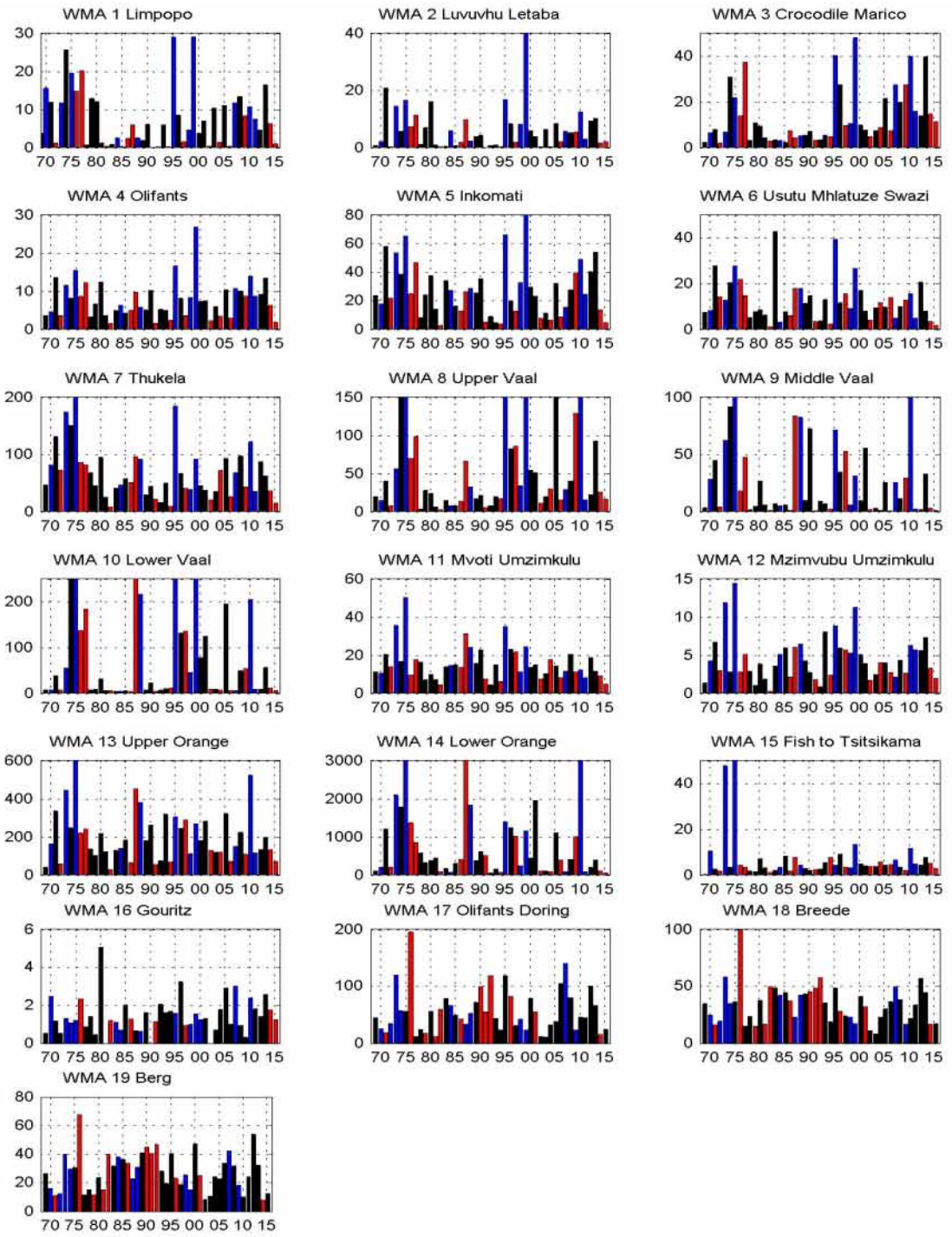

Figure 1.14: Mean total streamflows averaged monthly volume per WMA for peak season. El Niño years are in red and La Nina years are in blue. For WMA 1 to 15 rainfall is averaged from November to March. For WMA 17 from October to September and for WMA 18 to 19 from May to August. Year correspond to start of hydrological year.

For WMA 9, the 5 driest are 1991/1992 1982/1983 2015/2016 2006/2007 1978/1979 and the 5 wettest years are 1975/1976 1976/1977 1977/1978 1996/1997 2001/2002. 4 out of the 5 driest years are El Nino and one year out of the 5 wettest years are La Nina years. El Nino year 1976/1977 was a wet year. The 5 lowest volume year are 2006/2007 1991/1992 2015/2016 1982/1983 2004/2005. 5 of the lowest volume year out of 5 happen during El Nino

For WMA 10, the 5 driest are 1991/1992 1982/1983 2015/2016 2006/2007 1978/1979 and the 5 wettest years are 1975/1976 1976/1977 1977/1978 1996/1997 2001/2002. 4 out of the 5 driest years are El Nino and 1 year out of the 5 wettest years are La Nina years. There is a problem with those data. It seems that WMA 9 and 10 have the same rainfall. The 5 lowest volume year are 1986/1987 1991/1992 1984/1985 1983/1984 1985/1986. 2 of the lowest volume year out of 5 happen during El Nino

For WMA 11, the 5 driest are 2015/2016 1982/1983 1991/1992 1969/1970 1979/1980 and the 5 wettest years are 1983/1984 1977/1978 2004/2005 1997/1998 2000/2001. 3 out of the 5 driest years are El Nino and 2 years out of the 5 wettest years are La Nina years. 1997/1998 a strong El Nino year was a wet year. The 5 lowest volume year are 1992/1993 1982/1983 2015/2016 1994/1995 1979/1980. 4 of the lowest volume year out of 5 happen during El Nino

For WMA 12, the 5 driest are 1982/1983 1992/1993 1969/1970 1979/1980 1991/1992 and the 5 wettest years are 1975/1976 2001/2002 1971/1972 1984/1985 2004/2005. 2 out of the 5 driest years are El Nino and 3 years out of the 5 wettest years are La Nina years. The 5 lowest volume year are 1982/1983 1992/1993 1979/1980 1969/1970 2002/2003. 4 of the lowest volume year out of 5 happen during El Nino.

For WMA 13, the 5 driest are 1969/1970 1982/1983 2015/2016 1972/1973 1994/1995 and the 5 wettest years are 1975/1976 1980/1981 1974/1975 1977/1978 2007/2008. 3 out of the 5 driest years are El Nino and 3 years out of the 5 wettest years are La Nina years. The 5 lowest volume year are 1982/1983 1969/1970 1991/1992 1972/1973 1986/1987. 5 of the lowest volume year out of 5 happen during El Nino.

For WMA 14, the 5 driest are 1986/1987 1982/1983 1969/1970 2006/2007 1978/1979 and the 5 wettest years are 1973/1974 2012/2013 2009/2010 2001/2002 2013/2014. 2 out of the 5 driest years are El Nino and 1 year out of the 5 wettest years are La Nina years. 2009/2019, an El Nino year was in the top 5 wet years. The 5 lowest volume year are 1992/1993 2015/2016 1984/1985 1994/1995 2004/2005. 3 of the lowest volume year out of 5 happen during El Nino

For WMA 15, the 5 driest are 1982/1983 1969/1970 1986/1987 1992/1993 1981/1982 and the 5 wettest years are 1973/1974 1988/1989 1970/1971 1989/1990 1987/1988. 2 out of the 5 driest years are El Nino and 3 years out of the 5 wettest years are La Nina years. The 5 lowest volume year are 1969/1970 1982/1983 1979/1980 1986/1987 1978/1979. 4 of the lowest volume year out of 5 happen during El Nino and out of the highest volume year happen during La Nina.

For WMA 16, the 5 driest are1969/1970 1990/1991 1979/1980 1977/1978 1972/1973 and the 5 wettest years are 1980/1981 1981/1982 1991/1992 1989/1990 1975/1976. 3 out of the 5 driest years are El Nino and 1 year out of the 5 wettest years are La Nina years.

For WMA 17, the 5 driest are 1977 2002 1971 1999 1998 and the 5 wettest years are 1976 2001 1982 1990 1996. 2 out of the 5 driest years are La Nina and 2 years out of the 5 wettest years are El Nino years. Winter year in abscisse corresponds to the first of the hydrological cycle (15 means winter of 2016 of hydrological cycle 2015/2016)

For WMA 18, the 5 driest are 2003 1972 1999 2009 1998 and the 5 wettest years are 1992 1986 1985 1993 1991. 2 out of the 5 driest years are El Nino and 2 years out of the 5 wettest years are La Nina years.

For WMA 19, the 5 driest years are 1977 2002 2014 1999 1972 and the 5 wettest years are 1976 1991 2007 2013 1969. 2 out of the 5 driest years are El Nino and 3 years out of the 5 wettest years are El Nino.

1.4 References

Landman, W. A., Mason, S. J., Tyson, P. D., & Tennant, W. J. (2001). Statistical downscaling of GCM simulations to streamflow. *Journal of Hydrology*, *252*(1), 221-236.

Middleton, B.J. and Bailey A.K. (2011). Water resources of South Africa, 2005 study (WR2005) WRC report no. TT 512/11

Rouault M. and Y. Richard (2003). Spatial extension and intensity of droughts since 1922 in South Africa, Water SA 29, 489-500.

Sunday, R.K.M., Masih, I., Werner, M. and van der Zaag, P. (2014). Streamflow forecasting for operational water management in the Incomati River Basin, Southern Africa. *Physics and Chemistry of the Earth, Parts A/B/C*, *72*, pp.1-12.

2 The 2014/2015 and 2015/2016 summer rainfall drought

2.1 Introduction

Much of the precipitation received in the summer rainfall region of South Africa is of convective origin forced by large-scale dynamics (Tyson and Preston-White, 2000). South Africa has a subtropical climate and is affected by temperate and tropical weather systems. The country comes under the influence of the Southern Hemisphere high pressure system, but in summer, a heat low is found over the interior. This helps to break the subsidence associated with high pressure systems which prevent rain to occur. Most of the interior lies on an elevated plateau and orography play an important role (Tyson and Preston-White, 2000) in rainfall. The southwest region and the west coast get most of its rainfall in austral winter through temperate systems while the rest of the country gets most of its rainfall in austral summer. Summer rainfall is caused by a large-scale synoptic system leading to convection but the diurnal cycle of rainfall has an important effect in the interior and also along the east coast due to the presence of the Agulhas Current (Rouault et al., 2012). Such large rain bearing system includes Tropical Temperate Trough (TTT), Cut Off Low, and Mesoscale Convective Cloud system (MCCs). The standardized amplitudes, indicative of the strength of the diurnal cycle across a region, are strongest over the interior and along the east coast of South Africa with up to 70% explained variance associated with the diurnal cycle. The time of maximum precipitation is late afternoon to early evening in the interior, and midnight to early morning along the Agulhas Current as well as inland in the northeast of the county. During Austral summer 2015/2016 Southern Africa as a whole suffered the strongest drought since 1995. Severe drought was also experienced in 2014/2015. The 2014/2015 drought was the biggest contributing factor in the decline of the Gross Domestic Product in 2015 in South Africa and has depleted water reserve seriously. At the same time, austral summer 2014/2015, the Pacific Ocean was warmer than normal. During 2015 the Pacific became even warmer leading to one of the strongest El Nino ever observed. This led to very strong warm sea surface temperature anomalies in the Pacific in summer 2015/2016. Although there is no relation between strength of El Nino and intensity and spatial extension of the Southern African drought, former work has shown that 8 of the 10 strongest droughts since 1900 happened during the mature phase El Nino and that El Nino lead to a severe drought half of the time in all of Southern Africa (Rouault and Richard 2003, 2005). This gives ample early warning. Droughts lasting 2 seasons seem to always involve El Nino for one or two of the drought summer season. (Rouault and Richard, 2003, 2005). The El Niño Southern Oscillation also called ENSO which encompass both La Nina and El Nino and the neutral phase between the two. It is an ocean atmosphere coupled phenomenon which is the leading global natural climate mode of variability. El Niño events favour droughts in this region especially since the late 1970s (Fauchereau et al., 2003, Richard et al., 2000, 2001). The correlation between El Nino and drought is statistically significant during December to March and thus, mid-summer climate anomalies affecting Southern African rainfall are best predicted during ENSO years. Technically speaking, the mechanisms linking the Pacific and Southern Africa are relatively well observed, modelled and understood. In a nutshell, low level divergence, detrimental to rainfall, is observed over southern Africa due to changes in the Walker circulation and Hadley circulation during El Niño events. The anomalous lower level divergence over the landmass during El Niño season prevents maritime moisture transport from the Indian Ocean to Southern Africa. High pressure anomalies over the continent inhibit rainfall. Moreover El Nino generates atmospheric Rossby waves in the southern hemisphere which could be responsible for an eastward shift of the South Indian Convergence Zone (Cook et al., 2000, 2001), where most of the large scale synoptic-scale rain bearing systems that affect Southern Africa preferably develop, for instance the Tropical Temperate Trough (TTT). A last the Indian Ocean warming that occur during El Nino shift atmospheric convection and rainfall eastward above the ocean during El Niño events and contribute to

increase subsidence above Southern African El Nino and La Nina have also an impact on streamflows, vegetation and the fluxes of nutrients into the ocean. They change wind strength along the coast (Figure 2.4). In the upwelling system of the West Coast of South Africa, the South Benguela, El Nino often triggers lower than normal wind (Figure 2.4), warmer SST and a weaker upwelling (Rouault et al., 2010). During La Nina the opposite occurs. One should not study South Africa in isolation when trying to understand the impact of ENSO on South African climate because the effect is for the all of Southern Africa. Some years most of Southern Africa could be impacted by ENSO but one of the sub-regions or country could have a normal weather. However there is no relation between strength of El Nino and severity and spatial extension of droughts. For instance the 1997/1998 strong El Nino did not lead to wide spread drought and the strong drought can occur during weak El Nino. Model used for seasonal forecast have also their shortcoming as they always predict a drought when El Nino occurs which was the case for the 2009/2010 El Nino which did not lead to a drought. During the summer of 2015/2016 and 2014/2015, a severe drought affected the southern Africa continent. At the same time warm anomalies developed in 2014 in the Pacific and conditions in austral summer 2015/2015 was nearly El Nino like while one of the strongest El Nino developed in 2015. In general the drought lasted for about 2 years. Due to crop failure it has left 2.5 million of people in Malawi, Zimbabwe, Mozambique, Madagascar and Lesotho requiring quick humanitarian response while South Africa had a drop of 25% in maize production in summer 2014/2015 (AgriSA, 2016). The first objective of the study is to investigate the atmospheric and oceanic conditions that have prevailed during summer 2014/2015 and 2015/2016 over southern Africa. The second objective is to use the Standard Precipitation Index (SPI) used previously by Rouault and Richard (2003) to quantify whether the droughts of 2014/2015 and 2015/2016 were the strongest on record in South Africa compared to other droughts since 1921/1922. This study is divided into four chapters: chapter 2 describes the data and methods, while results are found in chapter 3 and concluding remarks at chapter 4.

2.2 Data and Methods.

2.2.1 Atmospheric circulation

In order to understand the atmospheric and oceanic influence on southern African summer rainfall, monthly Optimum Interpolation (OI) Reynolds SST dataset was used (Reynolds SST; Reynolds et al., 2002). The Reynolds SST (OI SST) data is found at $1^{o}\times1^{o}$ regular grid from January 1982 to present. The dataset is derived from daily merged, in situ, high resolution (9 km) infrared satellite observations from the AVHRR (Advanced Very High Resolution Radiometer) instrument on board NOAA (National Oceanic and Atmospheric Administrative). Rouault et al. (2010) emphasized that the Reynolds SST can be used to study the impact of ENSO on coastal zone of South Africa. For global rainfall monthly Global Precipitation Climatology Centre (GPCP, Huffmann et al., 2003) Version 2.2 was used. The monthly precipitation dataset is from January 1979 to present. The dataset combines the satellite and observation data into $2.5^{o}\times2.5^{o}$ global regular grid. The National Centre for Environmental Prediction (NCEP) Reanalysis dataset are used in this study to assess circulation changes associated with El Niño related droughts. The monthly NCEP dataset utilised have a time resolution and spatial resolution of 2.5^{o} latitude × 2.5^{o} longitudes. It should be noted that the spatial resolution of the NCEP reanalysis data does not properly solve upwelling regions (Rouault et al., 2010) and topographic details well (Mulenga et al., 2003). However, for the purpose of analysing the large-scale circulation anomalies over the South Atlantic to South Indian Ocean Region, NCEP resolution is adequate. In this study: geopotential height (m) at 1000 hPa and 500 hPa levels was considered. The composite atmospheric and oceanic anomalous conditions during El Niño years from December 1983 to March 2016, summer 2014/2016 and summer

2015/2016 was constructed using the NOAA Earth Research Laboratories Physical Sciences Division website found online at: www.esrl.noaa.gov/psd/. The composite are calculated by averaging summer seasons during the El Niño events from 1982 to 2016. The anomalies are the deviation from the summer mean climatology and are calculated by subtracting any quantity from the mean climatology.

2.2.2. Nino 3.4 Index

To calculate the El Niño Index over the Pacific Ocean SST between ([5° N-5° S, 120°-170° W]) in the Nino 3.4 domain using the Extended Reconstructed Sea Surface Temperature (ERSST) v4 that is obtained online from Earth System Research Laboratory (ESRL) at NOAA. The data is on a 2^0 x2 ^{0} regular grid and extends from 1854 until present. To compute the Nino 3.4 index, average summer, SST (December, January and February, DJF) were extracted from SST from the defined region above and further standardized over the climatological period from 1921 to 2016. The anomalies are the deviation from the summer mean climatology and are calculated by subtracting any quantity from the mean climatology

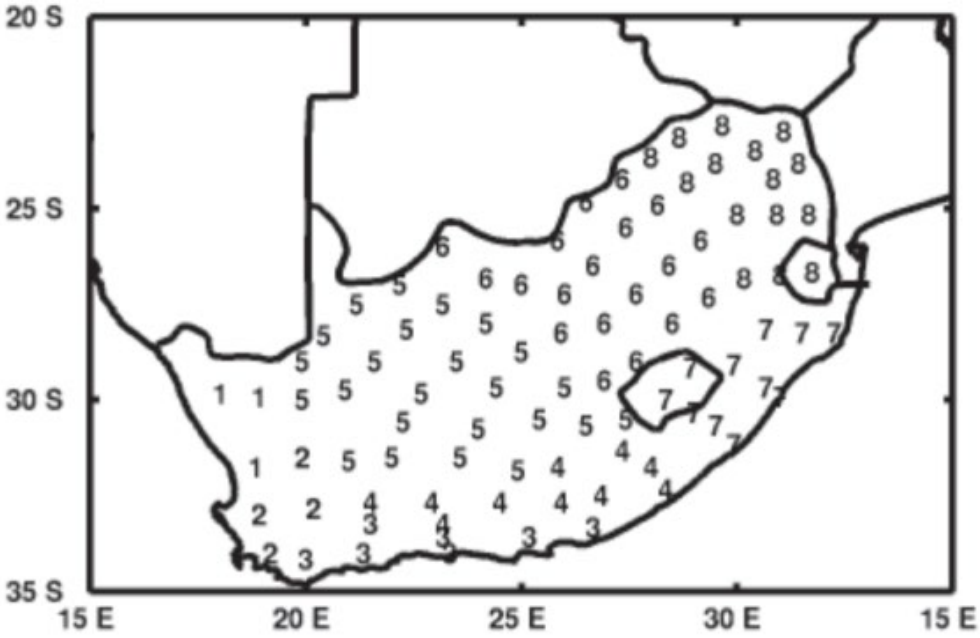

Figure 2.1: Location of the 94 rainfall districts of the SAWS. The 94 district are further categorised into 8 homogenous rainfall area defined by SAWS, namely: North-Western Cape (1), South-Western Cape (2), South Coast (3), Southern Interior (4), Western Interior (5), Central Interior (6), Kwa-Zulu Natal (7) and North-Eastern Interior (8) (Rouault and Richard, 2003)

2.2.3 SPI data

The study used monthly precipitation provided by the South African Weather Services (SAWS) from January 1921 to December 2016 to calculate the SPI. The SAWS categorises country into the 94 rainfall (Figure 2.1), of which each rainfall district at least combines the mean of 5 to 15 rain gauges (Rouault and Richard, 2003). The 94 Districts are further subdivided into 8 homogenous rainfall areas (figure 2.1). This study will only calculate the SPI for austral summer rainfall regions (region 4-8) from 1921 to 2016.The SPI were considered for 3 time scales: 3 month duration till the end of February for the heart of the summer rainfall season, 5 months duration till the end of March for all summer season and

17 months duration till the end of March for a nearly two year long summer season index. Further details on how to compute the SPI can be obtained from Hayes et al. (1999).

2.3 Results

2.3.1 Rainfall over southern Africa

In order to investigate the impact of ENSO over rainfall, composite maps of mean and anomalous rainfall during austral summer were constructed. Figure 2.2 shows the global summer rainfall composite (averages) anomaly during El Niño also called canonical El Nino conditions. It is established by calculating the mean condition during several El Niño events and subtracting the climatology for the corresponding period. El Niño summer years considered were 1982/1983, 1986/1987, 1991/1992, 1994/1995, 1997/1998, 2001/2002, 2004/2005, 2006/2007, 2009/2010, 2014/2015 and 2015/2016. Note that those events started the year before and El Niño usually matures in austral summer. For instance 1983 correspond to the 1982/1983 El Niño during its mature phase. In summary, Figure 2.2 shows the average impact in mm/day one can expect during an El Niño event, but it should be highlighted that different impacts can be expected during an individual year as we will see happening for 2014/2015 and 2015/2016.

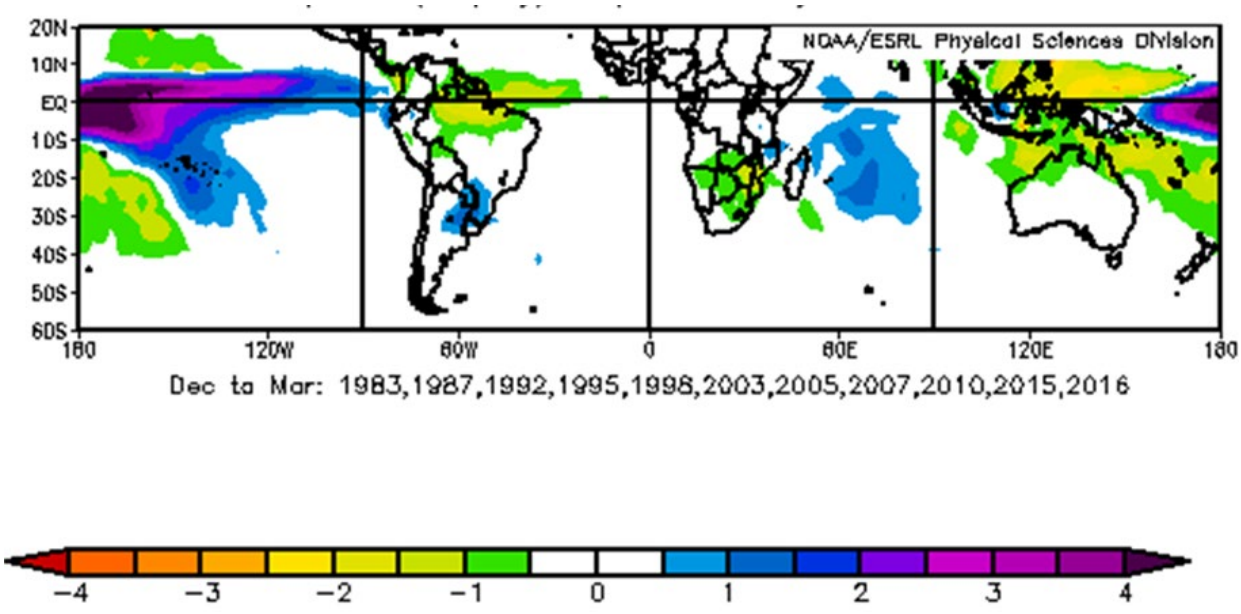

Figure 2.2. Global rainfall (mm/day) El Niño composite anomaly from climatology from December 1982 to March 2016 using GPCP data. A positive (negative) anomaly implies wetter (drier) than normal rainfall. El Niño years considered were 1982/1983, 1986/1987, 1991/1992, 1994/1995, 1997/1998, 2001/2002, 2004/2005, 2006/2007, 2009/2010, 2014/2015 and 2015/2016.

During El Niño event, wetter than normal conditions are observed over central and eastern Pacific Ocean, eastern part of South America, central Indian Ocean, northern Madagascar and eastern side of South America (Paraguay, eastern Argentina and southern Paraguay). While, during the same event, drier than normal are observed over southern Africa, north-eastern part of South America and maritime continent (Philippines, Malaysia, Papua New Guinea). Figure 2.3a (top left) is the same as Figure 2.2 but downscaled over southern Africa, and Figure 2.3b (top right) and c (bottom) show the summer season of summer 2014/2015 and 2015/2016, respectively. During the summer of 2014/2015 wetter than normal rainfall are found over eastern Mozambique and southern Madagascar while drier than

normal rainfall is over the subcontinent, with stronger anomalies than expected found over Zambia, north part of South Africa and Mozambique. Figure 2.3c displays similar patterns to figure 2.3b but with stronger negative rainfall anomalies towards the east and above Madagascar, while normal rainfall is experienced in central Botswana and Namibia. There are similarities and differences between El Niño composite anomalies, summer 2014/2015 anomalies and summer 2015/2016 anomalies. To better understand those differences, individual months for the two summer seasons will be discussed below.

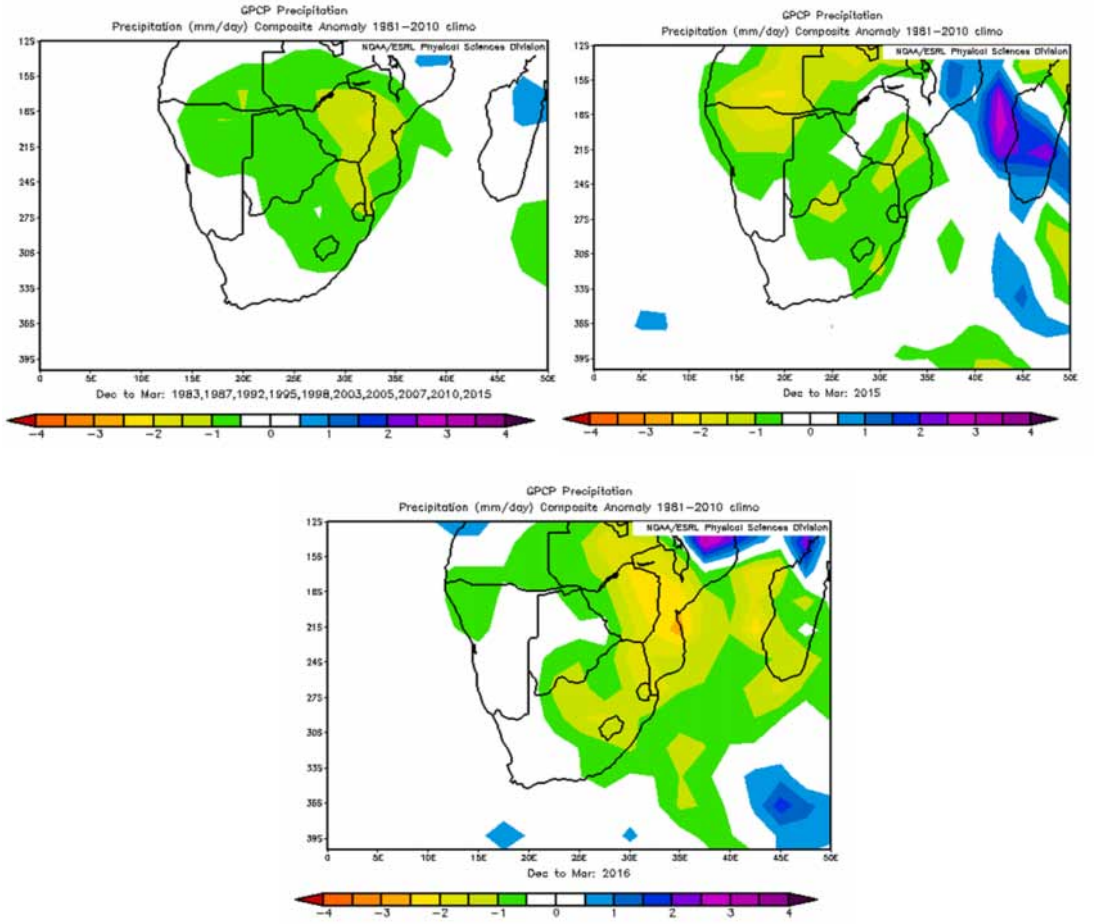

Figure 2.3. Top left: El Nino composite of rainfall anomalies (mm/day) from Dec1983 to Mar 2016 for Southern African. El Nino years considered were 1982/1983, 1986/1987, 1991/1992, 1994/1995, 1997/1998, 2001/2002, 2004/2005, 2006/2007, 2009/2010, 2014/2015 and 2015/2016. Top right: anomalies (mm/day) for 2014/2015 summer and, bottom: anomalies (mm/day) for 2015/2016 summer (c). Positive anomalies means wetter than normal rainfall and negative anomalies means drier than normal rainfall.

Individual months within the summer seasons of 2014/2015 (Figure 2.4) and 2015/2016 (Figure 2.5) are considered to understand the contributions they had on the negative rainfall anomalies and also to get more insights into the deviation from the canonical El Niño event. A canonical El Niño is a standard or typical El Niño to which other events are compared to. In December 2014, north-east South Africa, Botswana, Zimbabwe and Mozambique received more rainfall than normal compared to the other countries of the subcontinent (Figure 2.4a).

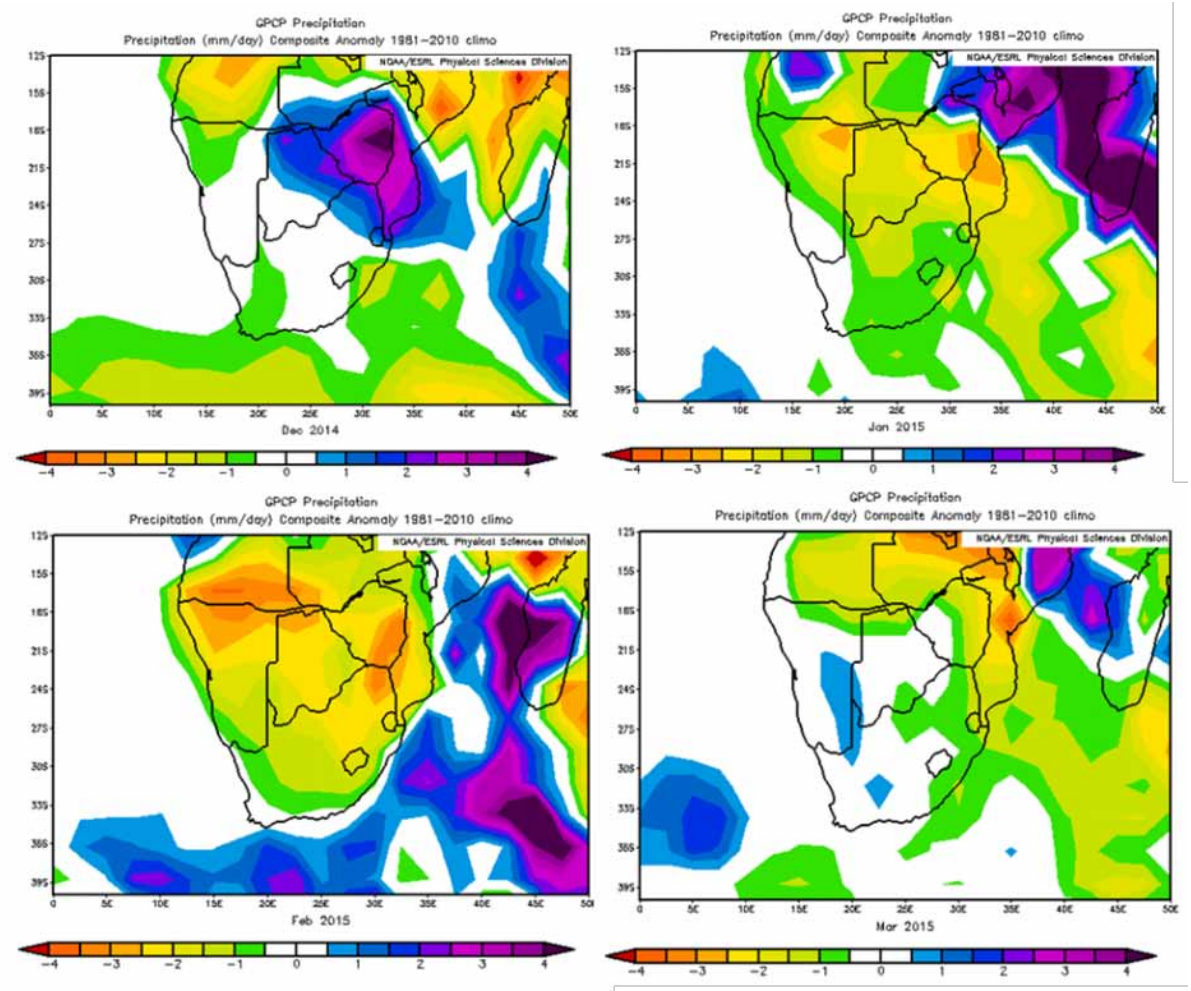

Figure 2.4. From top to bottom and left to right: rainfall anomalies (mm/day) from climatology over Southern African during the summer season 2014/2015 (a) December 2014 (b) January 2015 (c) February 2015 and (d) March 2015. Positive (negative) anomalies indicate wetter (drier) than normal rainfall.

During January 2015, it is notable that wetter than normal conditions occurred in central Angola, Northern Mozambique, Malawi and Madagascar (Figure 2.4b). However, South Africa, Namibia and Botswana were drier than normal and west coast of South Africa while southern Namibia received normal rainfall. February 2015 (Figure 2.4c) was the driest month over southern Africa except over Mozambique and eastern Madagascar. During March 2015, drier than normal conditions occurred over Malawi, Zimbabwe, Mozambique and the northern part of South Africa (Figure 2.4d) while normal rainfall occurred over most central South Africa, Namibia and Botswana.

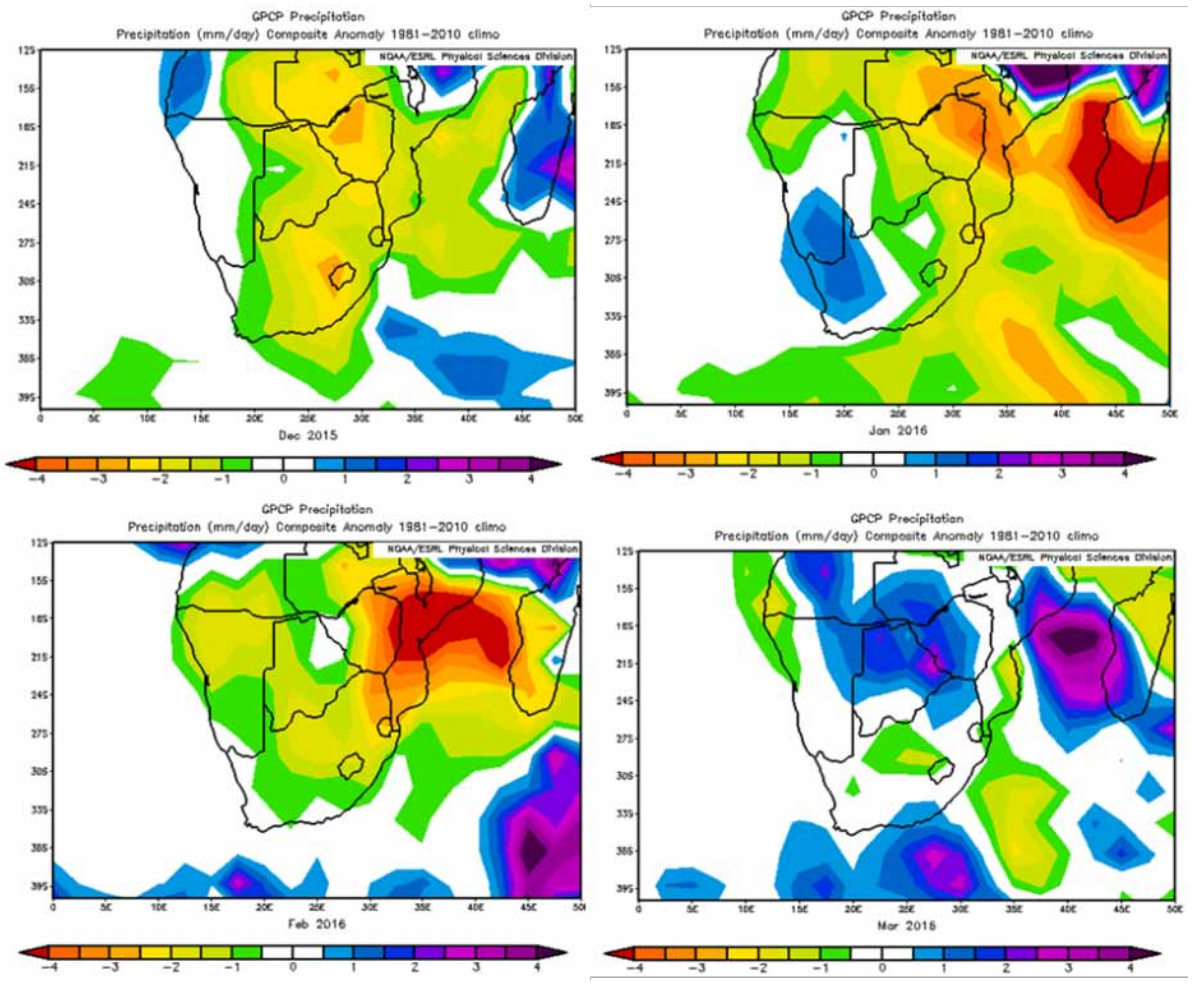

Figure 2.5. From top to bottom and left to right: rainfall anomalies (mm/day) from climatology over Southern African during the summer season 2015/2016 (a) December 2015 (b) January 2016 (c) February 2016 and (d) March 2016. Positive (negative) anomalies indicate wetter (drier) than normal rainfall.

Unlike December 2015 (Figure 2.4a), Figure 2.5a shows drier than normal rainfall over the subcontinent except over western Angola and Northern Mozambique. January 2016 (Figure 2.5b) presents similar results to January of 2015, the only differences are observed over south-western South Africa and south of Namibia with above normal rainfall experienced over these two regions while central Namibia experienced normal rainfall. February 2016 displays similar patters as February 2015, but with more intensified negative anomalies (> -4) over Mozambique. During March 2016 (Figure 2.5d) rainfall conditions around southern Africa are becoming normal, but north-eastern part of South Africa experienced wetter than normal rainfall, which is very different compared to March 2015. Analysing from these results, we can deduct that the stronger negative anomalies observed over the summer of 2015/2016 as compared to the 2014/2015, were rather influenced by stronger below normal patterns observed during January and February 2016.

2.3.2 Sea Surface Temperature

Figure 2.6 shows the typical spatial pattern of El Niño impact on global SST. It is a composite anomaly from a mean of summer conditions that occurred during El Niño seasons defined above. El Niño summer season years considered were 1982/1983, 1986/1987, 1991/1992, 1994/1995, 1997/1998,

2001/2002, 2004/2005, 2006/2007, 2009/2010, 2014/2015 and 2015. Warmer than normal SST anomalies are found in the eastern and central equatorial Pacific, Indian and South Atlantic Oceans and colder than normal SST are found in the southern Pacific and southern Atlantic Ocean (South of 34°S). Zooming over Southern Africa during El Niño years (Figure 2.7a), warmer than normal SST anomalies are found over the Southwest Indian Ocean (SWIO), Southeast Atlantic Ocean and along the west coast of South Africa. However, cooler than normal SST are found over the Namibia coast [17°-26°S]. Figure 2.7b shows the summer 2014/2015 SST anomalies over Southern Africa, evident is the abnormal negative SST anomaly over southern Africa coast, SWIO, Mozambique Channel as well as over the subtropical Atlantic (~ 33°-40° S; 0°-15°E). Positive SST anomalies are found over the South Atlantic Ocean, however the amplitude of SST anomaly is higher during summer 2014/2015 than during El Niño years.

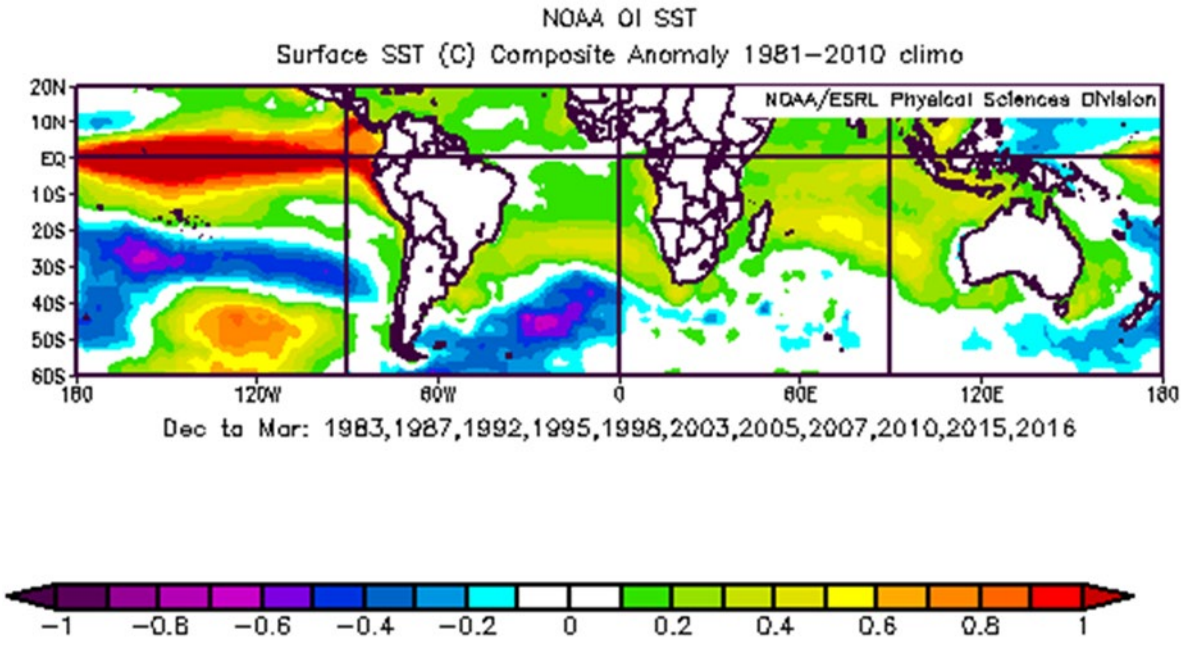

Figure 2.6. Global SST (^{0}C) composite anomaly from climatology for the summer season from December 1982 to March 2016) using NOAA OI SST data during El Niño years. Positive (negative) anomalies indicate warmer (colder) than normal SST. El Niño years considered were 1982/1983, 1986/1987, 1991/1992, 1994/1995, 1997/1998, 2001/2002, 2004/2005, 2006/2007, 2009/2010, 2014/2015 and 2015/2016.

Furthermore, SST anomalies are plotted for each month for the summer 2014/2015 in Figure 2.8 to understand the origin of difference from canonical El Niño pattern and possible regional impacts on the rainfall. In December 2014 (Figure 2.8a), warmer than normal SST in the South Atlantic Ocean and over the Angolan coast are similar to the canonical El Niño pattern over southern Africa. Cooler than normal SST are found over south Indian Ocean, Madagascar, south coast and Namibian coast which are different from the canonical El Niño pattern. Colder SSTs over the west coast are different from canonical El Niño. During January 2015 (Figure 2.8b), south Indian Ocean and south Atlantic Ocean mimics the canonical El Niño pattern over the subcontinent but with stronger warm SST anomaly.

The difference between the summer 2014/2015 (Figure 2.7b) SST anomalies and the canonical El Niño summer over southern Africa are the colder than normal SST over Madagascar Channel, south coast and west coast of South Africa. However, the warmer than normal SST over the south Atlantic and Pacific Ocean are similar to canonical El Niño summer over the region. Unlike summer 2014/2015, the summer of 2015/2016 (Figure 2.7c), experienced warmer than normal SST across the entire south Pacific and Indian ocean, except for a smaller domain over the south Indian ocean.

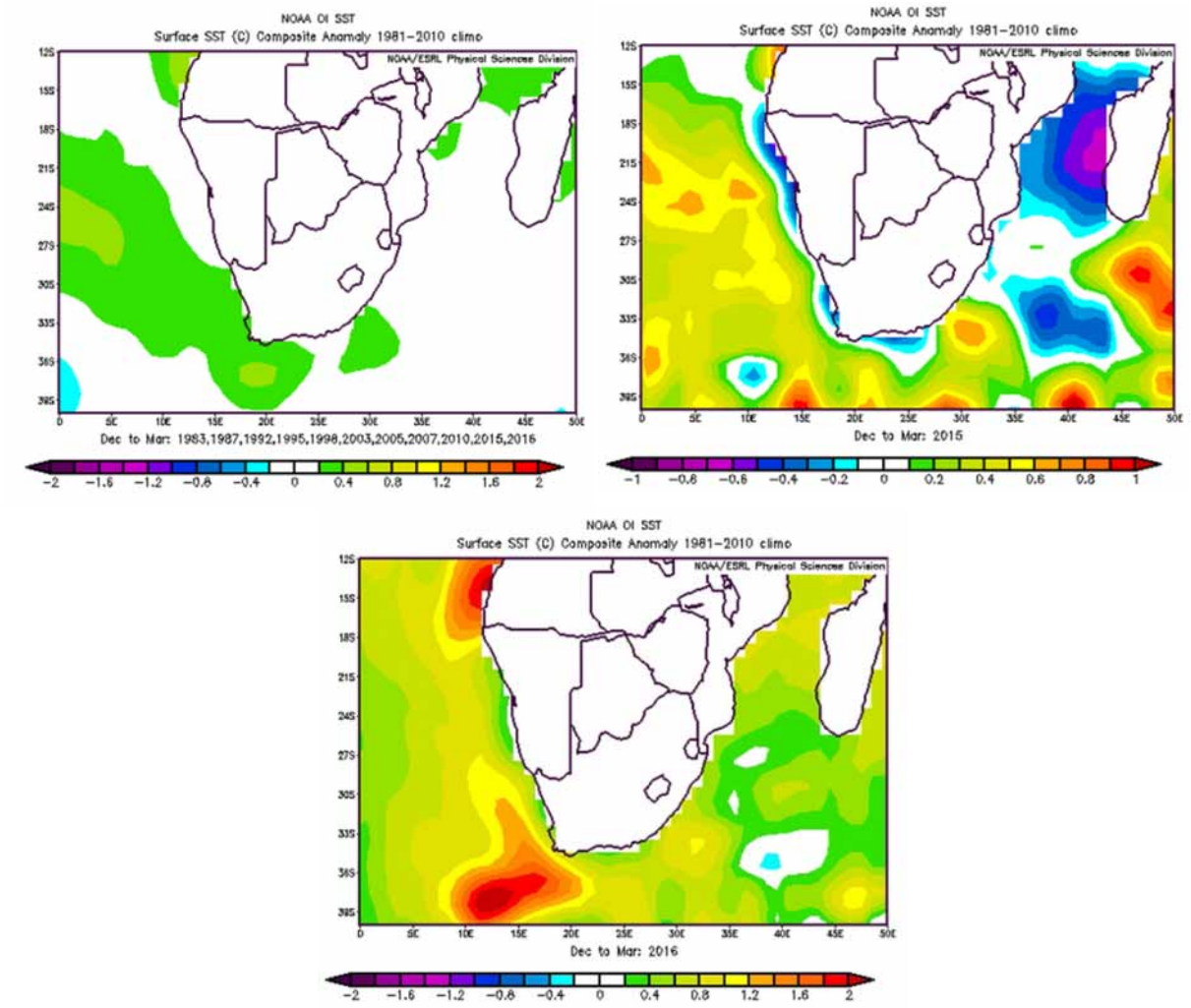

Figure 2.7. Composite of SST anomalies (mm/day) during El Niño for the summer season from Dec 1983 to Mar 2016 for Southern African (a, top left) El Nino years considered were 1982/1983, 1986/1987, 1991/1992, 1994/1995, 1997/1998, 2001/2002,2004/2005, 2006/2007, 2009/2010, 2014/2015 and 2015/2016, (b, top right) 2014/2015 and 2015/2016 (c, bottom). Positive anomalies means wetter than normal rainfall and negative anomalies means drier than normal rainfall.

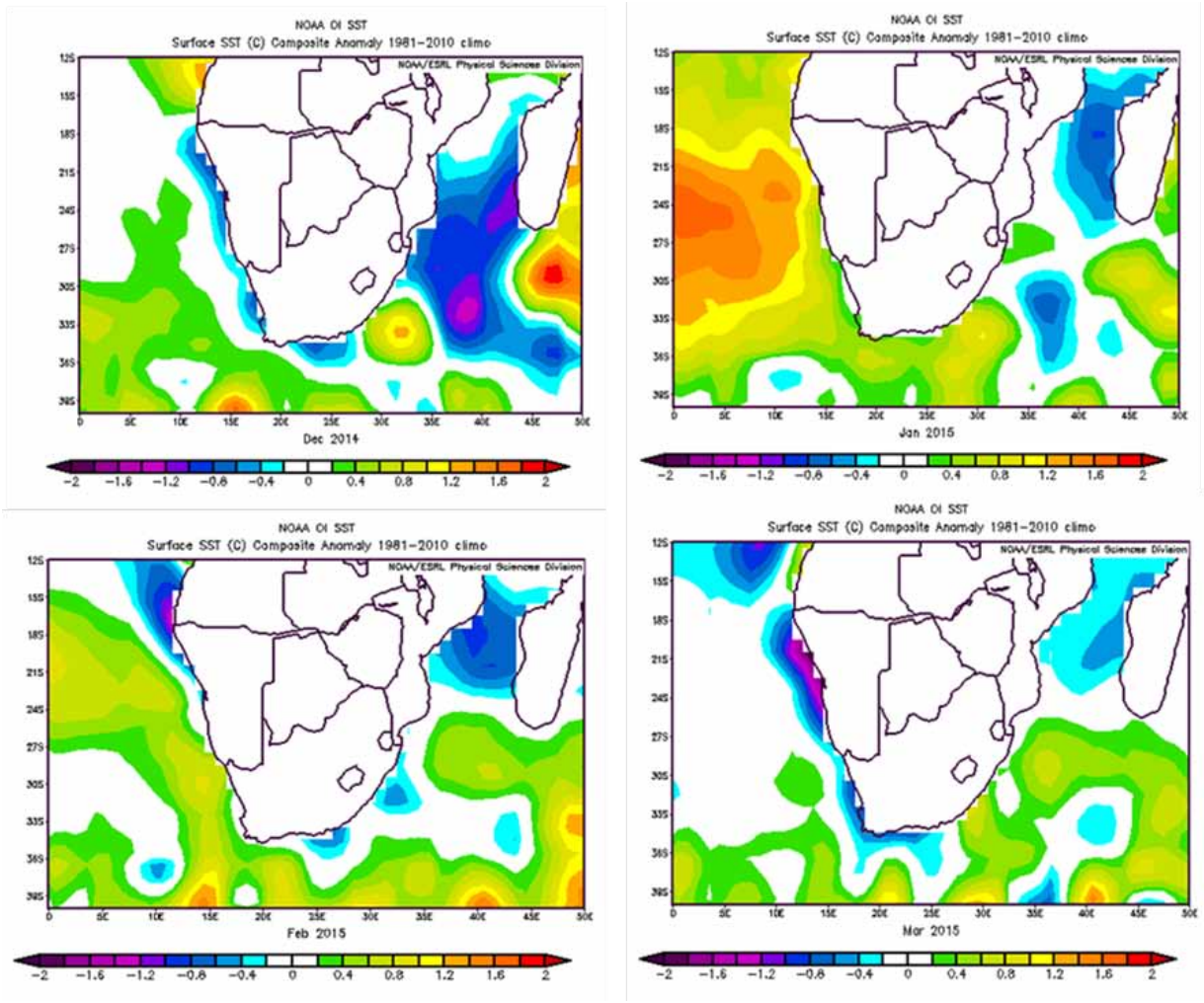

Figure 2.8. SST anomalies (^{0}C) from climatology over Southern African during the summer season 2014/2015. (a) December 2014 (b) January 2015 (c) February 2015 and (d) March 2015. Positive (negative) anomalies indicate wetter (drier) than normal rainfall.

The warming at the Namibian coast and the Mozambique Channel differentiate this month from typical El Niño pattern. Blamey et al. (2015) suggested that the warming at the subtropical Atlantic Ocean could be due to southerly migration of the SAA, the shift could have decreased the wind off the Namibia coast leading to suppressed upwelling. During February (Figure 2.8c), there is warmer SST anomaly from the west at the SWIO and weaker positive SST anomaly over south Atlantic Ocean when compared to January 2015 SST anomaly. The cooling over the Namibian coast and warming over the South Atlantic during this month is the typical El Niño pattern. However the cooling over the Angolan coast, Port Elizabeth coast, east coast of South Africa and Mozambique Channel are not expected during El Niño. Lastly during March 2015 (Figure 2.8d), warmer SST over the Angolan coast, south Atlantic and south Indian Ocean are similar to canonical El Niño pattern. However Mozambique Channel is different as compared to typical El Niño pattern over the area. The cooler SST along the Benguela Current system during December 2014 and January 2015 and Madagascar Channel throughout the whole months could have led to the seasonal cooling along the entire southern African coast and the Mozambique Channel evident on Figure 2.7b.

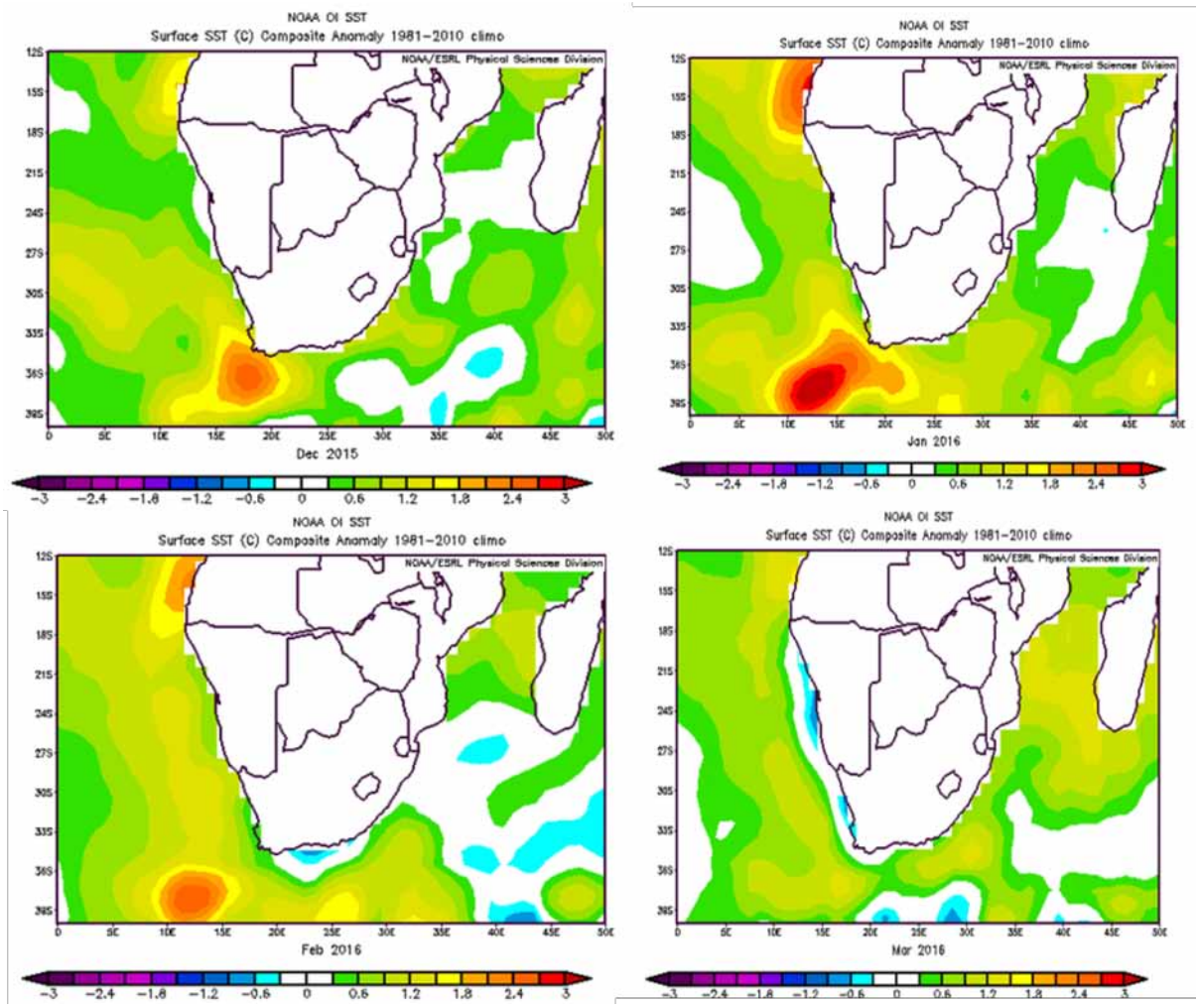

Figure 2.9. SST anomalies (^{0}C) from climatology over southern African during the summer season 2015/2016. (a) December 2015 (b) January 2016 (c) February 2016 and (d) March 2016. Positive (negative) anomalies indicate wetter (drier) than normal rainfall.

In comparison, December 2015 (Figure 2.9a) and January 2016 (Figure 2.9b) mimics the SST patterns observed over its summer average (2015/2016). During February 2016 (Figure 2.9c), there is colder SST extending from the Indian Ocean with the south coast having colder than normal SST. March 2016 (Figure 2.9d), shows similar patterns with a canonical El Niño, the only exception is observed over the west coast of South Africa, which is characterised by colder than normal SSTs.

2.3.3 Geopotential height at 1000 hPa

Figure 2.10 show the composite anomaly from the climatology during El Niño events over southern Africa for sea level pressure (1000 HPa). At the surface (~1000 hPa) higher than normal pressure anomalies are evident over Australia, Africa, South Pacific and the Indian Ocean. In general high pressure prevents rain to occur by preventing air masses from the surface to rise. In that respect it is interesting to note that no surface pressure anomalies are found in the middle of the subcontinent during ENSO which would be associated with normal rainfall which is clearly not the case. This is probably because higher than normal surface temperature can enhance vertical velocity which can overcome the general high pressure anomalies found at higher level of the troposphere during ENSO such as the 500

hPa which is shown in Figure 2.12 and other tropospheric levels (not shown). So the surface conditions is not enough to overcome pressure anomalies created in the troposphere by the teleconnection with Pacific and Indian ocean and to generate normal rainfall.

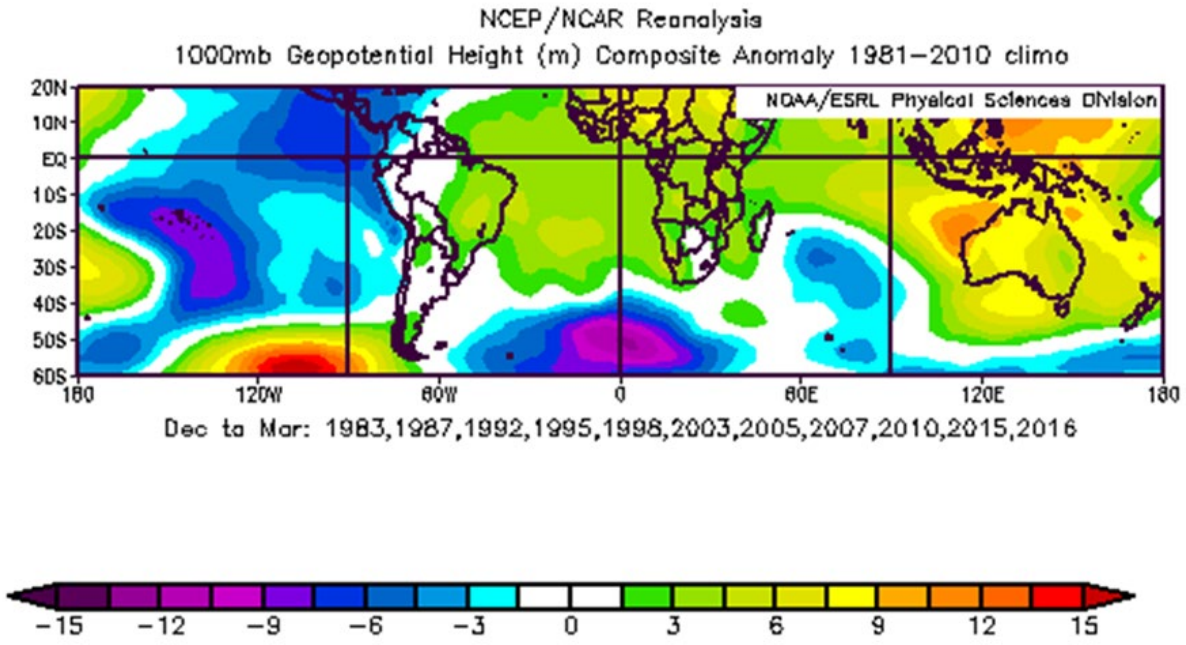

Figure 2.10: Composite for geopotential height anomaly for the summer season during El Niño years from December 1982 to March 2016 at 1000 hPa. Positive anomalies indicate higher than normal pressure and negative anomalies indicate lower than normal pressure.

Figure 2.11a shows geopotential height anomaly over southern Africa during El Niño summer while Figure 2.11b show the geopotential height anomalies the subcontinent during the summer 2014/2015.Higher than normal pressures cover southern Africa, lower than normal pressures are over the south Atlantic Ocean and normal pressure occur over central South Africa Botswana during a canonical El Niño summer. The summer season 2014/2015 mimicked the typical El Niño pattern with higher than normal pressures over the interior. However, the lower than normal pressures over Madagascar, South East Indian Ocean and central Botswana and South Africa are different as compared to Figure 2.11a. It is also evident anomalous high pressure occurred over northern Angola and western Namibia during the summer 2014/2015. Figure 2.11c shows the geopotential anomalies during the summer of 2015/2016 over the subcontinent. The pressure patterns during this summer mimics the canonical El Nino pattern but with higher magnitude. The only difference between this summer and the canonical summer event is the higher than normal pressure at South Atlantic Ocean. Figure 2.12a show geopotential height anomalies during individual months within the summer season of 2014/2015 over South Africa. The higher than normal geopotential height anomalies during December 2014 are found over the South Atlantic Ocean and Angola and are typical of El Niño conditions over southern Africa. However, the anomalous low pressures over central South Africa, Botswana, Madagascar, Zimbabwe and South East Indian Ocean are not similar to the geopotential height anomalies of a canonical El Niño pattern. The negative geopotential height anomalies at the South Atlantic Ocean (below 24^{o}S) and higher than normal anomalies over the subcontinent in January 2015 are following a typical El Niño pattern, while the lower than normal pressures anomalies in the Madagascar and higher than normal pressure at central South Africa are not expected.

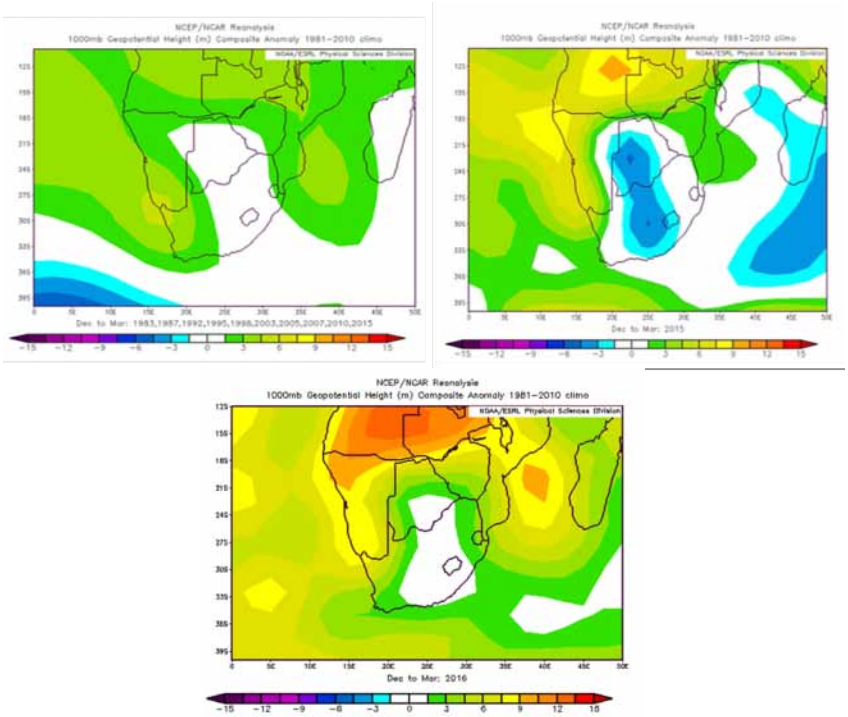

Figure 2.11. Top left: composite of 1000 hPa geopotential height anomaly (^{0}C) during El Niño for the summer season Dec 1982 to Mar 2016 for Southern African (a), Top right 2014/2015 (b) and bottom 2015/2016 (c). Positive anomalies means wetter than normal rainfall and negative anomalies means drier than normal rainfall.

The negative geopotential height anomalies at the South Atlantic Ocean (below 24^{o}S) and higher than normal anomalies over the subcontinent in January 2015 are following a typical El Niño pattern, while the lower than normal pressures at the Madagascar and higher than normal pressure at central South Africa are not expected during El Niño. During February 2015 the lower than normal pressure at the eastern side of Southern Africa intensified while higher than normal pressure at the South Atlantic Ocean weakened as compared to December 2014. The lower than normal geopotential height over the South Indian Ocean, South Africa, Zimbabwe and Mozambique were unfamiliar with a typical El Niño pattern. During March 2015, the higher than normal pressure over central South Africa and Botswana and lower than normal pressures at the east coast of South Africa do not mimic the typical El Niño pattern of geopotential height over the subcontinent. In January and March 2015, there was an eastward shift of the positive geopotential height anomalies allowing low pressure anomalies to reach the western part of southern Africa. The higher than normal geopotential height anomalies during these two respective months could have caused the drought over southern Africa by preventing the rising of moist air and, therefore, reducing rainfall for the summer season 2014/2015.The anomalous low pressure anomalies in December 2014 and February 2015 could have contributed to abnormal low pressure anomalies observed during the summer season 2014/2015.

2.3.4 Geopotential at 500 hPa.

The composite of geopotential anomalies at 500h Pa (Figure 2.12) of the canonical El Niño shows positive pressure anomalies over the subtropical and tropical regions across the globe, while negative pressure anomalies are found at lower latitudes. This would help to supress rainfall above southern Africa. According to Dieppois et al. (2015) such anomalies at the mid-tropospheric level are also

associated with an increase in pressure gradient over a substantial part of the southern hemisphere and is therefore associated with the increase in westerly wind brushing off southern Africa. The westerly winds would suppress south-easterly wind in the south Benguela upwelling regions generating warm SST anomalies at the coast. Furthermore, Figure 2.12 displays a Rossby wave train characterised by the cyclonic anomalies over the South Pacific Ocean extending into the south Atlantic. This Pacific-South American pattern acts together with higher pressure anomalies at upper and lower tropospheric levels to suppress convection over the north-east South Africa and the neighbouring regions. Figure 2.13(a), (b) and (c) shows the composite anomaly of geopotential height over southern Africa during El Niño, 2014/2015 and 2015/2016 summers, respectively. Higher than normal pressures are found over the entire southern Africa, except for the lower than normal pressures in the south-western Atlantic and normal pressures south of Madagascar (Figure 2.13a). The only similar features to canonical El Niño displayed by the summer 2014/2015 at 500 hPa (Figure 2.13b) geopotential pattern is the higher than normal pressure over the interior. Lower than normal pressures found over southern Madagascar and South Africa differs from the canonical El Niño pattern. Furthermore, intensified 500 hPa geopotential anomalies are observed over western Namibia and western Angola during 2014/2015.

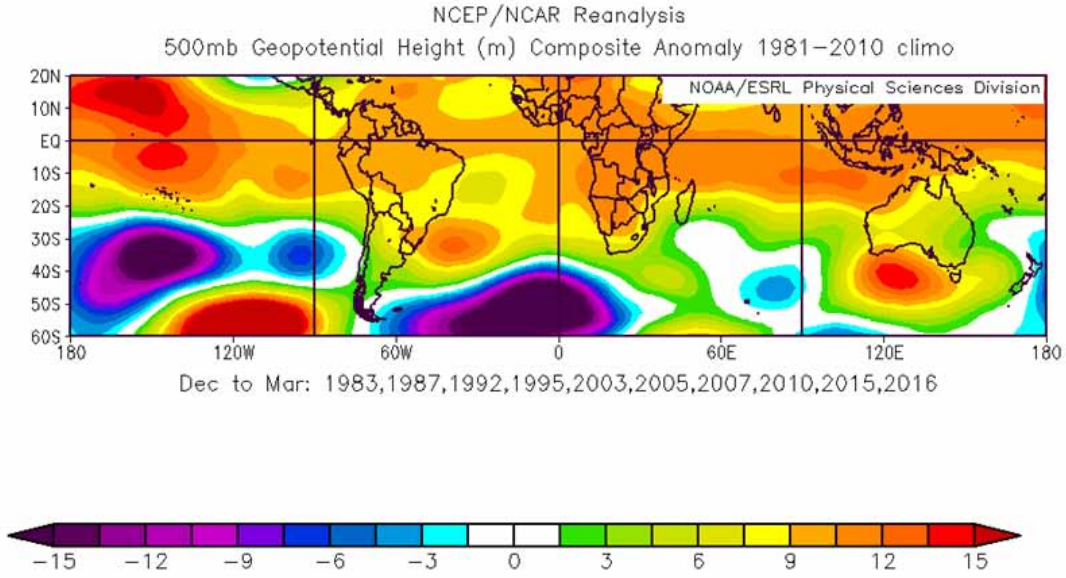

Figure 2.12. Composite anomaly for geopotential height for El Niño summers at 500 hPa. Positive anomalies imply higher than normal pressure while negative anomalies imply lower than normal pressure. El Niño years considered were 1983, 1987, 1992, 1995, 2003, 2005, 2007, 2010, 2015 and 2016.

During summer 2015/2016 (Figure 2.13c), the pressure patterns mimics that of a canonical El Niño event, except that the higher than normal pressure is covering the entire subcontinent. Figure 2.15 shows monthly 500 geopotential anomaly during the summer season of 2014/2015 over southern Africa while Figure 2.15 shows the same but during the summer of 2015/2016 at 500hpa. During the December 2015 (Figure 2.15a) normal pressure are found over the interior of the subcontinent which is peculiar to an El Niño pattern but December 2016 (Figure 2.15a) mimics the pressure pattern very well with increased magnitude over Southern Africa. The January of 2015 and 2016 mimics the higher than normal pressures over the interior experienced during a canonical El Niño.

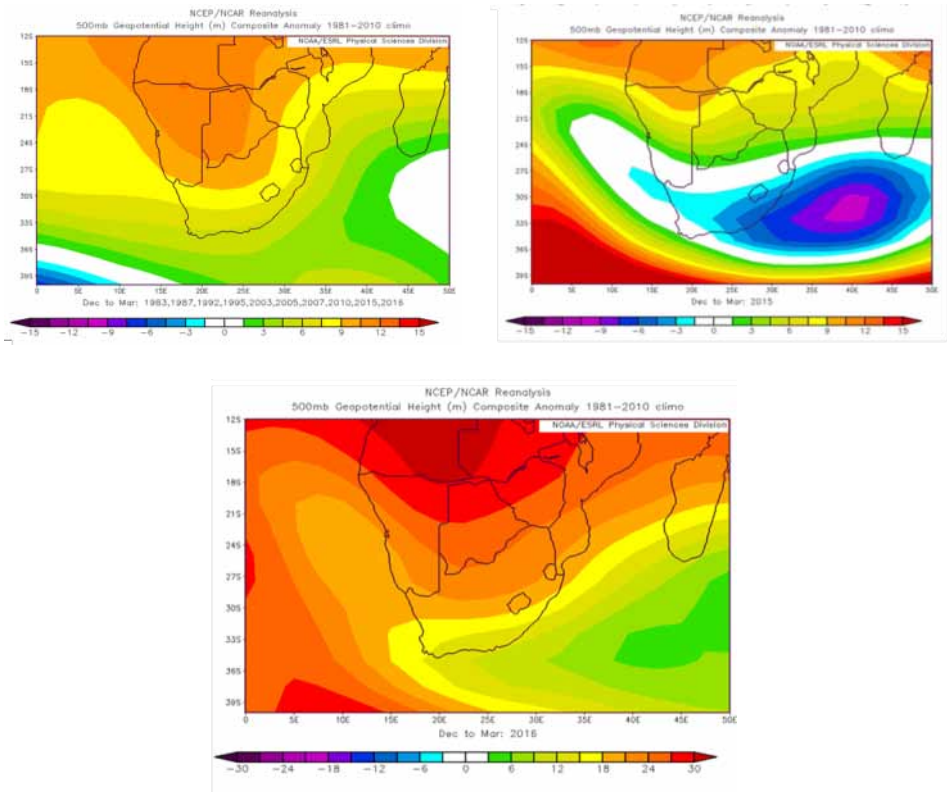

Figure 2.13. Top left: composite of 500 HPa anomalies during El Niño for the summer season Dec 1982 to Mar 2016 for Southern African (a), top right: (b) 2014/2015 and, bottom, 2015/2016 (c). Positive anomalies means wetter than normal rainfall and negative anomalies means drier than normal rainfall.

In summary, the large cyclonic anomaly found over the continent during the summer season of 2014/2015 can be attributed to lower to normal pressure conditions of Feb 2015 and March 2015. While the large anti-cyclonic anomaly evident on the summer of 2015/2016 can be associated with the higher than normal pressure anomalies during December 2015 and January 2016.

2.3.5 Rainfall climatology

Figure 2.14 displays the annual mean rainfall cycle over the 8 homogenous area defined by the SAWS. The north-western Cape and south-Western Cape are categorised as winter rainfall region. Both the areas experience maximum rainfall during June, but the south-western Cape (Figure 2.14b) accumulates higher rainfall amounts (76.2 mm/month) as compared to 29.37 mm/month acquired by the northern-Western Cape (figure 2.14a). The South Coast receives rainfall throughout the year ranging from 33 to 46 mm/month. The remaining five areas all represent the summer rainfall region of South Africa. The western and southern interior receives their maximum rainfall during March, with the southern interior at a maximum of 70.72 mm/month. Central Interior (Figure 2.14f), north-eastern Interior (Figure 2.14h) and KwaZulu-Natal all receives their maximum rainfall during January. The difference between monthly rainfall during summer and winter is very established over the north-eastern interior while KwaZulu-Natal is the wettest area (maximum of 130 mm/month) of the 8 homogenous rainfall zones.

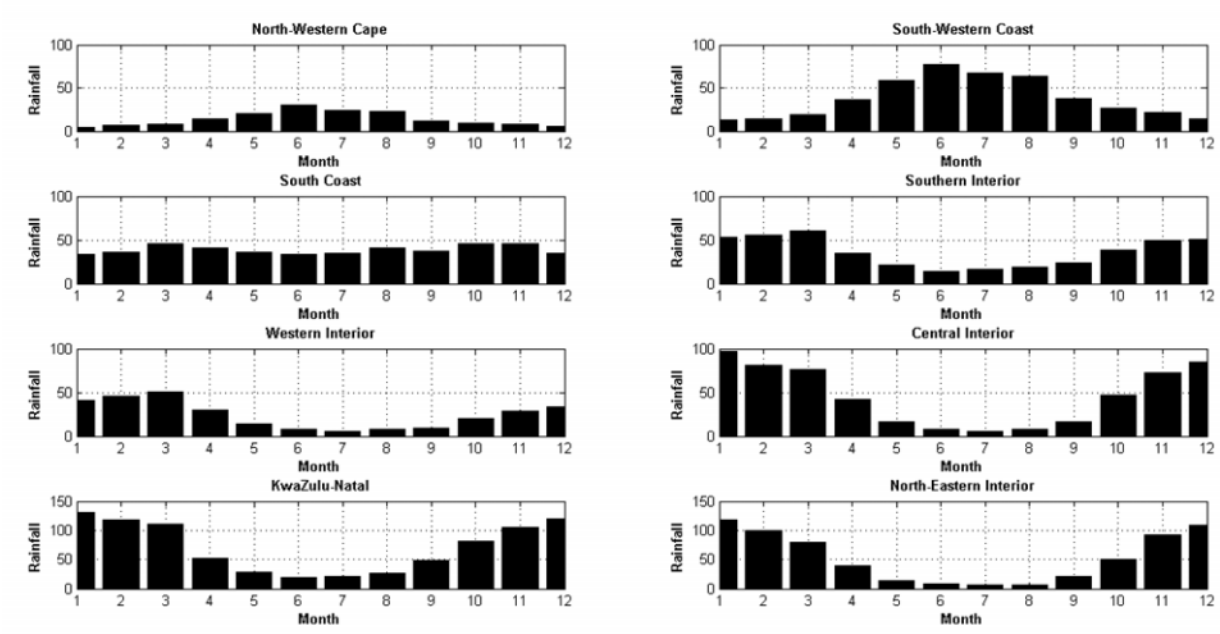

Figure 2.14. Monthly rainfall mean (mm/month) for the 8 homogenous area defined by SAWS from 1921 to 2016.

Due to the spatiotemporal variability in South Africa, it is necessary to understand the climatology of the 8 rainfall regions listed above, before the SPI can be applied. Additionally, at a shorter time scales (less than 3 months), in the regions such as south coast, because the precipitation totals is more similar to SPI, a very small anomaly (shortage of 15 mm) can lead to a drought (large SPI values), which will not be the case of KwaZulu-Natal. Therefore, the SPI makes it more useful to look at drought across region of different climatology (Rouault and Richard, 2003; Hayes et al., 1999).

2.3.6 El Niño Index

To understand the impact of ENSO on the South African droughts, an average Nino 3.4 index from the summer of 1920/1921 to summer 2015/2016 was plotted in Figure 2.15. Austral summer is usually the season where El Niño reaches its maximum intensity in sea surface temperature. The index was calculated by averaging the Nino 3.4 index from December to January and divided by the standard deviation of that season. Usually, the threshold for categorising El Niño or La Niña during austral summer for Nino 3.4 SST anomalies is 0.5^0C and this value must be reached for 5 month in a raw. We are just here considering the average in Austral summer. Therefore any SST value below -0.5^0C is classified as La Nina while above + 0.5°C is classified as El Niño condition. Based on the Nino 3.4 Index, 24 El Niño and La Niña conditions above and below +/- 0.5^0C were chosen from the austral summer of 1920/1921 to 2015/2016. This may be slightly different than El Nino event as defined by agencies in the USA but it serves well the purpose to define 24 El Nino condition 24 La Nina condition and 46 normal years. For instance although 2014/2015 was not classified as El Nino per say by the international community, our definition does take it as El Nino condition. Out of 94 summer seasons, 24 El Niño conditions occurred during the following summers: 1925/1926, 1930/1931, 1939/1940, 1940/1941, 1941/1942, 1957/1958, 1963/1964, 1965/966, 1968/1969, 1972/1973, 1976/1977,1977/1978, 1982/1983, 1986/1987, 1987/1988, 1991/1992, 1994/1995, 1997/1998, 2002/2003, 2004/005, 2006/2007, 2009/2010, 2014/2015 and 2015/2016. 24 La Niña conditions occurred during the summer of the following years: 1922/1923, 1924/1925, 1931/1932,1933/1934,

1937/1938, 1938/1939, 1942/1943, 1945/1946, 1949/1950, 1950/1951, 1953/1954, 1954/1955, 1963/1964, 1967/1968, 1970/1971, 1971/1972, 1973/1974, 1975/1976, 1984/1985, 1988/1989, 1998/1999, 1999/2000, 2007/2008 and 2010/2011. The three strongest El Niño events occurred during the summer 2015/2016 (1st) 1997/1998 (2nd) and 1982/1983 (3rd). While the strongest La Niña event occurred during the summer season of 1973/1974, followed by 1942/1943 and 1950/1951 being the third strongest La Niña event of the 94 year period. Finally a protracted El Niño event is evident from the summer years of 1939/1940 to 1941/1942.

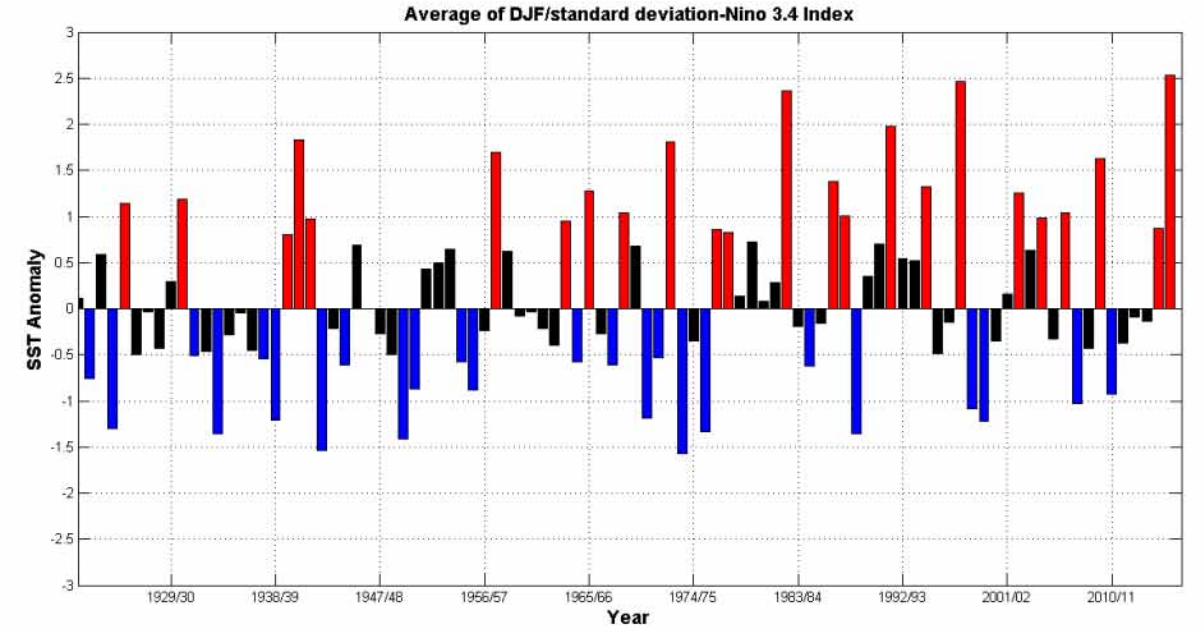

Figure 2.15. Nino 3.4 index. Red and blue bars represent El Niño and La Niña respectively, while the black bars represent normal year. ENSO episodes are defined from summer of 1921 to 2016.

Figure 2.16 shows the time series of droughts at 3 different monthly time scale, i.e. 3, 5 and 17 months over South Africa at the end of February for the 3-month scale and the end of March for the 5 month scale. At a 3-month scale the values of the SPI reflects short term drought index at the heart of the rainy season, usually used to monitor agricultural drought. At a 5-month scale the SPI values rather reflects most of the rainy summer. The 17 month SPI values rather reflect longer term precipitation anomalies, which affects hydrological systems. Rainfall shortage in medium terms and information from this scale can be further associated with deviation from the means in reservoir level (Dasso et al., 2014). For instance, if a SPI falls within a positive category it indicates that the value is greater than normal, while negative SPI value will indicate that a value is lesser than normal. Furthermore, the negative class of which this paper is dedicated to have different hierarchy of dryness. SPI value of -2.00 or lesser value classify a drought as extreme; while between -1 and -1.5 a drought will be classified as moderately dry. Figure 2.16 further represent the time series of SPI over the summer rainfall region of South Africa, which was averaged over all the summer rainfall sub-regions (Central Interior, KwaZulu-Natal, Northern Interior, Western Interior and Southern Interior).

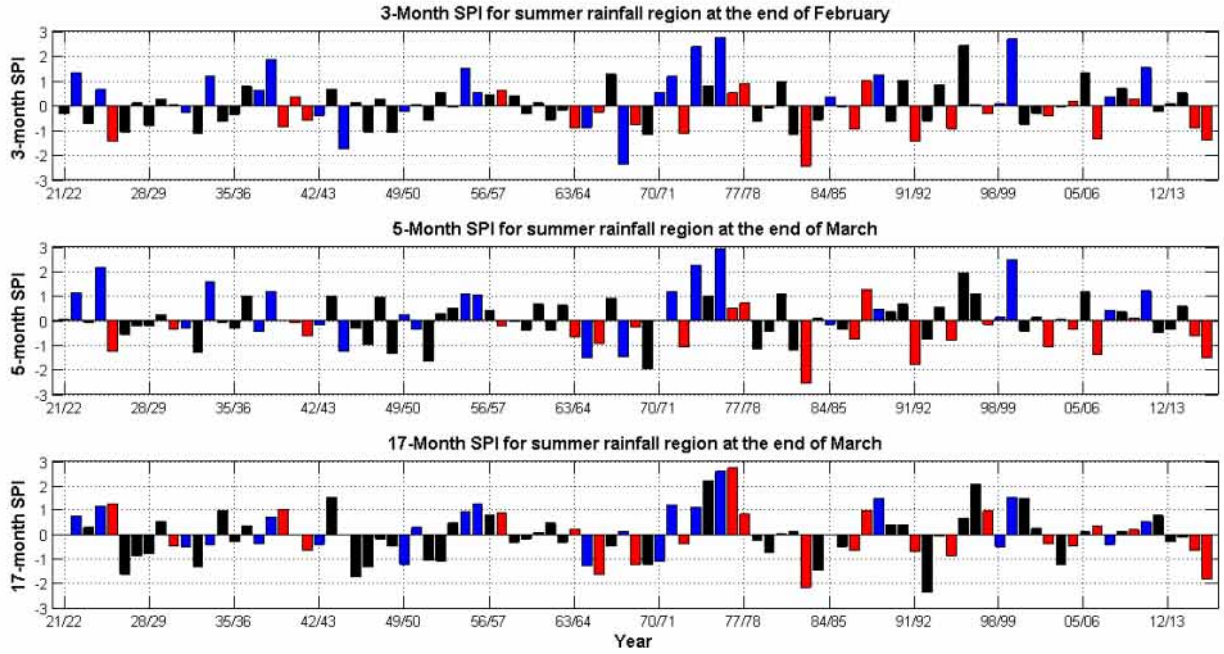

Figure 2.16. SPI at 3, 5 and 17 month time scale at the end of February for 3 month and March for 5 and 17 month for summer rainfall region.

At the 3 and 5 month time scale, South Africa experienced its extreme drought during the El Niño summer of 1982/1993, while at 17 month scale the driest summer is at 1991/1992. During the strongest El Niño event of 2015/2016, the country experienced its third strongest drought of the century (from 1921 to 2016). It should be further highlighted that after 1970, the relationship between ENSO and southern African rainfall strengthened (Rouault and Richard, 2005; Fauchereau et al., 2003; Richard et al., 2001), It is also important to note that sometimes El Niño does not lead to drought such as the 1997/1998 or small El Niño can lead to drought (2014/2015). However, most El Niño events are associated with droughts and most La Niña with wet summer especially since the 1970s. Since the 1970s the standard deviation and variation of SPI are bigger than from 1940 to 1970s, which confirm the work by Richard et al., 2001 for southern Africa. Sometimes, wet conditions can also occur during El Niño and dry conditions during La Niña. For instance, during the La Niña summer of 1970/1971 at the same monthly time scale, South Africa scored drier than normal conditions. Due to spatio-temporal variability of South African rainfall, it is important to investigate the impact of rainfall within different summer rainfall regimes in the country; therefore the following subsection will serve this purpose on a 94 year period.

2.3.7 South African subdomains and SPI

In central interior (Figure 2.17), the worst dry year at a 3-month scale occurred during La Nina summer of 1967/1968. During the same year, wetter conditions were found over the area at a 17-month time scale, which represent two consecutive seasons. At a 5 month scale, the central interior received its worst drought (> -2) during the El Niño summer of 1991/1992, while at the 17 month scale the most severe drought at this scale followed a summer after the El Niño event of 1991/1992.

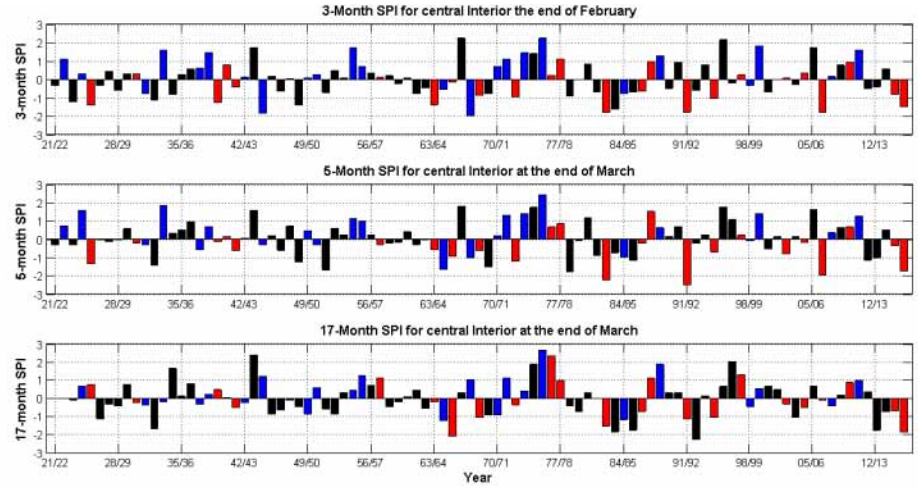

Figure 2.17. SPI at 3, 5 and 17 month time scale at the end of February for 3 month and March for 5 and 17 month for Central Interior

The worst drought at a 3 and 5 month time scale over KwaZulu-Natal (Figure 2.18) occurred during the El Niño event of 1982/1983 while the strongest drought at a 17 month scale occurred during the strongest El Niño year of the century in 2015/2016. It is interesting to note that at the 17 month scale, the two strongest wettest events were recorded during the El Niño years of 1977/1978 and 1987/1988. This is because 1976/1977 was slightly above normal but the preceding year was a very wet La Niña year.

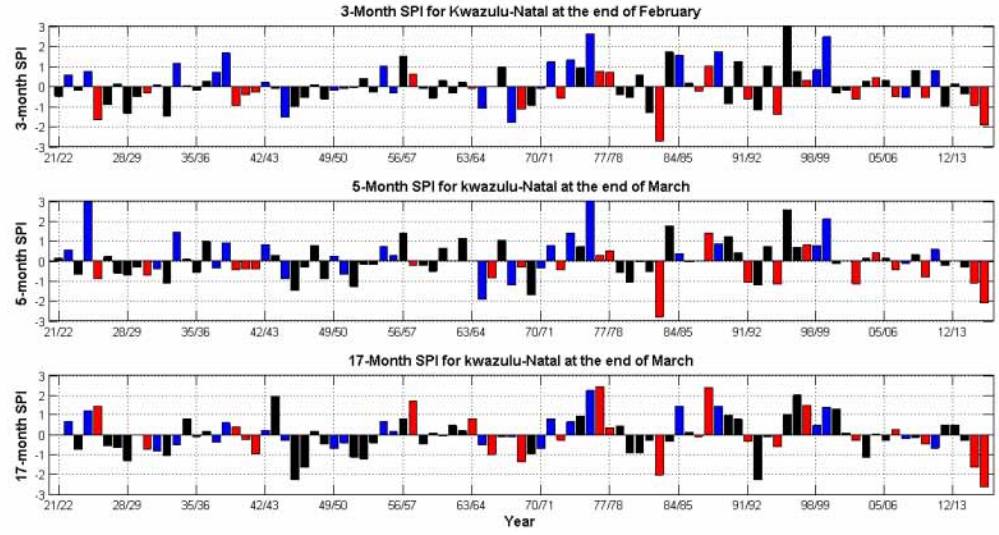

Figure 2.18. SPI at 3, 5 and 17 month time scale at the end of February for 3 month and March for 5 and 17 month for KwaZulu-Natal

Over the north-eastern (Figure 2.19) interior of South Africa the driest summer since 1920/1921 on a 3 and 17 month scale was recorded during the El Niño event of 1982/1983 while at a 5 month scale is recorded during the weak warm Pacific event of 2002/2003. It should be further noted that after 1970s at this region, the frequency and the magnitude of the drought is more pronounced than any sub-region within the South African subdomain.

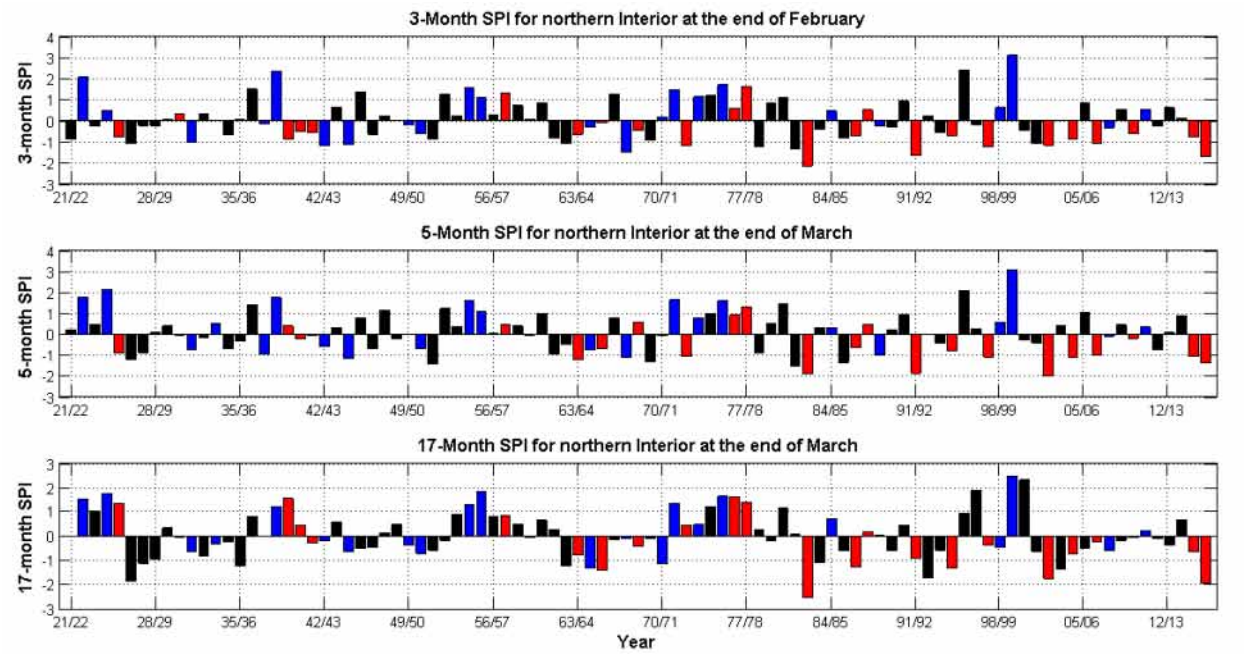

Figure 2.19. SPI at 3, 5 and 17 month time scale at the end of February for 3 month and March for 5 and 17 month for northern Interior.

At the southern interior area (Figure 2.18) of South Africa, the pattern is very distinctive from the other summer rainfall regions of South Africa, for instance the intensity and frequency of drought has decreased since the 1970s, especially at a 17 month time scale which is opposite from what has happened in southern Africa (Fauchereau et al., 2003; Rouault and Richard 2003, 2005). However, the worst drought since 1921/1922 in this region at the 3 and 5 month scale occurred after the 1970s during the 1982/1983 El Niño event. At a 17 month scale, it is notable that a severe drought occurred during the normal year of 1945/1946 following two below normal but not exceptionally below normal season summer season while the wettest summer is recorded during the El Niño year of 1976/1977. Furthermore, it is also very interesting to note that during the strongest El Niño event of the century 2015/2016, the area had normal to near normal SPI values at all scales. Over the western interior (Figure 2.21) of South Africa it is notable that all the driest years were recorded during normal years at 3, 5 and 17 month time scales during the following summers respectively: 1967/1968, 1932/1933 and 1992/1993. Note that 1992/1993 followed the 1991/1992 El Niño drought which impacted that region at a 2 year scale. Furthermore, at the 17 month time scale, dry conditions over these regions persisted from the normal summer of 1978/1979 to the El Niño summer of 1986/1987 and these prolonged droughts were relieved during the El Niño summer of 1987/1988. In conclusion the relationship between drought and El Niño at the regional scale is not as strong as it is for the all summer rainfall. This has some consequences for the seasonal forecast based on passed events at the regional scale. Additionally, two of the strongest El Niño events of 1997/1998 and 2015/2016 had different effect on the rainfall of South Africa. For instance, KwaZulu-Natal, the central and western interior of South Africa received normal SPI values for all the timescales during the summer of 1997/1998 while the north eastern interior of South Africa is the only region within the subdomains that had drought within this second El Niño event. During the strongest El Niño event of 2015/2016, all the subdomains within South Africa had droughts, but it was not the strongest of the 21st century based on the 94 year period. KwaZulu-Natal is the only subdomain within South Africa to record 2015/2016 as the driest year of the record but at 17 month scale.

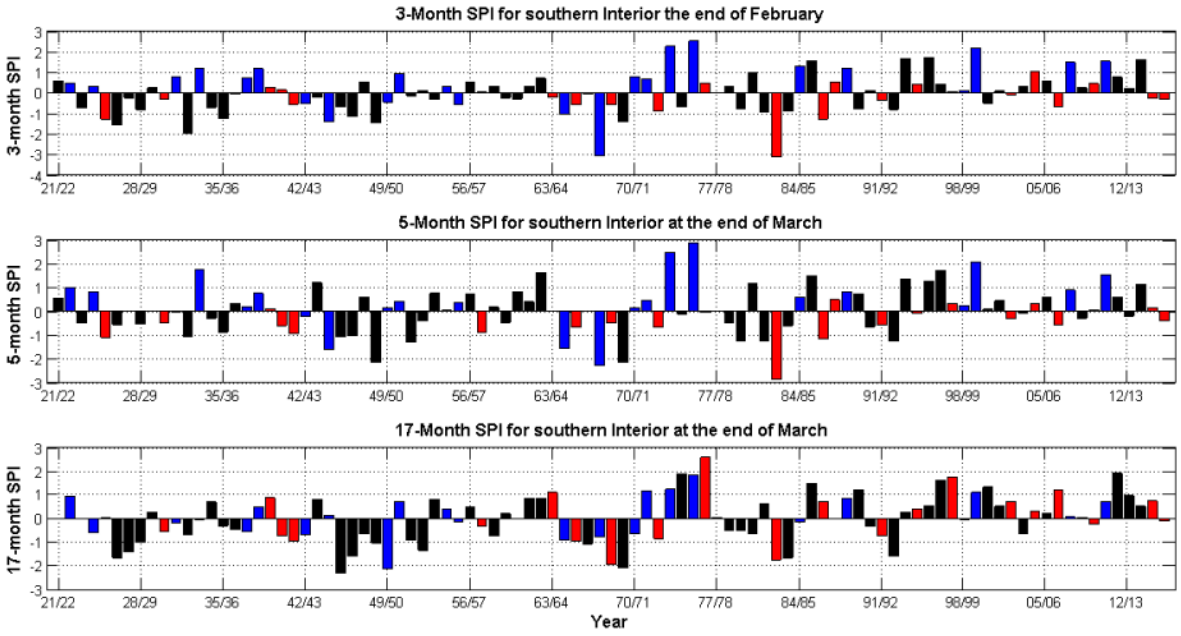

Figure 2.20. SPI at 3, 5 and 17 month time scale at the end of February for 3 month and March for 5 and 17 month for southern Interior.

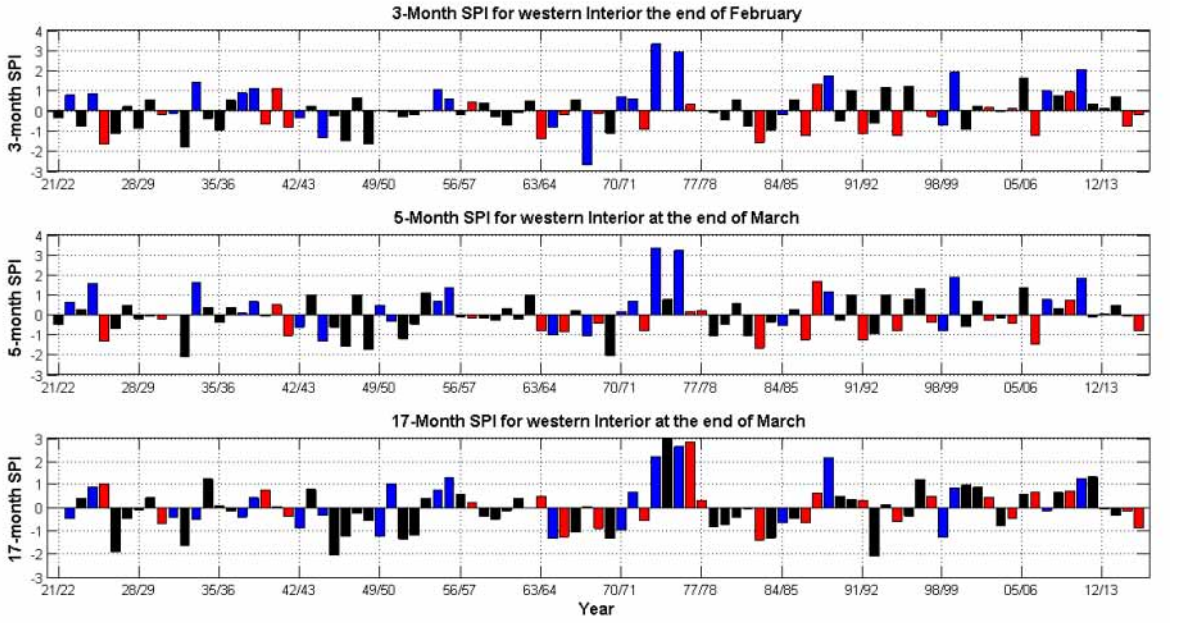

Figure 2.21. SPI at 3, 5 and 17 month time scale at the end of February for 3 month and March for 5 and 17 month for western Interior.

2. 4 Conclusion

Droughts occurred over South Africa during the summer seasons of 2014/2015 and 2015/2016. At the same time the Pacific Ocean was warmer than normal starting in 2014 and leading to the very strong 2015/2016 El Nino. While 2015/2016 was one of the strongest El Nino on record 2014/215 condition in the Pacific, while warmer than normal condition but not called officially El Nino. However both conditions led to extreme drought in Southern Africa and South Africa illustration the non-linearity

between ENSO and its climate effect on Southern Africa. The first objective of the thesis was to investigate the oceanic and atmospheric conditions associated with droughts that occurred during the austral summer season of 2014/2015 and 2015/2016. Results suggest that the oceanic and atmospheric conditions during the two summers were typical to canonical pattern, especially for 2015/2016, represented by averaging a number of El Niño events together and looking at the difference from climatology. The difference in the variables (rainfall, SST and geopotential height) was due to monthly anomalies that occurred during the distinctive summer rainfall regions. Not all months have the same El Niño pattern and even during El Nino normal rainfall or above normal rainfall can occur during an El Niño summer. This confirms that El Niño event have different signatures is southern Africa and at regional scale and also that not all months are dry, even during a very dry season. Same can be said for sea surface temperature. For instance, there was cooler than normal SST over the Benguela Current system during December 2014 and March 2015. Seasonal cooling over the Mozambique Channel in all the months of the summer seasons and warming of the South Pacific Ocean during January 2015. Those SST pattern are different from typical El Niño pattern. The cooler than normal SST over South Coast, west coast and Mozambique over the Mozambique Channel during December 2014 and March 2015 could have contributed to seasonal cooling along the Benguela Current System during 2015/2015. The SST anomalies during December 2015 and January 2016 mimic the El Nino pattern very well, but with higher magnitude. It is only the colder than normal SST at south coast during February 2016 and Namibian and west coast during March 2016 that doesn't mimic the canonical El Nino patterns. At 500 hPa, the large cyclonic anomaly for the average of the summer 2014/2015 is peculiar for an El Niño pattern over the subcontinent. It can be attributed to the lower than normal pressure conditions of Feb 2015 and March 2015. While the large anti-cyclonic anomaly (typical El Nino pattern), evident on the summer of 2015/2016 can be associated with the higher than normal pressure anomalies during December 2015 and January 2016. The second objective of this study was to examine, whether the summer 2015/2016 was the strongest of the century, and the results suggest otherwise, although it is still one of the strongest. Since, we did not account for the increase in temperature due to global warming, one could argue that 2015/2016 was the strongest drought based on rainfall only, however based on rainfall only this was not the case. During this strongest El Niño event of 2015/2016, KwaZulu-Natal was the only region to be hit by the strongest drought of the 94 year period since 1921 but at a longer time scale (17 months. There is little difference between 3 months SPI at the end of February and 5 months SPI at the end of March. To conclude for South Africa summer rainfall 2015/2016 was the fifth worst drought after the El Nino related drought of 1982/1983 and 1991/1992 and the Non El Nino related drought of 1967/1968 and 1944/1945 at the seasonal month scale. At the 17 month scale, an index that encompass two summer season 2015/2016 was the third worst drought since summer 1921/1922 due to dry conditions in 2014/2015.

2.5 References

Blamey, R.C. (2012). Mesoscale Convective Complexes over southern Africa (Doctoral dissertation, University of Cape Town).

Blamey, R.C. and Reason, C.J.C. (2013). The role of mesoscale convective complexes in southern Africa summer rainfall. Journal of climate, 26(5), 1654-1668.

Crétat, J., Richard, Y., Pohl, B., Rouault, M., Reason, C. and Fauchereau, N. (2012). Recurrent daily rainfall patterns over South Africa and associated dynamics during the core of the austral summer. International Journal of Climatology, 32(2), 261-273.

Dieppois, B., Rouault, M. and New, M. (2015). The impact of ENSO on Southern African rainfall in CMIP5 ocean atmosphere coupled climate models. Climate Dynamics, 1-18.

Dufois, F. and Rouault, M. (2012). Sea surface temperature in False Bay (South Africa): Towards a better understanding of its seasonal and inter-annual variability. Continental Shelf Research, 43, 24-35.

Fauchereau, N., Pohl, B., Reason, C.J.C., Rouault, M. and Richard, Y. (2009). Recurrent daily OLR patterns in the Southern Africa/Southwest Indian Ocean region, implications for South African rainfall and teleconnections. Climate Dynamics, 32(4), 575-591.

Fauchereau, N., Trzaska, S., Rouault, M. and Richard, Y. (2003). Rainfall variability and changes in southern Africa during the 20th century in the global warming context. Natural Hazards, 29(2), 139-154.

Hart, N.C.G., Reason, C.J.C. and Fauchereau, N. (2010). Tropical-extratropical interactions over southern Africa: three cases of heavy summer season rainfall. Monthly weather review, 138(7), 2608-2623.

Hayes, M.J., Svoboda, M.D., Wilhite, D.A. and Vanyarkho, O.V. (1999). Monitoring the 1996 drought using the standardized precipitation index. Bulletin of the American Meteorological Society, 80(3), pp.429-438.

Huffman, G.J. and Bolvin, D.T. (2013). GPCP Version 2.2 SG Combined Precipitation Data Set Documentation.

Manatsa, D., Mukwada, G., Siziba, E. and Chinyanganya, T. (2010). Analysis of multidimensional aspects of agricultural droughts in Zimbabwe using the Standardized Precipitation Index (SPI). *Theoretical and Applied Climatology*, *102*(3-4), pp.287-305.

McKee, T.B., Doesken, N.J. and Kleist, J. (1993, January). The relationship of drought frequency and duration to time scales. In *Proceedings of the 8th Conference on Applied Climatology* (Vol. 17, No. 22, pp. 179-183). Boston, MA: American Meteorological Society.

Meque, A. and Abiodun, B.J. (2014). Simulating the link between ENSO and summer drought in Southern Africa using regional climate models. Climate Dynamics, 44(7-8), 1881-1900.

Mulenga, H.M., Rouault, M. and Reason, C.J.C. (2003). Dry summers over northeastern South Africa and associated circulation anomalies. Climate Research, 25(1), 29-41.

Philippon, N., Rouault, M., Richard, Y. and Favre, A. (2012). The influence of ENSO on winter rainfall in South Africa. International Journal of Climatology, 32(15), 2333-2347.

Reason, C.J.C. and Jagadheesha, D. (2005). A model investigation of recent ENSO impacts over southern Africa. Meteorology and Atmospheric Physics, 89(1-4), 181-205.

Reynolds, R.W., Rayner, N.A., Smith, T.M., Stokes, D.C. and Wang, W. (2002). An improved in situ and satellite SST analysis for climate. Journal of climate, 15(13), 1609-1625.

Richard, Y., Trzaska, S., Roucou, P. and Rouault, M. (2000). Modification of the southern African rainfall variability/ENSO relationship since the late 1960s. Climate Dynamics, 16(12), 883-895.

Richard, Y., Fauchereau, N., Poccard, I., Rouault, M. and Trzaska, S. (2001). 20th century droughts in southern Africa: spatial and temporal variability, teleconnections with oceanic and atmospheric conditions. International Journal of Climatology, 21(7), 873-885.

Rouault, M., Florenchie, P., Fauchereau, N. and Reason, C.J. (2003). South East tropical Atlantic warm events and southern African rainfall. Geophysical Research Letters, 30(5).

Rouault, M. and Richard, Y. (2003). Intensity and spatial extension of drought in South Africa at different time scales. Water SA, 29(4), 489-500.

Rouault, M., Roy, S.S., Balling, R.C. (2013). The diurnal cycle of rainfall in South Africa in the austral summer. International Journal of Climatology, 33(3), 770-777.

Tyson, P.D. and Preston-Whyte, R.A. (2000). Weather and climate of southern Africa. Oxford University Press.

Vigaud, N., Richard, Y., Rouault, M. and Fauchereau, N. (2007). Water vapour transport from the tropical Atlantic and summer rainfall in tropical southern Africa. Climate dynamics, 28(2-3), 113-123.

Vigaud, N., Richard, Y., Rouault, M. and Fauchereau, N. (2009). Moisture transport between the South Atlantic Ocean and southern Africa: relationships with summer rainfall and associated dynamics. Climate Dynamics, 32(1), 113-123.

3 Decadal variability of climate in Southern Africa.

3.1 Introduction

Decadal fluctuations have also been found in summer southern African rainfall (Dyer and Tyson, 1977; Tyson, 1986; Mason and Jury, 1997; Malherbe et al., 2012; Jury 2014). Of particular importance is the interdecadal Dyer-Tyson cycle (18-20 year; Dyer and Tyson, 1977). Comparing synoptic maps during wet and dry years in the core areas of the interdecadal cycle, i.e. in the north-eastern regions of southern Africa, Tyson (1981, 1986) note concomitances with changes in the meridional circulation between the South Atlantic and Indian Oceans, which might be related to variations in the subtropical ridge of the first zonal standing wave over the Southern Hemisphere. According to Malherbe et al. (2014), this would be consistent atmospheric anomalies related to the SAM. A quasi-decadal cycle in summer southern African rainfall, which would be particularly pronounced along the south coast of South Africa (Tyson, 1981, 1986), has also been identified. Using the same methodology but focused on the southern Cape (i.e. a region sensible to summer and winter rainfall systems), Tyson (1981, 1986) associated these quasi-decadal fluctuations with longitudinal changes in position of the first ridge of standing wave 3 (Tyson, 1981, 1986). However, earlier studies examining the summer rainfall regions has then described these quasi-decadal fluctuations as a chaotic resonance of interannual variability (Mason, 1990; Kruger, 1999; However, studies on the decadal variability of southern African rainfall have focused only on the summer months, and discussions about potential mechanisms and processes have been limited. Oceanic and atmospheric datasets have evolved considerably since the first hypothesis proposed by Tyson (1981, 1986). The choice of datasets, which have to cover an extended period (i.e. at least a century) as homogenous as possible to detect robust signals associated with decadal timescale of variability, is, however, still not well-considered (cf. Sect. 2.1). In addition, most of the studies cited above are based on comparisons between two periods of approximately 10-years, which are too short to capture the decadal variability signals (i.e. roughly two ½ cycles; Maraun, 2006; Schaefli *et al*., 2007). They are thus likely to describe changes in interannual variability between two decades that are not necessarily related to decadal signals. In this context, discuss the quasi-decadal variability as a chaotic resonance of interannual variability is quite questionable. Other studies have used a ~10-year running mean, which acts as a primitive low-pass filter (which does not fully supressed interannual variability), and therefore prevents considering the existence of several independent decadal timescales in southern African rainfall variability. This chapter aims to address these gaps, by defining the changing characteristics of summer and winter southern African rainfall, and their specific teleconnections for the main timescale of climate variability. Using a time-space approach based on spectral analysis, this study therefore aims to: (1) provide a better understanding of decadal signals, which are likely to interfere with forced anthropogenic climate changes, and, thus, help in improving decadal climate predictions (Keenlyside et al., 2008; Kirtman et al., 2013); and (2) provide new insights in understanding the non-linear interactions between large-scale modes of climate variability and southern African rainfall.

3.2 Data and Methods

The latest update of the Climatic Research Unit (CRU) dataset is used to estimate southern African rainfall. The CRU TS 3.22 rainfall field is produced on a 0.5° × 0.5° grid, and is derived from monthly rainfall provided by about 4000 weather stations distributed around the world from 1901 to 2013 (Harris et al., 2014. As illustrated in Figure 3.1a-b, the wettest months occur between November and February (NDJF) in a major part of southern Africa (especially in the north-eastern part), and between May and August (MJJA) in the south-western and coastal regions (i.e. centred on the Western Cape region). While summer rainfall is primarily associated with synoptic-scale convective systems, such as tropical-temperature-troughs (TTT; Hart et al., 2012a, b; Macron et al., 2014), winter rainfall is associated with

the passage of westerly cold front systems. The spatial coherence of interannual rainfall anomalies of both indices has been assessed during their corresponding season (i.e. SRI in NDJF and WRI in MJJA; Figure 3.1b-f). The annual peak of rainfall is distinctly well phased for both regions (Figure 3.1b). The main differences between grid-points are related to rainfall amounts (i.e. the amplitude of the peak, Figure 3.1b). With respect to interannual rainfall anomalies, the median of the correlations between both regional indices and each grid-point used for their calculation (i.e. within the dark red and blue boxes in Figure 3.1a; n[SRI/WRI] = 617/75) is about 0.65 and 0.78 (and significant at $p \leq 0.05$) for the SRI and the WRI, respectively (Figure 3.1d, f). The range of correlation coefficients is larger for the WRI, as displayed by the boxplots (Figure 3.1d, f). Next, based on a pointwise correlation with the high-resolution rainfall grid over 34°-20°S and 10°-36°E, interannual SRI and WRI anomalies are both significantly correlated at $p = 0.05$ with a large patch over their calculation domains (Figure 3.1d, f). Maximum correlations occur within the calculation domains, i.e. east of Johannesburg for the SRI, and north of Cape Town for the WRI (Figure 3.1d, f). Although lower for the WRI than for the SRI, a robust spatial coherence is suggested for both indices. To examine the summer and winter teleconnections with global SSTs, we used the latest version of monthly SST data from the extended reconstructed SST (ERSST.v4) of the National Climatic Data Centre (NCDC). To infer monthly atmospheric dynamics, the Twentieth Century Reanalysis version 2 (20CR.v2) is used (Compo et al., 2006; Compo et al., 2011). This is a 57-member ensemble global reanalysis, available since 1871, over a 2° × 2° resolution grid that assimilates only surface pressure and uses monthly SST and sea-ice distributions as boundary conditions. Datasets covering only the second half of the 20th century (e.g. NCEP-1, ERA-40, and ERA-interim) are considered too short to capture robust decadal atmospheric signals. This is particularly true over the summer rainfall region where these signals are more pronounced before the 1960s and 1980s (cf. Sect. 3). Six parameters – latent heat flux (LHF), meridional (v) and zonal wind (u), specific humidity (q), geopotential height (z) and calculated outgoing longwave radiation (OLR) – are used here. Atmospheric circulation anomalies are described over three tropospheric levels: 1000 hPa, 500 hPa and 200 hPa. Moisture fluxes ($\vec{V}q$) have also been calculated above the first two tropospheric levels. 3.2.2. Exploring multiple timescales of variability, and teleconnections. In Section 3, time-scale analysis is carried out using continuous wavelet transform in order to visualize potential changes in the spectral content of each rainfall time-series, i.e. the SRI and the WRI (Torrence and Compo, 1998). By representing the time-series into time-scale domain, (which can be converted into a time-period domain), one can determine which scales of variability (or periods in a Fourier sense) are the dominant variability modes affecting SRI and WRI. Such decomposition of the monthly precipitation signals is conducted with a Morlet mother wavelet with angular frequency 6 to produce the local wavelet spectra. The significant timescales of SRI and WRI variability are then reconstructed using Fast Fourier Transform (FFT) band-pass filtering, which can be considered as a digital filter in frequency domain. To reduce trend effects, both indices are nevertheless first detrended using a locally weighted linear regression, with span equal to the length of the data. This is also likely to reduce the effects of abrupt changes in the series (i.e. change in the mean), which were identified in 1995 and 1950 in the SRI and the WRI. The power of the dominant modes of variability can then be compared over time on an orthogonal basis, and different metrics can be computed (cf. Sect. 3).In Sections 4 and 5, we examine the teleconnections between rainfall indices and the worldwide SSTs on the one hand, and atmospheric circulation on the other hand. In each grid-point from 1901 to 2013, the time-series are then detrended and next subjected to the FFT filter according to the significant timescales of southern African rainfall variability. Detrending the global SSTs, for instance, helps to reduce the effects of the nonlinear warming trends in the second half of 20th century, which have been shown to be principally driven by anthropogenic forcing (Hoerling et al., 2010; Wu and Chan, 2015).

Figure 3.1. Seasonal patterns of Southern African rainfall: time-evolution and spatial coherence. a) Spatial distribution of wettest month of the year over southern Africa (Calendar Month; *red*: November to March; *blue*: April to September). Bold lines delineate the area used for the calculation of summer and winter rainfall indices (SRI and WRI). b) Annual cycles of summer (*red*: SRI) and winter (*blue*: WRI) southern African rainfall indices, and of every grid-points used for their calculations (*light red and blue*). c) Interannual anomalies of SRI and all grid-points used for its calculation (i.e. n=617) over the 20th and early 21st centuries. d) Pointwise correlation between interannual anomalies in the SRI and the CRU TS 3.22 rainfall field over southern Africa. *Black contours* indicate correlations significant at the 95% confidence level (*p*=0.05). Box-plot indicates the spatial spread in the correlation coefficients over the area used in computing the index. e-f as for c-d but using WRITwo seasonal rainfall time-series have therefore been constructed by averaging the values over two irregular regions describing these seasonal patterns (dark red and blue contour in Figure 3.1a): Summer Rainfall Index (SRI in NDJF), and Winter Rainfall Index (WRI in MJJA).

We also perform a statistical sensitivity experiment, by removing ENSO influence from every climate anomaly, to disentangle the interactions involved properly. In addition, a question remains as to whether decadal Pacific variability is an inherent feature of ENSO itself, or a manifestation of a partially independent process (Power al., 1999; Rolland et al., 1999; Toured et al., 2005; Power and Colman, 2006). However, ENSO variability is widely known to be centred in the tropics, while the Pacific decadal variability can be centred in the north Pacific or be extended to the whole basin (cf. Sect. 4.1). The 1st EOF of tropical Pacific SST (35°S-35°N/120°E-60°W) has thus been generated, without applying band-pass filtering, for each season (i.e. NDJF and MJJA) and, then, statistically removed from the global SST and atmospheric data by subtracting linear regressions with the related principal component. Induced modifications in SST and atmospheric anomalies would therefore be, at least partially, linearly associated with ENSO or decadal ENSO-like variability, and vice versa. Similarity

between climate anomalies, which are identified before and after linearly subtracting ENSO, has been quantified at the global scale by computing spatial correlations. Timescales of summer and winter southern African rainfall variability appear similar according to the global wavelet spectra (Figure 3.2a). Interannual (i.e. 2-4 year), quasi-decadal (8-13 year; QDV) and interdecadal (15-28 year; IDV) timescales are significantly above the red noise background spectra (Figure 3.2a). According to the local wavelet spectra, all of these timescales are also significant in both indices and, due to the intermittency of the high-frequency timescales, dominant interannual timescales can be extended to 2-8 year (Figure 3.2b-c). A distinct separation (i.e. spectral gap) between the interdecadal and quasi-decadal signals is evident in Figure 3.2b-c. Timing of periods of increasing variance at the interdecadal and quasi-decadal scales is different between summer and winter (i.e. SRI and WRI; Figure 3.2b-c). The SRI displays significant increasing variance since the 1930s at the interdecadal and since the late 1960s at the quasi-decadal timescales (Figure 3.2b). Meanwhile, the WRI shows higher variance before the 1980s and the 1960s, and, then, is decreasing at interdecadal and quasi-decadal timescales, respectively (Figure 3.2c). The SRI and WRI are then decomposed with FFT (cf. Sect. 2.2), where each timescale of variability is displayed as rainfall anomalies, i.e. deviation from the mean of unfiltered data (i.e. SRI/WRI: 83.8/37.15 mm.month^{-1}; Figure 3.3).

3.3 Dominant timescale of southern African rainfall variability

Different metrics are calculated to evaluate their influence on seasonal rainfall amounts and fluctuations. Each rainfall index shows a robust spatial coherence over each timescale inside its calculation domain, with median correlation coefficients above 0.61 (and significant at $p \leq 0.05$; boxplots in Figure 3.3). The range of correlation coefficients is higher at the quasi-decadal timescale in both indices. By looking at the contribution of each timescale, here expressed as a percentage of total variance captured by the FFT filter on the overall rainfall variability (i.e. var[filtered data]/var[unfiltered data]), the interannual scale emerges unambiguously as the dominant mode of variability over both summer and winter regions, with a contribution of about 63.4-66.9% (against less than ~11% for the quasi- and interdecadal scales; Figure 3.3). Interdecadal variability (15-28 year; IDV) displays fluctuations of about ± 5 and 2 mm.month^{-1}, with maximum amplitude of fluctuations (i.e. maximum plus minimum) of about 19.8 and 8.25 mm.month^{-1} in the SRI and the WRI, respectively (Figure 3.3a, c). Although the timing of enhanced interdecadal variability is different, interdecadal SRI and WRI anomalies are correlated with similar regions over southern Africa (Figure 3.3b, d). Quasi-decadal fluctuations (8-13 year; QDV) and interdecadal fluctuations are of the same order of magnitude (Figure 3.3e, g). At this timescales, the SRI is positively correlated over most of southern Africa, with the exception of the south-western coastal regions (Figure 3.3f). Meanwhile the WRI is positively correlated with a large patch over their calculation domains, but also negatively correlated with the rest of southern Africa (Figure 3.3h).

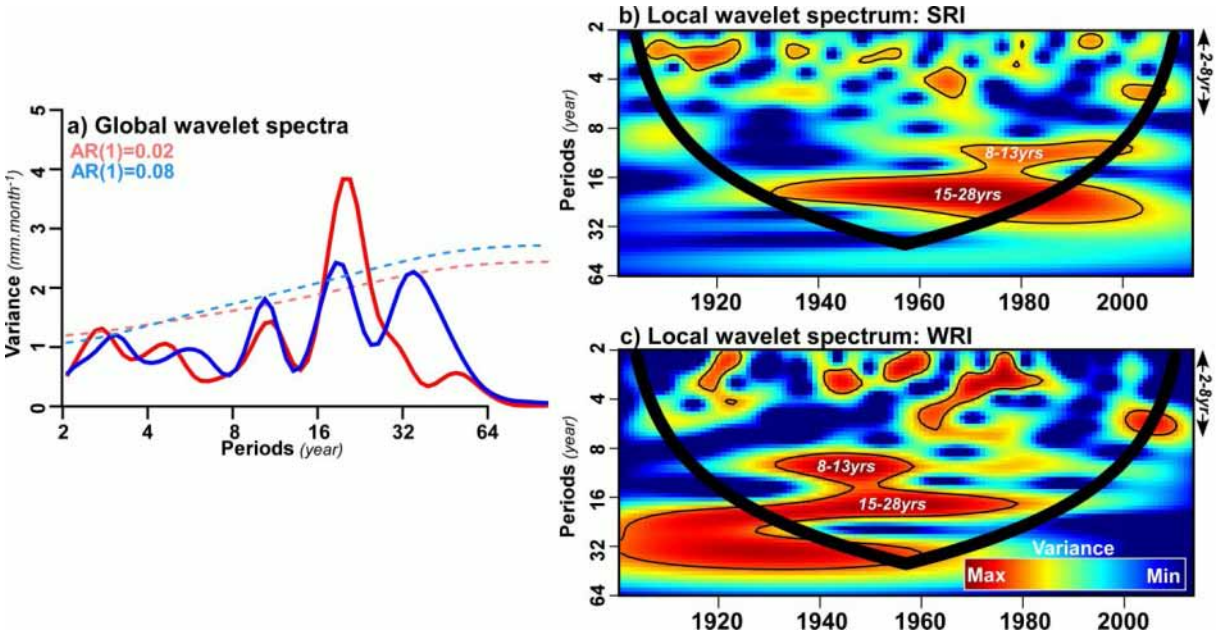

Figure 3.2. Time-scale patterns of variability in summer and winter southern African rainfall. a Global wavelet spectra of the SRI (blue) and the WRI (red). The dashed blue and red lines indicate the red noise spectra with regard to the first order autoregressive (SRI-AR[1] = 0.02; WRI-AR[1] = 0.08). b-c Continuous wavelet power spectrum of the SRI and the WRI. *Bold lines* (the so-called cone of influence) delineate the area under which power can be underestimated as a consequence of edge effects, wraparound effects and zero padding; *thin contour lines* show the 95% confidence limits based on 1000 Monte-Carlo simulations of the red noise background spectrum.

Interannual variability (2-8 year) shows fluctuations of about ± 13.5 and 7.2 mm.month^{-1}, with maximum amplitude of fluctuations of about 54.3 and 34.5 mm.month^{-1} in the SRI and the WRI, respectively (Figure 3.3i, k). Correlation patterns of interannual variability are almost the same as those obtained with unfiltered indices (Figure 3.1d, f), and constitute a large patch over their calculation domains (Figure 3.3j, l). Such results were expected regarding the percentage of variance captured by inverse FFT filtering, but this also demonstrates that results of comparing two 10-year periods will essentially describe changes in interannual variability between the two periods. 4 Multi-scale relationship with global SSTs. Figure 3.4 shows typical states of summer and winter global SSTs, constructed using composite analysis, and based on fluctuations of summer and winter southern African rainfall from interannual to interdecadal timescales. At the interdecadal timescale (15-28 year; IDV), Pacific SST anomalies associated with positive SRI display a horseshoe pattern, with cold anomalies in the central North Pacific surrounded by anomalies of opposite sign east of Asia, off California, in the Alaska gyre, and in Southern Hemisphere extratropical regions (Figure 3.4a). This SST pattern is consistent with the interdecadal signals described by Tourre et al. (1999, 2001, 2005), and it is also reminiscent of the Pacific Decadal Oscillation (PDO) during its negative phase (Mantua et al., 1997; Minobe, 2000; Mantua and Hare, 2002; Mills and Walsh, 2013). Using the PDO index as defined by Mantua et al. (1997), significant interdecadal fluctuations are detected, and these are coherent with interdecadal SRI variability (Figure 3.5a). Such anomalies are still identified after linearly subtracting the influence of ENSO and decadal ENSO-like variability, hence the strong (significant at p = 0.05) spatial correlation coefficient between the two global SST patterns (Figure 3.6a). Some regional differences are identified, however. North Pacific anomalies are magnified in the extratropical and eastern equatorial regions, while they are weakened over western equatorial regions (Figure 3.6a).

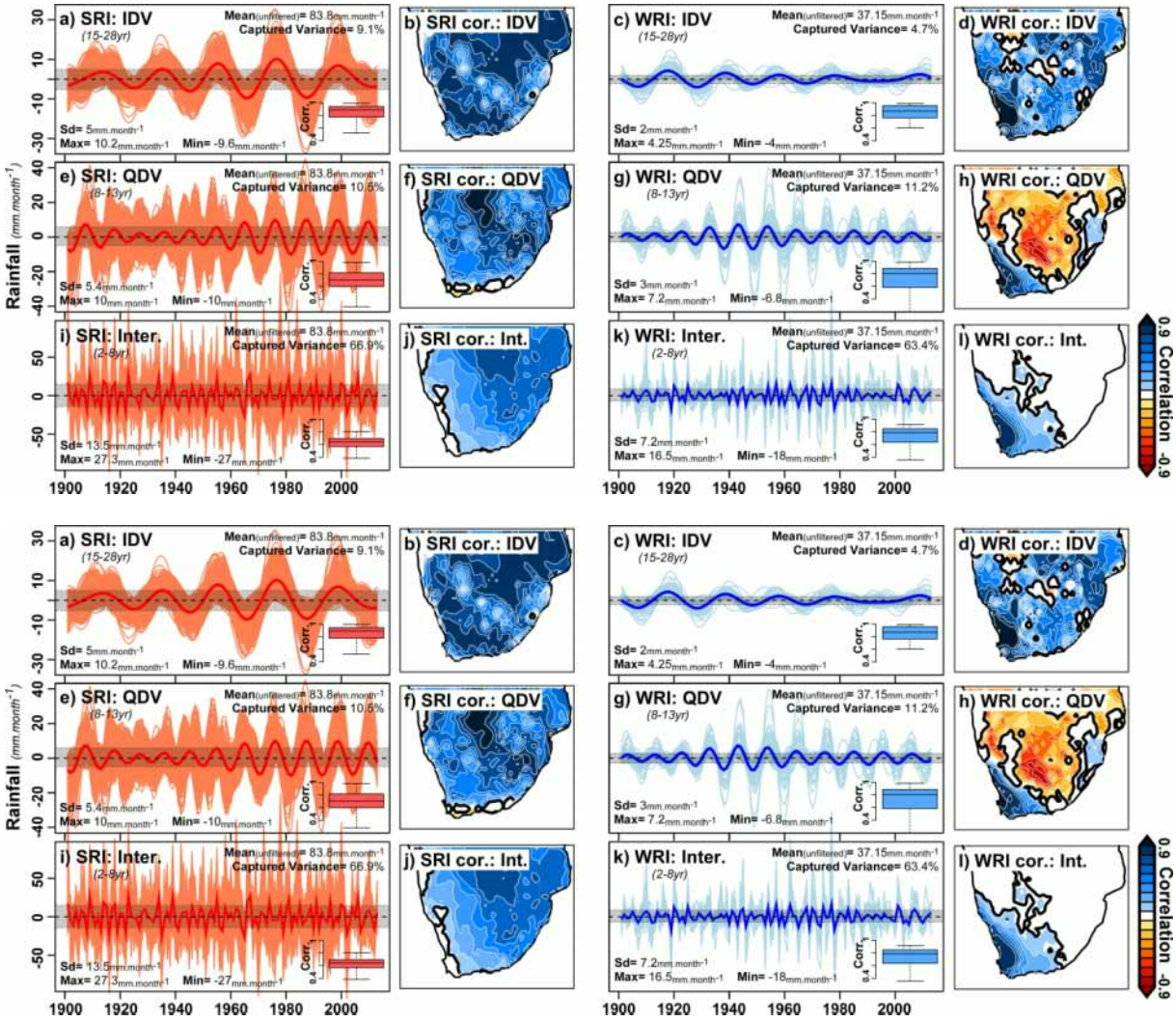

Figure 3.3. Reconstruction by FFT of dominant timescales modulating summer and winter southern African rainfall: contribution and spatial coherence. a Time-evolution and statistics (Captured variance in %, SD, Max, Min) of interdecadal variability (IDV: 15-28 year) in the SRI (*red*), and all grid-points used for its calculation (*light red*) over the 20th century. The boxplot indicates the range of correlation coefficients between the SRI and each grid-point used for its calculation. b Pointwise correlation between the SRI and the CRU TS 3.22 at the interdecadal timescale. Black contours indicate correlations significant at *p* = 0.05. c-d as for a-b but for the WRI (*blue*) and all grid-points used for its calculation (*light blue*). e-h as for a-d but for the quasi-decadal timescale (QDV: 8-13 year). i-l as for e-h but for the interannual timescale (2-8 year). The grey shaded bands delineate the area above which rainfall anomalies (i.e. greater than ± 1 SD) have been selected to performed composite analysis.

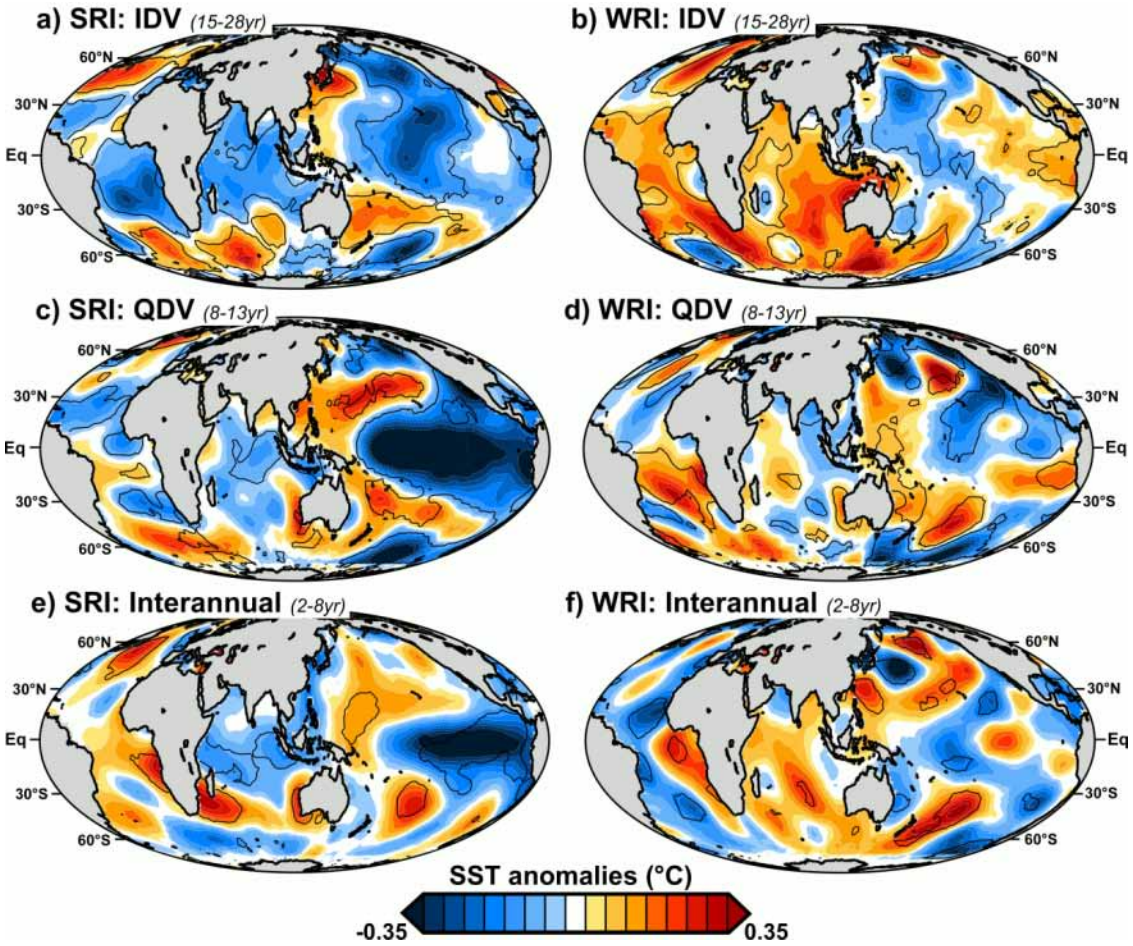

Figure 3.4. Summer and winter anomalies of SSTs associated with periods of high-amplitude over the dominant timescales of summer and winter southern African rainfall variability, respectively. a Interdecadal composite anomalies of SSTs (in °C) during periods of enhancing interdecadal variability (IDV ≥ 1 SD) in the SRI. b as for a but in the WRI. c-d as for a-b but for the quasi-decadal timescale (QDV). e-f as for c-d but for the interannual timescale. The statistical significance (*black contours*) has been estimated by testing the difference in mean between SST anomalies during periods of rainfall variability greater and lower than 1 SD (cf. anomalies outside grey shaded bands in Figure 3.3), through a modified *t*-test accounting for pseudo-replication in the series at $p = 0.05$.

Two thirds of the PDO decadal variance is explained by zonal advection in the Kuroshio-Oyashio Extension and anomalies in the Aleutian low region (Schneider and Cornuelle, 2005). Interactions between anomalies in the Kuroshio-Oyashio Extension, the Aleutian low region and tropical convections were also proposed as a key driver of interdecadal climate variability in Tourre et al. (1999, 2001, 2005). Positive interdecadal anomalies in the SRI are also related to cold anomalies in the tropical Indian Ocean and South Atlantic, while warm anomalies are detected in the extratropics (Figure 3.4a). This defines the South Atlantic dipole, which is the dominant SST pattern in this region, in particular at the interdecadal timescales (Venegas et al., 1997), and the South Indian Ocean Dipole (Behera and Yamagata, 2001).

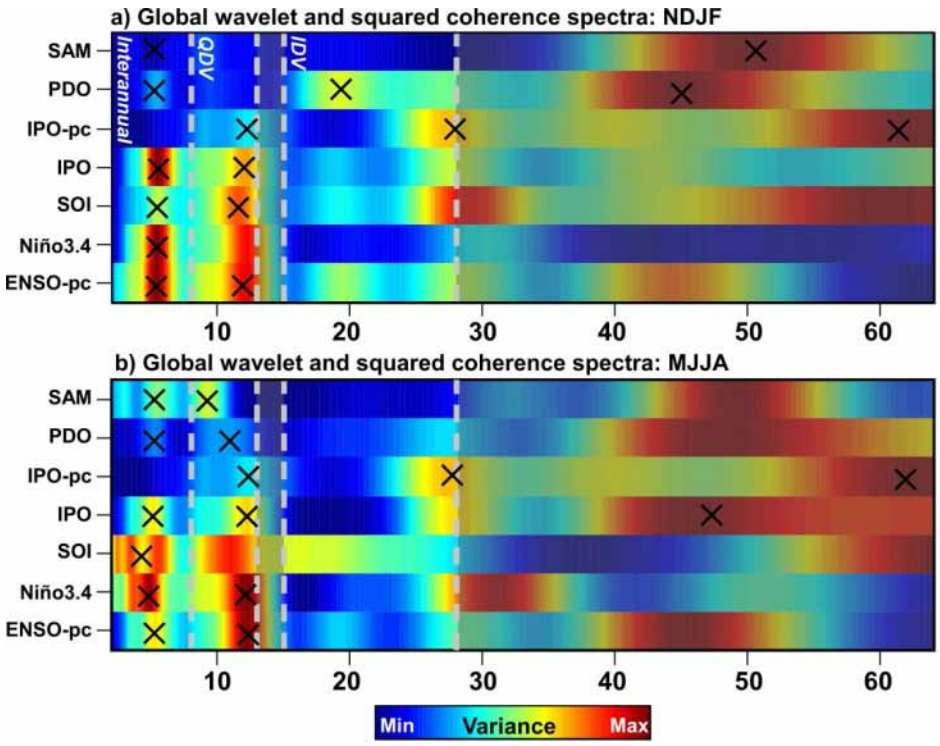

Figure 3.5. Time-scale of variability in key global climate indices, and their statistical relationship with South African rainfall. a) Comparison of global wavelet power spectrum in six global climate indices during summer, and their wavelet squared coherences with the SRI. b) as in a but in winter. The black crosses indicate the significant timescales and squared coherence at 95% confidence limits based on 1000 Monte-Carlo simulations of the red noise background spectrum. Grey dashed lines delineate the three dominant timescales of South African rainfall variability. Seven global climate indices have been computed for each season using ERSST.v4 or 20CR.v2 data sets: (1) an ENSO-pc based as defined in Sect. 2.2; (2) the Niño3.4 index; (3) the Southern Oscillation Index (SOI); (4-5) the tripole index for the Interdecadal Pacific Oscillation (IPO), which has been computed with or without 10-year low-pass filtering, as defined in Henley et al. (2015); (6) the Pacific Decadal Oscillation (PDO) index as defined in Mantua et al. (1997); and (7) the SAM index (Thompson and Wallace, 2000).

Such influence of the South Indian Ocean Dipole at decadal timescales has recently been proposed through Coupled Global Model (CGM) by Morioka et al. (2015). SST anomalies in the South Atlantic and South Indian Ocean are quite similar after removing the influence of tropical Pacific SST variability (Figure 3.6a): this suggests, at least linearly, little impact of ENSO or decadal ENSO-like variability. At the same timescale, Pacific SST anomalies associated with positive WRI anomalies are mostly centred on the North Pacific. Cold anomalies are detected over the south-western and the central east North Pacific (Figure 3.4b). Warm anomalies are also identified near the equator westward from the South American Coast (Figure 3.4b). Although those equatorial warm anomalies do not seem to extend over the canonical ENSO footprint westwards, this might indicate potential influences of decadal El Niño-like anomalies or of the Interdecadal Pacific Oscillation during its positive phase (IPO; Power al., 1999; Folland et al., 1999). However, there is no significant interdecadal signal in the ENSO and IPO indices during winter (Figure 3.5b).

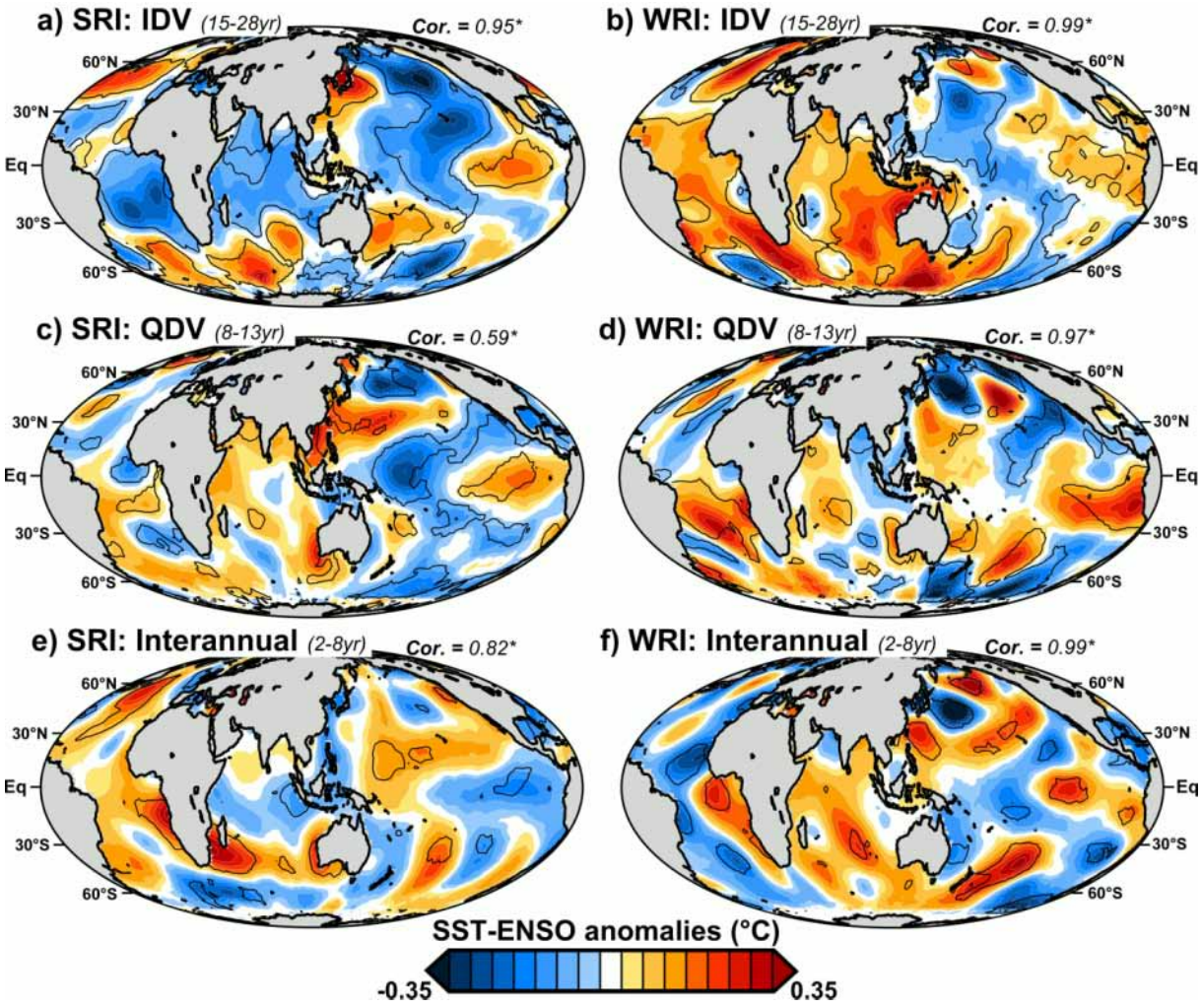

Figure 3.6. as for Figure 3.4, but after linear subtraction of ENSO influence. The spatial association between SST anomalies before and after removing the influence of ENSO has been quantified using a spatial correlation. Asterisks indicate significant spatial correlations at $p = 0.05$ with regard to Dutilleul's modified *t*-tests accounting for spatial autocorrelation.

All worldwide SST patterns are therefore very similar with or without influences of tropical Pacific SST variability (spatial correlation = 0.99; Figure 3.6b), which suggests that ENSO or decadal ENSO-like patterns cannot be the main driver of interdecadal variability in the WRI. These SST anomalies are dominated by a quasi-global SST warming in the Atlantic and in the Indian Ocean (Figs. 6b, 5b). Meanwhile, dipole SST anomalies occur southwest of southern Africa (Figure 3.4b, 6b). At the quasi-decadal timescales (8-13 year; QDV), Pacific SST anomalies associated with positive SRI fluctuations show cold anomalies in the tropical Pacific flanked by a horseshoe pattern of opposite sign, with marked anomalies in both North and South Pacific (Figure 3.4c). This SST pattern is consistent with the quasi-decadal signals described by Tourre et al. (1999, 2001, 2005), and is reminiscent of the IPO, which is a wide-basin pattern of ENSO, during its negative life-cycles (Zhang et al., 1997; Power et al., 1999; Folland et al., 1999). This negative IPO occurs concomitantly with cold anomalies in the tropical Indian Ocean, while the South Atlantic SST dipole is identified (Figure 3.4c). The physical and statistical independence between the IPO and ENSO is, however, debatable. This is evident when comparing the global wavelet spectra of different ENSO indices (ENSO-pc based, Niño3.4 and the Southern

Oscillation Indices [SOI]) with the tripole index for the IPO defined by Henley et al. (2015), which display very similar timescales of variability (Figure 3.5a). After linearly removing ENSO influence, tropical Indian and Pacific SST anomalies are thus very strongly weakened, while extra-tropical SST anomalies do not change (except for the South Atlantic SST dipole, which is substantially weakened; Figure 3.6c). The spatial correlation coefficient between the two global SST patterns is 0.59 (Figure 3.6c). This supports earlier findings (Tourre et al., 2005; Power and Colman, 2006), which showed that quasi-decadal fluctuations of equatorial Pacific SSTs, here related to the IPO, can be viewed as low-frequency ENSO phenomena. Only the tripole SST pattern in the North Pacific seems to be uncorrelated with the tropical Pacific SST variability (Figure 3.6c). Pacific SST anomalies associated with positive quasi-decadal WRI fluctuations are centred on the northern regions, and show warm anomalies being surrounded by cold anomalies in the South-eastern and North Pacific (Figure 3.4d). Warm SST anomalies in eastern equatorial Pacific, which can be influenced by decadal ENSO-like and/or the IPO, are also detected at the quasi-decadal timescale (Figs. 4d, 5b, 6d). However, although the eastern Pacific SST anomalies are slightly enhanced, most global SST anomalies remain qualitatively unchanged after removing the influence of tropical Pacific SSTs (spatial correlation = 0.97; Figure 3.6d). Over the adjacent ocean, the South Atlantic SST dipole is identified (Figs. 4d, 6d). Meanwhile, Indian Ocean SST anomalies display warm anomalies over the western tropical regions, and cold anomalies over the eastern and extratropical regions (as far south as the latitude of Australia; Figs. 4d, 6d). At the interannual scale (2-8 year), Klein et al. (1999) suggest that La Niña SST anomalies, which are associated with a cooler tropical Indian Ocean SST, are related to positive SRI anomalies. This is confirmed in Figure 3.4e, and is consistent with the significant fluctuations and squared coherences identified in the ENSO indices at the interannual timescale (Figure 3.5a). Such anomalies are substantially weakened after linearly removing ENSO influence, indicating that they are strongly influenced by ENSO (Figure 3.6e). ENSO influence is, however, not strictly linear at the interannual timescale. The ENSO footprint in the equatorial Pacific is thus still identified after linearly subtracting its influence (Figure 3.6e). The South Indian Ocean SST dipole is also identified in Figure 3.4e, and appears to be magnified when ENSO influences are linearly removed (cf. Figs. 4e, 6e). We also note a warmer tropical Atlantic in the northern Benguela upwelling region (Figs. 4e, 6e), which is reminiscent of Atlantic Niños and Benguela Niños (Lübbecke et al., 2010; Rouault, 2012). At the interannual scale (2-8 year), positive WRI fluctuations are associated with very sparse significant SST signals, which are unlikely to be distinguishable from a random noise. Significant SST anomalies are however identified in the North Pacific, i.e. cold anomalies east of Japan being which are surrounded by warm anomalies over the China Sea, off the Californian coast and South of the Bering Sea (Figs. 4f, 6f). We also note warmer eastern tropical Atlantic and Indian Ocean SSTs, as well as cooler western Atlantic SSTs (Figs. 4f, 6f). As for the longer timescales, global SST anomalies remain unchanged after removing ENSO influences (spatial correlation = 0.97; Figure 3.6f). In summary, SST anomalies related to SRI and WRI are different for each timescale examined. SST anomalies associated with SRI fluctuations are substantially influenced by ENSO (especially at the quasi-decadal and interannual timescales). However, this is not the case for WRI. As suggested in Wang et al. (2014), the PDO might dampen or exacerbate ENSO-like anomalies and, therefore, it could be influential driver of summer rainfall in southern Africa. Interestingly, according to Venegas et al. (1997) and Behera and Yamagata (2001), both South Atlantic and South Indian Ocean SST dipoles can develop independently of ENSO (but remain non-linearly influenced by the latter), and are also related to summer and winter South African rainfall.

3.4 Atmospheric forcing on SST

This section discusses potential mechanisms resulting in the SST anomalies described in Section 4.1 through composite anomalies of latent heat flux (LHF; Figure 3.7). Indeed, although the distribution of LHF anomalies is noisier than for SST, reduced latent heat fluxes associated with warmer SST increase latent heat flux associated with cooler SST. This suggests that atmospheric variability is driving the SST. The opposite relation between latent heat flux and SST would suggest the atmospheric variability damps the SST anomalies. For instance, on each timescale and using both summer and winter rainfall indices, South Atlantic and South Indian Ocean dipole SST anomalies are almost systematically associated with LHF anomalies of opposite signs (Figure 3.7). Such subtropical SST anomalies could therefore be linked to changes in surface fluxes in response to changes in surface winds, as hypothesized in earlier studies (Behera and Yamagata, 2001; Fauchereau et al., 2003; Suzuki et al., 2004). However, according to Vizy and Cook (2015), long-term decadal SST cooling anomalies over the subtropical South Atlantic are primarily associated with increased latent flux from the ocean, which are, in turn, associated with a poleward shift of South Atlantic atmospheric circulation and an intensification of surface wind speeds over this region. Similar feedback effects to the atmosphere have been related to the South Indian Ocean SST dipole (Washington and Preston, 2006; Morioka et al., 2015). Such air-sea interactions are, however, not identified in summer at the interdecadal timescale (Figure 3.7a). Morioka et al. (2012, 2013) and Vizy and Cook (2015) also highlight the importance of year-to-year variations in the mixed layer depth on the growth and maintenance of these SST anomalies. Furthermore, Vizy and Cook (2015) noted that poleward shift in the South Atlantic atmospheric circulation could also weaken coastal upwelling off the Angola Coast. This could, for instance, result in warmer tropical Atlantic over the Benguela upwelling region, such as noted in summer and winter at the interannual scale (Figs. 4e-f). Such timescale dependent air-sea interactions can also be detected in the North Pacific (Figure 3.7). North Pacific Tripole SST anomalies are only associated with LHF of opposite signs at the quasi-decadal and interannual timescales in the SRI and WRI, respectively (Figure 3.7c, f). Figure 3.7a and 7b show that, at the interdecadal timescale (and for the quasi-decadal fluctuations in the WRI; Figure 3.7d), enhanced LHF over warm SST anomalies, and vice versa, is apparent along the oceanic subarctic frontal zone: these act to damp SST anomalies while exerting a thermodynamic forcing on the overlying atmosphere (Frankignoul and Kestenare, 2002; Tanimoto et al., 2003; Taguchi et al., 2012). Tanimoto et al. (2003), also argue that weakened surface westerlies in the central Pacific associated with the Aleutian low contribute to the maintenance and eastward development of the warm SST anomalies by counteracting the damping effect through anomalous surface heat fluxes. SST anomalies, such as the SST dipole in the oceans adjacent to southern Africa, could thus be driven by regional shifts in the subtropical westerlies, even at the interdecadal and quasi-decadal timescales. Such decadal air-sea interactions in the Southern Hemisphere could be associated with changes in atmospheric circulation due to the SAM and ENSO (Deser et al., 2010). However, as proposed by other studies (Washington and Preston, 2006; Morioka et al. 2015; Vizy and Cook, 2015), a feedback effect to the atmosphere, manifested as an increase in the persistence time for the SAM (or ENSO-like anomalies), is also possible due to intrinsic atmospheric dynamic processes (Sen Gupta and England, 2007).

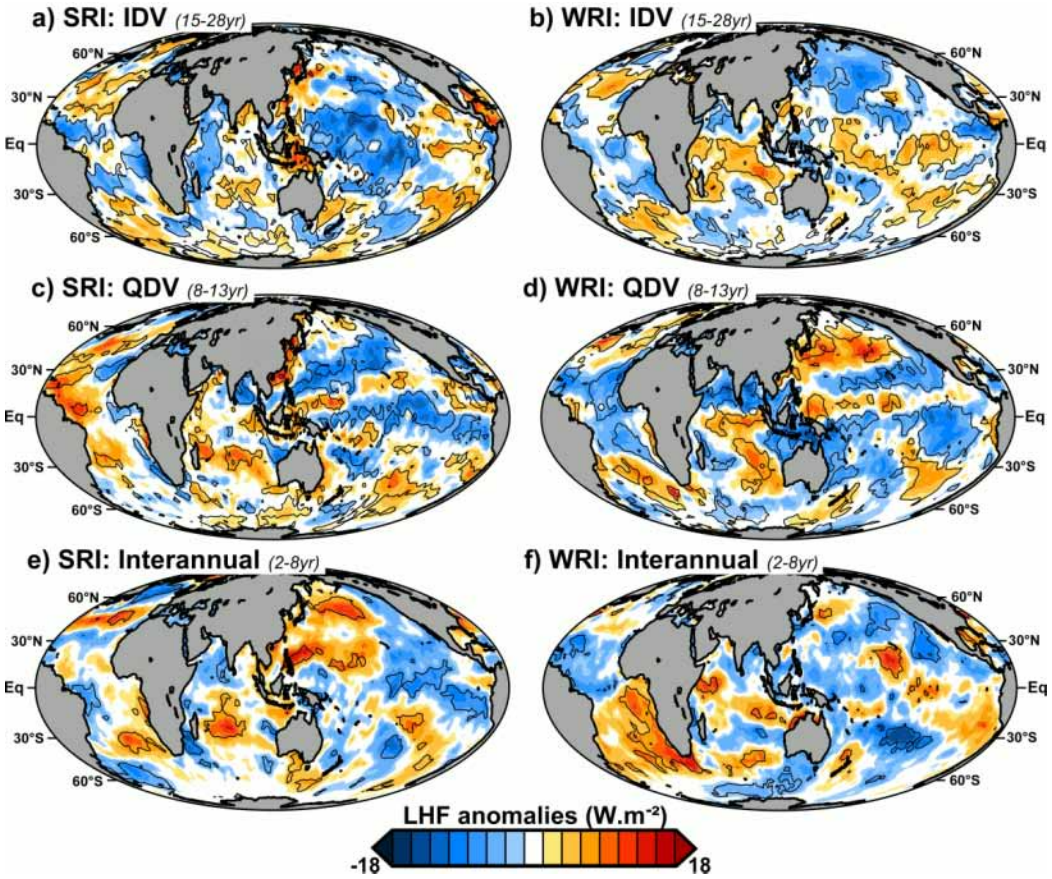

Figure 3.7. as for Figure 3.4, but for latent heat flux (LHF; in W.m^{-2}).

3.5 Atmospheric circulation

3.5.1 Low- to mid-tropospheric circulation anomalies

Figure 3.8 displays composite anomalies of geopotential (z) and moisture fluxes at 1000 hPa and 500 hPa based on significant timescales of summer and winter rainfall variability. Figure 3.9 shows the same results for 500 hPa after linear removal of ENSO influence. At the interdecadal timescale (15-28 year; IDV), low and mid-tropospheric circulations associated with positive SRI display a quasi-annular mode, with low-pressure anomalies between the Polar Regions and 36°S and high-pressure anomalies in the subtropical and tropical regions (Figure 3.8a). A southward shift of subtropical westerly moisture fluxes, which is associated with a weakening of westerly moisture flows toward southern Africa, is identified for a large part of the Southern Hemisphere (Figure 3.8a). This shift is also linked to an anomalous anticyclonic circulation in the Mascarene high-pressure region related to an anomalous low-level easterly moisture flux along 10-20°S towards southern Africa, which is favoured by low-pressure anomalies over the continent (Figure 3.8a). Such anomalies have some similarities with those related to the SAM (spatial correlation = 0.51, significant at p = 0.05), but there is no significant interdecadal signal in the summer SAM index (Figure 3.5a). 0.05. Only significant zonal or meridional moisture flux anomalies at p = 0.05 are shown by *arrows*. These geopotential anomalies are therefore unrelated to the SAM. Moreover, as illustrated by very low spatial correlations (non-significant at p = 0.05) between the two atmospheric patterns, the linear influence of ENSO and decadal ENSO-like variability seem to be restricted to anomalous subtropical/tropical high pressure and easterly moisture fluxes, which emerge as substantially weakened in Figure 3.9a. Easterly moisture fluxes related to anomalous

anticyclonic circulations in the Mascarene region are nevertheless consistent with idealized model experiments of South Indian Ocean SST forcing, which is similar to that observed in Figure 3.4a, in HadAM3 (Washington and Preston, 2006).

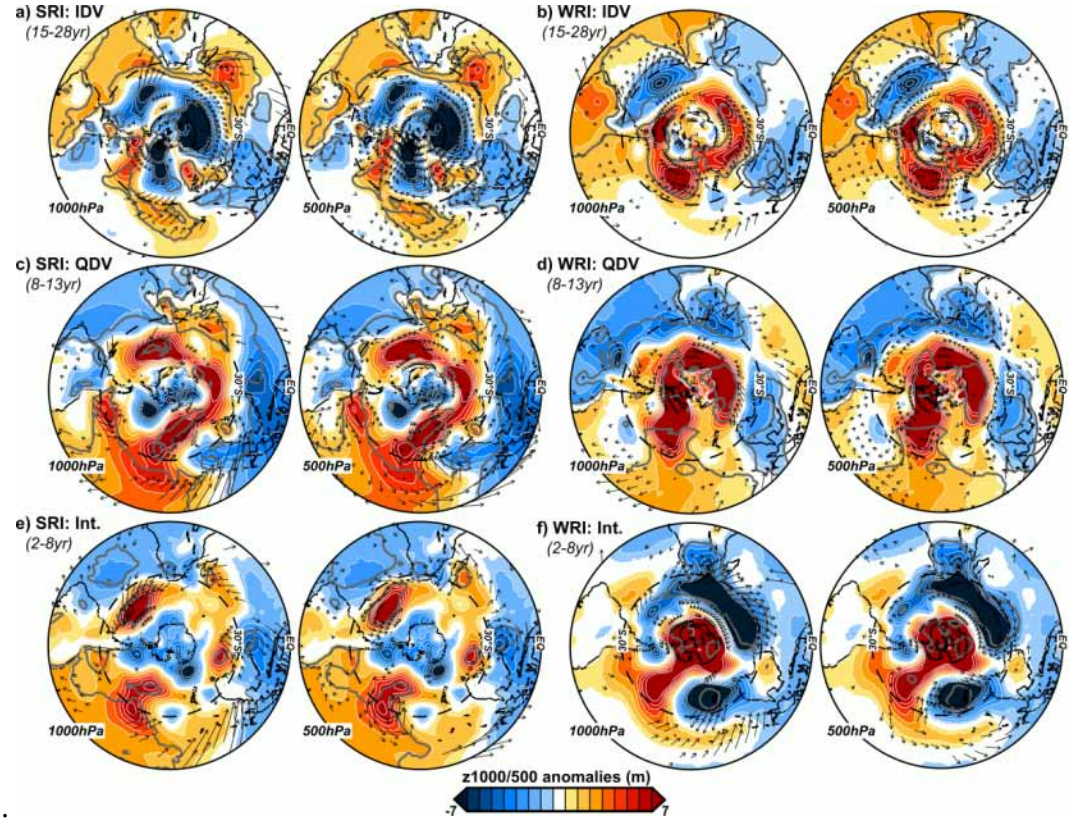

Figure 3.8. Anomalies of low- and mid-tropospheric circulations during periods of high-amplitude over the dominant timescales of summer and winter southern African rainfall variability. a Interdecadal composite anomalies of geopotential height (z in m) and moisture fluxes (*arrows*, $\vec{\nabla}$q in gkg^{-1}m.s^{-1}) at 1000 hPa (*right-hand panels*) and 500 hPa (*left-hand panels*) during periods of enhancing interdecadal variability (IDV ≥ 1 SD) in the SRI. b as for a but in the WRI. c-d as for a-b but for the quasi-decadal timescale (QDV). e-f as for c-d but for the interannual timescale. The statistical significance (*grey contours*) has been estimated by testing the difference in mean between geopotential height anomalies during periods of rainfall variability greater and lower than 1 SD (cf. anomalies outside grey shaded bands in Figure 3.3), through a modified *t*-test accounting for pseudo-replication in the series at *p* =

As proposed by Morioka *et al*. (2015) through CGCM experiments, such decadal air-sea interactions could be interpreted as feedback effects to the atmosphere, which could help increase the persistence of regional shifts in the subtropical circulations. Figure 3.8b shows that positive interdecadal WRI fluctuations are associated with a zonal geopotential pattern in the Southern Hemisphere, which is more pronounced in the South Atlantic. High-pressure anomalies are identified north of Antarctica, while low-pressure anomalies occur in the subtropics (Figure 3.8b). This indicates a weakening of the St Helena High, which is consistent with a northward shift of the subtropical westerlies in the South Atlantic (Figure 3.8b). An enhancement of westerly moisture fluxes toward south-western regions of southern Africa is thus identified consistently with an increase in the mid-latitude frontal activity (Figure 3.8b). After linearly removing the influence of tropical Pacific SSTs, these geopotential anomalies are largely unchanged at the hemispheric scale (spatial correlation = 0.75, significant at *p* = 0.05; Figure 3.9b). The tropical geopotential anomalies, however, are substantially reduced. This also associated with a weakening of subtropical low-pressure and westerly anomaly in the South Atlantic,

and to enhance subtropical high-pressure anomalies in the South Indian Ocean (Figure 3.9b). The tropical Pacific SST variability is likely to linearly influence the asymmetry in the zonal geopotential pattern between the Atlantic and the Indian Oceans. This influence appears stronger for the moisture flux analyses (spatial correlation ≥ 0.33), whose anomalies are substantially weakened in Figure 3.9b. Significant interdecadal fluctuations, which are coherent with those of the WRI, are indeed identified using a PC-based IPO index (Figure 3.5b). At the quasi-decadal timescale (8-13 year; QDV), positive SRI anomalies are associated with an annular signal in the Southern Hemisphere, with weak low-pressure anomalies over Antarctica and in the tropics over the Atlantic and Indian basins, as well as high pressure anomalies in the mid-latitudes and tropical Pacific (Figure 3.8c). Due to zonally asymmetric patterns in the annular geopotential anomalies between the Atlantic and the Indian Ocean, high-pressure anomalies are northward in the Indian Ocean up to Madagascar (Figure 3.8a, c). An anomalous low-level easterly moisture flux reaching south-eastern Africa is related to enhancing Mascarene High. These anomalies are partly reminiscent of those driven by the SAM (spatial correlation = 0.48, significant at $p = 0.05$), but there is no significant quasi-decadal fluctuations in the summer SAM index (Figure 3.5a). After linearly removing the influence of ENSO and decadal ENSO-like variability, geopotential anomalies disappear, especially in the tropics (Figure 3.9c). Even in the middle and high latitudes, annular geopotential anomalies are almost completely suppressed (Figure 3.9c). Summer rainfall variability is thus predominantly driven by the tropical dynamic linked to ENSO, decadal ENSO-like variability or the IPO. Without these effects high-pressure anomalies, which prevent rainfall, emerge (Figure 3.9c). This is consistent with the results of Pohl et al. (2009), which show the statistical dependence between the SAM and ENSO in austral summer, and their consequences for southern African rainfall. At the same timescale, positive WRI anomalies are linked to an almost continuous and zonally symmetric annular pattern of positive geopotential height anomalies over the Southern Ocean. This is reminiscent of the SAM anomalies (spatial correlation = 0.71, significant at $p = 0.05$). The Mascarene High and the St Helena High are both weakened (Figure 3.8d). A northward shift in the mid-latitude westerlies is identified over the South Atlantic and Indian Oceans (Figure 3.8d). This is associated with enhanced mid-latitude frontal activity and, thus, westerly moisture fluxes from the South Atlantic toward southern Africa, which are favoured by low-pressure anomalies there (Figure 3.8d). With this annular pattern are also associated contrasting geopotential height anomalies in the tropics, with high-pressure anomalies in the Pacific Ocean and low-pressure anomalies over the Atlantic Ocean and Australia (Figure 3.8d). Although subtropical/tropical low-pressure anomalies are substantially weakened after linearly removing the influence of ENSO and decadal ENSO-like variability (Figure 3.9d), annular geopotential anomalies increase in spatial coherence and are more centred on Antarctica. Associated shifts in the subtropical westerlies are still identified (Figure 3.9d). Both patterns are very significantly correlated at the hemispheric scale (Figure 3.9d). This suggests a specific influence of the SAM on the WRI at the quasi-decadal timescale. Quasi-decadal fluctuations, which are significantly coherent with those of the WRI, are indeed significant in the winter SAM index (Figure 3.5b). This corroborates the findings of L'Heureux and Thompson (2006) and Pohl et al. (2009), which show that the statistical relationship between the SAM and ENSO is strong only during austral summer and is not significant during the rest of the year. However, we note decreasing westerly moisture fluxes after removing the influence of tropical Pacific SST variability (Figure 3.9d). Southern African rainfall anomalies are thus likely to be of the same sign, but their intensity could be modulated at the quasi-decadal timescale by ENSO and/or decadal ENSO like variability, such as the IPO. At the interannual timescale (2-8 year), low-pressure anomalies in the Polar Regions and asymmetric enhancing of the St Helena and Mascarene Highs indicate a southward shift of the westerly wind belt (Figure 3.8e). Meanwhile, anomalous low-level easterly moisture flux into southern Africa, which is favoured by low-pressure anomalies over the continent, is generated from anticyclonic circulation in

the South Indian Ocean (Figure 3.8e). These anomalies, even though they are weak over Antarctica and reveal some zonal asymmetries in the mid-latitudes, show some similarities with the summer SAM (spatial correlation = 0.58, significant at $p = 0.05$). Low-pressure anomalies also occur in the tropical regions from the Atlantic to the western Pacific, while high-pressure anomalies are identified in the eastern tropical Pacific (Figure 3.8e). The spatial correlation between geopotential anomalies before and after subtracting ENSO influences is about 0.7 (significant at $p = 0.05$) at the hemispheric scale (Figure 3.9d). This is lower in the moisture fluxes than geopotential anomalies. Tropical geopotential anomalies are suppressed, and easterly moisture fluxes are substantially reduced after linearly subtracting the ENSO effect (Figure 3.9e). Back effects of SST anomalies on the atmosphere are also likely to contribute to maintaining shifted atmospheric circulations over the South Indian Ocean (Washington and Preston, 2006; Morioka et al., 2015), even after subtracting ENSO effects. Annular geopotential anomalies of opposite sign, which are centred on Antarctica, are associated with positive interannual WRI fluctuations, suggesting influence of the SAM (spatial correlation = 0.75, significant at $p = 0.05$; Figure 3.8f). This geopotential signal is nevertheless stronger over the South Indian Ocean, which indicates a weakening of the Mascarene High. Enhancing mid-latitude frontal activity is therefore suggested by a northward shift in mid-latitude westerlies, but it is more pronounced in the South Indian Ocean (Figure 3.8f). The resulting moisture flux only affects western to south-western coastal regions of southern Africa (Figure 3.8f). At the hemispheric scale, geopotential anomalies appear similar after linearly removing ENSO influences (spatial correlation = 0.89), while this is lower in the moisture fluxes (spatial correlation ≤ 0.44, significant at $p = 0.05$; Figure 3.9d). Linearly removing ENSO influences leads to enhanced annular geopotential anomalies, especially in the South Atlantic (Figure 3.9f). This therefore breaks regionally the asymmetry in the westerly flows, but also confirms the SAM influence on winter rainfall). However, without the linear influence of ENSO, the westerly moisture flux is substantially reduced (Figure 3.9f). Although ENSO does not influence the signs of interannual South African rainfall anomalies, amplifying effects on their intensity are noted. In summary, low- to mid-atmospheric circulation anomalies, which affect SRI and WRI, display barotropic quasi-annular modes throughout the Southern Hemisphere, which are influenced by ENSO and decadal ENSO-like, mostly in the austral summer, and related to the SAM, especially in winter. As emphasized by earlier studies, the SAM itself is significantly correlated with ENSO in summer. The ENSO influence is stronger in the tropics and subtropics and, according to Fogt and Bromwich (2006), this leads to asymmetrical geopotential anomalies between the South Atlantic and South Indian Oceans, which are likely to alter the canonical SAM pattern in summer. In winter, the influence of the SAM on southern African rainfall is strong and significant, particularly at the quasi-decadal and interannual timescale. Although it is sensibly weaker than in summer, the influence of ENSO and decadal-ENSO like variability remains strong in the tropics, and leads to asymmetrical geopotential anomalies over the South Atlantic and Indian oceans.

3.5.2 Upper-tropospheric circulations and convection anomalies

Figure 3.10 displays interdecadal to interannual anomalies of 200 hPa wind, as well as tropical/extratropical deep-convection anomalies, using Outgoing Longwave Radiation (OLR). At the interdecadal timescale (15-28 year; IDV), positive SRI anomalies are associated with a west/east contrast of enhanced deep-convection over the Maritime Continent and suppressed deep-convection from the central to eastern Pacific (Figure 3.10a).

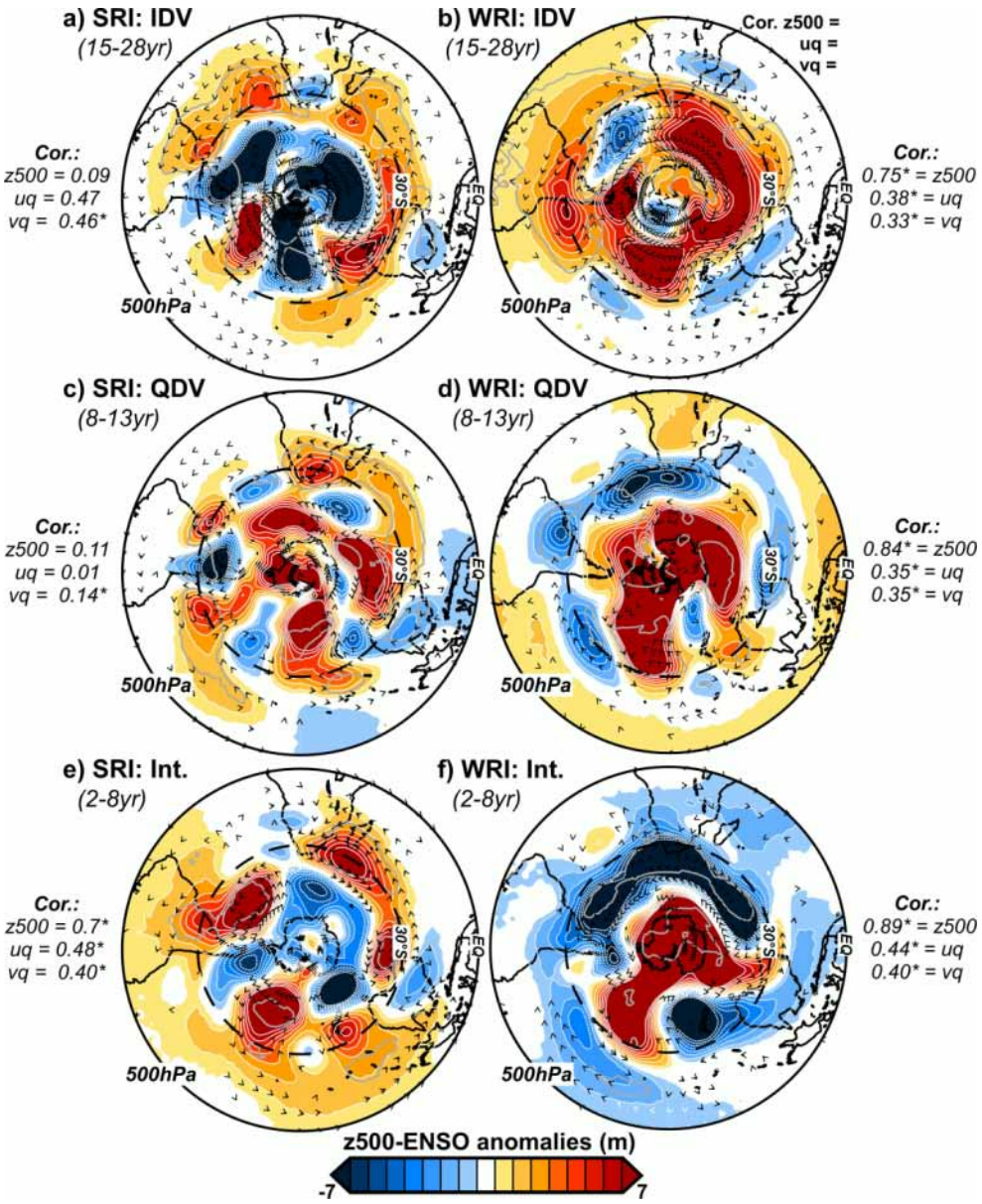

Figure 3.9. As for Figure 3.8, right-hand panels, but after linearly subtracting ENSO influence. The spatial association between atmospheric anomalies before and after removing influences of ENSO has been quantified using a spatial correlation. Asterisks indicate significant spatial correlations at p = 0.05 with regard to Dutilleul's modified *t*-tests accounting for spatial autocorrelation.

These anomalies are much pronounced over the Southern Hemisphere than in Northern Hemisphere (Figure 3.10a), but this could be consistent with a westward shift in the Walker circulation associated with a negative PDO. Suppressed deep-convections are also seen over the South Pacific Convergence Zone (SPCZ) and the poleward-shifted ITCZ (Figure 3.10a). In the southern African domain, we identify in Figure 3.10a a large band of enhanced convection, being surrounded to the east and to the west by suppressed deep-convection, with both extending in a NW-SE direction. Interestingly, this suggests a southwestward shift in the climatological position of the SICZ, which, according to earlier studies (e.g. Lyon and Mason, 2007; Hart et al., 2012a, b), leads to enhanced development of synoptic scale rain-bearing systems, such as the TTTs, over the north-eastern regions of southern Africa at the synoptic scale.

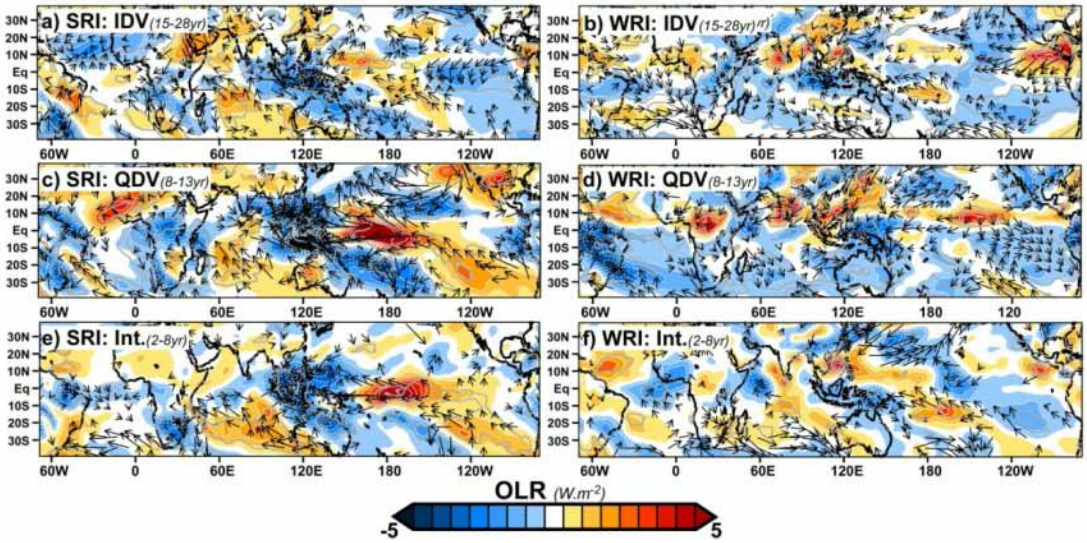

Figure 3.10. Anomalies of outgoing longwave radiation (OLR) and upper-tropospheric circulations during periods of high-amplitude over the dominant timescales of summer and winter southern African rainfall variability. a Interdecadal composite anomalies of OLR (in W.m^{-2}) and wind circulations at 200 hPa (*arrows*, in m.s^{-1}) during periods of enhanced interdecadal variability (IDV ≥ 1 SD) in the SRI. b as for a but in the WRI. c-d as for a-b but for the quasi-decadal timescale (QDV). e-f as for c-d but for the interannual timescale. The statistical significance (*black contours*) has been estimated by testing the difference in mean between OLR anomalies during periods of rainfall variability greater and lower than 1 SD (cf. anomalies outside grey shaded bands in Figure 3.3), through a modified *t*-test accounting for pseudo-replication in the series at *p* = 0.05. Only significant upper zonal or meridional wind anomalies at *p* = 0.05 are shown by *arrows*. Strong negative OLR anomalies (in blue) are associated with higher than normal clouds while positive anomalies (in red) refer to suppressed convection.

This shift in the SICZ could be due to: i) a response to atmospheric Rossby waves generated in the Southern hemisphere by ENSO modes of variability (here La Niña conditions; Cook, 2001; Fauchereau et al., 2009), and/or ii) Indian Ocean SST anomalies (Nicholson, 1997; Nicholson and Kim, 1997). Significantly, we find that, after linearly removing the influence of ENSO and decadal ENSO-like variability, such shifts in the SICZ are suppressed (Figure 3.11a), while Indian SST anomalies remain quite unchanged (Sect. 4.1; Figure 3.6a). Notably, this also highlights that, in the absence of tropical signals, interdecadal PDO variability cannot result in a shift of the Walker circulation and the SICZ. Also, a decrease of upper-tropospheric westerlies due to a southward position of the mid-latitude westerly jet is confirmed with or without the influence of tropical Pacific climate variability (Figs. 10a). At the global scale, upper-tropospheric wind anomalies, before and after linearly removing tropical Pacific climate variability, are non-significantly correlated at $p = 0.05$ (spatial correlation ≤ 0.37). Positive interdecadal anomalies impacting the WRI are quite different. Suppressed/enhanced deep-convections are regionally identified north/south of the Equator (~20°N-20°S), and of the subtropics (~20°-40°S; Figure 3.9b). This suggests regional changes of the tropical and subtropical meridional circulations, which are consistent with interdecadal zonal geopotential anomalies (Figure 3.8b). The subtropical westerly jet is therefore located further North (Figure 3.10b). Interestingly, upper-wind circulation drastically changes after linearly removing ENSO and decadal ENSO-like effects, while deep-convection anomalies remain unmodified. This is also detected through the spatial correlations, which display an almost perfect match for the OLR (spatial correlation = 0.99, significant at $p = 0.05$) and zero match for the wind anomalies (spatial correlations $\leq$ -0.004). Upper-wind circulation thus responds to small changes in the zonal gradient of equatorial SSTs, while deep-convection anomalies are likely to follow the dominant SST patterns that are not significantly influenced by ENSO or decadal

ENSO-like variability in winter (*cf*. Figs. 4, 6b, d, f). Upper westerly flow is thus reduced and shifted southward without this forcing: this underscores the amplification effects of tropical Pacific climate variability on interdecadal WRI anomalies. At the quasi-decadal timescale (8-13 year; QDV), positive SRI fluctuations are associated with similar upper-tropospheric anomalies to those observed at the interdecadal timescale (Figure 3.10a, c). However, these anomalies are quite symmetric between the Northern and Southern Hemispheres (Figure 3.10c), which suggest an equatorial forcing such as ENSO-like anomalies (here La Niña-like anomalies). A westward shift in the Walker circulation is identified, and is associated, at the regional scale, with a south-westward shift of the SICZ (Figure 3.10c). These anomalies are almost entirely linearly influenced by ENSO, decadal ENSO-like variability such as the IPO. Importantly, they are thus likely to favour the development of synoptic-scale rain-bearing systems (e.g. TTTs), which promote wet conditions, over the southern African landmass. The upper-wind circulation is therefore strongly influenced by tropical Pacific climate variability (spatial correlations ≤ 0.13). However, a southward shift of the mid-latitude westerly jet is identified in Figure 3.10c. For the WRI, positive quasi-decadal anomalies are very similar to those identified at the interdecadal timescale. OLR anomalies, which seem independent of tropical pacific climate variability, display suppressed convection in the ITCZ (and the mid-latitudes too) and enhanced convection in the tropics (Figs. 10d), indicating regional weakening in the meridional circulation. An increase of upper-tropospheric westerlies is detected around 10-30°S between the Atlantic and Indian Oceans (Figure 3.10d). Upper-tropospheric wind anomalies are strongly modified after linearly subtracting the influence of tropical Pacific SSTs (spatial correlations ≤ 0.1). However, at the regional scale, only the intensity of the mid-latitude westerly jet is reduced (Figure 3.11d). The tropical Pacific climate variability influences are thus only related to the amplitude of the quasi-decadal WRI anomalies. Positive interannual SRI anomalies (2-8 year) are very similar to those noted at the quasi-decadal timescale, but are significantly less pronounced over the equatorial Pacific (Figure 3.10c, e). A westward shift in the Walker circulation, which in turn is related to a south-westward shift of the SICZ, is thus identified (Figure 3.10e). The south-westward shift of the SICZ is, however, much less pronounced at the interannual scale than at the quasi-decadal scale (Figure 3.10c, e). Significantly, as for the interdecadal and the quasi-decadal scales, these anomalies, which lead to enhanced deep-convection, favour wet conditions over southern Africa (with the exception of the Western Cape region), and are almost entirely linearly influenced by ENSO. Furthermore, the intensity of mid-latitude westerly jet decreases in response to the southward shift (Figs. 10e-11e). Positive interannual WRI anomalies are also associated with regional modifications in the meridional circulation. Suppressed/enhanced deep-convections are regionally distributed north/south of the Equator (~30°N-10°S), and of the subtropics (~10°-40°S; Figure 3.10f). A northward shift of the mid-latitude westerly jet is detected around 30°S and, with a large band of enhanced deep-convection, leads to an increase in the westerlies toward southern Africa (Figure 3.10f). Interannual deep-convection anomalies are not modified after linearly removing ENSO effects (spatial correlation = 0.99), while the upper tropical circulation changes dramatically (spatial correlations ≤ -0.01). Without the linear influence of ENSO, a northward shift of the westerly jet is still detected, but a weakening of its intensity emerges. At each timescale considered, tropical teleconnections are the main driver of SRI variability. Strong influences of ENSO (which can be part of the PDO and IPO variance; cf. Sect. 4.1) are identified whatever the timescales, and seem to be related to interactions across scales through cascading effects in the upper-tropospheric circulation. In summer, the tropical Pacific climate variability linked to ENSO or decadal ENSO-like variability is associated with shifts in the Walker circulation, which in turn is associated with displacements of the SICZ at the regional scale and, thus, modulating precipitation over southern African. The mechanisms are more complex in winter, when the influence of the SAM, here expressed as shifts and intensifications of the mid-latitude jet stream, becomes more important, and ENSO becomes less important. These new analyses show, therefore, that

winter teleconnections are associated with mid- and high-latitude dynamics, which can respond to, or be coupled with, regional changes in the meridional circulation. Similarities are however identified across timescales, which suggest interlocking mechanisms between them (e.g. interannual coupled dynamic anomalies which are likely to be interlinked with those of the quasi- to interdecadal scales).

3.6 Conclusions

This study analyses the changing characteristics of summer and winter southern African rainfall, and their teleconnections with large-scale climate through the dominant timescales of variability. Austral summer is the main rainy season over much of southern Africa, which occurs over the tropical and subtropical regions. However, in the south-western tip of Africa, the annual rainfall peak occurs in austral winter. Two spatially coherent rainfall indices referred to as SRI and WRI are calculated with respect to these seasonal patterns. As determined by wavelet analysis, both indices exhibit three significant timescales of variability: interdecadal (15-28 year), quasi-decadal (8-13 year) and interannual (2-8 years). Timing of periods of strong variance at the interdecadal and quasi-decadal timescales is nevertheless different for both rainfall indices. For instance, at the interdecadal and quasi-decadal timescales, the SRI displays significantly increasing variance since the 1930s and the late 1960s, while WRI shows decreasing variance. Teleconnections with worldwide SST and atmospheric circulation anomalies impacting SRI and WRI fluctuations are different on all three timescales considered here. Importantly, the tropical Pacific climate variability emerges here as the main driver of summer rainfall variability at every timescale. However, different timings between interdecadal, quasi-decadal and interannual anomalies could provide some insights understanding the non-linear relationship between ENSO and southern African rainfall (Fauchereau et al., 2009). At the interdecadal timescale, ENSO or decadal ENSO-like forcing of the PDO decadal variance leads to shifts in the Walker circulation and, at the regional scale, in the SICZ. ENSO forcing is thus needed to generate modulations in the relationship between PDO and southern African rainfall, which was proposed by Wang et al. (2014), and is supported by the new analyses presented here. The IPO and ENSO, whose physical independence remains controversial (e.g. Power al., 1999; Folland et al., 1999; Tourre et al., 2005; Power and Colman, 2006), also drive such anomalies at the quasi-decadal and interannual timescale. At each timescale, colder or warmer Pacific SSTs result in changes in the Walker circulation modifying the position of the SICZ, which in turn is likely to modulate the TTT developments and deep-convection over the north-eastern regions of southern Africa. Annular geopotential anomalies, which could be related to the canonical SAM pattern or ENSO-like anomalies in the southern Hemisphere (e.g. Seager et al., 2003; Fogt and Bromwich, 2006; L'heureux and Thompson, 2006; Pohl et al., 2010), influence interdecadal to interannual variability in summer rainfall through shifts in the westerlies, which is associated with an anomalous low-level easterly moisture flux from the Mascarene region. At the decadal timescales, the influence of decadal ENSO-like variability or the IPO could result from the generation of atmospheric Rossby waves. This is consistent with earlier studies (e.g. Tourre et al., 2001; White et al., 2003), which proposed that interannual to quasi-decadal fluctuations in the equatorial Pacific require coupled Rossby wave dynamics. Such regional changes in the atmospheric circulation are likely to drive dipolar SST anomalies in the adjacent oceans *via* changes in latent heat fluxes (e.g. Behera and Yamagata, 2001; Fauchereau et al., 2003; Suzuki et al., 2004. Our results show that tropical Pacific climate variability is not the main driver of winter southern African rainfall variability, but it can modulate it. Although very sparse significant signals have been detected at the interannual time-scale, the inter- and quasi-decadal variability of winter southern African rainfall can be associated with SST anomalies in the North Pacific and more particularly with contrasted SST anomalies between the Atlantic and Indian oceans, the sign of which depends on the timescale considered. These asymmetric dipole SST anomalies in the oceans adjacent to southern Africa are likely to be driven by changes in

surface winds which would alter the turbulent latent heat and sensible heat fluxes. Winter rainfall variability is strongly related to regional changes in the subtropical Highs and, thus, in the mid-latitude westerly frontal activity. According to OLR anomalies, this could be in response or coupled to regional modulations in the meridional circulations. Although the main forcing of this modulation in the meridional circulation is not identified here, we show that small changes in the zonal equatorial SST gradient can significantly modify associated atmospheric dynamics, even in the subtropics. This conclusion provides useful support for the findings of Phillippon et al. (2012), who show similar asymmetry in the location of winter subtropical high pressures and of westerly tracks during ENSO events. This study provides new insights on climate interactions across different timescales and at global and regional scales and advances our understanding of decadal scale climate variability and predictability. These results present, for the first time, analyses of atmospheric dynamics associated with global ocean-atmosphere modes of variability which influence, seasonally and regionally, vital southern African rainfall receipts at decadal timescales. Such analyses will help to understand recurrent space-time evolution of rainfall and drought patterns across this dry region. It is also important to consider that, at the regional scale, anthropogenic climate change signals will be strongly modulated by natural climate variations, which are likely to induce variations at the decadal timescales (e.g. Keenlyside et al. 2008; Deser et al. 2012; Wallace et al. 2014).

3.7 References

Behera, S.K. and Y. Yamagata (2001). Subtropical SST dipole events in the southern Indian *Ocean. Geophys. Res. Lett.,* **28,** 327-330.

Colberg, F. and C.J.C. Reason (2007). Ocean model diagnosis of low-frequency climate variability in the South Atlantic region. *J. Clim.,* **20,** 1016-1034.

Compo, G.P., J.S. Whitaker and P.D. Sardeshmukh (2006). Feasibility of a 100 year reanalysis using only surface pressure data. *Bull. Amer. Met. Soc.,* **87,** 175-190.

Compo, G.P., J.S. Whitaker, P.D. Sardeshmukh, N. Matsui, R.J. Allan, X. Yin, B.E. Gleason, R.S. Vose, G. Rutledge, P. Bessemoulin, S. Brönniman, M. Brunet, R.I. Crouthamel, A.N. Grant, P.Y. Groisman, J.D. Jones, M. Kruk, A.C. Kruger, G.J. Marshall, M. Maugeri, H. Y. Mok, Ø. Nordli, T.F. Ross, R.M. Trigo, X.L. Wang, S.D. Woodruff and S.J. Worley (2011). The twentieth century reanalysis project. *Quarterly J. Roy. Meteorol. Soc.*, **137,** 1-28.

Cook, K.H. (2001). A Southern Hemisphere wave response to ENSO with implications for southern Africa precipitation. *J. Atmos. Sci.,* **15,** 2146-2162.

Cook, K.H. (2004). Wet and dry spells within particularly wet and dry summers in the South African summer rainfall region. *Clim. Res.,* **26,** 17-31.

Crétat, J., Y. Richard, B. Pohl, M. Rouault, C.J C. Reason and N. Fauchereau (2010). Recurrent daily rainfall patterns over South Africa and associated dynamics during the core of the austral summer. *Int. J. Climatol.,* **32,** 261-273.

Czaja, A., P. van der Vaart and J. Marshall (2002). A diagnostic study of the role of remote forcing in tropical Atlantic variability. *J. Clim.,* **15,** 3280-3290.

Deser, C., M.A. Alexander, S-P. Xie and A.S. Philips (2010). Sea surface temperature variability: patterns and mechanisms. *Ann. Rev. Mar. Sci.,* **2,** 115-143.

Deser, C., A.S. Phillips, V. Bourdette and H. Teng (2012. Uncertainty in climate change projections: The role of internal variability. *Clim. Dyn.,* **38,** 527-546.

Dieppois, B., M. Rouault and M. New (2015). The impact of ENSO on Southern African rainfall in CMIP5 ocean atmosphere coupled climate models. *Clim. Dyn.,* doi:10.1007/s00382-015-2480.

Dyer, T.G.J. and P.D. Tyson (1977. Estimating above and below normal rainfall periods over South Africa, 1972-2000. *J. Appl. Meteor.*, **16,** 145-147.

Enfield, D.B. and D. Mayer (1997). Tropical Atlantic sea surface temperature variability and its relation to El Niño-Southern Oscillation. J. Geophys. Res-Oceans, 102, 929-945.

Farge, M. (1992). Wavelet transforms and their applications to turbulence. *Annu. Rev. Fluid. Mech.,* **24,** 395-457.

Fauchereau, N., B. Pohl, C.J.C. Reason, M. Rouault and Y. Richard (2009). Recurrent daily OLR patterns in the Southern Africa/Southwest Indian Ocean region, implications for South African rainfall and teleconnections. *Clim. Dyn.,* **32,** 575-591.

Fauchereau, N., S. Trzaska, Y. Richard, P. Roucou and P. Camberlin (2003). Sea-surface temperature co-variability in the southern Atlantic and Indian Oceans and its connections with the atmospheric circulation in the Southern Hemisphere. Int. J. Clim., **23,** 663-677.

Fogt, R.L. and D.H. Bromwich (2006). Decadal variability of the ENSO teleconnection to the high-latitude South Pacific governed by coupling with the Southern Annular Mode. *J. Clim.,* **19,** 979-997.

Frankignoul, C. and E. Kestenare (2002). The surface heat flux feedback. Part I: Estimates from observations in the Atlantic and the North Pacific. *Clim. Dyn.,* **19,** 633-647.

Grinsted, A., J.C. Moore and S. Jevrejva (2004). Application of the cross wavelet transform and wavelet coherence to geophysical time series. *Nonlinear Proc. Geoph.,* **11,** 561-566.

Hamed, K.H. and A.R. Rao (1998). A modified Mann-Kendall trend test for autocorrelated data. *J. Hydrol.,* **204,** 182-196.

Harris, I., P.D. Jones, T.J. Osborn and D.H. Lister (2014). Updated high-resolution grids of monthly climatic observations – the CRU TS3.10 Dataset. *Int. J. Clim.,* **34,** 623-642.

Hart, N.C.G., C.J.C. Reason and N. Fauchereau (2012a). Cloud bands over southern Africa: seasonality, contribution to rainfall variability and modulation by the MJO. *Clim. Dyn.*, **41,** 119-1212

Henley, B.J., J. Gergis, D.J. Karoly, S. Power, J. Kennedy and C.K. Folland (2015). A Tripole Index for the Interdecadal Pacific Oscillation. *Clim. Dyn.,* doi:10.1007/s00382-015-2525-1.

Hoerling, M., J. Eischeid and J. Perlwitz (2010). Regional precipitation trends: distinguishing natural variability from anthropogenic forcing. *J. Clim.,* **23,** 2131-2145.

Huang, B., V.F. Banzon, E. Freeman, J. Lawrimore, W. Liu, T.C. Peterson, T.M. Smith, P.W. Thorne, S.D. Woodruff and H.M. Zhang (2015). Extended Reconstructed Sea Surface Temperature Version 4 (ERSST.v4). Part I: Upgrades and Intercomparisons. *J. Clim.,* **28,** 911-930.

Jury, M.K. (2014). Factors contributing to a decadal oscillation in South African rainfall. *Theor. Appl. Climatol.,* doi:10.1007/s00704-014-1165-4.

Kane, R.P. (2009). Periodicities, ENSO effects and trends of some South African rainfall series: an update. *S. Afr. J. Sci*., **105,** 199-207.

Keenlyside, N.S., M. Latif, J. Jungclauss, L. Kornblueh, and E. Roeckner (2008). Advancing decadal-scale climate prediction in the North Atlantic sector. *Nature,* **453,** 84-88.

Klein, S.A., B.J. Soden and N.C. Lau (1999). Remote sea surface variations during ENSO: evidence for a tropical atmospheric bridge. *J. Clim.,* **12,** 917-932.

Kruger, A.C. (1999). The influence of the decadal-scale variability of summer rainfall on the impact of El-Niño and La Niña events in South Africa. *Int. J. Clim.,* **19,** 59-68.

Latif, M., and T. P. Barnett (1994), Causes of decadal climate variability over the North Pacific and North America. *Science,* **266,** 634-637.

L'heureux, M.L. and D.W.J. Thompson (2006). Observed relationships between the El Niño-Southern Oscillation and the extratropical zonal-mean circulation. *J. Clim.,* **19,** 276-287.

Lindesay, J.A. (1988). South African rainfall, the Southern Oscillation and a Southern Hemisphere semi-annual cycle. *J. Climatol.,* **8,** 17-30.

Lyon, B. and S.J. Mason (2007). The 1997-98 summer season in southern Africa. Part I: Observations. *J. Clim.,* **20,** 5134-5148.

Macron, C., B. Pohl, Y. Richard and M. Bessafi (2014). How do tropical-temperate troughs form and develop over southern Africa? *J. Clim.*, **27,** 1633-1647.

Malherbe, J., F.A. Engelbrecht, W.A. Landman and C.J. Engelbrecht (2012). Tropical systems from the southwest Indian Ocean making landfall over the Limpopo River Basin, southern Africa: a historical perspective. *Int. J. Climatol.,* **32,** 1018-1032.

Malherbe, J., W.A. Landman, F.A. Engelbrecht (2014). The bi-decadal rainfall cycle, Southern Annular Mode and tropical cyclones over the Limpopo River Basin, southern Africa. *Clim. Dyn*., **42,** 3121-3138.

Mantua, N.J. and S.R. Hare (2002). The Pacific Decadal Oscillation. *J. Oceanogr*., **58,** 35-44.

Mason, S.J. and M. Jury (1997). Climatic variability and change over the Southern Africa: a reflection on underlying processes. *Prog. Phys. Geo.,* **21,** 23-50.

Mills, C.M. and J.E. Walsh (2013). Seasonal variation and spatial patterns of the atmospheric component of the pacific decadal oscillation. *J. Clim.,* **26,** 1575-1594.

Morioka, Y., T. Tozuka and T. Yamagata (2012). Subtropical dipole modes simulated in a coupled general circulation model. *J. Clim.,* **25,** 4029-4047.

Mulenga, H M., M. Rouault and C.J.C. Reason (2003). Dry summers over north-eastern South Africa and associated circulation anomalies. *Clim. Res*., **25,** 29-41.

Nicholson, S.E. and J. Kim (1997). The relationship of the El Niño-Southern Oscillation to African rainfall. *Int. J. Clim.,* **17,** 117-135.

Phillipon, N., M. Rouault, Y. Richard and A. Favre (2012). The influence of ENSO on winter rainfall in South Africa. *Int. J. Clim.,* **32,** 2333-2347.

Pierce, D.W. (2002). The role of sea surface temperature in interactions between ENSO and the North Pacific Oscillation. *J. Clim.,* **15,** 1295-1308.

Pohl, B., and N. Fauchereau (2012), The Southern Annular Mode seen through weather regimes. *J. Clim.,* **25,** 3336-3354.

Pohl, B., N. Fauchereau, C.J.C. Reason and M. Rouault (2010). Relationships between the Antarctic Oscillation, the Madden-Julian Oscillation, and ENSO, and consequences for rainfall analyses. *J. Clim.,*

Power, S., T. Casey, C.K. Folland, A. Colman and V. Mehta (1999). Inter-decadal modulation of the impact of ENSO on Australia. *Clim. Dyn.*, **15,** 319-323.

Ratnam, J.V., S.K. Behera, Y. Masumoto and T. Yamagata (2014). Remote effects of El Niño and Modoki events on the Austral Summer Precipitation of Southern Africa. *J. Clim.*, **27,** 3802-3815.

Reason, C.J.C. and M. Rouault (2002). ENSO-like decadal patterns and South Africa rainfall. *Geophys. Res. Lett.*, **29,** 161-164.

Reason, C.J.C. and M. Rouault (2005). Links between the Antarctic Oscillation and winter rainfall over western South Africa. *Geophys. Res. Lett.*, **32,** L07705, doi:10.1029/2005GL022419.

Reynolds, R.W., N.A. Rayner, T.M. Smith, D.C. Stokes and W. Wang (2002). An improved in situ and satellite SST analysis for climate. *J. Clim.*, **15,** 1609-1625.

Richard, Y., N. Fauchereau, I. Poccard, M. Rouault and S. Trzaska (2001).XXth century droughts in Southern Africa: spatial and temporal variability, teleconnections with oceanic and atmospheric conditions. *Int. J. Clim.*, **21,** 873-885.

Richard, Y., S. Trzaska, P. Roucou and M. Rouault (2000). Modification of the Southern African rainfall variability/El Niño southern oscillation relationship. *Clim. Dyn.*, **16,** 883-895.

Ropelewski, C.F. and M.S. Halpert (1989). Precipitation patterns associated with the high indices phase of the southern oscillation. *J. Clim.*, **2,** 268-284.

Rouault, M. and Y. Richard (2005). Intensity and spatial extent of droughts in Southern Africa. *Geophys. Res. Lett*., **32,** L15702, doi:10.1029/2005GL022436.

Schneider, N. and B.D. Cornuelle (2005). The forcing of the Pacific Decadal Oscillation. *J. Clim.*, **18,** 4355-4373.

Seager, R., N. Harnik, Y. Kushnir, W. Robinson and J. Miller (2003). Mechanisms of hemispherically summetric variability. *J. Clim.*, **16,** 2960-2978.

Tanimoto, Y., H. Nakamura, T. Kagimoto and S. Yamane (2003). An active role of extratropical sea surface temperature anomalies in determining anomalous turbulent heat flux. *J. Geophys. Res-Oceans*, **108,** 3304, doi:10.1029/2002JC001750.

Thompson, D.W.J. and J.M. Wallace (2000). Annular modes in the extratropical circulation. Part I: Month-to-Month Variability. *J. Clim.*, **13,** 1000-1016.

Todd, M.C. and R. Washington (1999). Circulation anomalies associated with tropical-temperate troughs in southern Africa and the southwest Indian Ocean. *Clim. Dyn.*, **15,** 937-951.

Toniazzo, T. (2009). Climate variability in the south-eastern Pacific and its relation with ENSO: a GCM study. *Clim. Dyn.*, **34,** 1093-1114.

Torrence, C. and G.P. Compo (1998). A practical guide to wavelet analysis. *Bull. Am. Meteorol. Soc.*, **79,** 61-78.

Tourre, Y.M. and W.B. White (1995). ENSO signals in global upper-ocean temperature. *J. Phys. Oceanogr.*, **25,** 1317-1332.

Tyson, P.D. (1981). Atmospheric circulation variations and the occurrence of extended wet and dry spells over southern Africa. **J. Climatol., 1,** 115-130.

Tyson, P.D. (1986). *Climatic Change and variability over southern Africa*. Oxford University Press, Cape Town.

Venegas, S., L.A. Mysak and D.N. Straub (1997). Atmosphere-ocean coupled variability in the South Atlantic. *J. Clim*., **10,** 2904-2920.

Vigaud, N., Y. Richard, M. Rouault and N. Fauchereau (2009). Moisture transport between the South Atlantic Ocean and southern Africa: relationships with summer rainfall and associated dynamics. *Clim. Dyn*., **32,** 113-123.

Wallace, J.M., C. Deser, B.V. Smoliak and A.S. Phillips (2014). *Attribution of climate chance in the presence of internal variability*. In: Chang CP, Ghil M, Latif M and Wallace JM (ed) Climate Change: Multidecadal and Beyond. World Scientific Series on Asia-Pacific Weather and Climate, 6, in press.

Wang, S., J. Huang, Y. He and Y. Guan (2014). Combined effects of the Pacific Decadal Oscillation and El Niño-Southern Oscillation on Global Land Dry-Wet Changes. *Scientific Reports*, **4,** 6651, doi:10.1038/srep06651.

Washington, R. and A. Preston (2006). Extreme wet years over southern Africa: Role of Indian Ocean sea surface temperatures. J. Geophys. Res-Atmos., 111, D15104, doi:10.1029/2005JD006724.

Zhang, Q., H. Körnich and K. Holmgren (2013). How well do reanalyses represent the southern African precipitation? *Clim Dyn*, **40,** 951-962.

Zhang, Y., J.M. Wallace and D.S. Battisti (1997). ENSO-like interdecadal variability: 1900-93. *J Clim*, **10,** 1004-1020.

4 The annual cycle of sea to air moisture flux in the Agulhas current system

4.1 Introduction

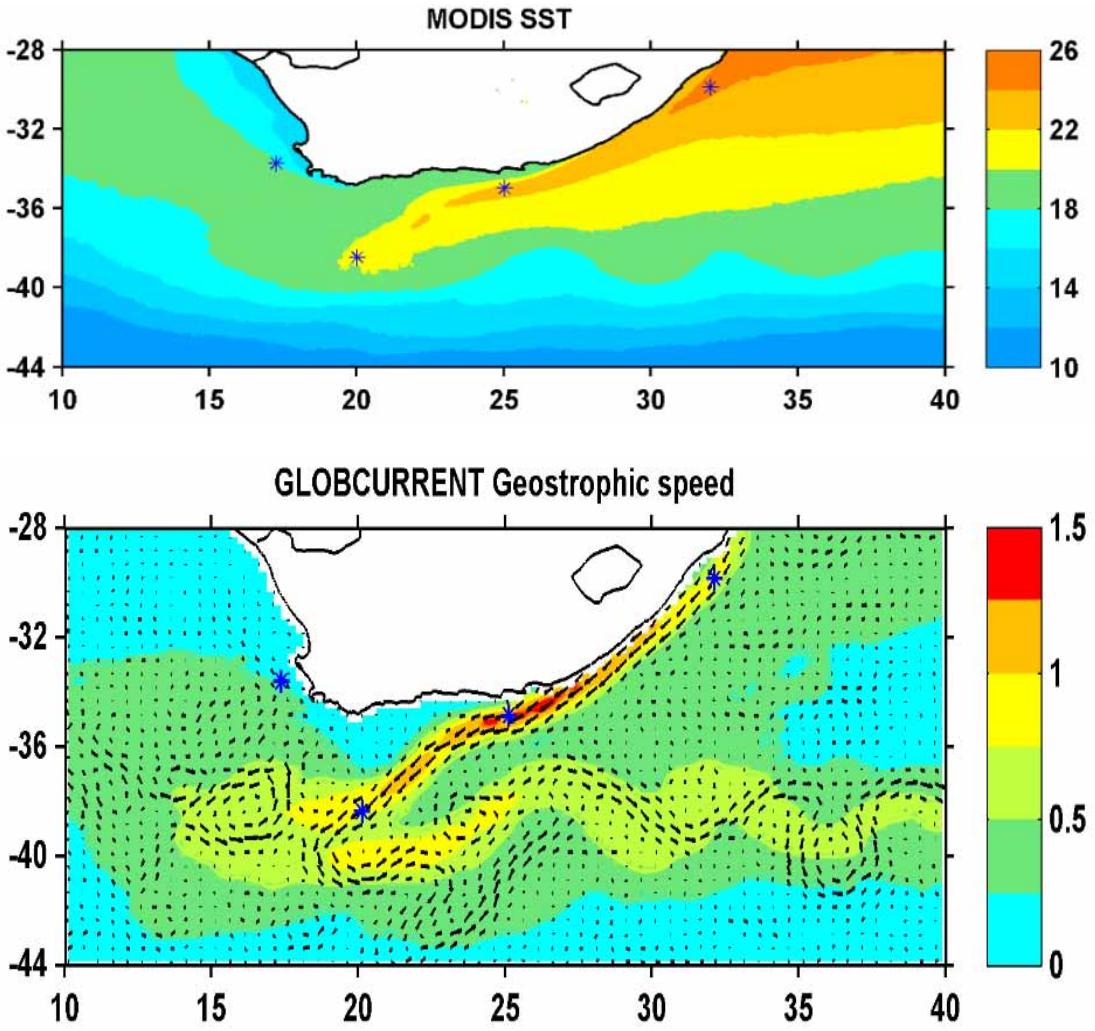

Figure 4.1: top) 2002-2014 annual average of MODIS SST (°C) and bottom) GlobCurrent geostrophic current speed (colour) and direction (arrows) at 0 m depth. Blue stars represent the fourth locations of time series used in the study: three points in the Agulhas system: Off Durban (32°E, 30°S), Off Port Elizabeth (25°E, 35°S) and in the Agulhas Retroflection (20°E, 38.5°S) and one point is Off Cape Town (17°E, 33.7°S).

The Agulhas current is the strongest western boundary current in the Southern Hemisphere. It flows along the east coast of South Africa. On average, the Agulhas retroflection lies between 16° and 20°E longitude and between 38° and 41°S latitude (Lutjeharms and Van Ballegooyen, 1988). The Agulhas current system is composed of the core of the Agulhas Current, about 100 km wide; the retroflection region with a loop diameter of 350 km (Lutjeharms and Van Ballegooyen, 1988); and the Agulhas Return current that flows and meanders in an eastward direction to the South of the Agulhas Current (Figure 4.1). Substantial turbulent latent heat flux as well as marine boundary layer modification was measured above the core of the Agulhas Current, the retroflection region and the Agulhas Return Current (Mey et al., 1990; Lee-Thorp et al., 1999; Rouault et al., 1996, 1997, 2000, 2003; Rouault and Lutjeharms, 2000). Those measurement shows that the turbulent latent heat flux which is akin to the turbulent flux of moisture at the air-sea interface increases by a factor of five across the core of the Agulhas Current. Cloud lines above the Agulhas Current witness the high exchange of moisture and

mixing that occur above the core of the Agulhas Current (Lutjeharms et al., 1986; Rouault et al., 1996; Lutjeharms and Rouault, 2000). Little is known on the influence of the Agulhas Current system on weather and climate of South Africa. Rouault et al. (2002) provided evidence of the influence of the Agulhas current on the evolution of a severe convective storm and associated tornado over southern South Africa and proposed that that low-level moisture from the Agulhas Current played a significant role in the storm evolution. There is also some evidence that the diurnal cycle of rainfall along the coast is influenced by the proximity of the Agulhas Current (Rouault et al., 2012). The Agulhas Current is also a preferred region for the development of thunderstorm (de Boer et al., 2013) which was attributed to strong convective activity warm and humid air originating over the Agulhas Current. In addition, this strong western boundary current has considerably warmed up since the 1980s (Rouault et al., 2009), which has increased the transfer of moisture from ocean to atmosphere but nothing is known on the impact of that increases in moisture on extreme weather and climate of the region. Gimeno et al. (2010) showed that the Agulhas Current system is a source of moisture for Southern Africa rainfall but the low resolution of data they used could have underestimated the intensity of ocean atmosphere exchanges in the core of the Agulhas Current. Likewise the turbulent latent heat flux is underestimated in reanalysis climate dataset because of the low resolution of the SST used (Rouault et al., 2003). This rendered difficult the study of the impact of the Agulhas current on weather and climate of South Africa using reanalysed climate dataset. As previously mentioned the latent heat fluxes measured above the Agulhas Current were not well reproduced in climate reanalysis (NCEP, ERA40). The data used by Gimeno et al. (2010) could have underestimated the ocean-atmosphere exchanges in the Agulhas Current as they also use ERA40. This underestimation is due to a low spatial resolution, 2.5° x 2.5° in model and reanalysis that were not able to represent the core of the Agulhas current. Now, new reanalysis for example ERA-Interim (0.125° x 0.125°), CFSR (0.31° x 0.31°) with a very high-resolution are available. At the same time numerous new air sea interaction datasets derived from satellite remote sensing such as SEAFLUX (1/4°) have been produced at a resolution that should represent the core of the Agulhas Current and its intense air sea exchange (Curry et al., 2004). The first aim of the present study is to find out if those new climate reanalysis dataset (MERRA2, ERA-Interim and CFSR) have a better representation of the Agulhas Current air sea exchange, particularly, the core of the current which is about 100 km wide and flows along the coast. The core of the Agulhas current is important because of its thermal contrast with the surrounding water leading to a fivefold increase in the turbulent fluxes of sensible and latent heat. Radiosondes launched during the ACASEX cruise show that the core of the current literally produces a wall of moisture (Rouault et al., 1996, 2000; Lee-Thorp et al., 1999) that can reach up to 2000 m above the Agulhas Current. When the wind is offshore, this moisture converges towards the coast (Jury et al., 1997; Lee-thorp et al., 1999; Rouault et al., 2000). The second aim is to understand which basic parameter (wind, SST, surface specific humidity) among various products is at the source of uncertainty in latent heat fluxes. The third aim is to quantify the annual cycle of the latent heat flux and its drivers in the Agulhas Current system. To that effect we are using various parameters obtained from observation, climate reanalysis and satellites remote sensing. In this study, the data and methodology used are presented in section 2. In section 3, we are presenting the comparison of different products and parameters related to the turbulent flux of latent heat and investigate the reason for their discrepancy. In section 4 we study the annual cycle of turbulent latent heat flux and its drivers.

4.2 Data and method

We are using monthly fields of latent heat flux, sea surface temperature, specific humidity and surface wind speed inferred from observation obtained from Voluntary Observation Vessel from the National Oceanography Center Southampton (NOCS) dataset (Berry and Kent 2009, 2011). The reanalysis

ERA-Interim (Dee et al., 2011), Modern era-retrospective analysis (MERRA-2; Molod et al., 2012; 2014) and the Climate Forecast System Reanalysis (CFSR) dataset (Saha et al., 2010) also provide sea surface temperature (SST), latent heat flux, surface wind speed at a reference of 10 m, temperature of air and specific humidity at a reference of 10 m, from the period 1998 to 2005. Corresponding monthly satellite remote sensing estimates data analysed are derived from the Air-sea turbulent fluxes dataset (SEAFLUX; Cury et al., 2004) and Hamburg Ocean Atmosphere Parameters and Fluxes dataset (HOAPS3; Andersson et al., 2010; 2011). SEAFLUX is a high-resolution satellite-based data set of surface turbulent fluxes over the global ocean. It also provides necessary parameters used to calculate the latent and sensible heat fluxes. We are using 0.25°x0.25° GlobCurrent geostrophic current at the surface (0 m) to show the structure of the Agulhas current (Figure 4.1). The 4 x 4 km degree resolution sea surface temperature is derived from Moderate Resolution Imaging Spectroradiometer (MODIS) aboard Terra and Aqua satellites. We are using the Scatterometer Climatology of Ocean Winds (SCOW, (Risien and Chelton, 2008)) as reference for surface wind speed. Low resolution reanalysis, ERA-40 (Uppala et al., 2005) and NCEP-R2 (National Centers for Environmental Prediction NCEP-DOE reanalysis version 2 (Kanamitsu et al., 2002) are also used to highlight the difference with new generation higher resolution climate reanalysis. The aim of the study is to find out if the new reanalysis dataset have a better representation of the Agulhas Current than the first generation product that had a 2.5 x 2.5 degree resolution and could not represent the core of the current that is about 100 km (Rouault et al., 2003). The period used to average the data is seasonal and monthly mean constrained by the availability of the satellite dataset. When dataset were not available at the same time, we used the same amount of time for the averaging to have a consistent result. Various products and parameters were used and the time span was used to average. Monthly data were used here. Eleven monthly or climatological products shown in Table 1 are used. These products are classified depending on their input data source or analysis method: in situ, satellite datasets and reanalysis. Various parameters are analysed: geostrophic current, latent heat flux, sea surface temperature (SST), surface wind speed at 10 m, specific humidity of air at 10 m (Qa) and saturated specific humidity (Qsst). Saturated specific humidity is not available for all products and is calculated using the Clausius-Clapeyron relation and the SST. Eleven products were used for this study, including the products type, the period considered the spatial grid and the parameters available for each product. The geostrophic current is given by GlobCurrent. MODIS and SCOW are used as reference product for SST and surface wind respectively.

4.2.1 In situ

We analysed gridded data of monthly field derived from observation data from National Oceanography Center Southampton, NOCS dataset version 2.0 based on Voluntary Observing Ship (VOS) obtained from the International Comprehensive Ocean-Atmosphere Data Set (ICOADS, Woodruff et al., 1987; Berry and Kent 2009, 2011). These observations are presented on a 1° x 1° spatial grid and use optimal interpolation of daily estimates of ship data, which cover the period 1973-2006. The optimal interpolation scheme used is based on the scheme developed by Reynolds and Smith (1994) and by Lornec (1981). The meteorological variables and fluxes, and their associated uncertainty estimates, are available for download at www.noc.soton.ac.uk/noc_flux/. The developers of NOCS data took the same approach as Josey et al. (1999). They used the bulk formulas of Smith (1980, 1988) to compute the final values of turbulent fluxes. A successive correction method is used to develop the monthly NOCS flux fields (Josey et al., 1999). We are using here the corrected version NOCS v2.

4.2.2 Satellite remote sensing

Two satellite estimated data are used: the third version of the Hamburg Ocean Atmosphere Parameters and Fluxes (HOAPS3) with a spatial resolution of 0.5° x 0.5°, and the high-resolution satellite-based data air-sea turbulent fluxes (SEAFLUX) available on a grid of 0.25° x 0.25° (Cury et al., 2004). HOAPS3 provides fields of turbulent heat fluxes over the global ice-free ocean. It is a completely reprocessed data set (Andersson et al., 2010; 2011) with a continuous time series from 1987 to 2005. HOAPS3 uses neural network based algorithms to calculate wind speed and SST is based on Advanced Very High Resolution Radiometer (AVHRR) (Andersson et al., 2010; 2011). A monthly HOAPS3 data product is available via http://www.hoaps.org/. For SEAFLUX, a general discussion of flux measurement issues is given in Cury et al. (2004), and Clayson et al. (2013). SEAFLUX benefits from an international effort under the GEWEX and CLIVAR umbrella (Curry et al., 2004). The SEAFLUX product is three-hourly (averaged from 0000-0300Z, 0300-0600Z, 0600-0900Z, etc.) or monthly. For this study, monthly field are used. All variables are available from 1998 to 2007. To validate SEAFLUX data, Cury et al. (2004) used measurements obtained from research ships and buoys (e.g. meteorological and flux data from World Ocean Circulation Experiment (WOCE) cruises). The bulk method algorithm developed by Fairall et al. (2003) for TOGA COARE3.0 is used to compute the final value of latent heat flux. The geostrophic current data is one of the data issue by the ESA Data User Element (DUE), funded by GlobCurrent project. The aims of this project can be found on http://www.globcurrent.org. GlobCurrent data are combination of Sentinel-3 and Sentinel-1 SAR data (Johannessen et al., 2015). For this study, the geostrophic current of GlobCurrent version 2 is used. The available period is from 2002 to 2014 with a 0.25° x 0.25° resolution at 0 m depth. The calculation of the geostrophic current components is fully described in Rio et al. (2014).The SST of MODIS is used as reference for sea surface temperature because of its very high resolution (4 x 4 km), also because this product represents well the shape of the Agulhas current especially near the coast. MODIS has a viewing swath width of 2.3 km and views the entire surface of the Earth every one to two days. Its detectors measure 36 spectral bands between 0.4 and 14.4 µm. The Level 2 product is produced daily and consists of global day and night coverage every 24 hours. Monthly field of SST of MODIS is used, from the period 2002 to 2014. MODIS data can be retrieved on ftp://podaac.jpl.nasa.gov/OceanTemperature. Chan et Gao (2005) compares MODIS, NCEP and TMI SST for the global ocean but only from March 2000 to June 2003.The Scatterometer Climatology of Ocean Winds (SCOW) is used as reference of wind speed and direction in this study. Because of its high resolution (0.25° x 0.25°) and also because SCOW is able to capture small-scale features that are dynamically important to both the ocean and the atmosphere but are not resolved in other observationally based wind (Risien and Chelton, 2008). They show that the ECMWF (Gibson et al., 1997) and NCEP-NCAR (Kalnay et al., 1996; Kistler et al., 2001) reanalysis winds that are often used to force ocean models have even coarser grid spacing of 2.5° and about 1.875°, respectively, resulting in a feature resolution of about 1500 km (Milliff et al., 2004). Then, the operational and reanalysis models are therefore not able to resolve small-scale wind features that are dynamically important to both the ocean and the atmosphere. SCOW wind fields product is based on 122 months (September 1999-October 2009) including QuikSCAT scatterometer data. SCOW is a climatology dataset with a regular grid of 0.25° x 0.25° longitude-latitude. SCOW wind is calculated using the methods detailed in Risien and Chelton (2008). The wind from SCOW is available on http://cioss.coas.oregonstate.edu/scow/.

4.2.3 Reanalysis

Monthly data from three reanalysis products is used. The first one is the Climate Forecast System Reanalysis (CFSR), operated by NCEP (National Centers for Environmental Prediction). CFSR has an irregular grid of 0.3125° x 0.3122° spatial resolution. We are also using the 0.50° x 0.66° resolution Modern era-retrospective analysis (MERRA-2) which is the NASA reanalysis for the satellite era. The third reanalysis used is produced by the European Centre for Medium-Range Weather Forecast (ECMWF, ERA-Interim), with a 0.125° x 0.125° spatial resolution. CFSR is from 1979 to 2010. MERRA-2 is from 1980 to present, and ERA-Interim is from 1979 to present. The idea behind using these reanalysis is to know if those products do represent the intense exchange of moisture from sea to air that occurs above the core of the Agulhas Current and the retroflection region. CFSR is a global coupled atmosphere-ocean-land surface-sea ice system designed to provide the best estimate of the state of these domains (Saha et al., 2010). Two low resolution reanalysis are used: the National Centers for Environmental Prediction NCEP-DOE reanalysis version 2 (NCEP-R2, Kanamitsu et al., 2002) and the ECMWF second generation reanalysis (ERA-40; Uppala et al., 2005). NCEP-R2 is provided by the NOAA-CIRES Climate Diagnostics Center. NCEP-R2 has an irregular grid of 1.87°x1.90°. ERA-40 is a reanalysis of meteorological observations from September 1957 to August 2002 produced by ECMWF in collaboration with many institutions. ERA-Interim represents an undertaking by the ECMWF to produce a reanalysis with an improved atmospheric model and assimilation system that replaces those used in ERA-40 (Dee et al., 2011). ERA-40 uses 3D-Var rather than 4D-Var used in Era-Interim. ERA-40 is available on a 2.5° x 2.5°grid via http://apps.ecmwf.int. A comparison of nine products including NCEP-R2 and ERA-40 was made by Smith et al. (2011). They showed that global comparisons of monthly means tend to reveal similar spatial patterns in latent heat flux (latent heat flux) for the nine products; however, the magnitudes and patterns of variability (expressed as maps of standard deviations) are widely different. In this study, the methodology is based on the calculation and comparison of seasonal mean and mean annual cycle of latent heat flux, SST, wind speed and specific humidity. The equation used to calculate the turbulent latent heat flux is given by

$$E = \rho_a C_E (U - U_S)(q_{sst} - q_a). \quad (1)$$

Where E is the turbulent flux of moisture aka turbulent latent heat flux; ρ_a is air density; C_E is transfer coefficient for water vapor; U is the surface wind speed; U_S is the surface current; q_{sst} is surface specific humidity and q_a is the specific humidity of air. Understand the variation of each parameter will help to a better understanding of the feature of latent heat flux. Reanalysis do not integrate the surface current which could lead to strong mistake in the estimation of latent heat fluxes in Agulhas current which has speed of up to 2 m/s (Rouault et al., 2000). Satellite product do however integrate the relative effect of the currents because they derive the wind speed from sea roughness which allows to estimate the relative wind speed to the surface, the correct parameter to infer latent heat flux above the oceans.

4.3 Results

Figure 4.1a (top) shows the annual mean of MODIS SST available at 4 km by 4 km resolution, averaged from 2002 to 2014. The area of warm water (> 22°C) follows the shape of the Agulhas current but the Agulhas Return current is not clearly identified in SST although the 18 °C meander to the South indicate its location. The Agulhas Current is an intense and narrow flow characterized by strong velocity gradients and a central warm core, with isopycnal lines sloping steeply toward the coast (Bryden et al., 2005; Casal et al., 2009). It follows the 200 m isobaths. Figure 4.1 (bottom) shows that the core of the Agulhas current has a mean velocity of up to 1.5 m/s. Cold water of the Benguela Current are visible to

the West of the South Africa while the warm water region further west is the eddy corridor where leakage of Agulhas Current to the South Atlantic occur. Figure 4.1b the annual mean of the Globcurrent geostrophic current at 0 m depth, in the 0.25° x 0.25° resolution. Figure 4.1 also represents the four locations of time series used in the study: off Durban (32°E, 30°S) and off Port Elizabeth (25°E, 35°S) in the Agulhas Current, in the Agulhas Retroflection (20°E, 38.5°S) and Off Cape Town (17°E, 33.7°S). The last location is used to compare the three Agulhas Current locations with a neutral location.

4.3.1 Seasonal mean and annual cycle of latent heat flux

Figure 4.2 and 4.3 present seasonal means of the latent heat flux for SEAFLUX, HOAPS3, CFSR, MERRA-2, ERA-Interim, NCEP-R2, ERA-40 and NOCS. Four seasons are represented in Figure 4.2: austral summer, from December to February (DJF); fall, from Mars to May (MAM); winter, from June to August (JJA) and spring, from September to November (SON). SEAFLUX (0.25° x 0.25°) is taken as reference of latent heat flux. Latent heat flux ranges between 50 and 250 W/m² in the domain of the study. The maximum of latent heat flux is located in the Agulhas system, during austral winter (Figure 4.2). This maximum is between 175 and 250 W/m² depending on the product. The minimum latent heat flux is around 50 W/m², in the Benguela upwelling system, and in the southern ocean where the water is cold. In The Agulhas Current system latent heat flux ranges from 100 to 250 W/m². In the Agulhas Current system the minimum is around 100 W/m² in summer. For HOAPS3 and SEAFLUX both satellites estimate, and high resolution CFSR and MERRA-2 reanalysis products, the large-scale patterns seasonal cycle of latent heat flux are similar; minimum in summer and maximum in winter. ERA-interim and ERA-40 have the same seasonality but it is lower than the four precedent products. NOCS is quite different of all products with maximum of ± 200 W/m² in austral summer above the Agulhas Retroflection region and a minimum in winter (between 125 and 175 W/m²). HOAPS3 has missing data along the coast and is quite similar to SEAFLUX. ERA-40 and NCEP-R2 do not have enough resolution to represent the core of the Agulhas Current along the coast all the way to the Retroflection region which could explain their low values off Port Elizabeth and Durban. ERA-40 and NCEP-R2 do not follow the meandering shape of the Agulhas Return Current. However, NCEP-R2 has some high latent heat flux in the retroflection region. The magnitude of ERA-40 latent heat flux is similar to that of ERA-Interim which is surprising, given the high resolution of ERA-Interim (0.125 by 0.125) compared with ERA-40 (2.5 by 2.5) especially in winter.

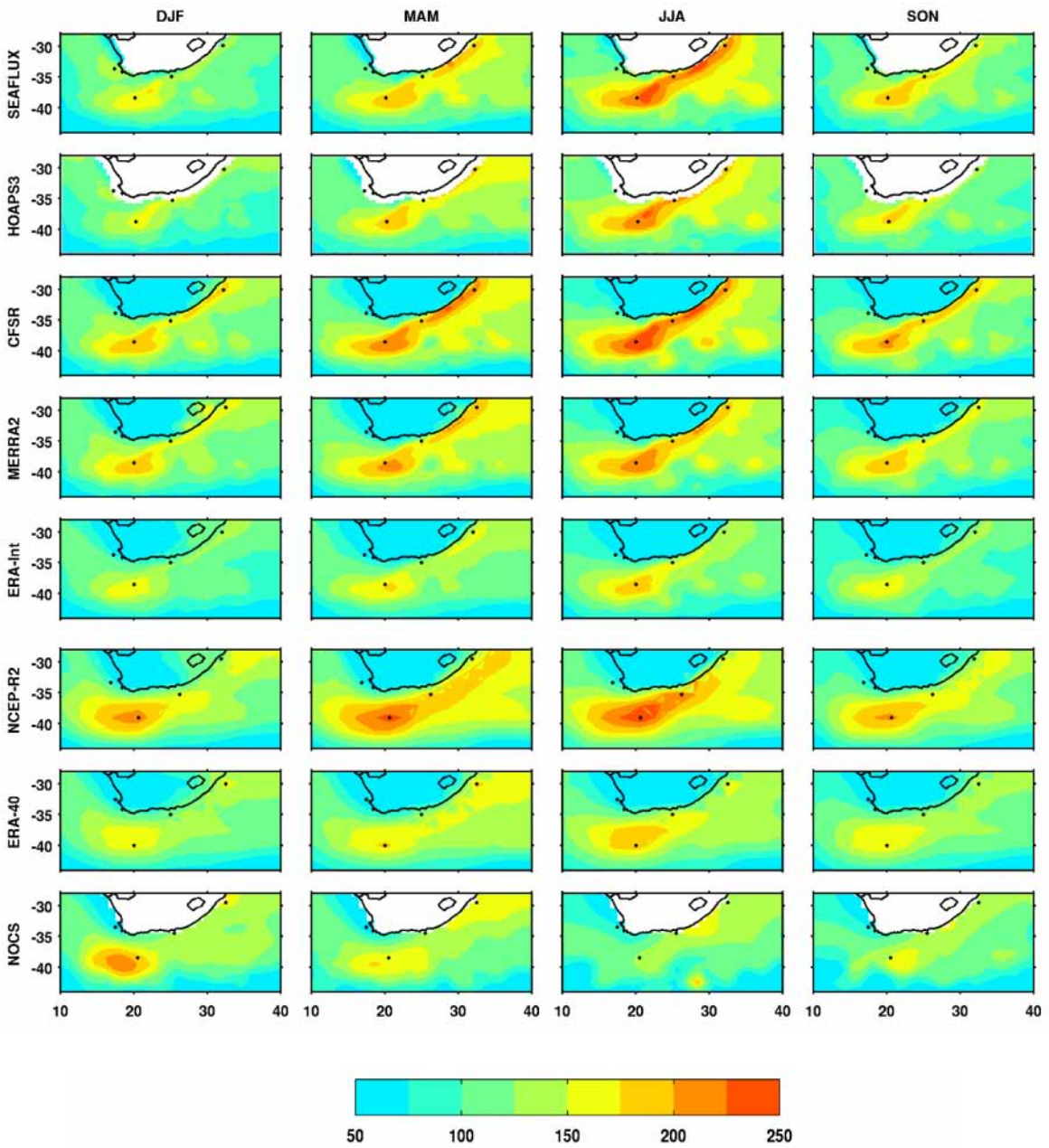

Figure 4.2: From top to bottom: seasonal average of latent heat flux (W/m²) of SEAFLUX, HOAPS3, CFSR, MERRA-2, ERA-Interim, NCEP-R2, ERA-40 and NOCS. From left to right Austral summer (DJF), austral fall (MAM), austral winter (JJA) and austral autumn (SON). Black stars represent the fourth locations taken for the study. Agulhas Current off Durban (32°E, 30°S), Agulhas Current off Port Elizabeth (25°E, 35°S), in the Agulhas Retroflection (20°E, 38.5°S) and Off Cape Town (17°E, 33.7°S).

Their annual variations are quite different. The latent heat flux from ERA-40 is up to 200 W/m² during austral winter in the Agulhas Retroflection while it is up to 180 W/m² for ERA-Interim. Along the coast ERA-40 latent heat flux is underestimated when compared with ERA-interim. Compared to others products, NCEP-R2 has the highest flux in and around the Retroflection region at all seasons (between 200 and 250 W/m²), especially in winter but NCEP-R2 underestimates the flux along the coast, maybe most probably of low resolution of its SST (and associated Qsst) as will be shown later

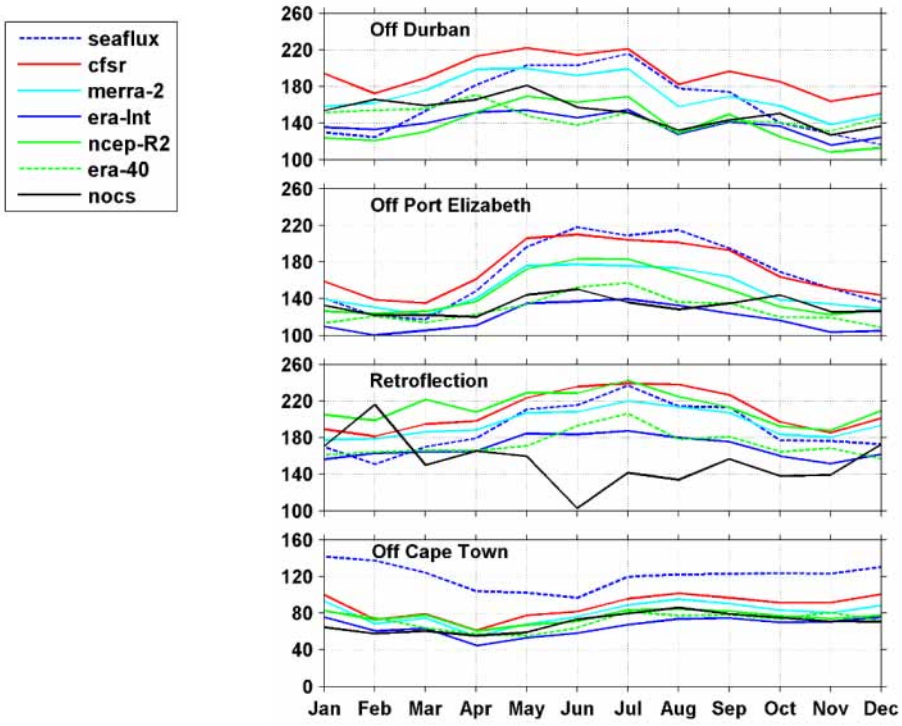

Figure 4.3: annual cycle of latent heat flux (W/m²). In Agulhas Current off Durban (32°E,30°S), Agulhas Current off Port Elizabeth (25°E, 35°S), Agulhas Retroflection (20.5°E, 38.5°S) and off Cape Town (17°E, 33.7°S) for SEAFLUX (blue dash), CFSR (red), MERRA-2 (cyan), ERA-Interim (blue), NCEP-R2 (green), ERA-40 (dash green) and NOCS (black). All products are averaged from 1998 to 2005, except ERA-40 averaged from 1995 to 2002.

Figure 4.3 represents the annual cycle of latent heat flux at four different locations: Agulhas Current off Durban (32°E, 30°S); Agulhas Current off Port Elizabeth (25°E, 35°S); Agulhas Retroflection (20°5E, 38.5°S) and off Cape Town (17°E, 33.7°S) for all products except HOAPS3. HOAPS3 is omitted because of its missing data along the coast which prevent the calculation off Durban. There are considerable differences between all products. Differences are also dependent on location and seasons. Latent heat flux varies between 100 and 250 W/m² in the Agulhas system, and between 42 and 150 W/m² off Cape Town. Off Durban, taking SEAFLUX as reference, maxima are observed in May and July and minima are observed in February and October. Off Port Elizabeth, SEAFLUX has two maximum in June and August, and minimum values in summer. The highest value is found in the Retroflection area in July (SEAFLUX, CFSR, NCEP-R2), and the lowest off Cape Town (ERA-Interim in April). Off Cape Town, all products are lower than SEAFLUX. Lowest values in the Agulhas Current system are found off Port Elizabeth in late summer. The annual cycle is most pronounced off Port Elizabeth. Without considering NOCS difference between products range roughly from 80 W/m² in winter to 60 W/m² in summer. Figure 4.3 also shows that the highest values of latent heat flux occur between April and July off Durban; between May and August off Port Elizabeth; and between May and September in the Retroflection region except for NOCS which has the lowest values (100 W/m²) during winter but the highest (219 W/m²) in February. The annual cycle of latent heat flux (Figure 4.3) shows that CFSR is higher than SEAFLUX, in summer and fall, and is lower than SEAFLUX in winter and spring. The time series of MERRA-2 behaves like the one of SEAFLUX off Durban and in the Retroflection region but is higher than SEAFLUX (Table 4.1). ERA-Interim has the same annual variations as SEAFLUX, but its values range from 42 (off Cape Town) and 140 W/m² (Retroflection).

NCEP-R2 has the same annual variations as SEAFLUX, CFSR and MERRA-2 in the fourth locations in spite of low resolution of NCEP-R2 SST. NCEP-R2 values are less than those of SEAFLUX values for all locations, except in the Agulhas Retroflection where NCEP-R2 is higher than SEAFLUX from November to mid-May. ERA-40 latent heat flux is similar to that of ERA-Interim. ERA-40 has higher fluxes compared to ERA-Interim (Figure 4.3, Table 4.1). The annual variation of NOCS is opposite off all products in the Retroflection area with one maximum in February and one minimum in June. However NOCS has similar annual variations than others products off Durban, off Port Elizabeth and off Cape Town. Table 4.1 shows the mean of latent heat flux (W/m²) at our four locations, for the average of the three Agulhas Current system points, and Off Cape town for seven considered datasets. Table 4.1 shows that CFSR has the highest latent heat flux in the Agulhas Current system. ERA-interim, ERA-40 and NOCS have the lowest latent heat flux. NCEP-R2 is the highest product in the Retroflection and one of the highest off Port Elizabeth but not off Durban where the current is close to the coast. SEAFLUX is way higher than any other product off Cape Town.

Table 4.1: Mean of latent heat flux (W/m²) at four locations: off Durban, off Port Elizabeth, and Retroflection region and for the average of the three Agulhas points, and off Cape Town for seven considered datasets. Average has been done using the data resampled on the grid of SEAFLUX (0.25° x 0.25°).

ZONES	SEAFLUX	CFSR	MERRA-2	ERA-INTERIM	NCEP-R2	ERA-40	NOCS
Off Durban	162	194	172	138	138	147	152
Off Port Elizabeth	168	173	150	118	146	128	132
Retroflection	191	209	195	169	213	173	154
Mean Agulhas	174	192	172	142	166	149	146
Off Cape town	121	86	80	66	76	72	69

4.3.2 Differentiation of latent heat flux products using SEAFLUX as reference

Figure 4.4 shows the seasonal means of the difference between latent heat flux of SEAFLUX and each product. All products have been re-gridded on the grid of SEAFLUX. The fourth seasons are represented: austral summer (DJF); fall (MAM); winter (JJA) and spring. The scale of this difference ranges ± 60 W/m², roughly. ±40% of the mean value of latent heat flux. Values of ±7.5 W/m² is plotted in white. Figure 4.4 shows that all reanalysis products and observation NOCS underestimates latent heat flux by 60 W/m² in the Benguela upwelling system when compared to SEAFLUX. Figure 4.4 shows that HOAPS3 is quite similar to SEAFLUX but it has missing data along the coast. Thus HOAPS3 cannot well represent latent heat flux along the coast especially for the Benguela upwelling and most of the Agulhas Current. The Agulhas Current follows roughly the 200 m isobaths till Port Alfred (33.5°S, 26.5°E) before it separates from the coast. HOAPS3 is lower than SEAFLUX in the Agulhas Return current from up to 20 W/m² for each season

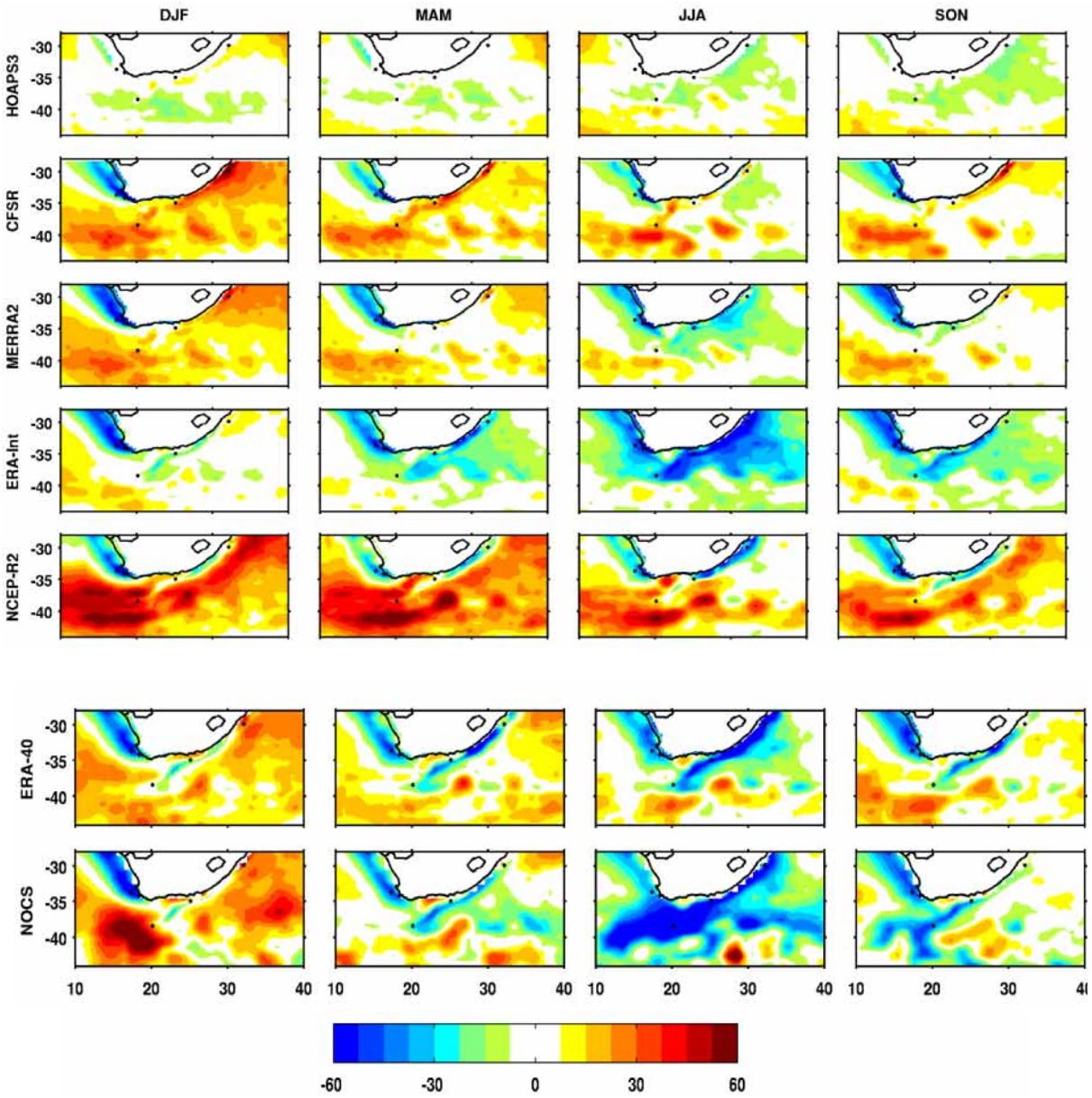

Figure 4.4: Same as Figure 4.2 but for the difference between each product and SEAFLUX. The products have been interpolated on the grid of SEAFLUX (0.25°x0.25°).

During the austral winter and spring, in the Indian Ocean, HOAPS3 is lower than SEAFLUX also up to 20 W/m². SEAFLUX and CFSR are quite similar (Figure 4.2, 4.3). The difference between CFSR and SEAFLUX (CFSR-SEAFLUX) shown by Figure 4.4 is mostly seen in the Benguela upwelling system, in the core of the Agulhas current, in the retroflection area and to the Southwest of the domain. In summer, fall and spring, CFSR is more than 50W/m² higher than SEAFLUX in those locations. The marker of the meandering Agulhas return current can be seen with a succession of lower and higher values. In winter, CFSR is lower than SEAFLUX (15 W/m²) in the Indian Ocean. The bias is lower during winter along the coast in the Agulhas Current. As for CFSR, Figure 4.4 also shows that all MERRA-2, ERA-Interim, NCEP-R2, ERA-40 and NOCS underestimate the flux in the Benguela system. This result can be confirmed by Figures 4.2, 4.3 and Table 4.1. Seasonally, MERRA-2 differences are quite different from CFSR except to the Southwest of the domain and in summer. In fall and spring, MERRA-2 is quite similar to SEAFLUX in the Agulhas system (Figure 4.2, 4.4). South of

38.5°E, MERRA-2 overestimates the flux by 30 W/m². However winter time is the season where SEAFLUX has higher flux than MERRA-2, especially along the coast and in the Agulhas Current.

4.3.3 Seasonal mean and annual cycle of Sea Surface Temperature

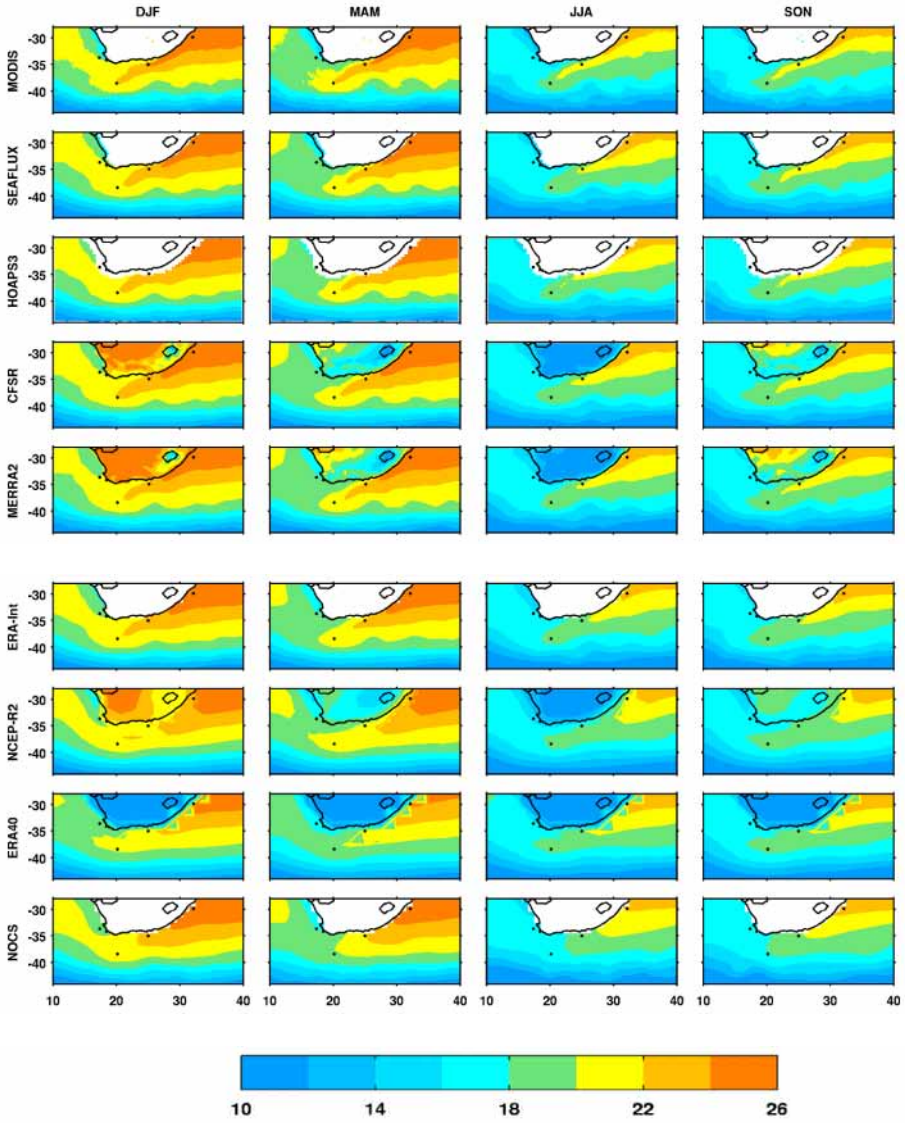

Figure 4.5: From top to bottom: seasonal average of sea surface temperature SST (°C) of MODIS, SEAFLUX, HOAPS3, CFSR, MERRA-2, ERA-Interim, NCEP-R2, ERA-40 and NOCS. From left to right Austral summer (DJF), austral fall (MAM), austral winter (JJA) and austral autumn (SON).

In the Agulhas system during summer, MERRA2-SEAFLUX is between 0 and 35 W/m², while CFSR-SEAFLUX is between 15 and 45 W/m² (Figure 4.4). In winter, still in the Agulhas system, MERRA-2-SEAFLUX is between 0 and -35 W/m², while CFSR-SEAFLUX is almost 0. Figure 4.4 and Table 4.1 show that seasonally and annually, ERA-Interim underestimates latent heat flux compared to SEAFLUX. ERA-Interim tends to be similar to SEAFLUX in summer time in the Indian Ocean (Figure 4.4). ERA-Interim has lower fluxes compared to all products, even compared to ERA-40 (Figure 4.4, Table 4.1) especially in winter. This behaviour will be explained later. When considering the three Agulhas locations, the difference between ERA-Interim and SEAFLUX is 32 W/m². In winter, this difference can be more than 60 W/m².NCEP-R2 latent heat flux is very high compared to SEAFLUX

(Figure 4.4). It is the highest positive difference of all products. The difference between NCEP-R2 and to SEAFLUX range from 30 to more 60 W/m² for all seasons especially in the western and southwest part of our domain during austral summer and fall.

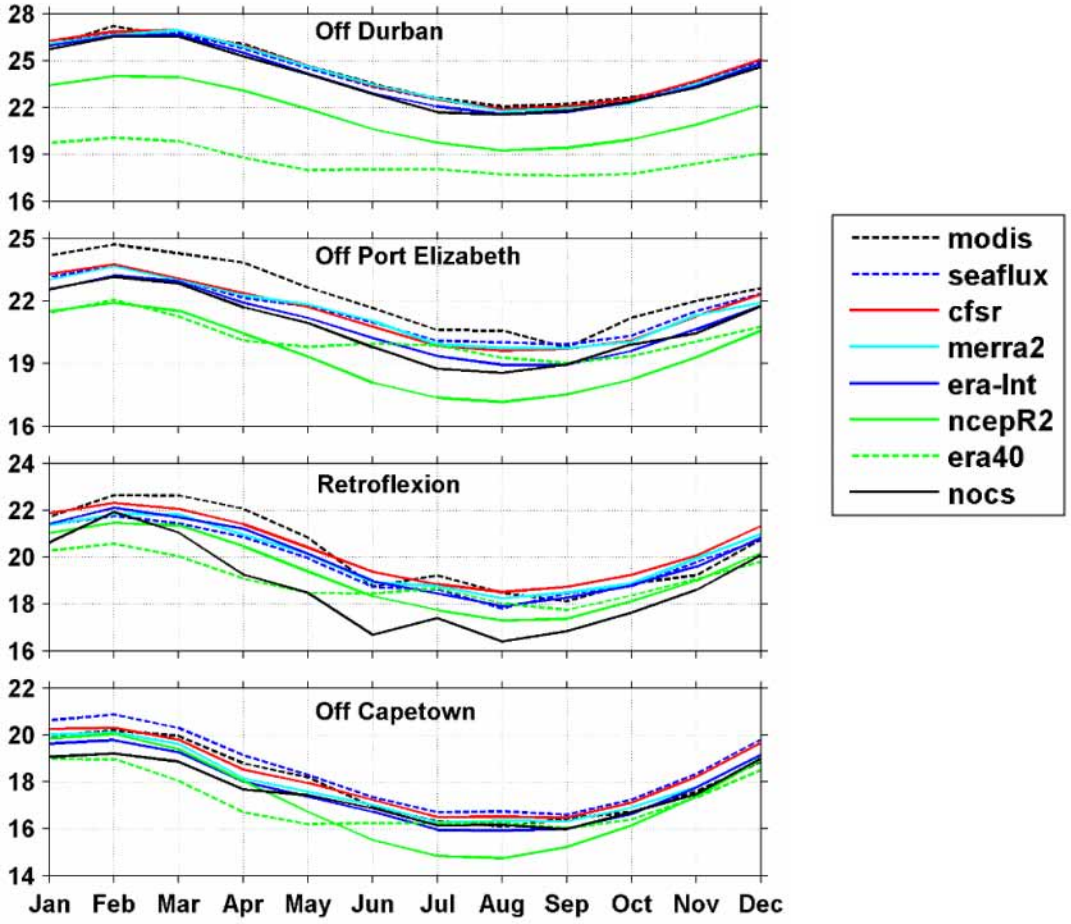

Figure 4.6: Annual cycle of sea surface temperature (°C). a) Agulhas Current off Durban (32°E,30°S), b) Agulhas Current off Port Elizabeth (25°E, 35°S), c) Agulhas Retroflection (20°5E, 38.5°S) and d) off Cape Town (17°E, 33.7°S) for MODIS (black dash), SEAFLUX (blue dash), CFSR (red), MERRA-2 (cyan), ERA-Interim (blue), NCEP-R2 (green), ERA-40 (dash green) and NOCS (black). Products have been interpolated on the grid of MODIS (4 x 4 km).

Latent flux is underestimated along the coast in the Agulhas Current for all seasons, especially in winter with difference of -60 W/m². This is due to the low resolution of its SST (1.90° x 1.87°) as seen below. Annually (Table 4.1), off Durban, off Port Elizabeth and off Cape Town, NCEP-R2 is respectively 24, 22 and 45 W/m² less than SEAFLUX. But in the Retroflection area, NCEP-R2 is 22 W/m² higher than SEAFLUX.As for ERA-Interim, ERA-40 underestimates the flux along the coast, especially in winter (Figure 4.4) maybe due to its coarse resolution (2.5° x 2.5°). During summer, NOCS has similar differences with SEAFLUX in many respects than the other reanalysis products (up to 60 W/m²), shown by Figure 4.4. But it is in winter that it differs from SEAFLUX by exaggerating the underestimation of latent heat flux in the Agulhas Current system. This could indicate that not enough vessel are in the Agulhas Current system, indeed vessels have a tendency to leave the Agulhas current at the location of PE cruising towards Cape Town or they avoid the west flowing Agulhas Current as much as possible

when sailing to Durban. Figure 4.5 represents the seasonal means of SST for MODIS, SEAFLUX, HOAPS3, CFSR, MERRA-2, ERA-Interim, NCEP-R2, ERA-40 and NOCS. It is completed by Figure 4.6 that shows the annual cycle of SST at our four locations. As for the latent heat flux, four seasons are represented: austral summer, fall, winter and spring. With its higher resolution (4 x 4 km) MODIS is taken as reference for SST. Seasonal SST varies between 10 and 26°C (Figure 4.5) in the Agulhas Current and its source further east and north. Summer and fall time have the hottest SST. The maximum is located Nord of 35°S in the South West Indian Ocean and the Agulhas Current east of Durban. This maximum of SST is also found along the coast for all products (Figure 4.5), except NCEP-R2 and ERA40. This is due to the low resolution of these two last reanalysis who do not represent the core of the Agulhas Current that is 100 km wide along the coast. SST decreases poleward and westward following the direction of the Agulhas current. Winter has the coldest SST. The minimum SST is around 10°C. It is located in the Southern Ocean throughout the seasons. In winter and spring, along the coast in the Agulhas Current and in its source region further east, values of MODIS SST are between 22 and 24°C. While NCEP-R2 SST and ERA-40 SST are between 18 and 20°C, i.e. 4° less than MODIS. The large-scale patterns of SEAFLUX and HOAPS3 are similar, but HOAPS3 does not have data along the coast (Figure 4.5). CFSR and MERRA-2 have the same seasonality. Along the coast, ERA-40 SST low resolution (2.5° x 2.5°) is clearly apparent. NCEP-R2 has lower values of SST along the coast compared to others products. Its resolution is 1.90° x 1.87°. There is a miss-representation of the meanders of the Return current in SST in NCEPR-2, ERA-40 and NOCS, all over the seasons, compared to other product (Figure 4.5). MODIS SST follows very well the Agulhas current (Figure 1). In winter, MODIS SST range between 20 and 22°C and its representation of the Agulhas Current is found between 40°E and 22°E. SST decreases poleward and westward. SST range between 20 and 22°C for SEAFLUX, HOAPS3, CFSR, MERRA-2 and ERA-40and and their representation of the Agulhas Current is found between 40°E and 24°E. For ERA-Interim and NOCS it is between 40°E and 27°E. NCEP-R2 has the shortest representation of the Agulhas Current, between 40°E and 30° of longitude Est. Figure 4.6 represents the annual cycle of sea surface temperature at the fourth locations used for this study: Agulhas Current off Durban (32°E, 30°S); Agulhas Current off Port Elizabeth (25°E, 35°S); Agulhas Retroflection (20°5E, 38.5°S) and off Cape Town (17°E, 33.7°S). HOAPS3 is omitted because of its missing data in the Agulhas system. The annual variation of the SST of each product is the same (Figure 4.6) with a maximum in summer time, and a minimum during the winter. Off Durban, the annual cycle of SST for SEAFLUX, CFSR, MERRA-2, Era-Interim and NOCS is similar as for MODIS. SST range between 21 and 27°C. NCEP-R2 and ERA-40 have the lowest values between 18 and 24°C, off by 3°C compared to MODIS. Off Port Elizabeth, SST varies between 17 and 25°C depending on the product (Figure 4.6). In this region all product are lower than MODIS. NCEP-R2 has the lowest SST, around 17°C in late winter. The Retroflection region is the area in the Agulhas system where SST is relatively low compared to others regions (Figure 4.5, 4.6, Table 4.2). In this region, SST is between 17 and 23°C. NOCS SST is the lowest around 17°C, during winter (Figure 4.6). NOCS has seasonal variations, with two maxima in February and July and two minima in June and August. In the Retroflection area, CFSR is 0.5°C lower than MODIS in summer and fall, but is 1°C higher in winter and spring (Figure 4.6). Off Cape Town, SST is between 14 and 21°C. In this region, the product with the lowest SST is NCEP-R2 with a value of 15°C in winter.

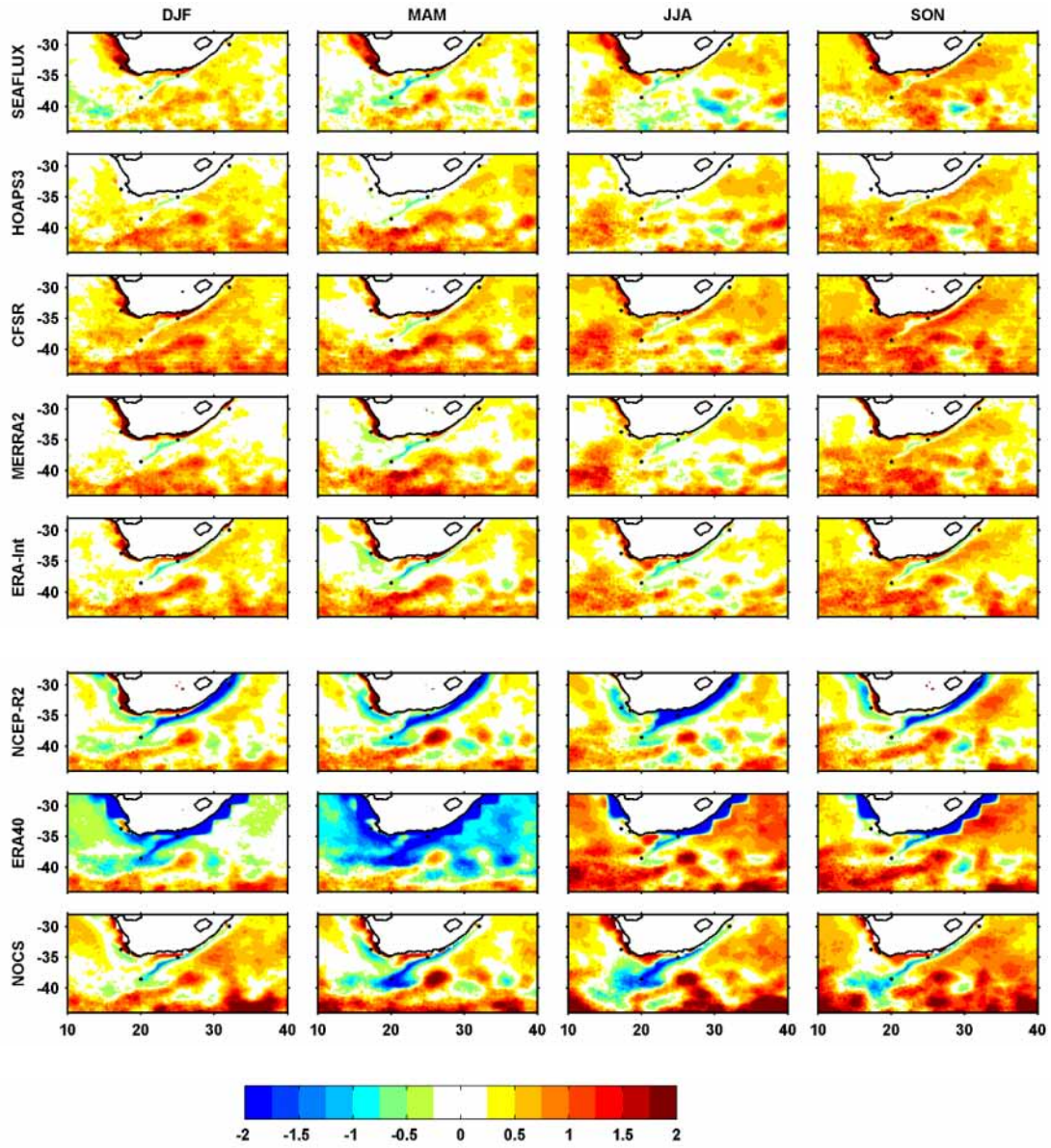

Figure 4.7: Same as Figure 4.5 but for the difference between each product and MODIS. Products have been interpolated on the grid of MODIS (4 x 4 km).

Table 4.2 completes the study by illustrating the values of annual mean of SST in the Agulhas system, and Off Cape Town. Off Durban (32°E, 30°S) the mean MODIS SST is 24.3°C. SEAFLUX and MERRA-2 are 0.1°C colder than MODIS; CFSR is equal to MODIS. Others products are between 0.3°C (ERA-Interim) and 5.7°C (ERA-40) colder than MODIS. Off Port Elizabeth (25°E, 35°S), the mean MODIS SST is 22.2°C (Table 4.2). SEAFLUX is 0.6°C colder than MODIS. CFSR and MERRA-2 are 0.7°C colder than MODIS. Others products are between 1.3°C (ERA-Interim) and 2.8°C (NCEP-R2) colder than MODIS. The Retroflection region is the coldest area in the Agulhas system (Table 4.2, Figure 4.5, 4.6). With an SST of 20.3°C for MODIS (Table 4.2). In this region, SEAFLUX and ERA-Interim are 0.4°C colder than MODIS. CFSR is equal to MODIS Off Durban. Others products are between 0.4°C (ERA-Interim) and 1.6°C (NOCS) colder than MODIS. To summarize, in the Agulhas system (off Durban, off Port Elizabeth and Retroflection region) the SST of each product is colder than MODIS. CFSR SST is the closest to MODIS SST. NCEP-R2 and ERA-40 are the coldest. Off Cape Town (33.7°S, 17°E) the mean MODIS SST is 18.0°C (Table 4.2). SEAFLUX and CFSR are

respectively 0.5 and 0.2°C warmer than MODIS. Others products are between 0.1°C (MERRA-2) and 0.9°C (ERA-40) colder than MODIS.

Table 4.2: Same as Table 4.1 but for SST (°C). Average has been done using the resampled data on the grid of MODIS (4 x 4 km).

ZONES	MODIS	SEA FLUX	CFSR	MERRA-2	ERA-INTERIM	NCEP-R2	ERA-40	NOCS
Off Durban	24.3	24.2	24.3	24.2	24.0	21.5	18.6	23.9
Off Port Elizabeth	22.2	21.6	21.5	21.5	20.9	19.4	20.2	20.8
Retroflection	20.3	19.9	20.3	20.0	19.9	19.3	19.0	18.7
Mean Agulhas	22.3	21.9	22.0	21.9	21.6	20.1	19.3	21.1
Off Cape town	18.0	18.5	18.2	17.9	17.7	17.2	17.1	17.5

4.3.4 Differentiation of SST using MODIS as reference

Looking at Figure 4.7, the difference between each product and MODIS is ±2°C i.e. ±11% of the mean MODIS SST in the Agulhas system. The Agulhas Current is visible in all products because of the very high resolution of MODIS compared to the rest. Difference of ±0.25°C is plotted in white. All products have been re-gridded on the grid of MODIS. SEAFLUX, HOAPS3, CFSR, MERRA-2 and ERA-Interim are up to 2°C higher than MODIS for all seasons in the Indian Ocean, off Durban, the Southern ocean and in the Benguela upwelling system. From off Port Elizabeth to the Retroflection region, MODIS SST is up to 1.25°C higher than satellites and reanalysis SST throughout the seasons (Figure 4.7). From austral fall to austral spring, SEAFLUX, HOAPS3, CFSR and MERRA-2 show the succession of warmer and colder or equal to zero SST. This highlights the misrepresentation of the meanders of the Agulhas Return current. (MERRA2 - MODIS) is similar to (Era-Interim - MODIS). For the SST of ERA-Interim, NCEP-R2, ERA-40 and NOCS, the misrepresentation of the meanders of the Agulhas Return current can also be seen for all seasons (Figure 4.7). From off Durban to the Retroflection region, NCEP-R2 and ERA-40 SST are more than 2°C lower than MODIS SST throughout the seasons (Figure 4.7). This can be due to the low resolution of their SST: 2.5 by 2.5 for ERA-40 and 1.98 by 1.87 for NCEP-R2. For all seasons, MODIS SST is higher compared to ERA-40 in the Benguela system. Particularly in austral fall ERA-40 is the coldest (more than 2°C less) compared to all products. In winter, ERA-40 SST is the highest in the Indian and southern ocean. Figure 4.7 also shows that NOCS underestimates SST in the Agulhas system, by 2°C, precisely in fall and winter. But NOCS overestimates SST in the Benguela upwelling and south of 43°S also by 2°C.

4.3.5 Seasonal mean and annual cycle of surface wind speed

Figure 4.9 shows the seasonal averages of surface wind speed for SCOW, SEAFLUX, HOAPS3, CFSR, MERRA-2, ERA-Interim and NOCS. As usual, four seasons are represented: austral summer; fall; winter and spring. SCOW (0.25° x 0.25°) is taken as reference of surface wind speed. In winter,

according to SCOW the wind speed off Durban is around 9 m/s. Off Port Elizabeth, it is around 10 m/s. It is more than 12 m/s in the Agulhas Retroflection and close to 6 m/s off Cape Town (Figure 4.9).

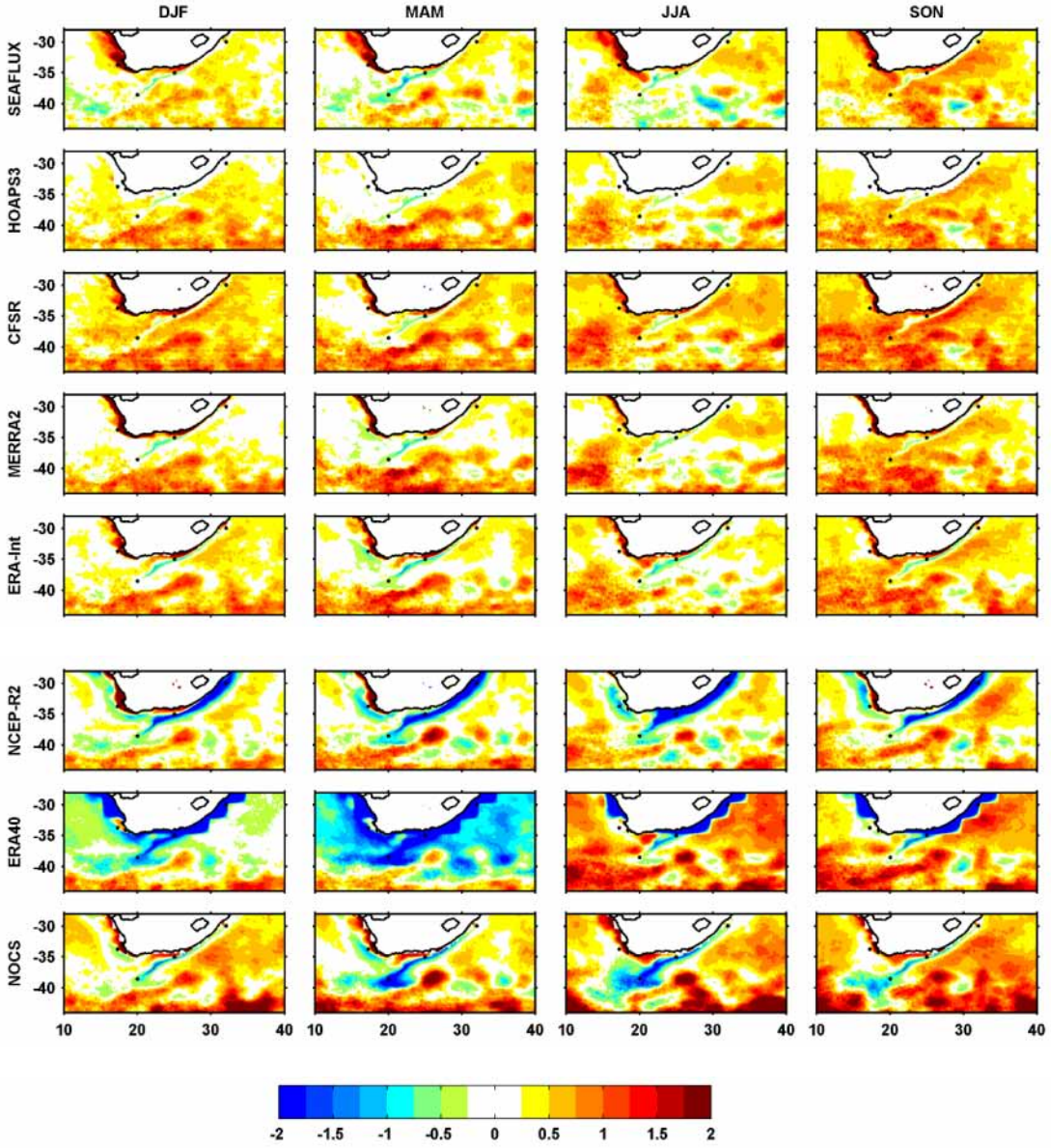

Figure 4.8: Same as figure 4.5 but for the difference between each product and MODIS. Products have been interpolated on the grid of MODIS (4 x 4 km).

The wind is clearly stronger above the Agulhas current than surrounding water by about 2 m/s due to the impact of SST perturbation on the surface wind field leading to an increase of surface wind speed across war SST front (Chelton et al., 2004). Conversely the wind is weaker above the cold Benguela upwelling. The wind speed also increases poleward at all season. SCOW and SEAFLUX have the same seasonality. The large-scale patterns for SCOW, SEAFLUX, HOAPS3 and CFSR are similar. But HOAPS3 has missing data along the coast. The meandering pattern of the Agulhas return current can be seen in the four products cited above (Figure 9). The maximum of wind speed is found in winter in the Retroflection region and surroundings for SCOW, SEAFLUX, HOAPS3 and CFSR (Figure 9). During this season, latent heat flux reaches its maximum around 250 W/m² (Figure 2). For MERRA-2

in winter (Figure 9), the wind speed maximum is in the southern ocean, including the Retroflection and Return current area. The Agulhas Current is not apparent in MERRA-2. Also for MERRA-2, some higher values can be found south of 43°S in fall and spring time. During these seasons, the latent heat flux of MERRA-2 is similar to that of SEAFLUX (Figure 2).

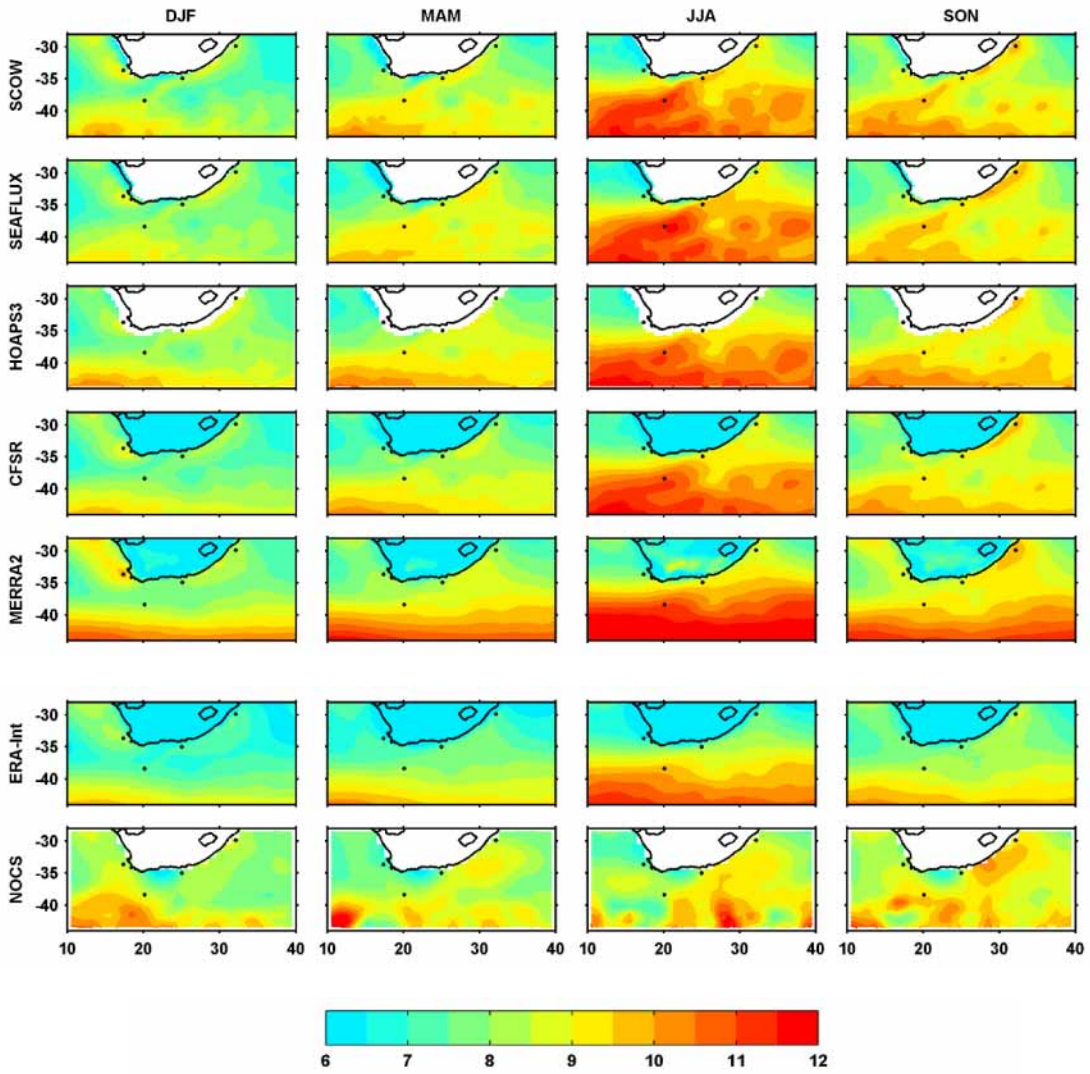

Figure 4.9: From top to bottom: seasonal average of surface wind speed (m/s) of SCOW, SEAFLUX, HOAPS3, CFSR, MERRA-2, ERA-Interim and NOCS. From left to right Austral summer (DJF), austral fall (MAM), austral winter (JJA) and austral autumn (SON). Black stars represent the fourth locations taken for the study. Agulhas Current off Durban (32°E, 30°S), Agulhas Current off Port Elizabeth (25°E, 35°S), Agulhas Retroflection (20°E, 38.5°S) and Off Cape Town (17°E, 33.7°S).

Era-Interim wind speed is weaker. In winter ERA-Interim wind speed maximum is in the Southwest Ocean, between 10 and 20° E (Figure 4.9). For NOCS, the wind speed maximum is observed in austral fall (40-44°S; 10-14°E) and in austral winter (40-44°S; 26-30°E). This can explain the low values of latent heat flux for ERA-Interim and NOCS around 200 and 150 W/m² respectively. The minimum values of wind speed are located in the Benguela upwelling system, in fall and winter time for all products (Figure 4.9). For NOCS, the minimum of wind speed is located off Plettenberg Bay (23°E, 35°S) along the South African coast. This weaker wind speed value could explain why we have low

value of NOCS latent heat flux (around 50 W/m²) there. In winter time, MERRA-2 has the highest wind speed, and NOCS the lowest.

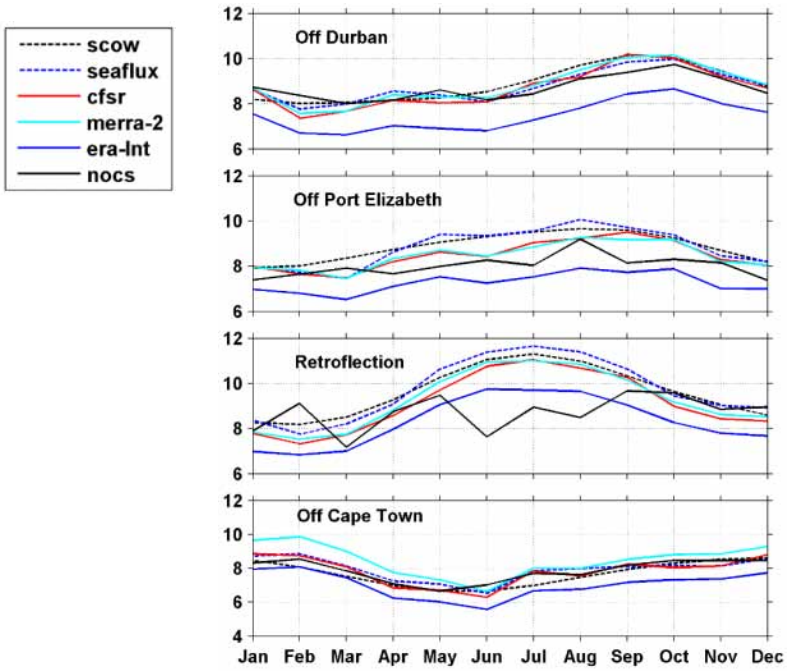

Figure 4.10: Annual cycle of surface wind speed (m/s). a) Agulhas Current off Durban (32°E,30°S), b) Agulhas Current off Port Elizabeth (25°E, 35°S), c) Agulhas Retroflection (20°5E, 38.5°S) and d) off Cape Town (17°E, 33.7°S) for SCOW (black dash), SEAFLUX (blue dash), CFSR (red), MERRA-2 (cyan), ERA-Interim (blue), and NOCS (black).

Figure 4.10 represents the annual cycle of surface wind speed for SCOW, SEAFLUX, CFSR, MERRA-2, ERA-Interim and NOCS at the fourth locations used for this study: All products are averaged in a common period from 1998 to 2005, except SCOW that is averaged between 1999 and 2007, due to the availability of data. HOAPS3 is omitted because of its missing data in the Agulhas system. Annually (Figure 4.10), the wind speed ranges from 5 to 10 m/s off Durban, Port Elizabeth and Cape Town. All products have more variations between seasons compared to SCOW. In the Retroflection area the wind speed range between 6 and 12 m/s. Here, only NOCS has some variations in between seasons (Figure 4.10), with two maximum (March and August). Off Durban, the wind starts to increase in June, till October. ERA-Interim has the weaker wind speed in the Retroflection area. Off Port Elizabeth, the wind has more variations compared to Off Durban. It increases from March till October (Figure 4.10). This could explain why the latent heat flux has more annual variation Off Port Elizabeth than Off Durban. Off Port Elizabeth and in the Retroflection, SEAFLUX is 0.1 m/s slightly higher than SCOW from mi-April to October. CFSR and MERRA-2 have the same annual variations at the fourth locations. ERA-Interim has the lowest wind speed. In the Retroflection region (Figure 4.10), the wind speed of each product (except NOCS) start to increase in March and reach a maximum (between 11 and 12 m/s) in July and decrease thereafter to a minimum around 9 m/s in November. ERA-Interim is around 2 m/s lower than SCOW and SEAFLUX. NOCS has four maximum in February, May, July and September and four minimum in March, June, August and November. Between May and mi-August NOCS has the lowest wind speed (between 7 and 9 m/s) compared to other product. Off Cape Town SCOW wind speed is between 0.1 and 0.8 m/s lower than SEAFLUX, CFSR, MERRA-2, and NOCS wind speed (Figure 4.10, Table 4.3). ERA-Interim is still the reanalysis with the lowest wind speed. In this region, MERRA-2 has the highest wind.

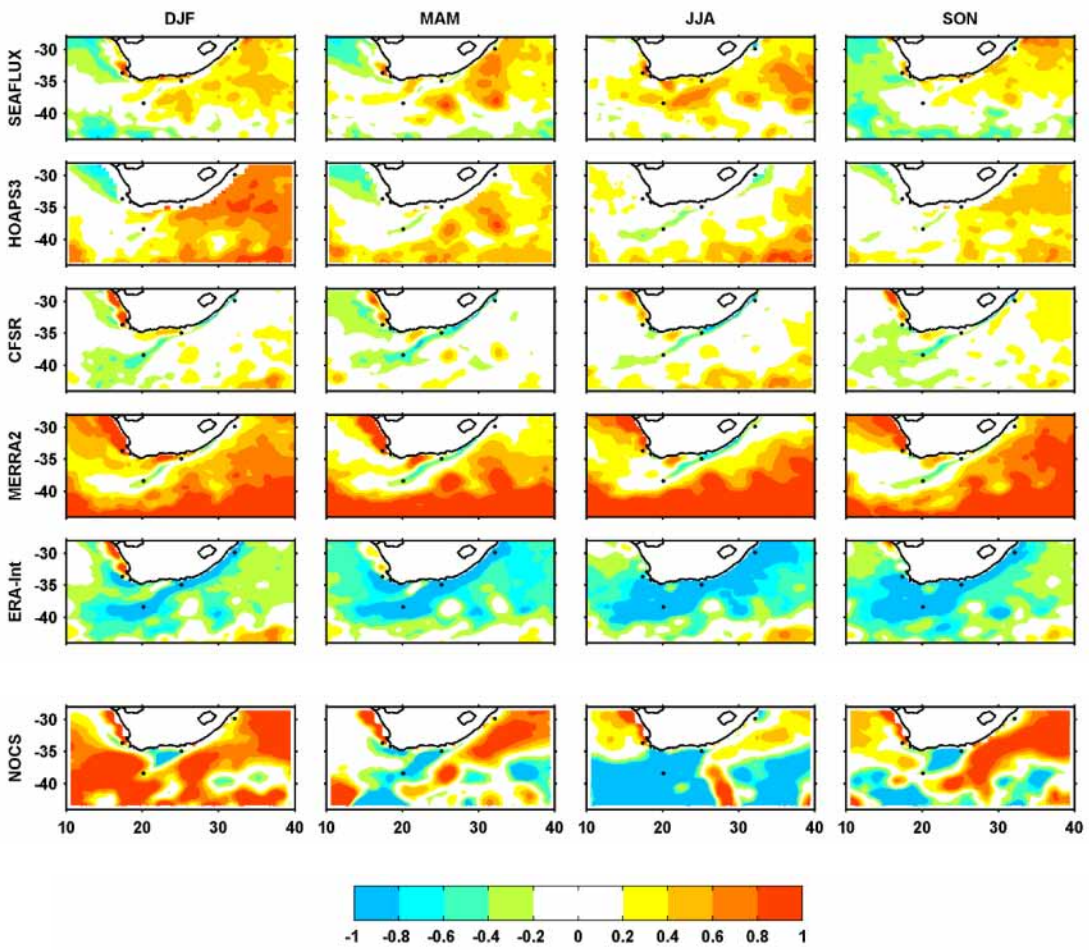

Figure 4.11: Same as figure 4.9 but for the difference between each product and SCOW. Products have been interpolated on the grid of SCOW (0.25° x 0.25°).

Table 4.3: Same as Table 4.1 but for the surface wind speed (m/s). Average has been done using the re-grid data on the grid of SCOW (0.25° x 0.25°).

ZONES	SCOW	SEAFLUX	CFSR	MERRA-2	ERA-INTERIM	NOCS
Off Durban	8.9	8.8	8.7	8.8	7.4	8.7
Off Port Elizabeth	8.9	8.8	8.5	8.5	7.3	8.0
Retroflection	9.6	9.7	9.1	9.3	8.3	8.7
Mean Agulhas	9.1	9.1	8.8	8.8	7.7	8.5
Off Cape town	7.7	7.9	7.8	8.5	7.0	7.9

Table 4.3 shows the annual mean values of wind speed at the four locations, and the average of the three Agulhas points. Off Durban and off Port Elizabeth, the mean wind speed for SCOW is 8.9 m/s. For SEAFLUX it is 0.1 m/s less than SCOW. This explain the similarity in latent heat flux of SEAFLUX (162 and 168 W/m²) off Durban and off Port Elizabeth (Table 4.2). Table 4.3 also shows that off Durban, others products are between 0.2 and 1.5 m/s (ERA-Interim) lower than SCOW. Off Port Elizabeth, those products are between 0.4 and 1.6 m/s (ERA-Interim) lower than SCOW. The Retroflection region is the zone where the wind speed is higher in the Agulhas system (Figure 4.9, 4.10, Table 4.3. In this region, SCOW wind speed is 9.6 m/s (Table 4e). SEAFLUX is 0.1 m/s higher than SCOW; others are between 0.3 (MERRA-2) and 1.3 m/s (ERA-Interim) lower than SCOW. Off Cape Town, the wind speed of SCOW is 7.7 m/s, i.e. between 0.1 and 0.8 m/s lower than SEAFLUX, CFSR, MERRA-2 and NOCS. But SCOW is 0.7 m/s higher than ERA-Interim off Cape Town. ERA-Interim has the lowest latent heat flux in this region (Figure 4.4, Table 4.1) in spite of its higher resolution (0.125° x 0.125°); this could be due to its wind speed.

4.3.6. Differentiation of wind speed using SCOW as reference

Figure 4.11 represents the difference between each product and SCOW. The difference ranges between -1 and 1 m/s i.e. around ±11% of the mean of surface wind speed. Values of ±0.2 m/s are plotted in white. In the Indian Ocean, all products have higher wind speed than SCOW, up to 1 m/s. The exception is made for ERA-Interim which completely underestimates the wind speed at all seasons (Figure 4.9, 4.10, Table 4.3) and particularly in the Agulhas system and surroundings. The Agulhas Current is clearly seen in the difference between reanalysis CFSR and MERRA-2 and SCOW. HOAPS3, CFSR and MERRA-2 have lower wind (0.6 m/s) than SCOW in the Agulhas system (Figure 4.11). Off Cape Town, SEAFLUX and CFSR wind speed are 0.8 m/s higher than SCOW throughout the seasons. SEAFLUX, HOAPS3 and CFSR have lower wind speed (0.8 m/s) than SCOW North of the Benguela system. The opposite is observed for MERRA-2 and NOCS. MERRA-2 overestimates the wind speed by more than 1 m/s in the southern ocean for all seasons. The same observation is made for NOCS during the summer and spring time. NOCS has its lowest wind speed in winter, south of 35°S and between 10 and 27°E.

4.3.7. Seasonal mean and annual cycle of specific humidity

4.3.7.1 Surface specific humidity (Qsst)

Figure 4.13 shows the seasonal means of the surface specific humidity for MODIS, SEAFLUX, HOAPS3, CFSR, MERRA-2, ERA-Interim and NOCS. As usual, four seasons are represented: austral summer; fall; winter and spring. ERA-Interim Qsst is computed using the SST and the surface pressure of ERA-Interim and the Clausius-Clapeyron law. MODIS Qsst is computed using MODIS SST, the surface pressure of ERA-Interim and the Clausius-Clapeyron law. MODIS Qsst (4 x 4 km) is taken as reference of Qsst. Qsst varies between 4 and 20 g/kg (Figure 4.13). Maximum of Qsst is found in summer and fall, Nord of 35°S in the South West Indian Ocean and in the Agulhas Current east of Durban. This maximum of Qsst is also found along the coast for all products. HOASP3 does not have data along the coast. As SST, Qsst decreases poleward and westward following the direction of the Agulhas current. Qsst minimum (4 g/kg) is in the Southern Ocean for all seasons. In winter, MERRA-2 has a higher Qsst compared to MODIS. NOCS Qsst miss represents the Agulhas current and the meanders of the return current for all seasons. In summer and fall, large-scale patterns of CFSR and MERRA-2 Qsst are similar to MODIS Qsst. In winter and in the Agulhas current, HOAPS3, CFSR and MERRA-2 Qsst are similar to MODIS Qsst; SEAFLUX Qsst is similar to ERA-Interim Qsst. Still in

winter, Qsst between 14 and 20 g/kg (Figure 4.13) is equivalent to SST between 20 and 26°C (Figure 4.6). (17°E, 33.7°S).

4.3.7.2 Specific humidity of air (Qa)

Specific humidity of air is represented by Figure 4.14. Qa is available for SEAFLUX, HOAPS3, CFSR, MERRA-2, ERA-Interim and NOCS. The fourth seasons of our study are represented. The same scale as the surface specific humidity has been kept (from 4 to 20 g/kg) for a better comparison with the surface specific humidity (Qsst). Qa is clearly lower than Qsst. Qa maximum (between 14 and 16 g/kg) is found in summer time for all products, Nord of the Indian Ocean. Qsst maximum can reach 18 g/kg for SEAFLUX off Durban in summer. Qa maximum is also found in fall, offshore Durban for all products except ERA-Interim (Figure 4.14). As Qsst, Qa decreases poleward and westward, following the direction of the Agulhas current. Qa minimum is in winter time. In this season, latent heat flux reaches the maximum. HOASP3 does not have data along the coast. Large-scale patterns of CFSR and MERRA-2 are similar compared to others products (Figure 1.14). During the winter, the distribution of SEAFLUX, HOAPS3, ERA-Interim and NOCS Qa are completely different from one to another. In winter in the Agulhas system, Qa ranges 6 and 12 g/kg for SEAFLUX and ERA-Interim; HOASP3, CFSR, MERRA-2 and NOCS Qa are between 8 and 12 g/kg. ERA-Interim has the lowest specific humidity of air for all seasons and compared to other product.

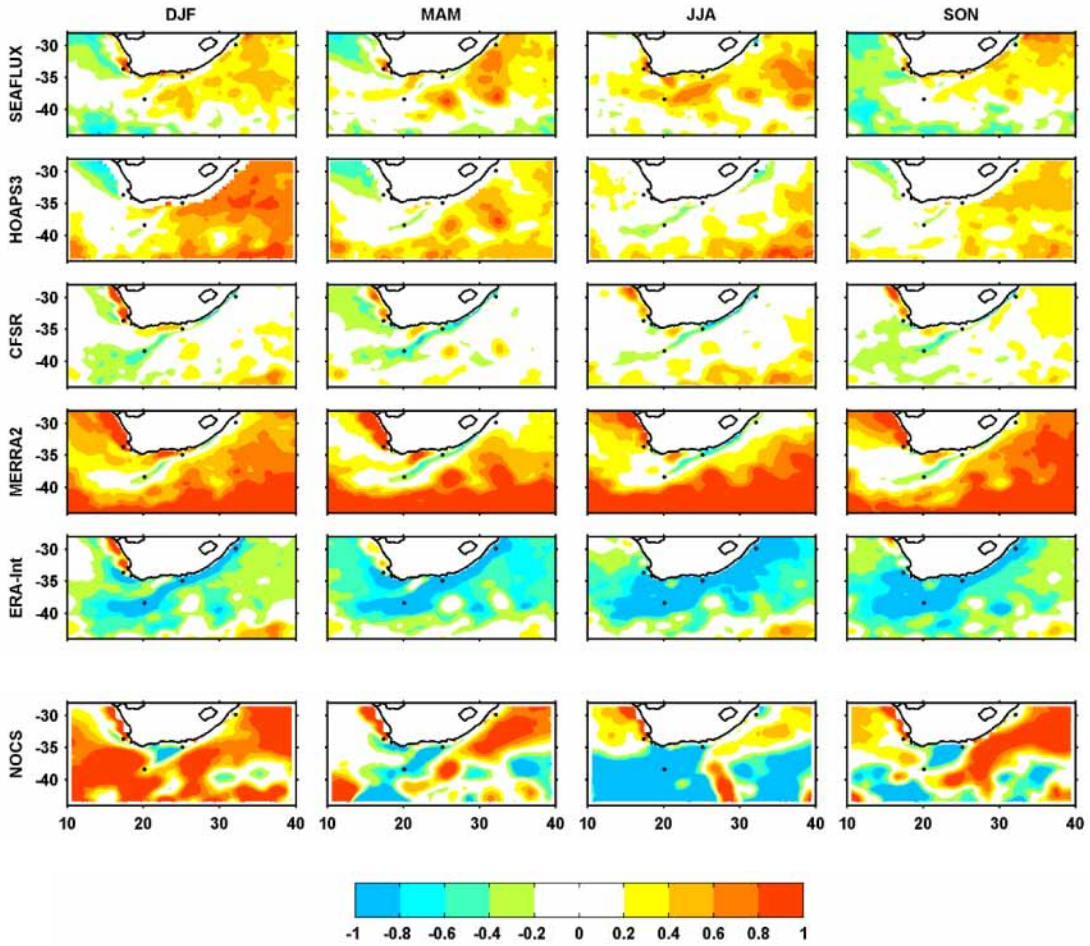

Figure 4.12: Same as figure 4.9 but for the difference between each product and SCOW. Products have been interpolated on the grid of SCOW (0.25° x 0.25°).

4.3.7.3 Difference between surface and air specific humidity (Qsst-Qa)

Figure 4.13 illustrates the seasonal difference between surface specific humidity and specific humidity of air (Qsst-Qa) for SEAFLUX, HOAPS3, CFSR, MERRA-2, ERA-Interim and NOCS. Qsst-Qa ranges between and 0 and 8 g/kg, around 33% of the mean value of Qsst and Qa. Qsst-Qa is positive, means that the surface specific humidity is higher than the specific humidity of air. Taking SEAFLUX as reference (Figure 4.13), the maximum is found in winter for SEAFLUX in the Agulhas current from off Durban to off Port Elizabeth. For HOAPS3, MERRA-2 and NOCS, the maximum is found in fall, in the Agulhas current off Durban. ERA-Interim has its maximum in fall (Nord of the Indian Ocean) and winter (between off Durban and of Port Elizabeth). In fall and winter, the meanders of the Agulhas Return Current are seen in all products except NOCS. NOCS has the lowest Qsst-Qa from fall to spring. For each product and for all seasons minimum Qsst-Qa is located in the southern ocean and in the Benguela system. All over the seasons for reanalysis, ERA-Interim has the highest Qsst-Qa, following by MERRA-2 and CFSR (Figure 4.13).

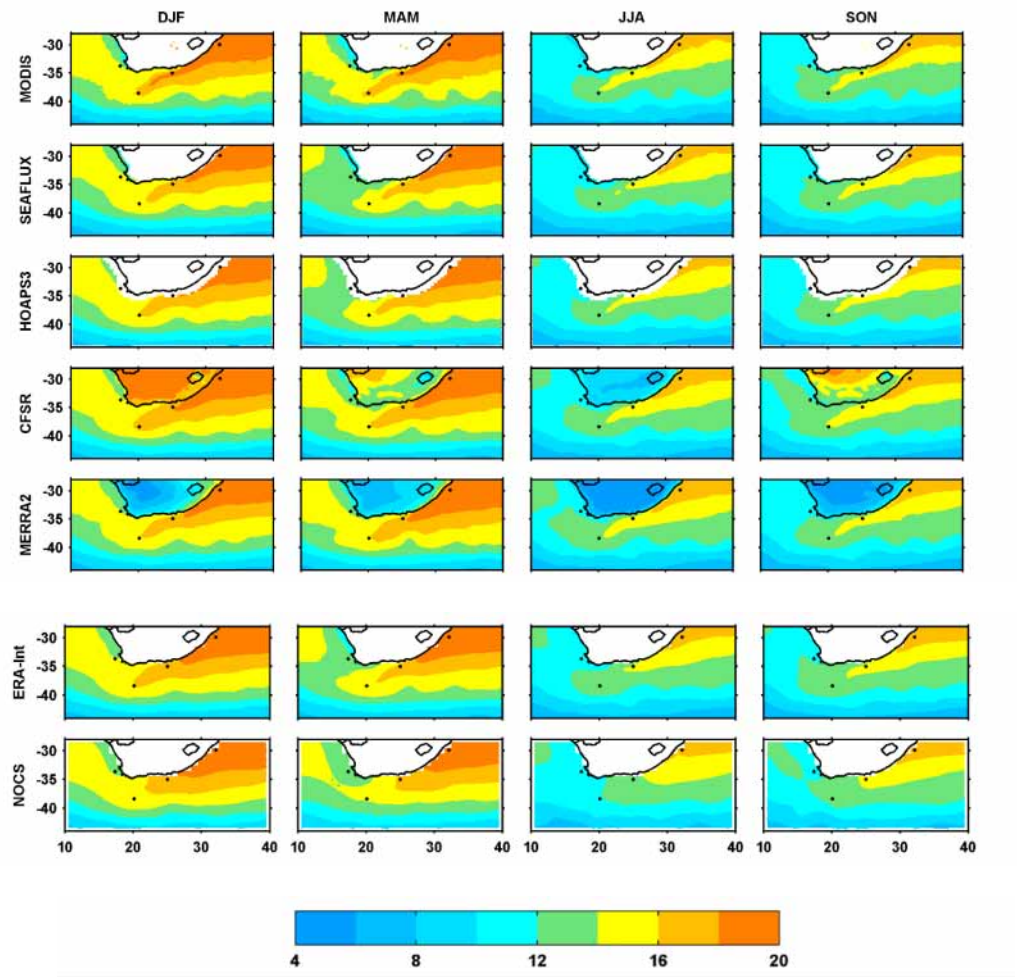

Figure 4.13: From top to bottom: seasonal average of surface specific humidity Qsst (g/kg) of MODIS, SEAFLUX, HOAPS3, CFSR, MERRA-2, ERA-Interim and NOCS. From left to right Austral summer (DJF), austral fall (MAM), austral winter (JJA) and austral autumn (SON). Black stars represent the fourth locations taken for the study. Agulhas Current off Durban (32°E, 30°S), Agulhas Current off Port Elizabeth (25°E, 35°S), Agulhas Retroflection (20°E, 38.5°S) and Off Cape Town

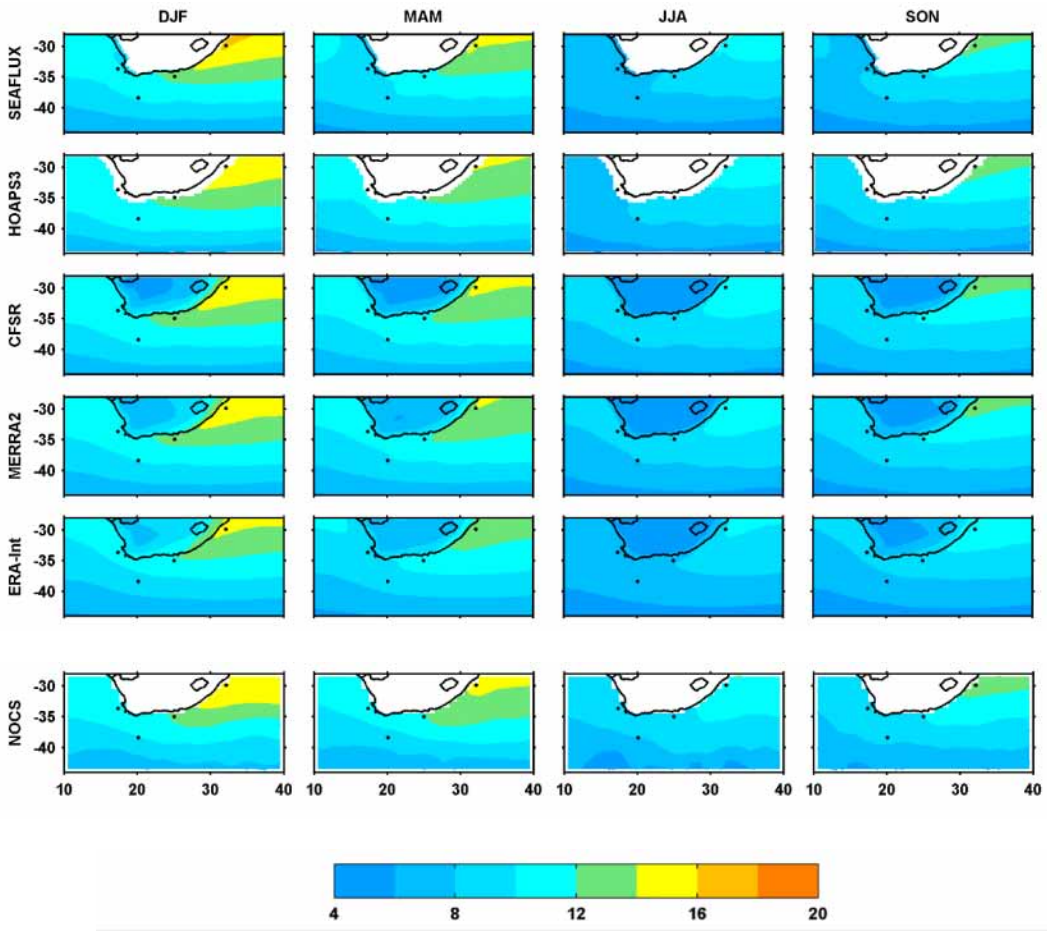

Figure 4.14: From top to bottom: seasonal average of specific humidity of air Qa (g/kg) of SEAFLUX, HOAPS3, CFSR, MERRA-2, ERA-Interim and NOCS. From left to right Austral summer (DJF), austral fall (MAM), austral winter (JJA) and austral autumn (SON). Black stars represent the fourth locations taken for the study. Agulhas Current off Durban (32°E, 30°S), Agulhas Current off Port Elizabeth (25°E, 35°S), Agulhas Retroflection (20°E, 38.5°S) and Off Cape Town (17°E, 33.7°S).

Figure 4.14 represents the annual cycle of Qsst-Qa for SEAFLUX, CFSR, MERRA-2, ERA-Interim and NOCS for the fourth locations used in this study. This figure confirmed that maximum of Qsst-Qa is located off Durban, with values rage 3.8 and 7.5 g/kg. Off Durban SEAFLUX (Qsst-Qa) increases up to 7 g/kg in mi-winter, and decreases from late winter to mi-spring (3.8 g/kg). CSFR (Qsst-Qa) increases up to 6.5 g/kg in early winter. From late winter to spring CFSR decreases up to 4.5 g/kg. Off Durban MERRA-2 (Qsst-Qa) increases up to 7.5 g/kg in mi-winter and decreases up to 3.8 g/kg in late spring. Phasing of ERA-Interim (Qsst-Qa) and NOCS (Qsst-Qa) are quite similar to CFSR (Qsst-Qa). Era-Interim and NOCS are respectively around 1 g/kg higher and 0.5 g/kg lower than CFSR (Qsst-Qa). ERA-Interim has the highest (Qsst-Qa) and NOCS the lowest Off Durban. Off Port Elizabeth (Figure 4.14) annual cycle of Qsst-Qa ranges between 3.8 and 6.5 g/kg. SEAFLUX, CFSR, MERRA-2 and ERA-Interim (Qsst-Qa) have one maximum in June. There are some variations between the seasons. MERRA-2 has two others maxima in March and September and three minima, in April, August and November. NOCS has its maximum in October and its minimum in August. With Qsst-Qa between 5 and 6.5 g/kg, ERA-Interim is the highest and NOCS the lowest with Qsst-Qa rage 3.9 and 4.9 g/kg. In the Retroflection region, the annual cycle of Qsst-Qa is between 3.5 and 7 g/kg. SEAFLUX has little annual variation (between 5 and 5.5 g/kg) compared to other product. CFSR (Qsst-Qa) range from 5.1 and 6 g/kg in summer. From mi-fall to spring, CFSR is around 5.5 g/kg. MERRA-2 increases up to

6.5 g/kg in mi-fall, and decreases thereafter to be quite constant from winter to early summer. ERA-Interim varies between 5.9 and 7 g/kg. NOCS has one maximum (6 g/kg) in February and one minimum in June (3.5 g/kg). In the Retroflection area, reanalysis Qsst-Qa are higher than SEAFLUX. This result can be confirmed by Figure 4.14. Offshore Cape Town, the annual cycle of Qsst-Qa rage 2 and 4.4 g/kg (Figure 4.14). SEAFLUX (Qsst-Qa) is almost flat (3.9 and 4.4 g/kg) compared to other product. CFSR and MERRA-2 rage 2.1 and 3.7 g/kg. ERA-Interim has one maximum (4.2 g/kg) in June. ERA-Interim is higher than CFSR and MERRA-2 for all seasons. NOCS is the lowest with Qsst-Qa between 2 and 3 g/kg. Table 4.4 represents the annual mean of Qsst-Qa in the Agulhas region and offshore Cape Town for SEAFLUX, CFSR, MERRA-2, ERA-Interim and NOCS.

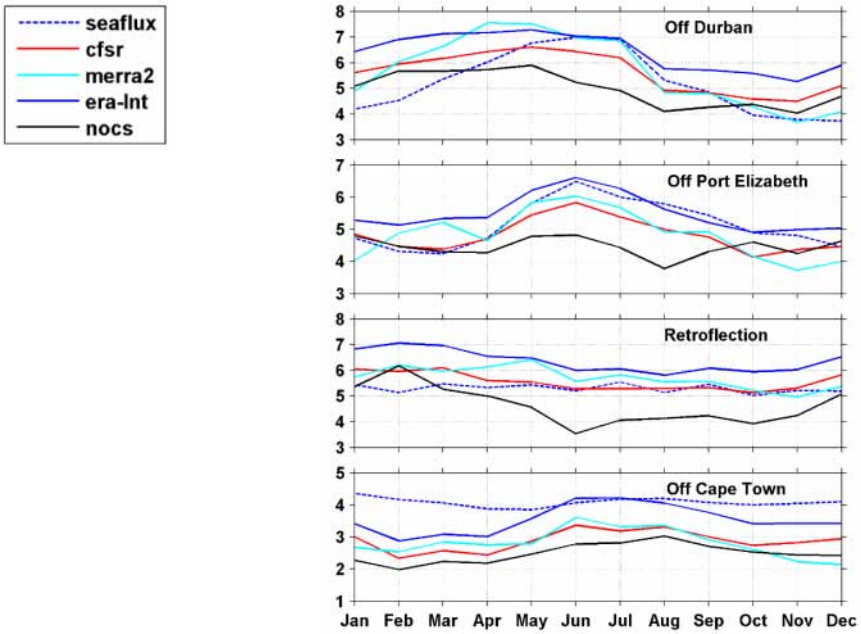

Figure 4.15: Annual cycle of the difference between Qsst and Qa: Off Durban, Off Port Elizabeth, Retroflection and Off Cape Town. For SEAFLUX, CFSR, MERRA-2, ERA-Interim and NOCS.

Table 4.4: difference between surface specific humidity and humidity of air (Qsst-Qa) in the Agulhas system and Off Cape Town. Average has been done using the re-grid data on the grid of SEAFLUX (0.25° x 0.25°).

ZONES	SEAFLUX	CFSR	MERRA-2	ERA-INTERIM	NOCS
Off Durban	5.2	5.6	5.7	6.4	5.0
Off Port Elizabeth	5.1	4.8	4.8	5.5	4.4
Retroflection	5.3	5.6	5.7	6.3	4.6
Mean Agulhas	5.2	5.3	5.4	6.1	4.7
Off Cape town	4.1	2.9	2.8	3.5	2.5

4.4 Drivers of latent heat flux using SEAFLUX

We are now trying to understand the drivers of the amplitude of the annual cycle of latent heat flux off Durban, Port Elizabeth, Cape Town and the Retroflection area. We are using SEAFLUX as reference for the representation of latent heat flux. SEAFLUX is also chosen because seasonally and annually, SEAFLUX SST is quite similar to MODIS SST (Figure 4.5, 4.6) which will impact Qsst directly.
Drivers of latent heat flux for SEAFLUX: Latent flux and surface wind speed

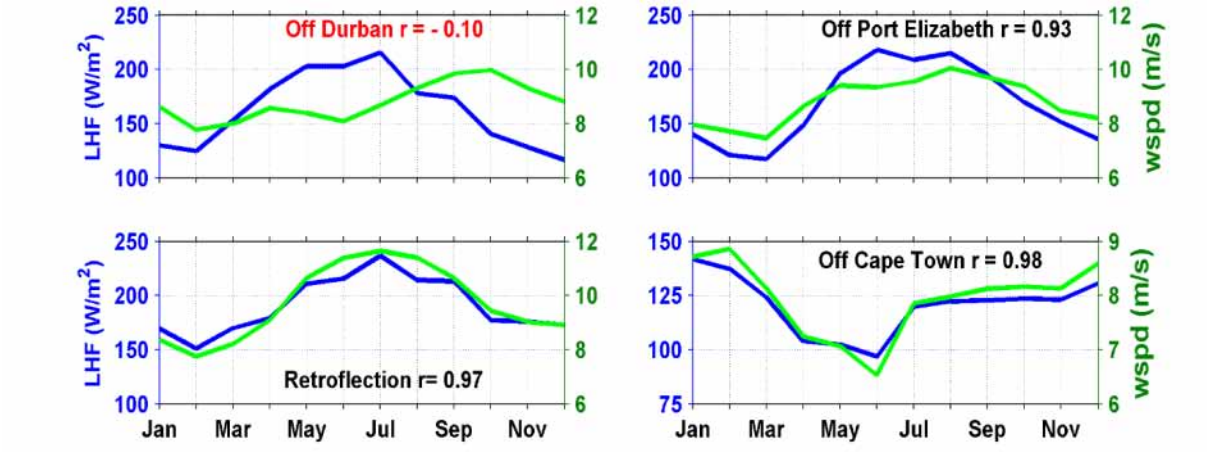

Figure 4.16: Annual cycle of latent heat flux (W/m²) (blue) and wind speed (m/s) (green) for SEAFLUX. From left to right and from top to bottom Agulhas Current off Durban, Agulhas Current off Port Elizabeth, Agulhas Retroflection and off Cape Town.

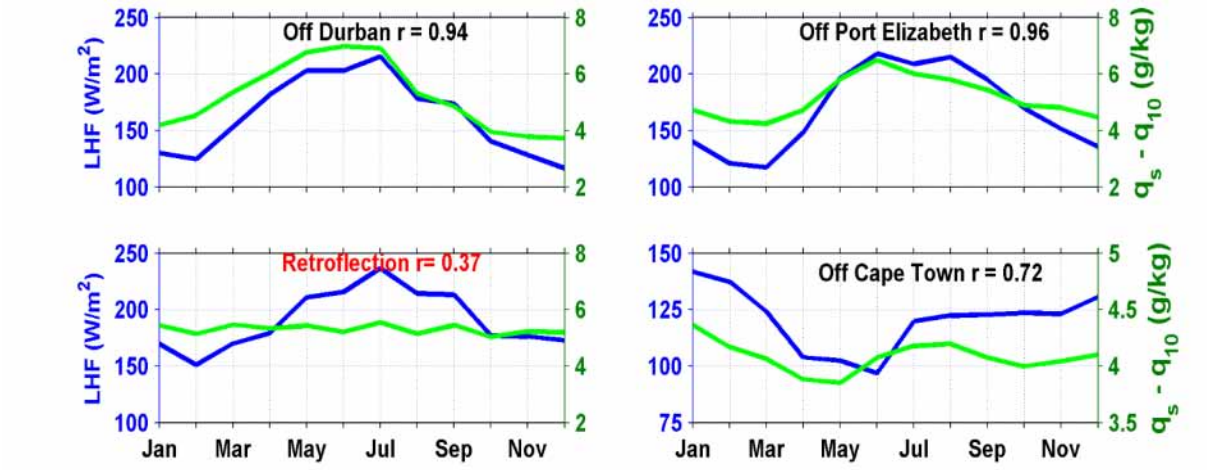

Figure 4.17: Same as Figure 4.16 but for annual cycle of latent heat flux (W/m2) (blue) and Qsst - Q10 (g/kg) (green).

SEAFLUX wind speed also compared well with SCOW wind speed (Figure 4.9, 4.10). SEAFLUX is able to capture small scale features such as the core of the Agulhas Current or the meanders of the Return Current. The annual cycle of latent heat flux has been described in the sections above. In these sections, we show that the annual cycle of latent heat flux for SEAFLUX ranges between 100 and 250 W/m² in the Agulhas system, and between 90 and 150 W/m² off Cape Town (Figure 4.3, 4.15, 4.16). The highest value of latent heat flux is found in the Retroflection area in July and the lowest off Cape Town in June. Lowest values of latent heat flux in the Agulhas Current system are off Port Elizabeth in late summer. Off Durban SEAFLUX latent heat flux has two maxima in May and July, and two minima

in February and October. Off Port Elizabeth, SEAFLUX has two maxima in June and August, and minimum values in summer. Off Port Elizabeth the annual cycle of latent heat flux is most pronounced (Figure 4.3, 4.16, 4.17). Off Cape Town SEAFLUX has one minimum (100 W/m²) in June (Figure 4.3, 16, 17). Figure 16 also shows the annual cycle of wind speed of SEAFLUX, for the fourth locations used in this study. Annually SEAFLUX wind speed varies between 7.5 and 12 m/s in the Agulhas system, and between 6.5 and 9 m/s off Cape Town. Off Durban, the wind starts to increase in June, till October, while latent heat flux increases up to 220 W/m² in July and decreases thereafter. Off Port Elizabeth, latent heat flux and wind speed have almost the same phasing. The maximum of wind speed is found in winter in the Retroflection region. In this region, the wind speed and the latent heat flux have a maximum in July. Off Cape Town, wind speed and latent heat flux vary together, and both of them have a minimum in June. Off Port Elizabeth, in the Retroflection region and off Cape Town, latent heat flux and wind speed have almost the same annual variation (Figure 4.16). This is not the case offshore Durban, because latent heat flux increases from late summer till mi-winter and decreases afterward, while wind speed increases from late summer to mi-spring. Correlations between latent heat flux and wind speed are -0.10; 0.93; 0.97 and 0.98 respectively off Durban, off Port Elizabeth, in the Retroflection area and off Cape Town. These correlations indicate that the wind speed is the driver of the amplitude of latent heat flux offshore Port Elizabeth, in the Retroflection and offshore Cape Town, which is not the case offshore Durban. In addition of the annual cycle of latent heat flux of SEAFLUX, Figure 4.17 also represents the annual cycle of the difference between surface specific humidity and humidity of air, for SEAFLUX at our fourth locations. Annual cycle of Qsst-Qa has been described in section 3.7. Qsst-Qa rages from 3.9 to 7 g/kg offshore Durban and Port Elizabeth. Off Durban SEAFLUX (Qsst-Qa) increases up to 7 g/kg in mi-winter, and decreases from late winter to mi-spring (3.8 g/kg). In this region, latent heat flux and Qsst-Qa have the same variations. Off Port Elizabeth SEAFLUX (Qsst-Qa) has one maximum in June while latent heat flux has two maximum, one in June and another in August. In the Retroflection area Qsst-Qa is between 5 and 5.5 g/kg, while latent heat flux has its maximum value in July. Off Cape Town Qsst-Qa rages from 3.8 to 4.4 g/kg. In this region, Qsst-Qa has a minimum in May while latent heat flux has its minimum in June. Off Durban, off Port Elizabeth in the Retroflection and off Cape Town, correlations between latent heat flux and Qsst-Qa are respectively 0.94; 0.96; 0.37 and 0.72. These correlations indicate that Qsst-Qa is the main driver of the amplitude of the annual cycle of latent heat flux off Durban; this is not the case in the Retroflection area. Off Port Elizabeth and Cape Town, Qsst-Qa is one of the drivers of the amplitude latent heat flux. We note that off Port Elizabeth correlation between latent heat flux and Qsst-Qa is 0.03 higher than that between latent heat flux and surface wind speed. The opposite is observed off Cape Town, where correlation between latent heat flux and wind speed has decreased by 0.26 compared to correlation between latent heat flux and Qsst-Qa.

4.5 References

Andersson, A., K. Fennig, C. Klepp, S. Bakan, H. Graßl and J. Schulz (2010). The Hamburg Ocean Atmosphere Parameters and Fluxes from Satellite Data HOAPS-3, Earth Syst. Sci. Data, 2, 215-234, doi: 10.5194/essd-2-215-2010.

Andersson, A., Fennig, K., C. Klepp, S. Bakan, H. Graßl and J. Schulz (2011) Evaluation of HOAPS-3 ocean surface freshwater flux components, Journal of Applied Meteorology and Climatology, 50, 379-398, doi: 10.1175/2010JAMC2341.1

Bentamy A., J.F. Pillé, A. Grouazel, F. Paul, H. Azelmat, P.P. Mathieu, K. V. Schuchmann, S. Sathyendranah, H.E. King, R. Danielson, I. Essau, J. Johanessen, S. Gulev, C.A. Clayson, R. Pinker, S. Grodsky, M. Bourassa, S.R. Smith, K. Haines, Maria Valdivieso, C. Merchant, B. Chapron, A. Andersson, R. Hollman, J. Simon (2016). Towards Improvement of the Estimation of Turbulent Heat Flux over Global Oceans.

Berry, D.I. and E.C. Kent (2009) A new air-sea interaction gridded dataset from ICOADS with uncertainty estimates. Bulletin of the American Meteorological Society, 90, 64-656. DOI: 10.1175/2008BAMS2639.1.

Bosilovich, M.L.G., J. Chen, F.R. Robertson and R.F. Adler (2008) Evaluation of global precipitation in reanalyses. J. Appl. Meteor. Climatol., 47, 2279-2299.

Bryden, H.L., L.M. Beal and L.M. Duncan (2005). Structure and transport of the Agulhas Current and its temporal variability, J. Oceanogr., 61, 479-492.

Casal, T.G.D., L.M. Beal, R. Lumpkin and W.E. Johns (2009). Structure and downstream evolution of the Agulhas Current system during a quasisynoptic survey in February-March 2003, J. Geophys. Res., 114, C03001, doi: 10.1029/2008JC004954.

Chan, Pui-King et Gao, Bo-Cai. A comparison of MODIS, NCEP, and TMI sea surface temperature datasets. IEEE Geoscience and Remote Sensing Letters. (2005) vol. 2, no 3, p. 270-274.

Chelton, D.B., Schlax, M.G., Freilich, M.H. and Milliff, R.F. (2004). Satellite measurements reveal persistent small-scale features in ocean winds. **Science** 303, 978-983.

Chou, S.H., Nelkin, E., Ardizzone, J. and Atlas, R.M. (2004). A comparison of latent heat fluxes over global oceans for four flux products. *Journal of climate*, *17*(20), 3973-3989.

Clayson, C.A., Roberts, J.B. and A. Bogdanoff (2013). SeaFlux Version 1: a new satellite-based ocean-atmosphere turbulent flux dataset. International Journal of Climatology, in revision.

Curry, J., A. Bentamy, M.A. Bourassa, D. Bourras, E.F. Bradley, M. Brunke, S. Castro, S.H. Chou, C. A. Clayson, W.J. Emery, L. Eymard, C.W. Fairall, M. Kubota, B. Lin, W. Perrie, R. Reeder, I.A. Renfew, W.B. Rossow, J. Schulz, S.R. Smith, P.J. Webster, G.A. Wick and X. Zeng (2004) SEAFLUX. Bull. Amer. Meteor. Soc., 85,409-424.

Dee, D.P., S.M. Uppala, A.J. Simmons, P. Berrisford, P. Poli, S. Kobayashi, U. Andrae, M.A. Balmaseda, G. Balsamo, P. Bauer and P. Bechtold (2011). The ERA-Interim reanalysis: Configuration and performance of the data assimilation system. Quarterly Journal of the Royal Meteorological Society, 137(656), pp.553-597.

Fairall, C.W., E.F. Bradley, J.E. Hare, A.A. Grachev and J.B. Edson (2003). Bulk parameterization of air-sea fluxes: updates and verification for the COARE algorithm. Journal of Climate 16: 571-591, DOI: 10.1175/1520-442(2003)016<0571: BPOASF>2.0.CO; 2.

Gibson, J.K., P. Kållberg, S. Uppala, A. Noumura, A. Hernandez and E. Serrano (1997) ERA description. ECMWF Re-analysis Project Rep. Series 1, ECMWF, 77 pp.

Gimeno, L., A. Drumond, R. Nieto, R.M. Trigo and A. Stohl (2010). On the origin of continental precipitation. Geophysical Research Letters, 37(13).

Huffman, G.J., D.T. Bolvin, E.J. Nelkin, D.B. Wolff, R.F. Adler, G. Gu, Y. Hong, K.P. Bowman and E.F. Stocker (2007). The TRMM multisatellite precipitation analysis (TMPA): Quasi-global, multiyear, combined-sensor precipitation estimates at fine scales. Journal of Hydrometeorology, 8(1), pp.38-55.

Johannessen, J.A., B. Chapron, F. Collard, M.H. Rio, J.F. Piollé, G. Quartly, J. Shutler, R. Escola, C. Donlon, R. Danielson, A. Korosov, R.P. Raj, V. Kudryavtsev, M. Roca, J. Tournadre, G. Larnicol, S. Labroue, P. Miller, F. Nencioli, M. Warren and M. Hansen (2015) GlobCurrent: Sentinel-3 Synergy in Action. In *ESA Special Publication* (Vol. 734, p. 2).

Josey, S.A., E.C. Kent and P.K. Taylor (1999). New insights into the ocean heat budget closure problem and analysis of the SOC air-sea flux climatology. J. Climate, 12, 2856-2880.

Kalnay, Eugenia, Kanamitsu, Masao, Kistler, Robert et al. The NCEP/NCAR 40-year reanalysis project. Bulletin of the American meteorological Society (1996). vol. 77, no 3, p. 437-471.

Kanamitsu, M., W. Ebisuzaki, J. Woollen, S.-K. Yang, J. J. Hnilo, M. Fiorino and G.L. Potterl, 2002: NCEP-DOE AMIP-II Reanalysis (R-2). Bull. Amer. Meteor. Soc., 83, 1631-1643.

Kistler, Robert, Collins, William, Saha, Suranjana et al. The NCEP-NCAR 50-year reanalysis: Monthly means CD-ROM and documentation. Bulletin of the American Meteorological society, 2001, vol. 82, no 2, p. 247-267.

Lee-Thorp, A., M. Rouault, and J.R.E. Lutjeharms: Moisture uptake in the boundary layer above the Agulhas Current: a case study, J. Geophys. Res., 104, 1423-1430, 1999.

Lutjeharms J.R.E., Mey R.D. and Hunter I.T. (1986). Cloud lines over the Agulhas Current. *S. Afr. J. Sci.* **82**, 635-640.

Lutjeharms, J. R. E. and R.C. Van Ballegooyen (1988). The retroflection of the Agulhas Current Journal of Physical Oceanography,

Lutjeharms J.R.E. and Rouault M. (2000). Observations of cloud formation above Agulhas Current intrusions in the South-east Atlantic. *S. Afr. J. Sci.* **96**, 577-580.

Molod, A., L. Takacs, M. Suarez, J. Bacmeister, I.-S. Song and A. Eichmann (2012). The GEOS Atmospheric General Circulation Model: Mean Climate and Development from MERRA to Fortuna. NASA Technical Report Series on Global Modeling and Data Assimilation, NASA TM—2012-104606, Vol. 28, 117 pp.

Reynolds, R.W. and T.M. Smith (1994). Improved global sea surface temperature analyses using optimum interpolation. J. Climate, 7, 929-948.

Rienecker and Co-authors (2011). MERRA – NASA's Modern-Era Retrospective Analysis for Research and Applications. J. Climate, 24, 3624-3648, doi:10.1175/JCLI-D-11-00015.1.

Risien, C.M. and D.B. Chelton (2008). A Global Climatology of Surface Wind and Wind Stress Fields from Eight Years of QuikSCAT Scatterometer Data. J. Phys. Oceanogr., 38, 2379-2413.

Rouault, M. and A.M. Lee-Thorp (1997). Fine-time resolution measurements of atmospheric boundary layer properties between Cape Town and Marion Island. S. Afr. Mar. Sci., 17, 281-296.

Rouault, M., A.M. Lee-Thorp and J.R.E. Lutjeharms (2000). Observations of the atmospheric boundary layer above the Agulhas Current during along current winds. Journal of Physical Oceanography, 30, 70-85

Rouault, M., P. Penven and B. Pohl (2009). Warming in the Agulhas Current system since the 1980's, Rouault, M., C. J. C. Reason, R. E. Lutjeharms, and A. Beljaars, 2003: NCEP Reanalysis and ECMWF operational model underestimation of latent and sensible heat fluxes above the Agulhas Current, Journal of. Climate, 16, 776-782

Rouault, M., S.A. White, C.J.C. Reason, R.E. Lutjeharms and I. Jobard (2002). Ocean-Atmosphere Interaction in the Agulhas Current and a South African extreme weather event. Weather and Forecasting, Vol 17, 4, 655-669

Saha, S., S. Moorthi, H.L. Pan, X. Wu, J. Wang, S. Nadiga, P. Tripp, R. Kistler, J. Woollen, D. Behringer and H. Liu (2010). The NCEP climate forecast system reanalysis. Bulletin of the American Meteorological Society, 91(8), pp.1015-1057

Smith, S.R., P.J. Hughes, and M.A. Bourassa (2011). A comparison of nine monthly air-sea flux products. International Journal of Climatology, 31, 1002-1027, doi:10.1002/joc.2225.

Uppala, S.M., Kallberg P.W., A.J. Simmons and co-authors (2005). The ERA-40 re-analysis. Q. J. R. Meteorol. Soc. 131: 2961-3012.

Woodruff, S.D., R.J. Slutz, R.L. Jenne and P.M. Steurer (1987). A comprehensive ocean-atmosphere dataset, Bull. Am. Meteorol. Soc., 68, 1239-1250.

5 Atmospheric signature of the Agulhas Current

5.1 Introduction

As the strongest southern hemisphere western boundary current, the Agulhas Current transports around 70 Sverdrup (Sv, 1Sv = $10^6 m^3 s^{-1}$) (Beal et al., 1999) of warm Indian Ocean water along the southeast coast of Africa. As the Gulf Stream and the Kuroshio, the Agulhas Current is warmer than the surrounding ocean, and this leads to high turbulent sensible and latent heat fluxes (Rouault et al., 2003). However, only a few studies have investigated the impact of the Agulhas Current on local weather and climate. Radiosondes and heat fluxes measurements above the Agulhas Current show that the vigorous exchange of moisture and energy above the current penetrates into the troposphere to at least 1500 m (Lee-Thorp et al., 1999; Rouault et al., 2000). This phenomenon causes distinct cloud lines above the Agulhas Current during fair weather high-pressure synoptic conditions (Lutjeharms et al., 1986; Rouault et al., 2000). Moreover moisture produced by the Agulhas Current can be advected inland (Lee-Thorp et al., 1999; Rouault et al., 2000). Rain rate and the diurnal cycle of rainfall along the eastern coast of South Africa were related to the proximity of the Agulhas Current (Jury et al., 1993; Rouault et al., 2013). Furthermore moisture advected from the Current was hypothetically linked to an extreme weather system (Rouault et al., 2002). Regional impacts of the Agulhas Current on climate have not been thoroughly investigated using numerical models, although the climatic impact of the greater Agulhas Current system was studied using a coarse resolution model (Reason, 2001). Similarly, first generation climate reanalysis were inadequate for studying climatic impacts of the current (Rouault et al., 2003), because they did not resolve its core where the turbulent sensible and latent heat fluxes are five times stronger than the surrounding water. Thus, the influence of the Agulhas Current on the weather and climate of Southern Africa is not well-known. The aim of this study is to investigate using observations, reanalysis, and numerical model experiments how the warm SST associated with the Agulhas Current affects the low-level atmosphere and rainfall.

5.2 Data and methods

5.2.1 Data and atmospheric model

We use the Climate Forecast System Reanalysis (CFSR, Saha et al., 2010) provided by NCEP (National Centers for Environmental Prediction). As satellite data, we use the 0.05° by 0.05° climatology of Tropical Rainfall Measuring Mission Precipitation Radar (TRMM PR, Biasutti et al., 2012) for precipitation. We use 0.25° by 0.25° resolution GlobCurrent surface geostrophic current derived from altimetry (Rio et al., 2014; Johannessen et al., 2015) for the representation of the Agulhas Current. The 0.25° by 0.25° resolution AVHRR-based Optimal Interpolation Sea Surface Temperature (OISST, Reynolds et al., 2007) is used for the validation of CFSR SST; and the 0.25° by 0.25° resolution Scatterometer Climatology of Ocean Winds (SCOW, Risien and Chelton, 2008) for the validation of CFSR 10 m-wind speed (Table S1). The Weather Research and Forecast/Advanced Research (WRF, Skamarock and Klemp, 2008) system version 3.7.1 is applied to investigate the impact of the core of the Agulhas Current on the atmosphere. The model domain is 17°S-43°S and 8°E-52°E (Figure S2) and the resolution is 25 x 25 km, with 56 vertical eta-coordinate levels 0.5°. We perform two experiments: a control (CTL) driven with interannually varying, high-resolution, observed SST; and a sensitivity experiment (SMTH) driven with SST smoothed to remove the sharp SST gradients associated with the Agulhas Current (Figure S2) and otherwise identical to CTL. Both experiments cover the period 2001 to 2005, with lateral boundary conditions taken from reanalysis (Simmons et al., 2007; Dee et al., 2011). Further details on the model experiments can be found in the supplementary material.

5.2.2 Method: Diagnostic analysis of pressure adjustment mechanism

With the objective of understanding how rainfall is formed above the Agulhas Current, we use a simple Marine Atmospheric Boundary Layer model (MABL) to investigate the relationship between the near surface wind convergence and SLP Laplacian (Lindzen and Nigam, 1987; Minobe et al., 2008): $\varepsilon u - fv = -p_x/\rho_0$, $\varepsilon v + fu = -p_y/\rho_0$, where x and y are the zonal and meridional coordinates; u and v are the zonal and meridional surface wind (frictional stresses from above the MABL are neglected); ρ_0 and p are the density and pressure in the MABL; ε denotes the constant damping coefficient; and f represents the Coriolis parameter. Surface wind convergence is linked to the SLP Laplacian by a linear relationship, $-\rho_0(u_x + v_y) = (p_{xx} + p_{yy})\,\varepsilon/(\varepsilon^2 + f^2)$. SLP and underlying SST are also related (Lindzen and Nigam, 1987) according to $+H(u_x + v_y) = -\gamma T$, where T is the SST, γ is a constant, and H is the equivalent depth of the MABL. Thus, a linear relation between surface pressure and SST may indicate an impact of the ocean on the atmosphere. Here, we compare the Laplacian of these two quantities to isolate the strength of this relation at the finer scale of the Agulhas warm core.

5. 3 Results

5.3.1 High-resolution observations over the Agulhas Current

We analyse the annual climatological mean state using satellite observations and modern atmospheric reanalysis. This reveals a clear relation between the Agulhas Current and precipitation (Fig 5.1). The Agulhas Current is 80-100 km wide and runs south-westward along the eastern coast of South Africa, following roughly the continental shelf until it retroflects and flows westward (Figure 5.1a). Here, we focus on the core of the current, which is a few degrees warmer than the surrounding ocean (contours Fig 5.1), and its coastal part where the current hugs the coast. The SST varies from 27°C off the East Coast of South Africa and 23°C in the retroflection in late summer to 22°C and 18°C respectively in late winter (not shown). Above the associated sharp SST perturbation there is a high turbulent latent heat flux (turbulent flux of moisture) up to 220 W/m² annually. The high flux is caused by the advection of oceanic colder and drier air over the current, together with the destabilising effect of SST gradient on the surface MABL and the wind speed (Lee-Thorp et al., 1999; Rouault et al., 2000). The annual mean rainfall rate from the TRMM Precipitation Radar (PR, Biasutti et al., 2012) derived observations and CFSR reanalysis (Saha et al., 2010) both show a narrow band of precipitation along the eastern coast of South Africa, just over the core of the Agulhas Current (Figure 5.1c, d). TRMM PR derived rainfall frequency show an equally striking relation. In the Agulhas region, annual precipitation average varies from 3 to 4 mm/day for TRMM PR, while a few degrees to the east it is about 1 mm/day less. CFSR has a good representation of the rain band, especially near the coast to the east, although it differs from TRMM PR by 1 to 2 mm/day (and by more over the interior of the continent which is not our domain of research).

5.3.2 Mechanisms for rainfall over the Agulhas Current

The CFSR reanalysis shows that local evaporation exceeds rainfall by between 2 to 5 mm/day over the entire region, with the greatest excess over the Agulhas Current (Fig 5.1b). Thus, local moisture supply is consistent with the broad scale rainfall over the region, as well as the enhanced rainfall over the Agulhas. However, moisture alone does not lead to rainfall; air masses must be lifted to saturation by low-level wind convergence, atmospheric convective processes, or by frontal processes. Frontal processes are likely responsible for the broad scale rainfall occurring over the region. Sharp SST gradients can anchor extra-tropical cyclones (Nakamura et al., 2004) and thereby frontal rainfall (Hand et al., 2014).

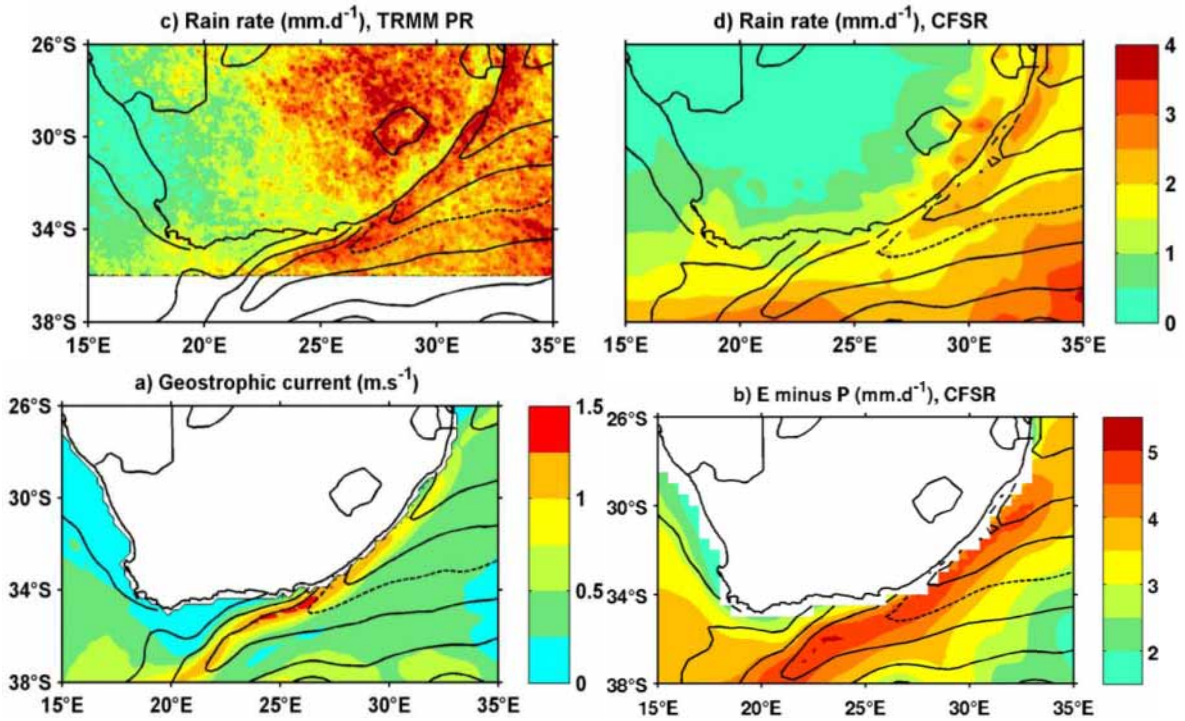

Figure 5.1. Annual climatology: a) surface geostrophic current from GlobCurrent at 0 m depth, b) CFSR evaporation minus precipitation and rain rate of c) TRMM PR, d) CFSR. Solid contours represent annual climatology of OI SST and CFSR SST respectively for a),c) and b),d) with 1° interval, dash line is 22°C SST.

This mechanism may explain rainfall patterns over the Agulhas Return Current, where the current and the southern hemisphere storm track align (Hoskins and Hodges, 2005). Sharp SST gradients can also impact surface winds and thereby generate lower-level atmospheric convergence and vertical motion, which can penetrate deep into the free troposphere (Chelton and Xie, 2010). Vertical mixing is one mechanism for the wind response to SST fronts (Wallace et al., 1989): above warm SST, the low-level atmosphere becomes unstable due to large turbulent heat fluxes. This is observed in regions with strong SST gradients (Xie, 2004), including the Agulhas Return Current (O'Neill et al., 2005). Another dynamical explanation for the wind response to SST is the pressure adjustment mechanism (Lindzen and Nigam, 1987; Back and Bretherton, 2009), in which SST modifies the MABL temperature, so that the resultant pressure anomalies induce surface wind convergence over warm SST and wind divergence over cold SST. The pressure adjustment mechanism is crucial in producing the observed pattern of wind convergence and divergence over major SST frontal regions (Minobe et al., 2008; Shimada and Minobe, 2010) Over the Gulf Stream, vertical motion penetrates deep into the free troposphere and is associated with deep atmospheric convection, and a narrow band of precipitation (Minobe et al., 2008).To diagnose the relevance of the pressure adjustment in causing the increase of rainfall over the core of the Agulhas Current, we compare the annual climatology of SST Laplacian, wind convergence and SLP Laplacian. A tight relation among these quantities indicates that warmer (colder) SST drives lower (higher) SLP, and in turn enhances surface wind convergence (divergence) (Minobe et al., 2008) (Sec. 2). The Laplacian acts as a spatial high-pass filter that highlights sharp gradient. The negative SST Laplacian (Figure 2a) exhibits a distinct structure along the eastern coast of South Africa, collocated with the rain band. (The SST Laplacian is reversed in sign for the convenience of comparing results.) The satellite-derived SST Laplacian (Figure 5.1b) is similar to the CFSR one, but stronger in amplitude because of

the data's higher resolution. Along the eastern coast of South Africa, a narrow band of 10 m wind convergence is predominant and collocated with the rainfall and negative SST Laplacian (Figure 5.2b). CFSR reproduces quite well the band of wind convergence of the higher resolution satellite based SCOW climatology (see Figure 5.1c). Convergence and divergence are also present in the retroflection region around 38.5°S, 22°E and downstream along the meandering Agulhas Return Current (Shimada and Minobe, 2010) (not shown). The SLP Laplacian shows a positive band along the eastern coast of South Africa (Figure 5.2c) that is also collocated with the SST Laplacian, wind convergence and rainfall.

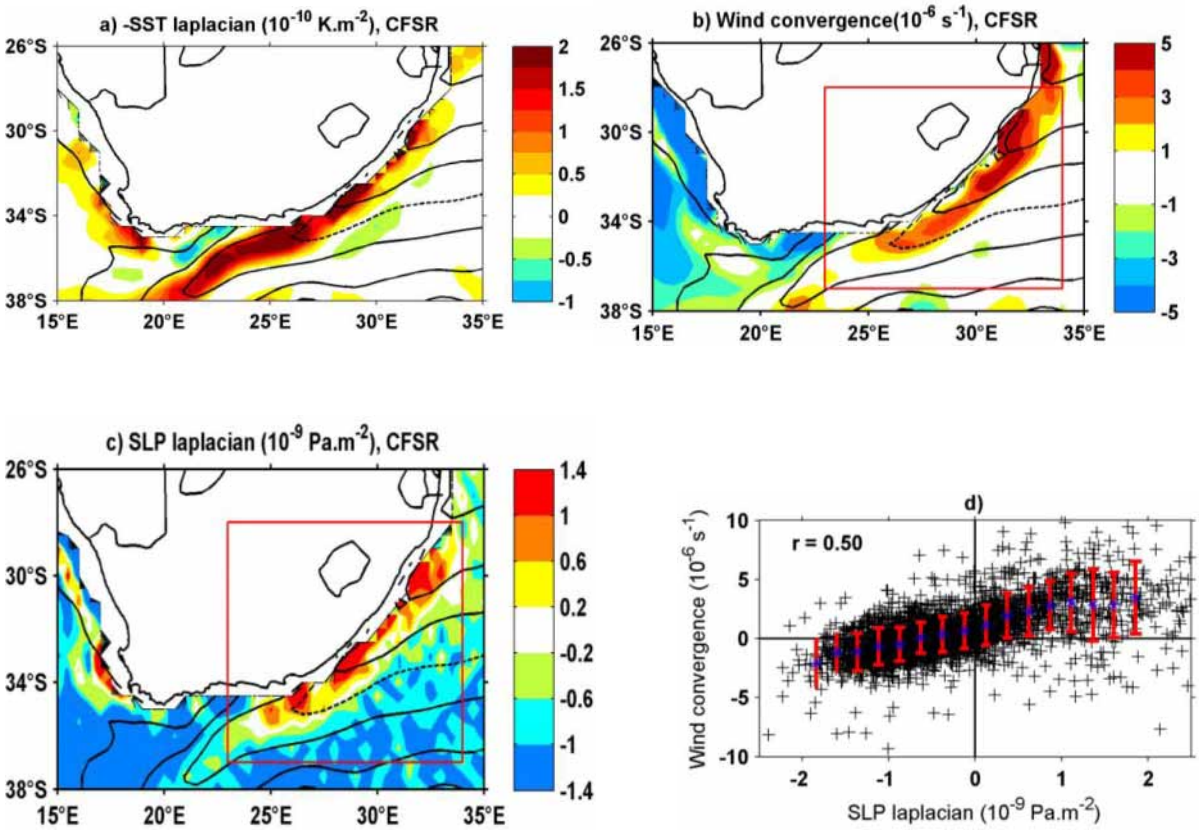

Figure 5.2. CFSR annual climatology of: a) sign reversed SST Laplacian; b) wind convergence (positives values); c) SLP Laplacian. Annual mean SST is contoured as in Figure 5.1. d) Scatter plot showing the relation between wind convergence and SLP Laplacian based on monthly climatology within the region 28-37°E, 23-34°S indicated by the red boxes in (b) and (c). Blues stars represent the means values for each interval, error bars in red are ±1 standard deviation of wind convergence for each bin of SLP Laplacian.

This indicates that SLP above the Agulhas Current is linked to the underlying SST and the pressure adjustment mechanism (Lindzen and Nigam, 1987; Minobe et al., 2008) is responsible for the low-level convergence and increased rainfall above the current. We quantify the importance of the pressure adjustment mechanism for maritime region over the Agulhas Current (28-37°S, 23-34°E; red boxes in Figure 5.2b, c). The relationship between SLP Laplacian and surface wind convergence exhibits a spatial correlation coefficient of 0.50, statistically significant at the 95% level (Figure 5.2d). The scatter plot shows that the relation between SLP Laplacian and surface wind divergence is approximately linear (Figure 5.2d). Positives values of SLP Laplacian and wind convergence are much more widespread compared to negatives values, but there is a good correspondence for positive values. The negative SST Laplacian and SLP Laplacian exhibit a stronger spatial correlation of 0.71 (Figure 5.1d). These

significant and strong relations show that pressure adjustment is important in driving rainfall over the Agulhas Current.

5.3.3 Agulhas Current impact in regional atmospheric model experiments

We perform two regional model experiments (Skamarock and Klemp, 2008) to isolate the role of the Agulhas warm core on the atmosphere (Sec. 2). The regional model driven with observed SST (CTL) reproduces the rain band along the Agulhas Current realistically (Figure 5.3a). In CTL, the Agulhas Current precipitation rate varies between 2 and 4 mm/day (Figure 5.3a) and is similar to the TRMM PR observations (Fig 5.1c), but is up to 2 mm/day more than CFSR (Fig 5.1d). Over land the simulated annual precipitation is stronger than the observations and reanalysis. This may be due to a strong sensitivity of cumulus convection schemes to the topography, a common issue with this regional model (Pohl et al., 2014). The rain band along the South Africa coast adjacent to the Agulhas Current is strongly reduced in the experiment with smoothed SST (SMTH) compared to CTL (Figure 5.3b). The difference is up to 1.4 mm/day with a maximum offshore KwaZulu-Natal (around 30.5°S; 31.5°E). The coastal rainfall in SMTH is around 40% less than in CTL (Figure 5.3a). The coastal rain band is mostly due to convective precipitation: rainfall due to large-scale circulation is almost identical between the two simulations (Figure 5.3b, c), while the coastal convective precipitation is highly diminished in SMTH (Figure 5.3d, e). Thus, the experiments show that the warmer Agulhas Current SST enhances precipitation along the eastern coast of South Africa. The wind convergence and the positive SLP Laplacian over the Agulhas Current are well simulated (Fig 5.3c, e). (Note that the simulated SLP Laplacian is influenced by inland values along the ocean grid adjacent to land probably due to orography). The difference of wind convergence between CTL and SMTH shows a well-defined maximum over the Agulhas Current (Figure 5.3d) collocated with the corresponding difference of SLP Laplacian (Figure 5.3f). The magnitude of the difference in wind convergence is about half of the magnitude of CTL, while the differences in SLP are of similar magnitude to CTL. The spatial correlation between the SLP Laplacian and wind convergence from the difference of the experiments is 0.55 (Figure 5.3g), which is similar to the value from CFSR reanalysis ($r = 0.50$). The spatial correlation between SLP Laplacian and the negative SST Laplacian from the difference of the experiments is 0.70 (Figure 5.3h), which is also similar to that from CFSR reanalysis ($r=0.71$). These results provide strong support for the pressure adjustment mechanism in anchoring the rain band over the Agulhas.

5.3.4 Vertical atmospheric structure over the Agulhas

The CFSR reanalysis shows strong upward motion in the lower troposphere between 950 and 850 hPa that is collocated with the rain band over the core of the Agulhas Current (Figure 5.4a). Above, there is a distinct structure of the wind divergence between 850 and 700 hPa, and by 650 hPa the upward motion is much reduced and there is mostly large-scale convergence (Figure 5.4d, S4a,d). The signature of the Agulhas Current is hardly found at 650 hPa within the region 28-37°E, 23-34°S. At lower-levels there are corresponding narrow bands of subsidence either side of the upward motion that contribute to a local lower tropospheric overturning circulation. Thus reanalysis suggest that convection reaches only the lower troposphere in accord with measurements done above the Agulhas Current (Lee-Thorp et al., 1999; Rouault et al., 2000). The difference between CTL and SMTH confirms that SST associated with the Agulhas Current drives this vertical circulation, which is associated with the rain band along the southern African coast (Figure 5.4c,f; S5c,f).

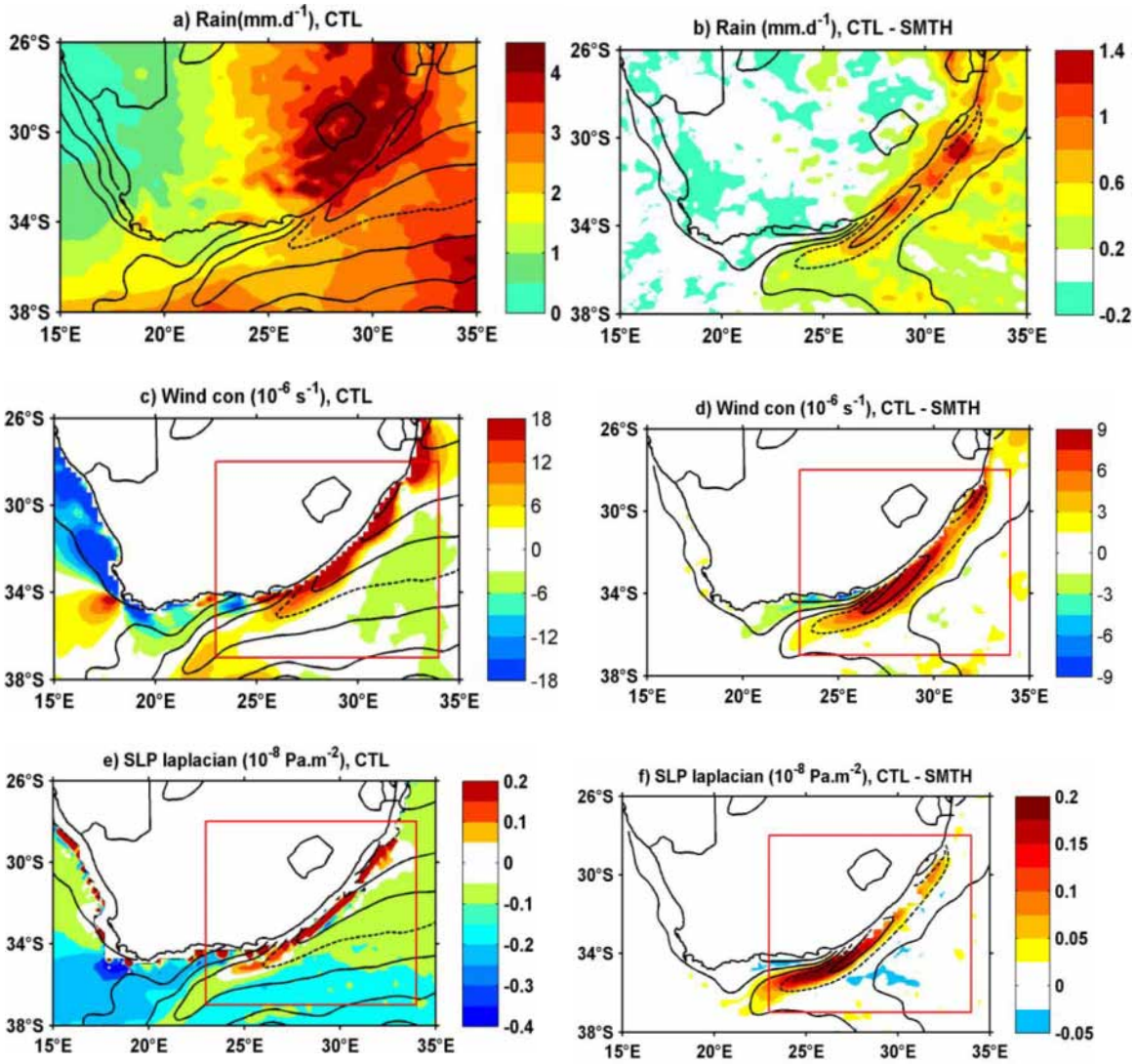

Figure 5.3. The annual mean a) rainfall, c) wind convergence, e) SLP Laplacian simulated by CTL are plotted as in Figure 5.2 with the SST contours of CTL overlaid. The impact of smoothing the SST gradients in the Agulhas Current region on these quantities is shown by the differences between CTL and SMTH in the corresponding panels to the right (b,d,f); the contours show the SST difference between CTL and SMTH (0.5°C interval and dashed line for 1°C). Shown also are the relations (g) between wind convergence and SLP Laplacian, and (h) between SLP Laplacian and sing inversed SST Laplacian for monthly climatology differences CTL and SMTH

5.4 Discussion and implication for climate modelling and prediction

We have shown using high-resolution satellite derived estimates, climate reanalysis and regional atmospheric model experiments that the warm core of the Agulhas Current drives a band of coastal precipitation off South Africa. Our results reveal that the pressure adjustment mechanism is relevant for the formation of the rain band and drives a local narrow overturning circulation in the lower troposphere. We found that spatially smoothening the SST leads to a decrease of 50% for wind convergence, of 100% for SLP Laplacian, and a 40% reduction in coastal precipitation close to the core of the Agulhas Current. This has implications for the prediction of South African weather and climate, and for understanding past and present climate.

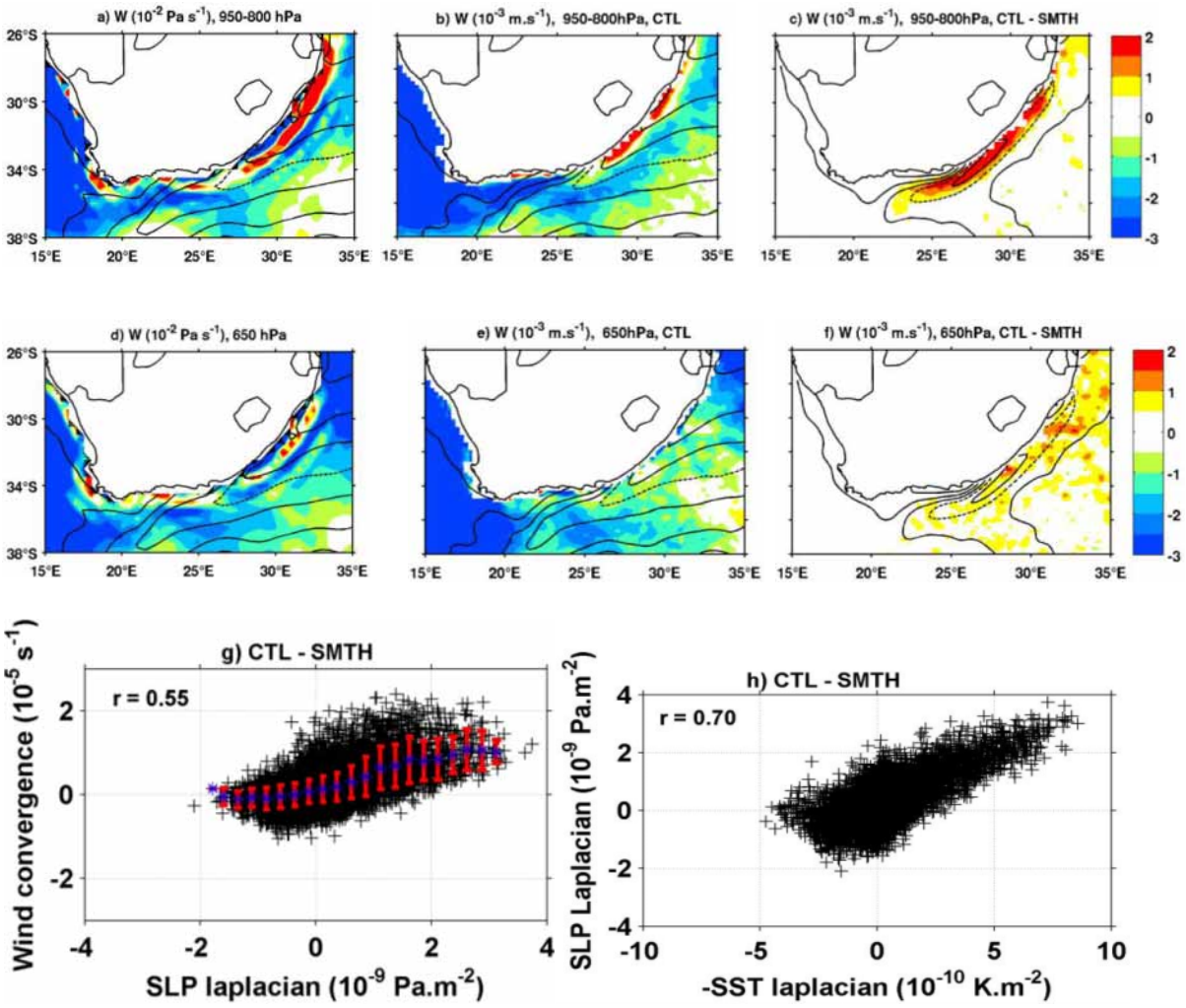

Figure 5.4. The annual mean of vertical velocity vertically averaged between 950 and 800 hPa a) CFSR, b) CTL and c) the difference between CTL and SMTH. Their respective 650 hPa vertical velocity is represented (d,e,f)

5.5 References

Beal, L.M. & Bryden, H.L. The velocity and vorticity structure of the Agulhas Current at 32 S. *Journal of Geophysical Research: Oceans*, *104*(C3), 5151-5176 (1999).

Betts, A.K. A new convective adjustment scheme. Part I: Observational and theoretical basis. *Quarterly Journal of the Royal Meteorological Society*, *112*(473), 677-691 (1986).

Biasutti, M., Yuter, S.E., Burleyson, C.D. & Sobel, A.H. Very high resolution rainfall patterns measured by TRMM precipitation radar: seasonal and diurnal cycles. Climate dynamics, 39(1-2), 239-258 (2012).

Chelton, D.B. & Xie, S.P. Coupled ocean-atmosphere interaction at oceanic mesoscales. *Oceanography*, 23(4), 52-69 (2010).

Chen, F. & Dudhia, J. Coupling an advanced land surface-hydrology model with the Penn State-NCAR MM5 modeling system. Part I: Model implementation and sensitivity. Monthly Weather Review, 129(4), 569-585 (2001).

Dudhia, J. Numerical study of convection observed during the winter monsoon experiment using a mesoscale two-dimensional model. *Journal of the Atmospheric Sciences*, *46*(20), 3077-3107 (1989).

Grell, G.A. & Freitas, S.R. A scale and aerosol aware stochastic convective parameterization for weather and air quality modeling. *Atmospheric Chemistry & Physics Discussions*, *13*(9) (2013).

Hong, S.Y. & Lim, J.O.J. The WRF single-moment 6-class microphysics scheme (WSM6). *J. Korean Meteor. Soc*, *42*(2), 129-151 (2006).

Lee-Thorp, A.M., Rouault, M. & Lutjeharms, J.R.E. Moisture uptake in the boundary layer above the Agulhas Current: A case study. *Journal of Geophysical Research: Oceans*, *104*(C1), 1423-1430 (1999).

Lindzen, R.S. & Nigam, S. On the role of sea surface temperature gradients in forcing low-level winds and convergence in the tropics. *Journal of the Atmospheric Sciences*, *44*(17), 2418-2436 (1987).

Lutjeharms, J.R.E., Mey, R.D. & Hunter, I.T. Cloud lines over the Agulhas Current. *South African Journal of Science*, *82*(11), 635-640 (1986).

Minobe, S., Kuwano-Yoshida, A., Komori, N., Xie, S.P. & Small, R.J. Influence of the Gulf Stream on the troposphere. *Nature*, *452*(7184), 206-209 (2008).

Nakamura, H., Sampe, T., Tanimoto, Y. & Shimpo, A. Observed associations among storm tracks, jet streams and midlatitude oceanic fronts. *Earth's Climate*, 329-345 (2004).

O'Neill, L.W., Chelton, D.B., Esbensen, S.K. & Wentz, F.J. High-resolution satellite measurements of the atmospheric boundary layer response to SST variations along the Agulhas Return Current. *Journal of Climate*, *18*(14), 2706-2723 (2005).

Pohl, B., Rouault, M. & Roy, S.S. Simulation of the annual and diurnal cycles of rainfall over South Africa by a regional climate model. *Climate dynamics*, *43*(7-8), 2207-2226 (2014).

Reason, C.J.C. Evidence for the influence of the Agulhas Current on regional atmospheric circulation patterns. *Journal of Climate*, *14*(12), 2769-2778 (2001).

Reynolds, R.W., Smith, T.M., Liu, C., Chelton, D.B., Casey, K.S. & Schlax, M.G. Daily high-resolution-blended analyses for sea surface temperature. *Journal of Climate*, *20*(22), 5473-5496 (2007).

Risien, C.M. & Chelton, D.B. A global climatology of surface wind and wind stress fields from eight years of QuikSCAT scatterometer data. *Journal of Physical Oceanography*, *38*(11), 2379-2413 (2008).

Rouault, M., Lee-Thorp, A.M. & Lutjeharms, J.R.E. The atmospheric boundary layer above the Agulhas Current during alongcurrent winds. *Journal of physical oceanography*, *30*(1), 40-50 (2000).

Rouault, M., Reason, C.J.C., Lutjeharms, J.R.E. & Beljaars, A.C.M. Underestimation of latent and sensible heat fluxes above the Agulhas Current in NCEP and ECMWF analyses. *Journal of Climate*, *16*(4), 776-782 (2003).

Rouault, M., Roy, S.S. & Balling, R.C. The diurnal cycle of rainfall in South Africa in the austral summer. *International Journal of Climatology*, *33*(3), 770-777 (2013).

Rouault, M., White, S.A., Reason, C.J.C., Lutjeharms, J.R.E. & Jobard, I. Ocean-atmosphere interaction in the Agulhas Current region and a South African extreme weather event. *Weather and Forecasting*, *17*(4), 655-669 (2002).

Saha, S., Moorthi, S., Pan, H.L., Wu, X., Wang, J., Nadiga, S., Tripp, P., Kistler R., Woollen, J., Behringer, D. & Liu, H. The NCEP climate forecast system reanalysis. *Bulletin of the American Meteorological Society*, 91(8), 1015-1057 (2010).

6 Origin, development and demise of the 2010-2011 Benguela Niño

6.1. Introduction

Ocean temperatures off the South-western African coast are characterized by a strong gradient between the warm tropical Atlantic and the cold Benguela current. This region is called the Angola Benguela Front and is on average located at about 17ºS (Veitch et al., 2006). Every few years, Sea Surface Temperature (SST) off the coast of Angola and Namibia reach values of up to 5ºC higher than seasonally normal. These warm events have been named Benguela Niños (Shannon et al., 1986) by analogy to their Pacific counterpart. They tend to peak in March/April (Florenchie et al., 2003, 2004; Rouault et al., 2007; Lübbecke et al., 2010). These warm events have large impacts on local fisheries (Boyer and Hampton, 2001) and on rainfall variability over south-western Africa (Rouault et al., 2003; Lutz et al., 2015). Understanding and potentially forecasting their development is thus of high socio-economic importance and the couple of months lead time between the decrease in winds along the Equator and the development of SST anomalies along the Angolan and Namibian coastline offer some predictability. While local wind forcing might play a role in the development of some of the Benguela Niño events, especially in the Benguela upwelling region (Richter et al., 2010, Junker et al., 2015), it has been shown that they are mainly generated by wind stress changes in the western equatorial Atlantic (Florenchie et al., 2003, 2004; Rouault et al., 2007; Lübbecke et al., 2010; Bachèlery et al. 2014). The hypothesis put forward is that wind stress variations in the western equatorial Atlantic generate equatorial and subsequent coastal Kelvin waves along the African coast. These waves are associated with thermocline deepening and thus subsurface temperature anomalies. They propagate along the African west coast up to the Angolan coast and generate strong SST anomalies due to a shallow thermocline there. The warm anomaly associated with Benguela Niño events is, however, not restricted to the region off Angola and down to the location of the Angola Benguela Front at 17ºS where the thermocline outcrops. Warm anomalies are observed as far south as 25ºS. Based on a regional ocean model study, Bachèlery et al. (2015) showed that at interannual time scales, remotely forced coastal trapped waves propagate poleward along the African southwest coast up to the northern part of the Benguela upwelling system. Based on model outputs, Rouault et al. (2012) attribute the warming off Namibia to southward advection of subsurface warm water. The latest strong Benguela Niños and other warm events occurred in Austral summer 1984 and 1995 (Shannon et al., 1986, Gammelsrød et al., 1998, Florenchie et al., 2003, 2004, Rouault, 2012The focus of this study is the latest warm anomaly off the southwest African coast that occurred in early 2011. This event was also special in that it started already in Austral fall 2010. It is the strongest event since 1995 and it was observed by the PIRATA array of mooring as early as October 2010. In this study, we will analyse the evolution of the 2010/2011 Benguela Niño event from its origin to its demise using direct observations from the PIRATA array, satellite estimate of SST and SSH, as well as wind stress from ERA Interim atmospheric Reanalysis. Observation will be interpreted in the light of experimentation with an Ocean Linear Model and analysis of the GODAS ocean reanalysis product.

6.2 Data, methods and models

We are using monthly fields of 1º horizontal resolution Reynolds SST (Reynolds et al., 2002) available from 1982 to 2013 and weekly and monthly TRMM TMI SST. TMI measures the microwave energy emitted by the earth and its atmosphere over a wide swath width of 760 km and can estimate SST measured through clouds. Weekly and monthly TMI SST is available in near real time from December 1997 to December 2013 at a 1/3° resolution. There are no data within 35 km from the coast. We further use weekly 1993-2013 1/3º horizontal resolution of AVISO merged altimetry SSH. We use the “reference product” that uses only two altimeters in order to have some homogeneity in the calculation

of monthly anomaly from climatology. Wind stress estimates are provides by the ERA Interim atmospheric reanalysis (Uppala et al., 2005). We also make use of the PIRATA mooring array (Bourles et al., 2008). PIRATA has recorded subsurface temperature since 2000, providing a climatology upon which the anomalies are calculated online with the NOAA PIRATA data delivery and display web site Java toolsat (http://www.pmel.noaa.gov/tao/disdel/). There are 13 temperature sensors deployed at depths of 1, 10, 13, 20, 40, 60, 80, 100,120, 140, 180, 300 and 500 m (Rouault et al., 2009). There are two pressure sensors at 300 and 500 m depth. We are using here PIRATA monthly anomalies of the 20°C isotherm as a proxy for thermocline depth anomalies and measured dynamic height from 0 to 500 Db. In order to investigate equatorial wave propagations, we use the Equatorial Atlantic Ocean Linear Model (OLM) developed by Illig et al. (2004). The linear model domain extends from 50°W to 10°E and from 28.875°S to 28.875°N, with a horizontal resolution of 2° in longitude and 0.25° in latitude. The model time-step is 2 days. It includes 6 baroclinic modes with phase speed, wind stress projection coefficient and friction derived from a high-resolution OGCM. In the present study, the model is forced by detrended ERA-Interim wind stress interannual anomalies relative to the 1980-2013 monthly climatology. We focus on the OLM Sea Level Anomaly (SLA) signal along the equator and in particular on the gravest baroclinic mode (1 and 2) long equatorial Kelvin wave contribution. In addition to the OLM Control Run (OLM-CR) simulation, a sensitivity experiment is carried out with the OLM in which no reflection of Kelvin and Rossby waves are allowed at the western and eastern boundaries. Comparing these paired experiments allows highlighting and calculating the contribution of reflected Rossby and Kelvin waves to overall signal. In addition, monthly ocean velocity and temperature fields for the time period 1980 to 2013 are taken from the National Centers for Environmental Prediction (NCEP) Global Ocean Data Assimilation System (GODAS) from the NOAA/NWS/CPC (Behringer and Xue 2004). They are available at a horizontal resolution of 1/3º latitude and 1º longitude, and the model has 40 vertical levels.

6.3. Results

6.3.1 Origin, development and demise of the warm event

In October 2010, weaker than normal easterly wind occurred in most of the Tropical Atlantic sector from 5°N to 10°S and from 50°W to 0°E (Figure 6.1 and Figure 6.2).

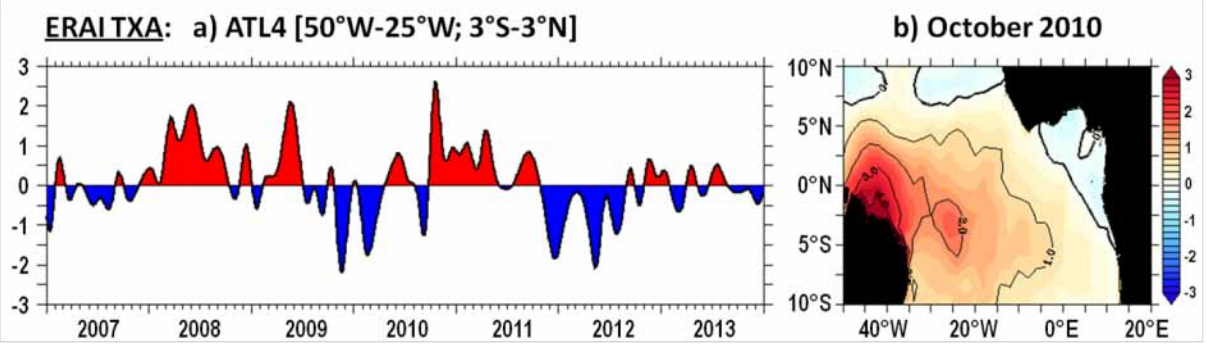

Figure 6.1: Left: Time series of monthly anomalies of zonal component of wind stress in the Western Equatorial Atlantic (WEA, averaged over [40°W-10°W; 2°S-2°N]). Right: map of monthly anomalies of zonal wind stress component in October 2010. Anomalies are computed as the departure from the 1980-2013 monthly climatology

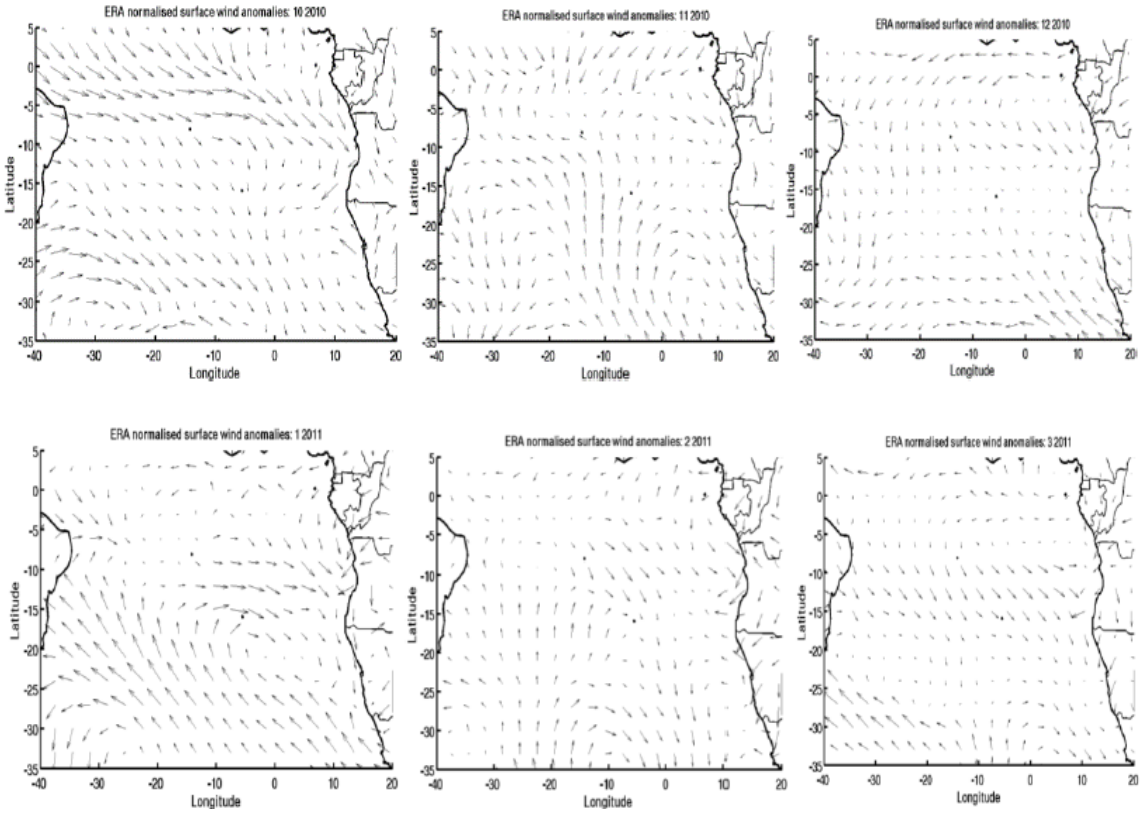

Figure 6.2: ERA Interim monthly mean anomaly divided by standard deviation from October 2010 to March 2011 (left to right and top to bottom).

According to ERA Interim reanalysis data, it was the largest decrease at the monthly scale in zonal wind speed since at least 1982 along the equator when averaged from 40°W to the African Coastline and from 2°N to 2°S with positive anomaly above 2 standard deviation (not shown). Hovmøller diagram of FLK Atlas satellite (not shown) derived zonal wind speed along the Equator confirms the results inferred from ERA Interim reanalysis. Following the decrease in equatorial easterly winds, a deepening of the thermocline larger than 30 m was observed by the PIRATA mooring array, propagating from East to West in October 2010, taking a month to reach the African coastline (Figure 6.3 and Figure 6.4). Moorings are located at 35°W, 27°W 10°W and 0°W. Data shown in Figure 6.3 and Figure 6.4 are interpolated between moorings and between depths where subsurface temperature is measured. The actual positions of the sensors are indicated by a cross on Fig 6.3.

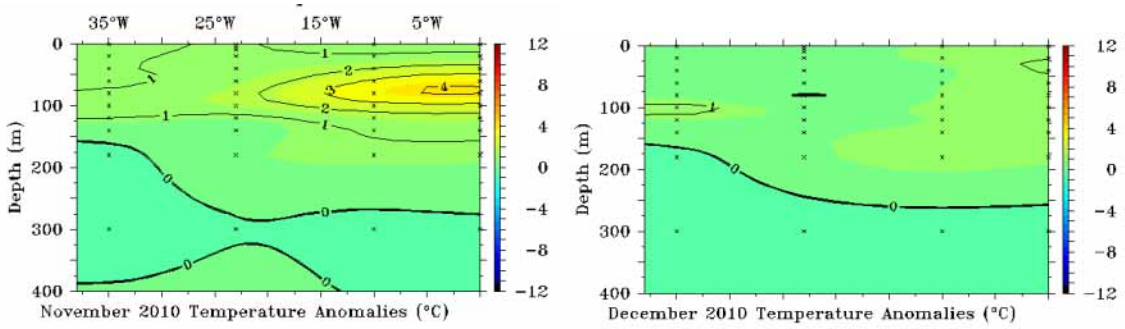

Figure 6.3: PIRATA observed subsurface temperature monthly anomaly interpolated between 4 mooring location and at depth indicated by a cross from September to December 2010 from 40 W to 0 W and from 0 to 400 m.

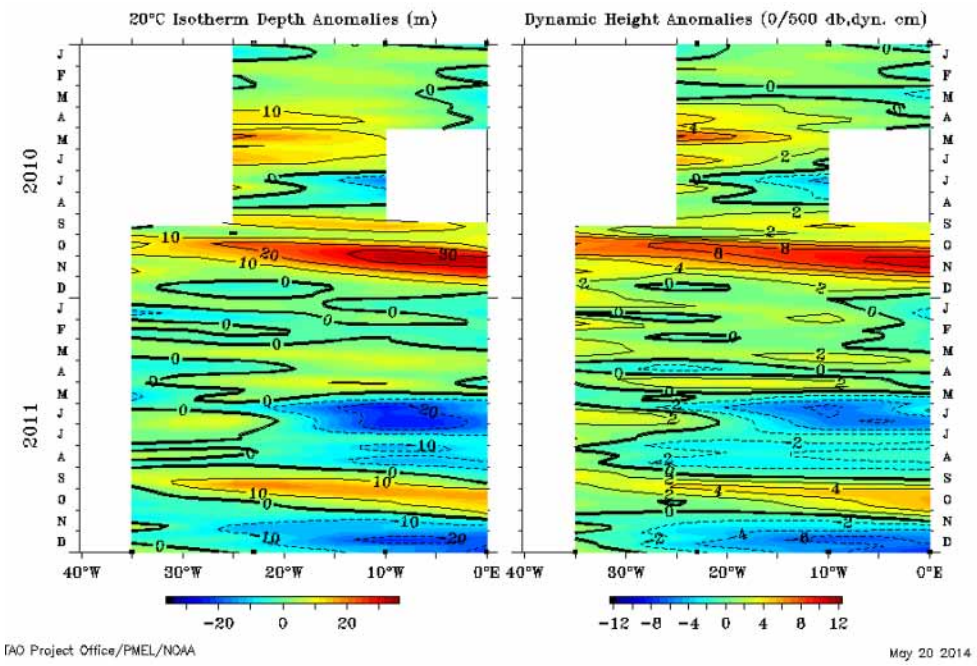

Figure 6.4: left Hovmøller diagram of 20°C isotherm depth anomaly (m) and dynamic height anomaly from 2010 (top) to 2011(bottom) inferred from PIRATA moorings and interpolated between mooring locations.

Maximum subsurface temperature anomalies of up to 3ºC are observed by the PIRATA mooring in October 2010 from 80 m to 130 m depth at 35°W, from 70 m to 120 m at 27°W,from 50 m to 90 m at 10°W and from 50 m to 80 m at 0°W. In the following month, November 2010, subsurface anomalies of 2°C to 4°C are observed only in the East of 20°W (Figure 6.3a) suggesting an eastward propagation. A maximum anomaly of 4°C is observed at 0°W at 60 m in November. In December the subsurface anomaly has vanished. PIRATA derived monthly anomalies of the 20°C isotherm depth and dynamic height monthly anomalies from 0 to 500dB (Figure 6.4) as well as altimetry derived detrended monthly interannual anomaly of sea surface height (Figure 6.5) confirm the propagation of subsurface temperature anomalies across the basin, the deepening of the thermocline and the duration of the event that lasted for two months along the Equator in October/November 2010. Figure 6.5 presents the Hovmøller diagram of monthly anomalies of SSH along the equator (left panel) from 40°W to the African coast and from 0°S to 30°S along the coast (right panel). Data is averaged between 1°S to 1°N along the equator and from the coast to 2º offshore along Southern Africa from January 2010 (bottom) to December 2011 (top). Data is detrended to remove a strong positive trend in SSH in the basin since 1993. We note that October corresponds to the maximum of climatological SSH in the Tropical Atlantic and one of the two maxima of SSH along the African coastline from 0°S to the Angola Benguela Front situated around 17°S. Climatological easterly winds also start to decrease at that time of the year in the western tropic Atlantic. In that respect, the event can be seen as an exaggeration of the annual cycle, but with important consequence further south as we will see later. The propagation of above normal SSH along the Equator is followed by a poleward propagation of positive SSH anomalies along the African coastline from 0°S to 20°S, i.e. 3 degrees further south than the Angola Benguela Front. In contrast to the equatorial region, the SSH anomalies are observed to last from November 2010 to April 2011. In May 2011 abnormal negative anomaly of SSH are detected along the eastern equator and along the African coastline, putting an abrupt end to the positive SSH anomalies along the African coast.

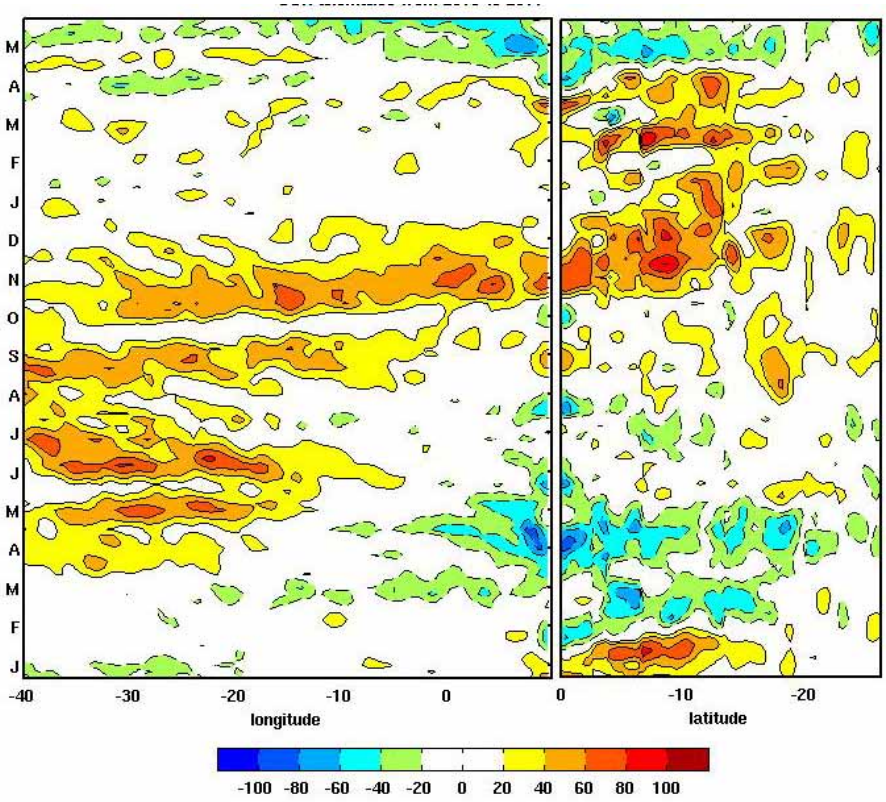

Figure 6.5: Hovmøller diagram of altimetry derived SLA anomalies from monthly climatology along the equator (averaged over 1ºS to 1ºN, left) from 40ºW to the African coastline and along the Southern African coast (averaged from coast to 2º offshore, right) from O to 25ºS from January 2010 (bottom) to May 2011 (top).

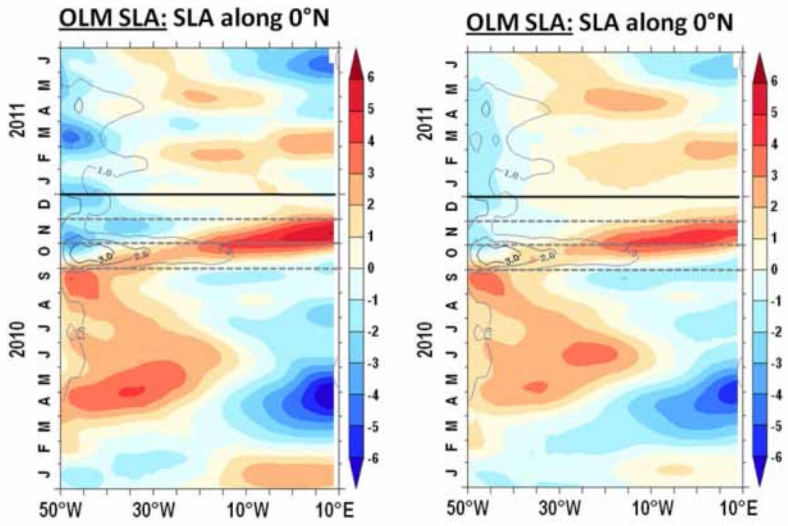

Figure 6.6: Longitude-time Hovmøller diagrams along the equator of monthly Ocean Linear Model SLA from January 2010 to June 2011. Left (right) panel: with (without) wave reflection at the meridional boundaries of the basin. Unit is cm. Contour lines highlight the ERA Interim zonal wind stress anomalies along the equator (averaged between 2°S to 2°N). Unit is in cm.

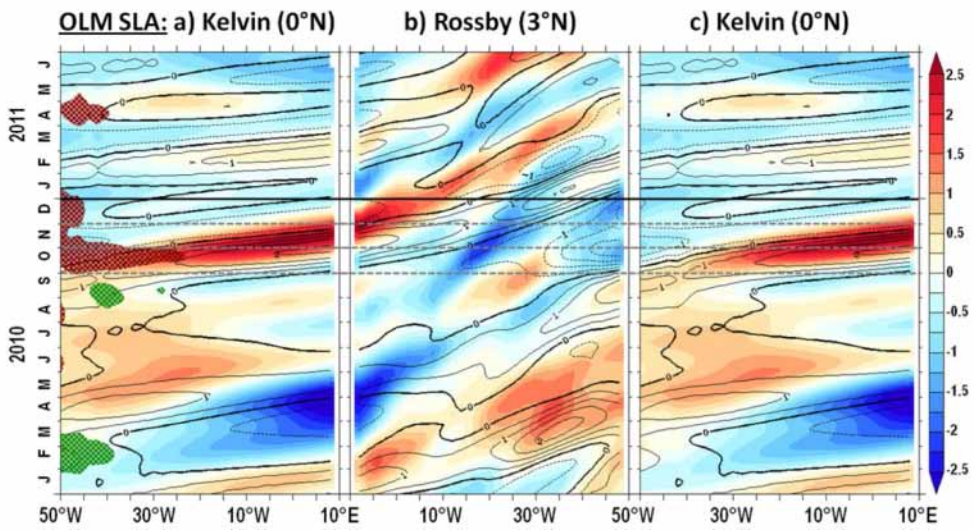

Figure 6.7: Panel a (b): Longitude-time Hovmøller diagrams of the eastward (westward) propagating Kelvin (Rossby) wave contribution to the monthly SLA along the equator (at 3°N) from the Ocean Linear Model from January 2010 to June 2011. The second baroclinic Kelvin wave contribution (dominant mode) is in colour, while contours denote the first baroclinic Kelvin wave contribution (fastest mode). Unit is cm. Note that Kelvin is repeated in panel c and the longitude axis in the Rossby is reversed in order to appreciate the reflexion at the meridional boundaries of the basin. In panel a, orange (green) shadings corresponds to zonal wind stress anomalies along the equator (averaged between 2°S-2°N). Unit is in cm.

Shoaling of the thermocline along the equator of up to 20 m propagating from west to east and concomitant negative anomalies of dynamic height are measured by the PIRATA mooring array (Figure 6.4) from 20°W to 0°W in agreement with the altimetry derived SSH anomalies (Figure 6.5). We note that ERA Interim zonal wind stress anomaly was also negative in April and May 2011 from 30°W to the African coast, indicative of stronger than normal easterly wind stress. The results obtained from the Ocean Linear Model forced by ERA Interim wind stress emphasize the role of long equatorial Kelvin and Rossby waves in the origin of this Benguela Niño event (Figure 6.6 and Figure 6.7). It confirms that anomalies of zonal wind stress in October 2010 are the main forcing of the thermocline anomaly along the Equator, in agreement with the PIRATA observations and altimetry results. Moreover, the wind forced Kelvin wave signature in October 2010 coincides with reflected Rossby waves at the Brazilian border in the Western part of the basin. The latter were forced by Kelvin waves reflected into Rossby waves at the African border in April 2010 for Kelvin wave mode 1, while the mode 2 Rossby wave appears to be forced by positive anomalies of meridional wind stress in austral winter 2010. There is a lag of one month between the arrival of Kelvin wave mode 1 and Kelvin wave mode 2 at the African border. Kelvin wave mode 1 arrived at the end of October 2010 while Kelvin wave mode 2 arrived at the end of November 2010. Together with the reflected Rossby wave, this could explain the anomaly in thermocline depth and subsurface anomaly in November 2010 observed with PIRATA. Reflections at the meridional boundaries explain 20% of the SSH anomaly along the Equator in November/December 2010. This results is obtained by calculated the ratio of SLA calculated with OLM with reflection allowed at the border and without reflection at the border (not shown). There is a small amplitude Kelvin wave along the Equator associated with a positive anomaly of zonal wind stress at that time (Figure 6.1).

6.3.2 The 2010/2011 Benguela Niño

Figure 6.8 shows a Hovmøller diagram similar to Figure 6.5 but for TRMM TMI SST monthly anomalies. Along the Equator, a moderate increase in SST is visible from October to December along the equator with SST anomalies reaching +1.5°C, while along the coast of Africa and especially at the Angola Benguela Frontal zone the increase is more substantial. It reaches values of up to 4ºC, lasts for five months and extends as far south as 25°S in the Northern Benguela upwelling. An SST anomaly larger than 1°C is first observed at the Angola Benguela front in November 2010 and appears to spread southward and northward until May 2011, when the warm event suddenly ceases. We note that, off Namibia, the upwelling favourable wind decreased in November, December 2010, and March 2011 (Figure 6.2) and this can partially explain the warming south of the Angola Benguela Front in the Northern Benguela upwelling. Wind was normal in February but failed to cool the event. In fact, there is a secondary maximum of positive SST anomaly in February corresponding to the maximum of positive SSH anomaly along the African coast at that time (Figure 6.5) which is not observed along the Equator. Fig 6.8 shows maps of monthly TRMM TMI SST anomaly from November 2010 to April 2011 in the Tropical and South Atlantic. Highest positive SST anomalies are clearly seen of Angola and Namibia. In April, lower than normal SST starts to appear north the Angola Benguela Front marking the start of the demise of the warm event.

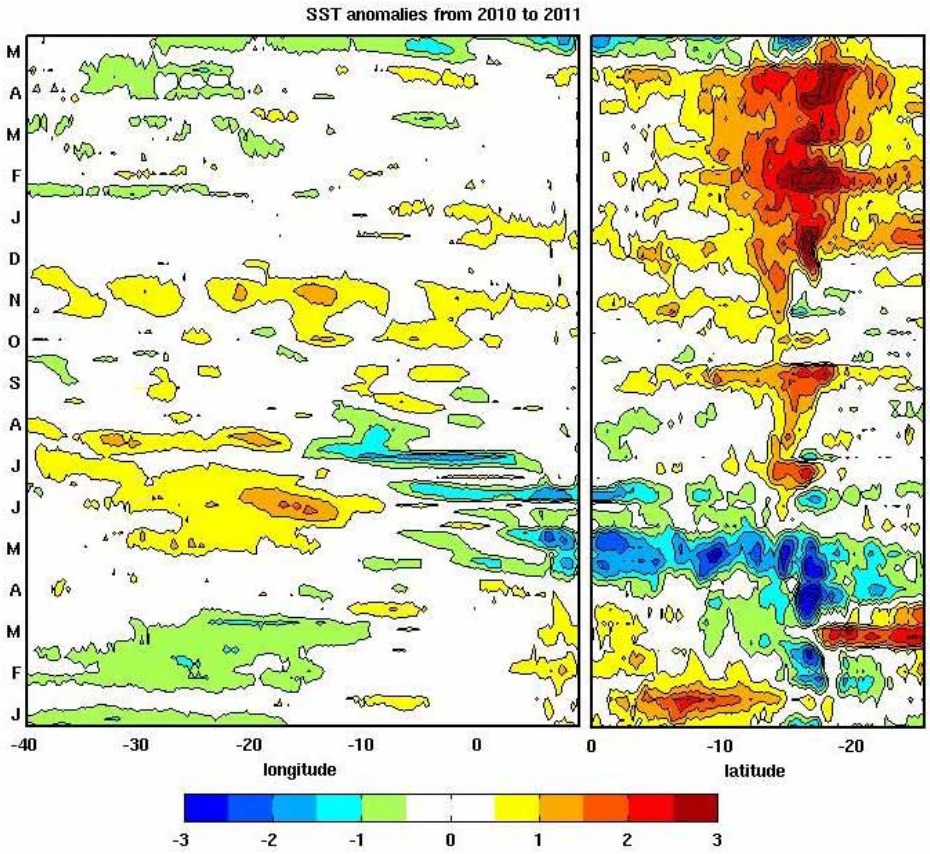

Figure 6.8: Hovmøller diagram of TRMM TMI SST anomaly from January 2010 (bottom) to May 2011 (top) along the equator (left) and along the South West African coast.

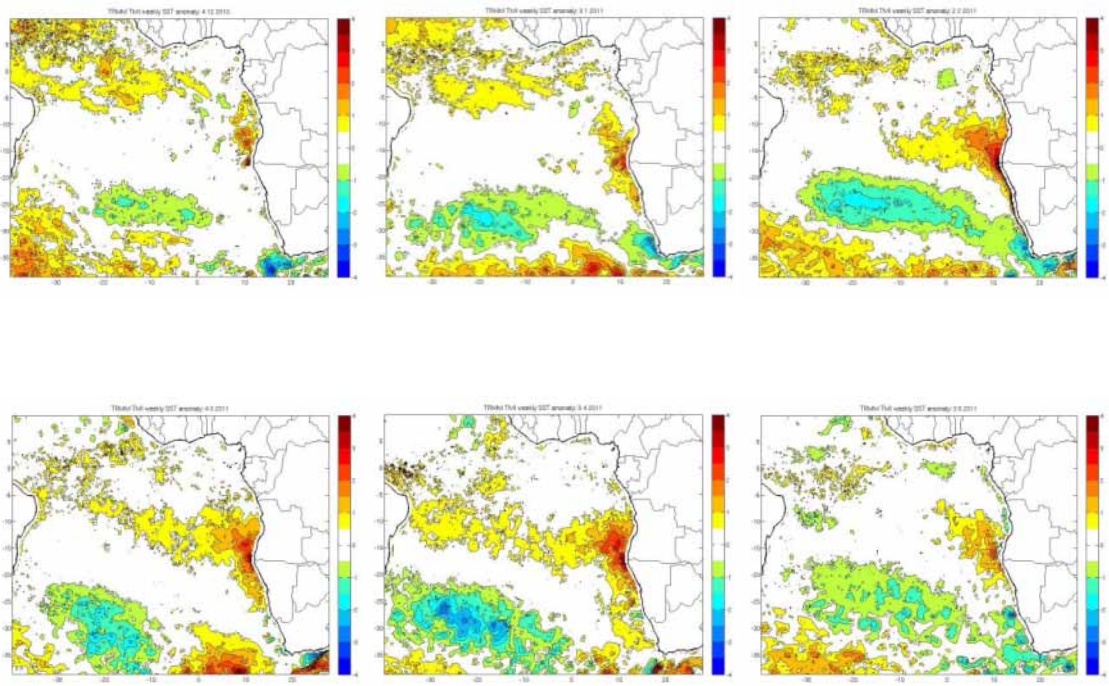

Figure 6.9: From top to bottom and left to right TRM TMI SST anomaly from monthly climatology from December 2010 to May 2011

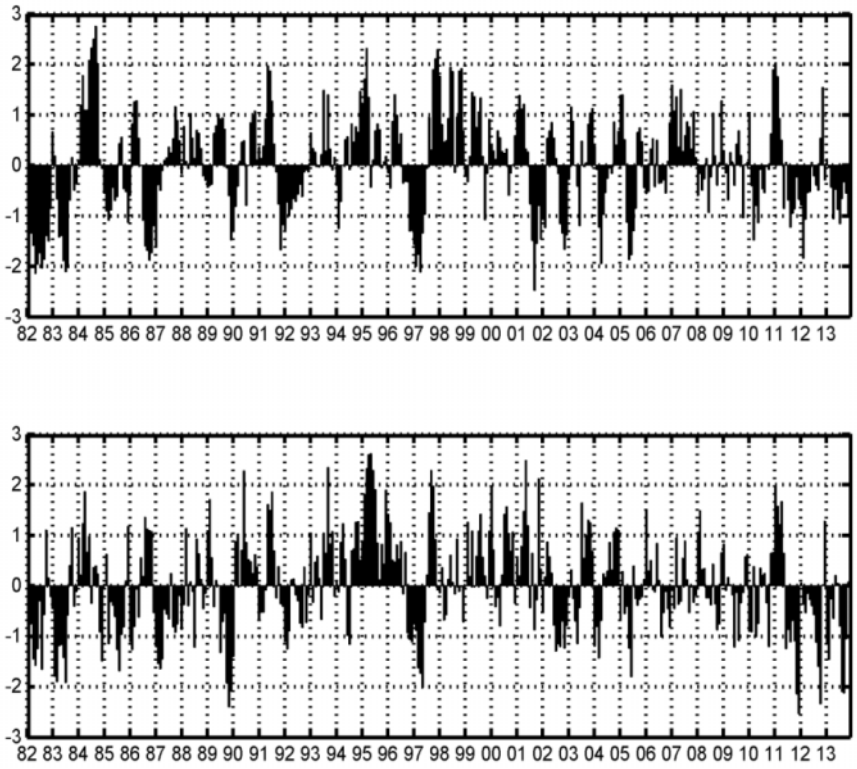

Figure 6.10: Time series of monthly detrended Reynolds SST anomalies f divided by standard deviation in Southern Angola averaged from 10ºS to 15ºS and from the coast to 1 degree offshore (top) and Northern Namibia averaged from 19ºS to 24ºS and from the coast to 1 degree offshore(bottom) from 1982 to 2013

Additionally, basin wide cooling in the subtropics all the way to the South African coastline is observed in Austral summer 2010/2011. This is consistent with the effect of the Pacific Ocean La Niña event on the South Atlantic and the South West African coastline (Colberg et al., 2004; Blamey et al., 2015). During La Niña events, a poleward shift of the Santa Helena High pressure system displaces the easterly wind poleward and leads to an intensification of upwelling favourable South-Easterly wind in South Africa (and a weakening of upwelling favourable in Namibia (Blamey et al., 2015) concurrent to the appearance of below normal SST anomalies in South Africa south of 30°S. In Namibia, the shift in high pressure triggered lower than normal South-easterly upwelling favourable South-Easterly wind in 2010/2011 and above normal SST temperature in Namibia. This mechanism has been documented by Rouault et al. (2010), Dufois and Rouault (2012) and Blamey et al. (2015). Those basin wide shifts in the high pressure system and shifts in associated wind stress involving the Tropical and South Atlantic are at the origin of Benguela Niño and Atlantic Niño events as also document by Lübbecke et al. (2010, 2014) and can happen independently of Pacific La Niña conditions. The decrease in upwelling favourable winds off Namibia indicates that part of the warming in 2010/2011 might also have been locally driven, at least for the Northern Benguela. However, this warm event was the strongest austral summer warm event in Angola and Northern Namibia and also the longest since the 1995 Benguela Niño (Figure 6.10). It was also the warmest event at the Angola Benguela Front since 1982, with positive SST anomaly exceeding 3 standard deviations, as illustrated in Figure 6.10 which shows the magnitude of the Benguela Niño events in term of standard deviation and thus allows us to compare the 2010/2011 event with other warm event. Figure 6.10 presents the detrended monthly SST anomaly estimated from Reynolds data (Reynolds et al., 2002), averaged within 1° coastal band, and normalised from 1982 to 2013 in three coastal domains. At the top, data is averaged from 10°S to 15°S, which represents South Angola area. In the middle panel, data is averaged from 16°S to 17°S and represent the Angola Benguela Front zone, while at the bottom, data is averaged from 19°S to 24°S and represent the Northern Namibian upwelling. The 2010/2011 warm event is clearly on par with major warm events that occurred in austral summer since 1982, such as 1984 (January to June) 1994/1995 (November to July), 1997/1998 (October to January) or 2001 (February to April). A peculiarity of the 2010/2011 warm event is that it started quite early in the austral summer season.

6.3.3 Southward advection of warm tropical water

As for previous Benguela Niños, the warming was not restricted to the Angola Benguela Frontal zone where the coastal tropical thermocline outcrops but was observed as far south as 25°S (Figure 6.8 and Figure 6.9). Rouault (2012) argued that such a southward expansion is related to anomalous poleward advection of warm water in the Benguela upwelling. Looking at monthly anomalies of meridional volume transport at the Angola Benguela Front at 17ºS from 0 to 250 m depth and 8.75ºE to the coast at 11.5ºE from the NCEP/GODAS ocean reanalysis product, we find that there is indeed an enhanced southward transport across the section in late 2010 (Figure 6.11). This anomalous transport corresponds to a strengthening of the seasonal cycle of modelled transport (Rouault et al., 2012). There is also a secondary anomalous poleward advection of warm water in February that can explain the secondary maximum in SST and SSH mentioned above. The equatorial subsurface warming is also well represented by GODAS, showing a strong thermocline anomaly along the equator in October to November 2010 (Figure 6.12). In May 2011, i.e. at the time of the demise of the warm event, an anomalous equatorward transport occurs in the GODAS data at the Angola Benguela Front. This suggests that the propagation of shallow thermocline anomalies – caused by stronger zonal winds along the equator – all the way to the Angola Benguela front is a way to interrupt a warm event in Angola and Northern Namibia.

6.4 References

Bachèlery, M.-L., S. Illig and I. Dadou (2015). Interannual variability in the South-East Atlantic Ocean, focusing on the Benguela Upwelling System: Remote versus local forcing, J. Geophys. Res. Oceans, 120, doi:10.1002/2015JC011168.

Behringer, D. and Y. Xue (2004). Evaluation of the global ocean data assimilation system at NCEP: The Pacific Ocean. Preprints, Eighth Symp. on Integrated Observing and Assimilation Systems for Atmosphere, Oceans, and Land Surface, Seattle, WA, Amer. Meteor. Soc., 2.3.

Blamey, L.K., L.J. Shannon, J.J. Bolton, R.J.M. Crawford, F. Dufois, H. EversKing, C.L. Griffiths, L. Hutchings, A. Jarre, M. Rouault, K. Watermeyer, H. Winker (2015). Ecosystem change in the southern Benguela and the underlying processes. Journal of Marine Systems.

Bourlès, Bernard, Rick Lumpkin, Michael J. McPhaden, Fabrice Hernandez, Paulo Nobre, Edmo Campos, Lisan Yu et al. "THE PIRATA PROGRAM." *Bulletin of the American Meteorological Society* 89, no. 8 (2008): 1111.

Boyer, D.C. and I. Hampton (2001). An overview of the living marine resources of Namibia, South Afr. J. Mar. Sci., 23, 1, 5-35.

Dufois, F., Rouault, M. (2012). Sea surface temperature in False Bay (South Africa): Towards a better understanding of its seasonal and interannual variability. Continental Shelf Research, 43, 24-35, http://dx.doi.org/10.1016/j.csr.2012.04.009

Florenchie, P., J.R.E. Lutjeharms, C.J.C. Reason, S. Masson and M. Rouault (2003). The source of Benguela Niños in the South Atlantic Ocean, Geophys. Res. Lett., 30(10), 1505, doi: 10.1029/2003GL017172.

Florenchie, P., C.J.C. Reason, J.R.E. Lutjeharms and M. Rouault (2004). Evolution of interannual warm and cold events in the southeast Atlantic Ocean, J. Clim., 17, 2318-2334.

Illig, S., Dewitte, B., Ayoub, N., du Penhoat, Y., Reverdin, G., De Mey, P., Bonjean, F., Lagerloef, G.S.E. (2004). Interannual longequatorial waves in the Tropical Atlantic from a high resolution OGCM experiment in 1981-2000. J. Geophys. Res. 109 (C2),

Junker, T., Schmidt, M. &Mohrholz, V. (2015). The relation of wind stress curl and meridional transport in the Benguela upwelling system. *Journal of Marine Systems*, *143*, 1-6.

Lübbecke, J.F., N.J. Burls, C.J.C. Reason and M.J. McPhaden (2014), Variability in the South Atlantic Anticyclone and the Atlantic Niño Mode. J. Climate, 27, (21), 8135-8150, doi: 10.1175/JCLI-D-14-00202.1

Lübbecke, J.F., C.W. Böning, N.S., Keenlyside, and S.-P. Xie (2010). On the connection between Benguela and equatorial Atlantic Niños and the role of the South Atlantic Anticyclone, J. Geophy. Res., 115, C09015, doi:10.1029/2009JC005964.

Richter, I., S. Behera, Y., Masumoto, B., Taguchi, N., Komori and T. Yamagata (2010). On the triggering of Benguela Niños – remote equatorial vs. local influences, Geophys. Res. Lett., 37, L20604, doi: 10.1029/2010GL0444461.

Rouault, M. (2012). Bi-annual intrusion of tropical water in the northern Benguela upwelling, Geophys. Res. Lett., 39, L12606, doi: 10.1029/2012GL052099.

Rouault, M., P. Florenchie, N. Fauchereau and C.J.C. Reason (2003). South East tropical Atlantic warm events and southern African rainfall, Geophys. Res. Lett., 30, doi:10.1029/2003GL014840.

Rouault, M., S. Illig, C. Bartholomae, C.J.C. Reason and A. Bentamy (2007). Propagation and origin of warm anomalies in the Angola Benguela upwelling system in 2001, J. Mar. Syst., 68, 473-488.

Rouault, M., B. Pohl and P. Penven (2010). Coastal Oceanic climate change and variability from 1982 to 2009 around South Africa, African Journal of Marine Science 32(2): 237-246

Shannon, L.V., A.J. Boyd, G.B. Brundrit and J. Taunton-Clark (1986). On the existence of an El Niño-type phenomenon in the Benguela system, J. Mar. Sci., 44, 495-520.

Uppala, S.M. et al. (2005). The ERA-40 re-analysis. Q. J. R. Meteorol. Soc. **131** 2961-3012.

Veitch, J.A., P. Florenchie and F.A. Shillington (2006). Seasonal and interannual fluctuations of the Angola-Benguela Frontal Zone (ABFZ) using 4.5 km resolution satellite imagery from 1982 to 1999, Int. J. Rem. Sens., 27, 5-6, 987-998, doi: 10.1080/01431160500127914.

7 Role of Interannual Kelvin wave propagations in the equatorial Atlantic on the Angola Benguela current system

7.1 Introduction

In the tropical Atlantic, the annual cycle is the most dominant driver, when compared to interannual variability [Xie et Carton, 2004]. At interannual timescales, the tropical Atlantic upper ocean temperature, especially along the equator and at its eastern border, is primarily controlled by equatorial wave dynamics [Illig et al., 2004]. Indeed, the sudden relaxation or intensification of easterly Tradewinds in the western equatorial Atlantic leads respectively to the generation of downwelling or upwelling Interannual Equatorial Kelvin Waves (IEKW) which propagate eastward up to the African coast. Part of the IEKW energy bounces back westwards as equatorial Rossby waves, while a substantial amount of their energy is transmitted poleward along the coast of Africa as coastal trapped waves [Bachèlery et al., 2016]. In the Pacific, along their poleward propagation, associated with anomalous alongshore currents, IEKW deepen or raise the thermocline and ultimately trigger coastal Sea Surface Temperature (SST) interannual anomalies. Such wave dynamics is thought to be at the origin of major warm and cold events in the Angola-Benguela current system also called Benguela Niños and Niñas [Florenchie et al., 2004; Lübbecke et al., 2010; Ostrowski et al., 2009; Rouault et al., 2007, Rouault, 2012] but this hypothesis has not been yet properly demonstrated to our knowledge. IEKW change the thermocline depth and can be identified through their signature in Sea Surface Height (SSH) using altimetry or moorings data. They can be modelled with Ocean Linear Model (OLM) forced only by wind stress. In order to monitor Kelvin and Rossby waves along the equator in the Tropical Atlantic, the Prediction and Research Moored Array in the Tropical Atlantic (PIRATA) program has been established since 1997 [Bourlès et al., 2008]. But no systematic study of equatorial Kelvin and Rossby waves has been conducted in the equatorial Atlantic. Such study, conducted here, provide an opportunity to link equatorial wave dynamics to warm and cold upper ocean abnormal events along the Angolan and Namibian Atlantic coastline (from 10°S to 24°S).. The prediction of these coastal extreme events is important because of their significant impacts on the regional marine ecosystem [Ostrowski et al., 2009; Blamey et al., 2015] and on the rainfall [Rouault et al., 2003, 2009]. In this paper, using outputs from an Ocean Linear Model, altimetry and PIRATA array *in situ* measurements, we demonstrate that major IEKW propagations along the equator are indeed linked to major warm and cold events in the Angola Benguela Current system. We show that IEKW signature leads the development of coastal events by about one month.

7.2 Data and model

We use monthly fields of 1 degree horizontal resolution Reynolds SST (Reynolds et al., 2002) available since 1982. We also use monthly PIRATA dynamic height anomalies [Bourlès et al., 2008] from 3 PIRATA's buoys located along the equator at 23°W, 10°W and 0°E over the 1998-2012 period. PIRATA Moorings record and sample the water column with five temperature/conductivity sensors deployed at depths of 1, 10, 20, 40 and 120 m, five temperature sensors positioned at depths of 60, 80, 100, 140 and 180 m and two temperature/pressure sensors at 300 m and 500 m along the equatorial Atlantic. They were established to detect and monitor the propagation of Kelvin and Rossby waves along the equator. In addition, we used the reference SSH gridded product distributed by AVISO, that combines data from TOPEX/POSEIDON and JASON-1 altimeters. Data are distributed by CLS with a 7-day temporal resolution and 1/3° spatial resolution. We first detrend the data because of a significant positive trend in temperature and SSH in the region and then we calculate monthly means. Interannual monthly anomalies of parameters presented below are estimated as the departure from the monthly

climatology. In order to extract the IEKW amplitude along the equator, we carry out simulation with the equatorial Atlantic Ocean Linear Model (OLM) developed by Illig et al. [2004] and used in Rouault et al. [2007].The linear model domain extends from 50°W to 10°E and from 28.875°S to 28.875°N, with an horizontal resolution of 2° in longitude and 0.25° in latitude. It includes 6 baroclinic modes with phase speed, projection coefficient and friction derived from a high-resolution OGCM. The OLM is forced by wind stress fields provided by DRAKKAR Forcing Set (DFS) version 5. DFS5.2 is similar to ERA-Interim reanalysis with 3h outputs at a horizontal resolution of 0.75 degree. Forcing is first detrended and interannual anomalies are calculated over the 1980-2012 period. The model is forced with 2 day wind stress averages obtained by cubic extrapolation of monthly means.

7.3 Results

7.3.1 Identification of abnormal SSH propagations along the equator

We present in Figure 7.1 the monthly detrended interannual anomalies of dynamic height from PIRATA (blue line), along with monthly altimetry derived and OLM derived SSH anomalies (black line and red line, respectively) from January 1998 to December 2012 at [0°E; 0°N], top, [10°W; 0°N], middle and [23°W; 0°N], bottom. The standard deviation of PIRATA derived dynamic height anomaly at [0°E; 0°N] is 2.83 cm, it is at [10°W; 0°N] and [23°W; 0°N] and is represented by the horizontal green lines over the three panels. We then define an abnormal positive and negative SSH event when detrended SSH anomalies at [0°E; 0°N] (Figure 7.2a) exceed the standard deviation of a PIRATA time series for at least 2 months in a row. Abnormal positive and negative SSH anomalies events at the eastern equatorial Atlantic are represented by red and blue rectangles respectively and their width is function of the duration of the episode. These coloured rectangles will constitute our equatorial variability index; it will be used throughout this paper and reproduced in the subsequent figures. At the monthly scale, there is a 95% significant correlation of 0.68 between PIRATA dynamic height anomalies and altimetry derived SSH anomalies at [0°E; 0°N]. There is a significant correlation of 0.65 between the OLM SSHA and PIRATA dynamic height anomalies at the same location. Gaps occur occasionally in PIRATA at different location due to vandalism or data failure so we are using altimetry and OLM SSHA to fill up the gaps. A combined analysis of PIRATA, altimetry and OLM time series allows us to identify numerous significant upwelling and downwelling IEKW. According to our classification downwelling IEKW SSH signatures occurred in 1998 (May to September), 1999 (March to July), 2001 (January to March), 2002 (March to May), 2003 (August to December), 2008 (April to July), 2008 (October to December), 2009 (April to June), 2010 (October to December), 2012 (September to November). Negative SSH events occurred in 2001/2002 (October to January), 2004 (March to June), 2005 (April to July), 2009 (June to September), 2010 (February to June), 2011 (May to August) and 2011/2012 (November to February). Those events are clearly detected in the two other moorings (Figure 7.1) at [10°W; 0°N] and [23°W; 0°N] confirming a propagation in SSH from west to east. These abnormal propagations are also noticeable in the Hovmøller plot of altimetry derived SSH anomalies (Figure 7.2) and in the Hovmøller plot of SST anomalies (Figure 7.3) along the equator (averaged from 1°S to 1°N) and along the coast (averaged from the coast to 1° offshore for SST and from the coast to 2° offshore for Altimetry). The abnormal positive SSH propagation in 2001 was reported in [Rouault et al., 2007] and linked to a warm event in the Angola-Benguela Current system while the start of the positive SSH 1999 event described here corresponds to a warm events at the Angola Benguela front reported by Mohrholz et al.[2001] and Doi et al.[2007]. The austral fall 2002 abnormal positive SSH event is described in the study of Hoffman and Brandt [2009] who mentioned strong downwelling Kelvin wave activities in 2002 along the Equator. Some abnormal negative SSH are occurring during the seasonal Atlantic cold tongue period (austral autumn and winter). For instance, during the negative SSH 2005

event, upwelling kelvin waves were identified along the Equator at the origin of that event [Hoffman and Brandt. 2009; Marin et al., 2009].

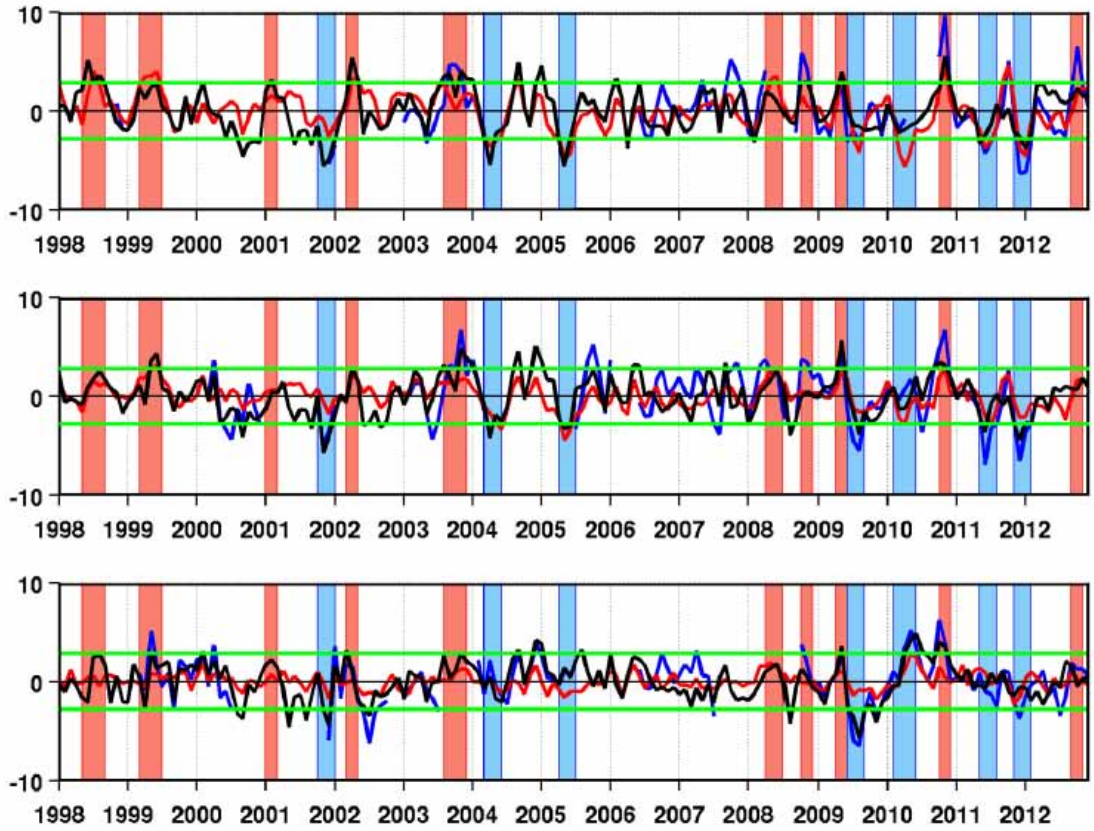

Figure 7.1: Monthly Detrended interannual anomalies of dynamic height (cm) from PIRATA in blue line, Aviso SSH monthly anomaly in black line and SSH monthly anomaly OLM in red line; top, at [0°E,0°N]; middle, at [10°W,0°N] and bottom, at [23°W,0°N]. The standard deviation derived from PIRATA is represented by the green horizontal line. Based on Figure 7.1 (top), abnormal positive and negative propagations of SLA are represented by red and blue rectangles respectively.

7.3.2 Forcing and propagation of equatorial Kelvin waves from 1998-2012

Although some major Kelvin waves propagation were mentioned in the literature, they do not make the link with the Angola Benguela Current system (Hoffman and Brandt. 2009; Marin et al., 2009). In order to document the link between Kelvin waves and the Angola-Benguela Current system, we have detrended and averaged the OLM key forcing parameter, viz. the zonal wind stress interannual anomalies (N/m^2) over the ATL4 domain (i.e. [50°W-25°W; 3°S-3°N], cf. Illig and Dewitte, 2006). This time series is displayed in Figure 7.3 (top). Most of the SSH positive and negative propagations described earlier are associated with weaker and stronger than normal easterlies wind stress anomalies respectively. 1998 exception will be discussed later. Following the decrease or the increase of the easterlies wind stress in the western equatorial Atlantic, positive or negative events respectively propagate eastwards through the PIRATA array of moorings (Figure 7.1). There are also identified in the Hovmøller plot of altimetry derived SSH anomalies (Figure 7.2). Close inspection of lag correlation between zonal wind stress anomalies and OLM SSH anomalies (not shown) reveals a 0.6 correlation significant at 95% when the western equatorial zonal wind stress anomalies lead the OLM SSH

anomalies at [0°E; 0°N] by a month. This lag of 1 month is consistent with the propagation of Kelvin wave mode 2 with an observed phase speed of 1.6 m/s, consistent with the study of Illig et al. [2004].

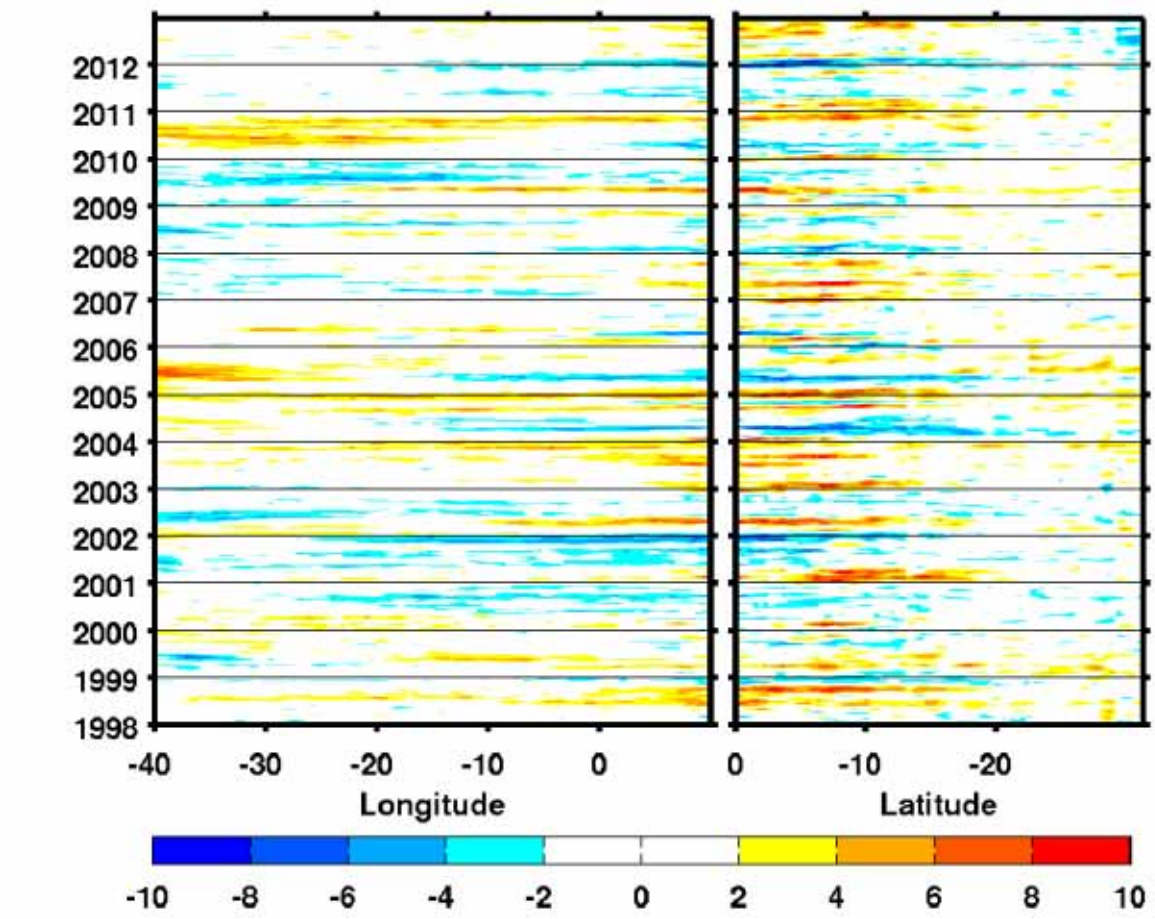

Figure 7.2: Longitude-time and latitude-time Hovmøller diagrams of weekly detrended SSH anomalies in cm, left panel averaged between 1°S and 1°N along the Equator and (right panel) along the African coast from 0°S to 30°S and averaged from the coast to 1° offshore

This leads us to focus on IEKW and examine the output of the OLM in order to characterize the role of equatorial wave dynamics in the propagations of the events. Figure 7.4 (bottom) presents the first three gravest baroclinic modes of equatorial Kelvin wave contributions to sea level variation from the eastern Atlantic as monitored by PIRATA, rather than using the wind stress amplitude in the western Tropical Atlantic, in order to forecast SST anomalies along the coast of Angola and Namibia, which will be done in the following. These different contributions are averaged between 20°W and 0°E, at 0°N. Note that similar results are obtained when averaging these 3 different contributions from 20°W to 10°E, at 0°N (not shown). This suggests that the interannual signal of Kelvin waves do not vary considerably in the eastern equatorial Atlantic. The second baroclinic mode of IEKW is the most energetic mode, followed by the first one [Illig et al., 2004; Bachèlery et al., 2016].The linear model represents well the equatorial variability of IEKW propagations. The amplitude of IEKW averaged between 20°W and 0°E, at 0°N (Figure 7.4, bottom) is compared with our equatorial index (Figure 7.1) with good agreement

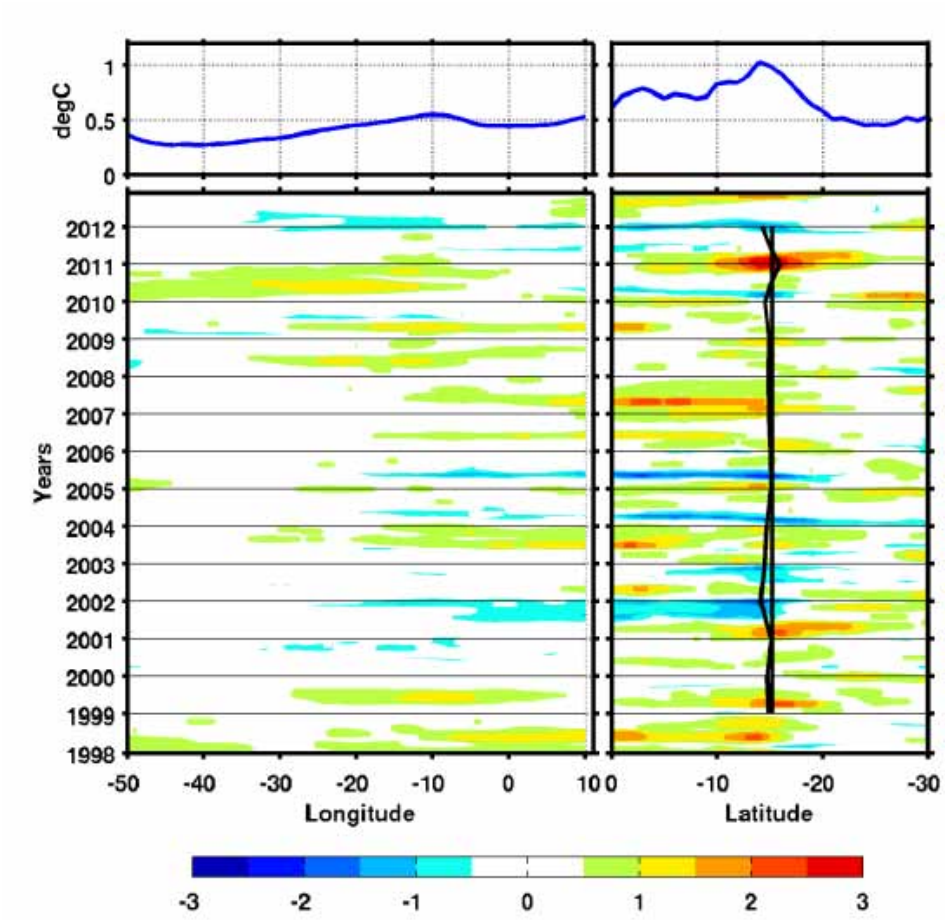

Figure 7.3: Left panel from top to bottom standard deviation and Hovmøller diagram of monthly detrended OI-SST anomalies in °C along the equator and averaged between 1°S and 1°N, and for the right panel from top to bottom standard deviation and Hovmøller latitude-time diagram of monthly detrended but along the African coast from 0°S to 30°S and averaged from the coast to 1°offshore. The mean latitude from 1998 to 2012 October to March fluctuations of the isotherm 22°C is represented by the black line and its averaged position by the straight line along the African coast.

We observe that most of western zonal wind stress anomalies are related to propagation of downwelling or upwelling IEKW respectively. These waves propagate eastward and are observed through the positive or negative abnormal SSH at the eastern equatorial Atlantic (Figure 7.1(top) and Figure 7.2 (left)). We note however that, according to what is expected from Kelvin wave dynamics and forcing, the modulation of zonal wind stress anomalies (Figure 7.4) do not match the abnormal SSH propagations along the equator for some particular years, as in 1998, 2002 or 2009. In agreement with Foltz and McPhaden [2010], the analysis of the wave sequence reveals that for some particular years (above mentioned), positive (negative) zonal wind stress interannual anomalies force preferentially westward downwelling (upwelling) Rossby waves, which in turn reflect at the Brazilian coast into Kelvin waves of opposite effect. Note that this is more likely due to the spatial pattern of the wind stress anomalies that is maximal off equator. 6.3.3 Link between equatorial variability and the Angola Benguela system. Most of the abnormal positive and negative propagation events described above are clearly observed in the Hovmøller diagram (Figure 7.2) of monthly detrended altimetry derived SSH anomalies along the equator and along the African coast all the way to the Angola Benguela From (17^{o}S) or further south. Hovmøller diagram (Figure 7.3) of monthly detrended SST somehow shows the connection between the equatorial domain and the African coastline but with less success.

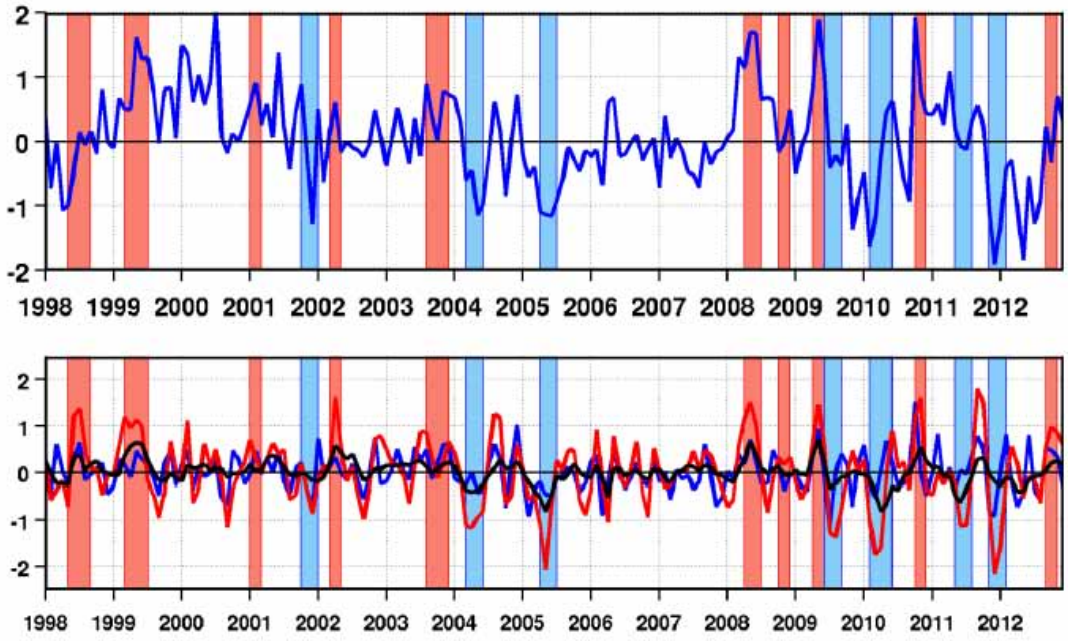

Figure 7.4: Top, Detrended monthly anomalies of zonal wind stress (N/m 2) averaged over ATL4 (50°W-25°W, 3°S-3°N); bottom, OLM detrended anomalies of Kelvin waves monthly contribution to sea level in cm: 1st baroclinic mode in blue line, 2nd baroclinic mode in red line, and 3rd baroclinic mode in black line, averaged over (20°W-0°E, at 0°N). Based on Figure 7.1 (top), abnormal positive and negative propagations of SLA are represented by red and blue rectangles respectively.

The main IEKW identified here propagate poleward when reaching the African coast. Recently, Bachèlery et al. [2016] demonstrated that the propagations along the coast were due to coastal trapped Kelvin waves, also mentioned in Ostrowski et al. [2009]. Figure 7.3 presents OI SST [Reynold et al., 2002] detrended monthly anomalies from 1998 to 2012 along the Angola Benguela Current system. On top, we have the Southern Angola domain with data averaged from 10°S to 15°S and one degree from the coast; in the middle, the Angola Benguela Frontal zone with data averaged from 16.5°S to 17.5°S and one degree from the coast; at the bottom, the Northern Namibia upwelling domain with data averaged from 19°S to 24°S and one degree from the coast. After removing a significant warming trend in the region [Blamey et al., 2015], monthly anomalies are calculated relative to the monthly climatology over the 1998-2012 period. A standard deviation of 0.5°C of the SST anomalies in the Angola Benguela Front domain is estimated. It is represented in Figure 7.5 by the horizontal blue lines over the three panels. Here we define a Benguela Niño or a Benguela Niña as a period in which the detrended SST anomalies in the 3 zones exceed the standard deviation for at least 3 months in a row in least 2 of the 3 domains. Most major warm and cold events along the African coast especially in Southern Angola and Northern Namibia domains are linked to the equatorial variability index, IEKW propagations and western zonal wind stress anomalies.

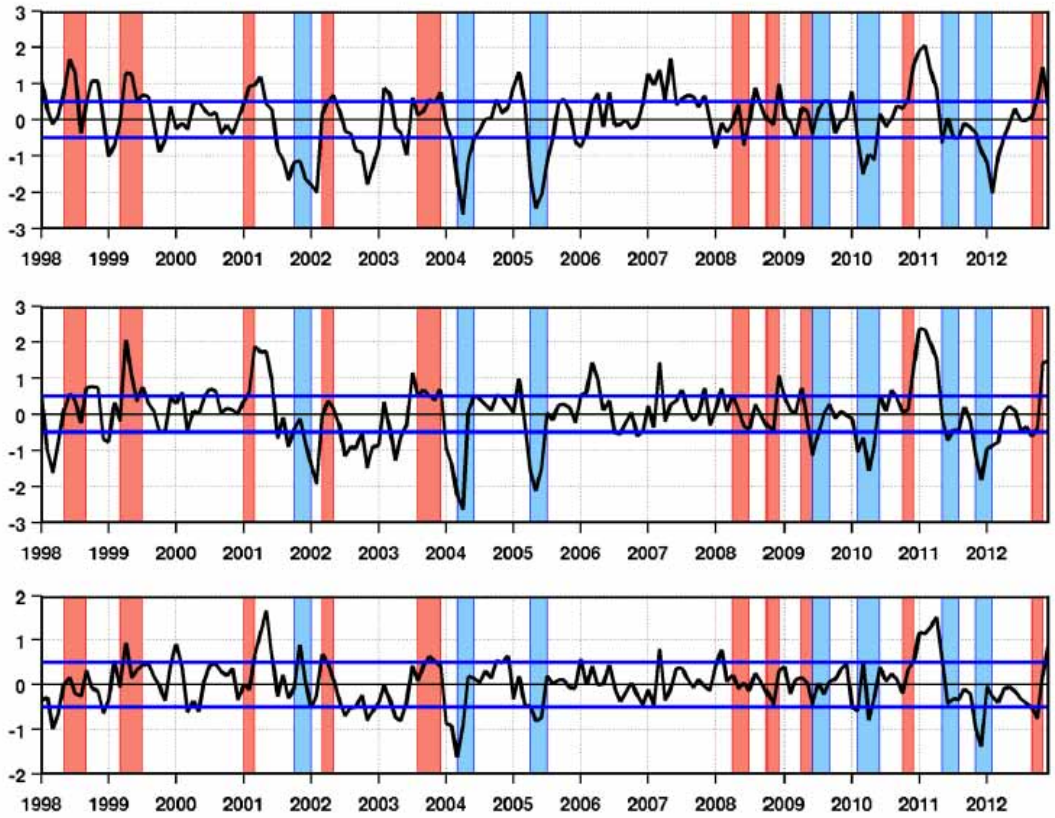

Figure 7.5: Monthly detrended anomalies of SST (°C) in (top) Southern Angola averaged from 10°S to 15°S and from the coast to 1° offshore, (middle) Angola Benguela Front averaged from 16.5°S to 17.5°S and from the coast to 1°offshore and (bottom) Northern Namibia averaged from 19°S to 24°S and from the coast to 1°offshore. The standard deviation is represented by the blue horizontal line. Based on Figure 7.1 (top), abnormal positive and negative propagations of SLA are represented by red and blue rectangles respectively.

Based on our criteria, we have selected 5 extreme warm events: in 1999 (March to August), 2001 (January to May), 2008 (November to December), 2010/2011 (November to April), 2012 (October to December) and 5 cold events in 2001/2002 (December to February), 2004 (January to April), 2005 (April to June), 2010 (February to May), 2011/2012 (November to March). Most of these Benguela Niños were already identified previously [Rouault et al., 2007; Ostrowski et al., 2009; Lübbecke et al., 2010; Rouault, 2012] except for the Benguela Niño 2008, 2011/2012 and 2012/2013. There is little in the literature concerning Benguela Niña after 2002. The 1999 Benguela Niño at the Angola Benguela Front was described by Doi et al. [2007] and Mohrholz et al. [2001]. A 0.4 lag correlation statically significant at 95% is found, when IEKW mode 2 averaged between 20°W-0°E at 0°N leads SST anomalies in the Southern Angola domain by 1 month. There is no significant correlation with the ABF and Northern Namibia domains. We observe in Figure 7.5, slow propagations of SST anomalies as we move from Southern Angola to Northern Namibia. The persistence and slow propagations of SST anomalies from Southern Angola to Northern Namibia in those domains were already mentioned in Rouault. [2012] were attributed to advection of warm tropical water in the Northern Benguela upwelling domain. He found significant lag correlations between the two domains when Southern Angola SST anomalies lead Northern Namibia SST anomalies by one to four months. Also local effect could modulate the SST of those events south of the ABF.

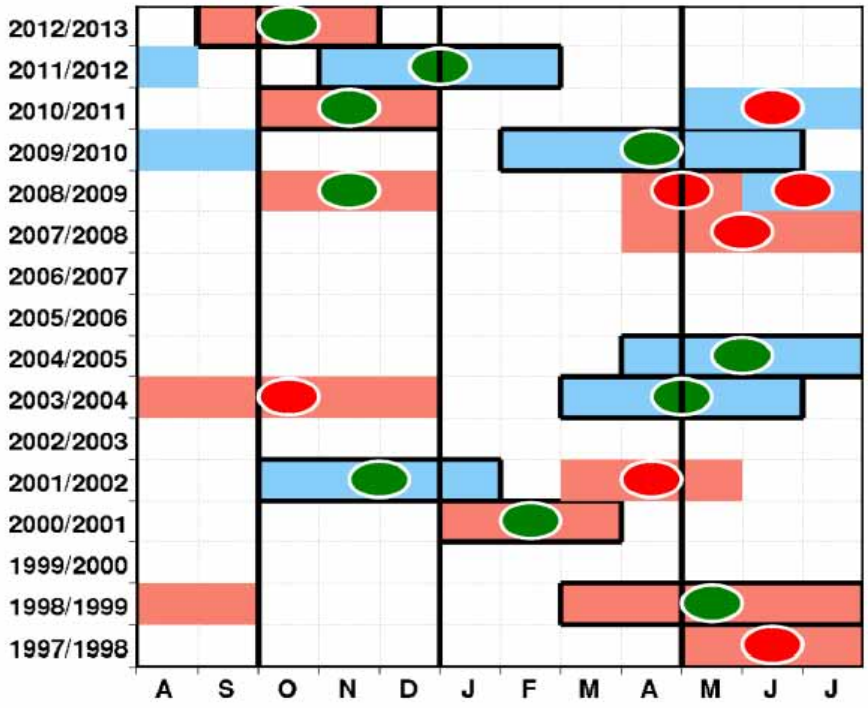

Figure 7.6: Score of prediction of coastal warm and cold events using the equatorial variability index from 1998 to 2012. Red rectangles with green circle inside and bold contours represent extreme coastal warm events which match abnormal equatorial SSH propagations. Red rectangles with red circle inside represent coastal warm events which do not match abnormal equatorial SSH propagations. Red rectangles with green circle inside represent coastal warm events which match with abnormal equatorial SSH propagations. Blue rectangles with green circle inside and bold contours represent extreme coastal cold events which match with abnormal equatorial SSH propagations. Blue rectangles with red circle inside represent coastal cold events which do not match with abnormal equatorial SSH propagations.

We summarize our equatorial variability index in relation with Benguela Niños and Niñas in Figure 7.6. The red rectangles describe the positive propagation and their duration while the blue rectangles describe the negative events. Red circles inside a rectangle mean no match between equatorial propagations and warm or cold events in the Angola-Benguela Current system. Green circle mean good match between equatorial propagations and extreme warm or cold. The circle location is placed in the middle of the rectangle arbitrarily. From October to April nine out of twelve events matches. There is more of a mismatch from May to June. In general, From Figure 7.5 and Figure 7.6**,** we observed a good score without including the local wind stress forcing and stratification effects. The 1998 mismatch is explained by Foltz and McPhaden. [2010] who highlighted the retroflection at the Brazilian coast of a Rossby waves forced by stronger Tradewinds into a downwelling Kelvin waves that lead to the 1998 positive propagation along the equator. In general, October to April seems the best time for the successful prediction of the warm and cold events in the Angola Benguela current system. Our study is consistent with the modeling study of Bachèlery et al. [2016] who observed that at interannual timescales, remote equatorial forcing is more efficient than local forcing along the Angola Benguela coast. But the effects of the local forcing, unfavourable or favourable local upwelling wind and stratification are not negligible since they could modulate the signature of an equatorial propagation. Also Polo et al. [2008a] studied the intraseasonal EKW and found 2 dominant periods for the appearance of KW: Austral Spring (September-December) for downwelling KW and Austral summer (November-January) for upwelling KW. The favourable season where a potential propagation of the 2nd baroclinic

mode of Kelvin waves could create a Benguela Niño or Niña one month later is mostly between October and April.

7.4 Conclusion

We demonstrate here that warm and cold events in the Angola Benguela Current system, also called Benguela Nino and Niñas, are remotely forced by Kelvin waves propagation in the tropical Atlantic, especially the 2nd baroclinic mode. This confirms the hypotheses emitted by several authors. Major variations in thermocline depth at the origin of those events are observed by PIRATA and altimetry and simulated by an Ocean Linear Model forced by wind stress only. An Ocean Linear Model can be easily implemented in real time using satellite estimate or model output and easily implemented. PIRATA data and altimetry data are also available in real time and can be used in an early warning system. An Index based on PIRATA data at [0 S, 0 N] seems to work better than an index based on Wind stress anomalies in the Western Tropical Atlantic along the equator. Altimetry derived SSH link the equatorial propagation to the coastal region. It seems that local forcing has little to do with the generation of most of major cold and warm events although they could modulate their intensity. The PIRATA array of mooring is crucial to the observation of those Kelvin waves and must be maintained. At last, the study opens the possibility to forecast Benguela Niños and Niñas, especially from October to April, using an Ocean Linear Model forced by wind speed, altimetry and PIRATA data. Tide gauge and current meter available in real time in Angola and Namibia would complete the system. Further work will involve studying the reason why some events did not fit our scenario although some answer can already be found in the literature and also better ascertain the relation between the Southern Angola and Northern Namibia domains.

7.5 References

Bachèlery, M.-L., S. Illig and I. Dadou (2016). Interannual variability in the South-East Atlantic Ocean, focusing on the Benguela Upwelling System: Remote versus local forcing, J. Geophys. Res. Oceans, 120, doi:10.1002/2015JC011168.

Blamey, L.K., L.J. Shannon, J.J. Bolton, R.J.M. Crawford, F. Dufois, H. EversKing, C.L. Griffiths, L. Hutchings, A. Jarre, M. Rouault, K. Watermeyer, H. Winker (2015). Ecosystem change in the southern Benguela and the underlying processes. Journal of Marine Systems.

Bourlès, Bernard, Rick Lumpkin, Michael J. McPhaden, Fabrice Hernandez, Paulo Nobre, Edmo Campos, Lisan Yu et al. "THE PIRATA PROGRAM." *Bulletin of the American Meteorological Society* 89, no. 8 (2008): 1111.

Doi, T., Tozuka, T., Sasaki, H., Masumoto, Y., Yamagata, T. (2007). Seasonal and interannual variations of oceanic conditions in the Angola Dome. *J PhysOceanogr*, 37, 2698-2713.

Florenchie, P., C.J.C. Reason, J. R.E. Lutjeharms and M. Rouault (2004). Evolution of interannual warm and cold events in the southeast Atlantic Ocean, J. Clim., 17, 2318-2334.

Illig, S., Dewitte, B., Ayoub, N., du Penhoat, Y., Reverdin, G., De Mey, P., Bonjean, F., Lagerloef, G.S.E. (2004). Interannual long equatorial waves in the Tropical Atlantic from a high resolution OGCM experiment in 1981-2000. J. Geophys. Res. 109 (C2), C02022. doi:10.1029/2003JC001771.

Lübbecke, J.F., C.W. Böning, N.S. Keenlyside and S.-P. Xie (2010). On the connection between Benguela and equatorial Atlantic Niños and the role of the South Atlantic Anticyclone, J. Geophy. Res., 115, C09015, doi:10.1029/2009JC005964.

Marin, F., G. Caniaux, H. Giordani, B. Bourle`s, Y. Gouriou and E. Key (2009). Why were sea surface temperatures so different in the eastern equatorial Atlantic in June 2005 and 2006? J. Phys. Oceanogr., 39(6), 1416-1431, doi:10.1175/2008JPO4030.1.

Mohrholz, V., Schmidt, M., Lutjeharms, J.R.E. (2001). The hydrography and dynamics of the Angola-Benguela frontal zone and environment in April 1999. South Afr. J. Sci. 97, 199-208.

Polo, I., A. Lazar, B. Rodriguez-Fonseca and S. Arnault (2008). Oceanic Kelvin waves and tropical Atlantic intraseasonal variability: 1. Kelvin wave characterization, *J. Geophys. Res*., 113, C07009, doi:10.1029/2007JC004495

Ostrowski, M., J.C B. da Silva, and B. Bazik-Sangolay (2009). The response of sound scatterers to El Niño- and La Niña-like oceanographic regimes in the southeastern Atlantic, ICES J. Mar. Sci., 66(6), 1063-1072,doi:10.1093/icesjms/fsp102.

Rouault, M. (2012). Bi-annual intrusion of tropical water in the northern Benguela upwelling, Geophys. Res. Lett., 39, L12606, doi: 10.1029/2012GL052099.

Rouault, M., P. Florenchie, N. Fauchereau and C.J.C. Reason (2003). South East tropical Atlantic warm events and southern African rainfall, Geophys. Res. Lett., 30(5), 8009, doi:10.1029/2002GL014840

Rouault, M., S. Illig, C. Bartholomae, C.J.C. Reason and A. Bentamy (2007). Propagation and origin of warm anomalies in the Angola Benguela upwelling system in 2001, J. Mar. Syst., 68, 473-488.

Rouault, M., J. Servain, C.J.C. Reason, B. Bourlès, M.J. Rouault and N. Fauchereau (2009). Extension of PIRATA in the tropical South-East Atlantic: An initial one-year experiment, Afr. J. Mar. Sci., 31(1), 63-71, doi:10.2989/AJMS.2009.31.1.5.776.

Schouten, M.W., R.P. Matano and T.P. Strub (2005). A description of the seasonal cycle of the equatorial Atlantic from altimeter data, Deep SeaRes., Part I, 52, 477-493, doi:10.1016/j.dsr.2004.10.007.

Xie, S.-P. and J.A. Carton (2004). Tropical Atlantic variability: Patterns, mechanisms, and impacts, in Earth Climate: The Ocean-Atmosphere Interaction, Geophys. Monogr. Ser., vol. 147, edited by C. Wang, S.-P. Xie, and J. A. Carton, pp. 121-142, AGU, Washington, D.C.